Study of partial discharge and gas breakdown phenomena at a triple junction under various pressure and temperature conditions

Robert Szilágyi

To cite this version:

Robert Szilágyi. Study of partial discharge and gas breakdown phenomena at a triple junction under various pressure and temperature conditions. Electric power. Université Paris-Saclay, 2024. English. NNT : 2024UPAST007 . tel-04548906

HAL Id: tel-04548906
https://theses.hal.science/tel-04548906

Submitted on 16 Apr 2024

Study of partial discharge and gas breakdown phenomena at a triple junction under various pressure and temperature conditions

Étude des phénomènes de décharges partielles et de claquage du gaz à partir d'un point triple sous conditions variées de pression et de température

Thèse de doctorat de l'université Paris-Saclay

École doctorale n° 575, electrical, optical, bio : physics and engineering (EOBE)
Spécialité de doctorat : Génie électrique
Graduate School : Sciences de l'ingénierie et des systèmes
Référent : Faculté des sciences d'Orsay

Thèse préparée dans l'unité de recherche **Laboratoire de Génie Électrique et Électronique de Paris** (Université Paris-Saclay, CentraleSupélec, CNRS),
sous la direction de **Philippe MOLINIÉ**, Maître de Conférences à CentraleSupélec,
le co-encadrement de **Michael J. KIRKPATRICK**, Maître de Conférences à CentraleSupélec,
le co-encadrement d'**Emmanuel ODIC**, Professeur à CentraleSupélec,
et le co-encadrement de **Philippe DESSANTE**, Professeur à CentraleSupélec

Thèse soutenue à Paris-Saclay, le 08 février 2024, par

Robert SZILÁGYI

Composition du Jury

Membres du jury avec voix délibérative

Gilbert TEYSSÈDRE Directeur de Recherche, Université de Toulouse, LAPLACE	Président
Nelly BONIFACI Maître de Conférences, HDR, Université Grenoble Alpes, G2ELab	Rapporteur & Examinatrice
Noureddine ZOUZOU Maître de Conférences, HDR, Université de Poitiers, Institut Pprime	Rapporteur & Examinateur
Jinbo BAI Directeur de Recherche, Université Paris-Saclay, LMPS	Examinateur
Stéphane DUCHESNE Professeur, Université d'Artois, LSEE	Examinateur
Pedro LLOVERA-SEGOVIA Maître de Conférences, Universitat Politècnica de València, ITE	Examinateur

THESE DE DOCTORAT

NNT : 2024UPAST007

Titre : Étude des phénomènes de décharges partielles et de claquage du gaz à partir d'un point triple sous conditions variées de pression et de température

Mots clés : décharges partielles (DP), claquage du gaz, point triple, conditions variées de pression et de température, alumine

Résumé : Les points triples (jonction entre un gaz, un isolant solide et un conducteur), présents dans de nombreuses applications industrielles, constituent, en raison du renforcement local du champ électrique, une zone critique pour le déclenchement des décharges électriques. De plus, ces points triples peuvent être exposés à des conditions environnementales parfois sévères. Ainsi, l'objectif de cette étude était de parvenir à une meilleure compréhension des phénomènes de décharges partielles (DP) et de claquage du gaz à partir d'un point triple sous différentes conditions de pression et de température. En particulier, ont été examinées les tensions-seuil d'amorçage/d'extinction des DP (*Partial Discharge Inception Voltage*, PDIV/*Partial Discharge Extinction Voltage*, PDEV) et la tension de claquage du gaz en surface de l'isolant solide (*Flashover Voltage*, FOV). Dans ce contexte, un dispositif expérimental a été conçu et exploité dans une atmosphère d'azote dont la pression était comprise entre 50 mbar et pression atmosphérique pour des températures imposées variant de l'ambiante à 400 °C. Une attention particulière a été accordée à l'alumine, matériau isolant solide qui peut être utilisé dans cette plage de température. L'influence de la température sur la PDIV (et PDEV) d'une part, et la FOV d'autre part, a été caractérisée, analysée et interprétée au moyen de mesures diélectriques, d'imagerie rapide et de simulations numériques. Enfin, dans les conditions de température élevée et malgré les précautions prises, une oxydation de l'électrode haute tension a été observée dont l'influence sur la PDIV a été analysée.

Title: Study of partial discharge and gas breakdown phenomena at a triple junction under various pressure and temperature conditions

Keywords: partial discharges (PD), gas breakdown, triple junction, various pressure and temperature conditions, aluminium oxide

Abstract: Triple junctions (between a gas, a solid insulator, and a conductor), which are present in numerous industrial applications, constitute a critical zone for the triggering of electrical discharges due to local reinforcement of the electric field. In addition, these triple points can be exposed to harsh environmental conditions. The aim of this study was therefore to come to a better understanding of the phenomena of partial discharge (PD) and gas breakdown from a triple junction under different pressure and temperature conditions. In particular, the Partial Discharge Inception Voltage (PDIV), the Partial Discharge Extinction Voltage (PDEV), and the Flashover Voltage (FOV) of surface breakdown of the solid insulator were examined. In this context, an experimental set-up was designed and operated in a nitrogen atmosphere ranging from 50 mbar to atmospheric pressure, for imposed temperatures varying from ambient to 400 °C. Particular attention was paid to aluminium oxide, a solid insulator material that can be used in this temperature range. The influence of temperature on PDIV (and PDEV) on the one hand, and FOV on the other, was characterised, analysed and interpreted by means of dielectric measurements, high-speed imagery and numerical simulations. Finally, under high temperature conditions and despite the precautions taken, an oxidation of the high voltage electrode was observed whose influence on the PDIV was analysed.

Acknowledgements

To begin with, I would like to thank my supervisors Philippe Molinié, Mike Kirkpatrick, Emmanuel Odic, Philippe Dessante and Giacomo Galli. Due to their support from all points of view, they have made it possible for me to achieve the objectives of this doctoral thesis. Therefore, I want to express my appreciation for all their contributions to this work, the valuable input during the design of the experimental setup and the experimental work, the scientific discussions of the results, the constructive feedback on the articles and the manuscript and all the other things which were related to the thesis and, in general, to everyday life in the laboratory.

I would also like to thank the members of the jury, the president Gilbert Teyssèdre, Jinbo Bai, Stéphane Duchesne, Pedro Llovera-Segovia as well as Nelly Bonifaci and Noureddine Zouzou for agreeing to be examiner of my thesis.

Then, I would like to thank the director of the laboratory, Claude Marchand, for giving me the opportunity to work in the laboratory, not only during my thesis but also already during my internship which strengthened my decision to do a doctoral programme.

Besides, I want to thank all the members of the laboratory who contributed with their support in various ways to the achievement of this work. Thanks go especially to Thierry Leblanc, Pascal Chrétien and Yann Le-Bihan for their assistance with several measurements, to Damien Huchet and Richard Beljio for their help with various issues concerning the experimental setup, to Laurent Santandrea, Anthony Guindon and Olivier Hubert for the technical support in IT and to Ingrid Koperski for the support with all administrative concerns.

Further, I want to thank Jinbo Bai and Laurent Zimmer for being available for the *comité de suivi*, Jean-Christophe Ginefri, director of the doctoral school EOBE, for his support in administrative matters concerning the doctoral programme as well as giving me the opportunity to be part of the doctoral representatives, Daniela Moncys-Moncevicius, head of the German department at CentraleSupélec, for giving me the opportunity to teach German during two academic years, and Mariella Argiolas for allowing me to attend her Italian courses.

Many thanks go to my fellow doctoral students Vladimir, Chih-Min and Yousra not only for sharing their different cultures but also for interesting discussions around professional and personal topics.

Last but not least, I would like to thank my family for the encouragement during the doctoral programme. Many thanks go also to my friends here in France (especially to Philomène, Bouchra, Viviane, Émeline, Julie, Raida, Martin) for their support and the time spent together during various activities, and in Germany (especially to Tobias, Eugen, Markus, Yaser, Felix, Philipp, Danny, Monsieur Rauch, Chiara, Melik) for their support and for the time spent together during Skype calls and during my stays in Chemnitz.

List of contents

List of figures

List of tables

List of symbols

Symbol	Definition
a	Gas atom or molecule
A	Constant of Paschen's law
A_T	Tungsten electrode surface
a^+	Ionised gas atom or molecule
B	Constant of Paschen's law
c_P	Correction factor (Peek correction)
C, C_1, C_2	Capacitance
d	Electrode gap distance
d_i	Thickness of the solid insulator
e	Elementary charge
e^-	Seed electron
E	Electric field strength
$\bar{E}$	Mean electric field strength
f	Radiation frequency
h	Planck constant
I, i	Current
k, k'	Constant of proportionality
k_B	Boltzmann constant
n	Number of moles
n_d	Number of travelled distances *x*
n_v	Number of particles
N	Gas density
N_E	Number of generated electrons during an electron avalanche
N_{PD}	Number of partial discharge events
N_{SE}	Number of seed electrons
N_n, N_1, N_2	Number of generated seed electrons
N_{1-}, N_{2-}, N_{n-}	Number of created electrons during the 1st, 2nd, nth electron avalanche
N_{1+}, N_{2+}, N_{n+}	Number of created ions during the 1st, 2nd, nth electron avalanche
N_c	Critical number of electrons
p	Pressure
p_0	Pressure at atmospheric standard conditions
P_c	Probability of collision between an electron and another gas atom or molecule
P_i	Probability of ionising collision
P_{nc}	Probability of no collision between an electron and another gas atom or molecule
Q	PD magnitude / charge
r, r_1, r_2	Radius
R	Resistance
t	Time

T	Temperature
T_0	Temperature at atmospheric standard conditions
V, V_1, V_2, v	Voltage
V_{BD}	Breakdown voltage
V_G	Gas volume
W_i	Ionisation energy
x	Travelled distance of the (seed) electron
α	Townsend’s first ionisation coefficient
α_e	Effective ionisation coefficient
γ	Townsend’s second ionisation coefficient
ε_0	Permittivity of vacuum
ε_r	Relative permittivity
η	Attachment coefficient
λ	Mean free path
ρ	Volume resistivity
σ	Collision cross section
φ	Phase position

General introduction

This doctoral thesis deals with electrical partial discharge and gas breakdown phenomena at triple junctions under various conditions of pressure and temperature. Triple junctions, which are present in numerous industrial applications, denote the common boundary between a metal conductor, a solid insulator, and the surrounding gas. Due to the possible presence of a low radius of curvature at the edge of the conductor, a local enhancement of the electric field created by the potential of the metal conductor can be observed at the triple junction. This field enhancement may be further enhanced by a discrepancy in permittivity between the solid insulator and the surrounding gas. Consequently, the probability of an inception of partial discharge activity and, with increased voltage, a development towards a dielectric breakdown or insulator flashover is enhanced. Thus, triple junctions constitute a weak point of the insulation system.

The triple junctions inherent in most insulation systems are in some circumstances exposed to severe environmental conditions in terms of pressure and temperature.
This may be the case in the aeronautical sector where systems are exposed to low pressure conditions down to 100 mbar [1]. This sector is currently transitioning towards more environmentally friendly technologies to face the challenges which come along with climate change and the aim to reduce carbon emissions. For this purpose, the concept of the "More Electrical Aircraft" or even "All Electrical Aircraft" to reduce the use of conventional fuels thus reducing greenhouse gas emissions has been developed [2]. It is intended to replace in a first step non-propulsive power sources such as mechanical or hydraulic by electrical power. The additional demand of electrical power is reached using higher voltages thus increasing the risk of partial discharge activity [3]; this risk is also influenced by varying environmental conditions, such as temperature and pressure, during the flight [2].
Harsh environmental conditions may also be encountered in the nuclear sector in which applications are exposed to high temperatures up to 650 °C and where partial discharge activity in neutron flux detection devices among other system elements may disturb the control of the reactor [4]. With regard to the further development of this technology, this may be an issue in the coming years, given the European Union's decision to consider nuclear energy not as a renewable but nevertheless as a low-carbon technology contributing to the objective of at least 42.5 % of energy consumed coming from renewable sources by 2030 [5], [6], [7] and the French government's investment in six new nuclear reactors (EPR – Evolutionary Power Reactor) by 2050 [8], [9].
These examples therefore show that the results of the present work may be of interest to the industrial sectors mentioned.

Although this type of problem is commonly known in industry, there are still some significant gaps in the understanding of these phenomena because some basic physical models, such as Paschen's law, which allows the breakdown voltage to be determined as a function of pressure and electrode gap distance in a homogeneous electric field, do not apply to the case of triple junctions.

Consequently, there is a need for a fundamental study of these phenomena. The aim of the present work is to obtain a more detailed understanding of the partial discharge and breakdown phenomena taking place at triple junctions under various conditions of pressure (atmospheric pressure down to 50 mbar) and temperature (ambient temperature up to 400 °C). In particular, the behaviour of the partial discharge inception voltage (PDIV) and partial discharge extinction voltage (PDEV) as well as the flashover voltage (FOV) of surface breakdown is experimentally studied, taking into account the influence of changes in temperature on both gas (nitrogen) and solid insulator (aluminium oxide disc) properties.

The manuscript is divided into five chapters.

In chapter one, after a short introduction to the problem, theoretical background concerning electrical discharges is given, with particular attention to partial discharges and additionally to surface discharges.

Chapter two presents an overview of the experimental work and equipment, as well as the solid insulators chosen for the experiments. A test setup including its various equipment, and which serves as the basis for the experiments carried out in this work, is presented. In addition, the results of some preliminary PDIV measurements and their dependence on several geometrical and dielectric properties of the solid insulator at ambient temperature but under different pressure conditions are presented and discussed.

Chapter three presents the main experimental results of this work, namely the PDIV (and PDEV) measured under varied conditions of pressure and temperature. For this purpose, the experimental setup and procedure, which were adapted to obtain consistent measurements, as well as the considerations of several aspects of the temperature control are described and discussed.
A complementary study of the temperature dependence of the properties of the aluminium oxide solid insulator is included in this chapter. The experimental setup, procedure and results for these dielectric measurements (volume resistivity and relative permittivity) are detailed. A discussion of the obtained results and their influence on PDIV (and PDEV), including a numerical simulation, follows. The influence of oxidation of the electrodes on the measurement results is also discussed.

Chapter four is dedicated to the experiments carried out to measure the flashover voltage (FOV) at which surface breakdown is observed. FOV measurement setup and procedure are presented, and the measurements discussed and compared with the previously measured PDIV. This chapter is completed by observations of the discharge behaviour at ambient temperature and varied pressure conditions using a high-speed camera.

A general conclusion summarises the main results of this work and suggests an outlook for future work.

Chapter 1

Electrical discharges – theoretical background

1.1 Motivation

A great number of industrial and electrical applications feature triple junctions, which are constituted of an electrode in contact with a solid insulator and the surrounding gas, as illustrated schematically in Figure 1.1.

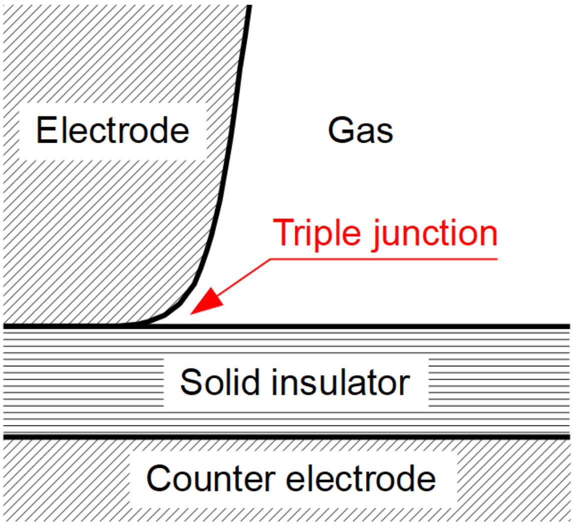

Figure 1.1. Schema of a triple junction.

Due to the presence of a low radius of curvature at the edge of the electrode, the local electric field created by its electric potential is enhanced. This enhancement is even greater in presence of a solid insulator due to the discrepancy in permittivity between the solid insulator and the surrounding gas. This can be seen in Figure 1.2 where a numerical simulation using finite element modelling (COMSOL Multiphysics) of the electric field in the gas without (left) and with (right) the solid insulator (relative permittivity of $\varepsilon_r = 2$) thus constituting the triple junction is pictured. For both simulations, a voltage of 1 V is applied to the upper electrode, while the lower counter-electrode, located 1 mm below (not visible in the figure), is at ground potential. On the left, the gap is filled with gas; on the right, the gap is filled with a solid insulator.

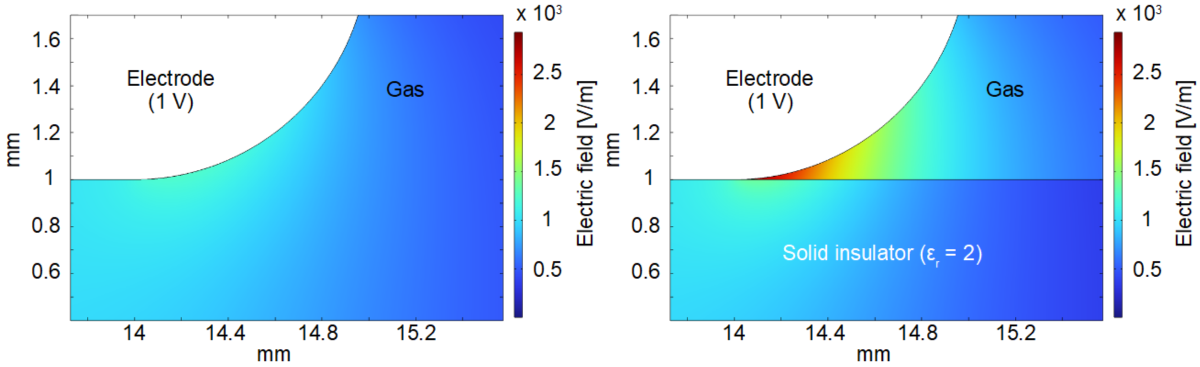

Figure 1.2. Numerical simulation of the electric field near the triple junction for an applied voltage of 1 V without (left) and with (right) the solid insulator (relative permittivity of $\varepsilon_r = 2$).

Even though the maximal value of the electric field is dependent on the parameters related to the numerical simulation software such as the mesh size, it is evident that the electric field strength additionally increases when a solid insulator is present.

These sources of local enhancement in the electric field facilitate the formation of partial discharges (PDs) above a given voltage threshold. PDs can cause low-level damage which could accumulate over time thus leading to accelerated ageing and weakening of the insulation system and eventually resulting in complete breakdown (dielectric breakdown and/or insulator flashover). Hence, triple junctions are a weak point in industrial systems [10], [11].
Triple junctions are present in high voltage industrial applications as for example in Gas-Insulated Switchgears, Gas-Insulated Lines [12], [13], [14], high voltage feedthroughs [15], [16] or power busbars in power converters [17].
In some circumstances, these solid insulators and the surrounding gas are exposed to harsh environmental constraints in terms of pressure and temperature. This is the case for applications in the nuclear sector in which they are exposed to temperatures up to 650 °C [4] and in the aeronautical sector in which they are exposed to pressures down to 100 mbar [1].

For these fields of application, the influence of the solid insulator material and the surrounding gas, as well as the influence of environmental conditions such as temperature and pressure on the PD behaviour, including the partial discharge inception voltage (PDIV) and, for further increase in voltage, the flashover voltage (FOV), as well as the discharge propagation on the surface of the solid insulator, must be considered.

This chapter presents the theoretical background of electrical discharges and reviews current knowledge concerning partial discharges as well as discharge propagation on solid insulator surfaces. It is divided into three main sections:

Section 1.2 presents the physical principles involved in the formation of electrical discharges in a gas. This is followed by a short description of the Townsend mechanism, of electrical discharge types and of Paschen’s law which characterises the conditions leading to gas breakdown in a homogeneous electric field. In addition, different influences on Paschen’s law such as temperature are discussed.

In section 1.3, focus is made on partial discharges. Beginning with a definition for partial discharges, a classification of partial discharges is then proposed followed by an explanation of the corona and the streamer discharge mechanism. Influences on partial discharges including environmental conditions are discussed and detection techniques as well as methods to identify and interpret partial discharges are presented.

Section 1.4 deals with surface discharges. After a short overview of the classification of surface discharges, focus is made on the development of discharges along the surface of a solid insulator. In this context, influences on surface discharge propagation such as the nature of the solid insulator material are discussed summarising results presented in various studies.

1.2 Electrical discharges

1.2.1 Phenomenon of electrical discharges

Electrical discharges have been observed in nature since time immemorial in various forms of appearance, such as lightning (during thunderstorms or volcanic eruptions) or St. Elmo's Fire. In modern terms, an electrical discharge can be understood as the transition from the insulating to the conducting state of a gas releasing and transmitting electricity in an electric field due to a potential difference.

The creation of a conducting channel in a gas is also associated with the term "plasma" (from ancient Greek "mouldable substance") which was first introduced by the American scientist Irving Langmuir in 1928 [18], [19]. A plasma is an ionised gas which is from a macroscopic point of view electrically neutral but due to its free charge carriers electrically conductive. It can be regarded as the fourth state of matter which constitutes 99 % of the universe in the form of stars and ionised interstellar gas. For a plasma to be formed, thermal or electromagnetic energy is required for the gas atoms or molecules neutral gas to become ionised [19], [20]. Plasma theory is important to a wide range of scientific topics, from astrophysics to nuclear fusion research. This work is limited to only a part of plasma theory, specifically to the description of the mechanisms leading to electrical discharges.

1.2.2 Formation of electrical discharges – electron avalanche

The formation of electrical discharges in a gas is related to the transfer of energy due to inelastic collisions between charge carriers accelerated by an external electric field with neutral particles. Electrons play a major role in this process due to their low mass and therefore high mobility [21].

The presence of at least one free charge carrier, sometimes referred to as a seed electron, in an otherwise neutral gas is the first step necessary to initiate an electrical discharge. It may be generated by ionisation of neutral gas atoms or molecules, provoked by natural radioactivity of the earth, cosmic radiation, or UV light. This process can be expressed as follows:

$$a + hf \longrightarrow a^{+} + e^{-} \tag{1.1}$$

where a represents a gas atom or molecule, h the Planck constant, f the radiation frequency, a^{+} the ionised gas atom or molecule and e^{-} the seed electron [22].

It can be estimated that the order of magnitude of the seed electron generation rate due to this processes amounts approximately to 5 to $20 \cdot 10^{6}$ m^{-3} s^{-1} [21].

Seed electrons can also be generated by thermal ionisation (collision between gas atoms or molecules due to their thermal motion, only important for temperatures beyond 1000 K) or by field emission (emission of electrons from metallic surfaces under high electric fields).

To initiate an electrical discharge, seed electrons need then to be accelerated by an external electric field within the gas. In a laboratory context, this will often mean in the gas gap separating two electrodes, a positively polarised anode, and a negatively polarised cathode. Due to its acceleration in the electric field, seed electrons collide with the gas atoms or molecules. Two collision types can be distinguished [23]:

- Elastic collisions

Elastic collisions between an electron and a neutral gas atom or molecule will lead simply to a transfer of kinetic energy supplied to the accelerated electron by the external electric field and the neutral gas species. This may be interpreted as an energy transfer from the external system to the kinetic energy of the gas (i.e., heating) but no energy is used in this case for the creation of excited or ionised species in the gas.

- Inelastic collisions

During inelastic collisions, a part of the kinetic energy of the impacting particles (here meaning the electrons accelerated by the external field) is transformed into internal energy in the impacted gas atoms or molecules, resulting in the excitation or ionisation of those atoms or molecules. This type of collision thus contributes to the formation and development of electrical discharges because ionisation will lead to a multiplication of electrons in the system.

Further, the seed electron acquires during its acceleration an amount of kinetic energy which is proportional to the electrostatic potential difference ΔV applied to the travelled distance. For an ionising collision, which is necessary to provoke an electrical discharge, the acquired energy needs to be superior to the ionisation energy W_i of the bulk gas atoms or molecules [24]:

$$e \cdot \bar{E} \cdot x \ \geq W_i \tag{1.2}$$

where e is the elementary charge, $\bar{E}$ the mean electric field strength and x the travelled distance of the seed electron. Table 1.1 shows as an example some values of W_i for air and nitrogen, gases used in this work [25].

Table 1.1. Ionisation energy W_i of air and nitrogen [25].

Gas	**Ionisation energy [eV]**
Air	14.84
N_2	15.58

Provided that the seed electron acquired sufficiently energy for an ionising collision, an increase of electrons due to impact ionisation can take place:

$$e^- + a \longrightarrow e^- + a^+ + e^- \tag{1.3}$$

Consequently, an impact with sufficient energy leads to the ionisation of the gas atom or molecule, releasing a second electron. As the two electrons are in turn also accelerated in the electric field, this process repeats itself resulting in an exponential increase in the number of electrons and eventually an electron avalanche, see Figure 1.3 [21].

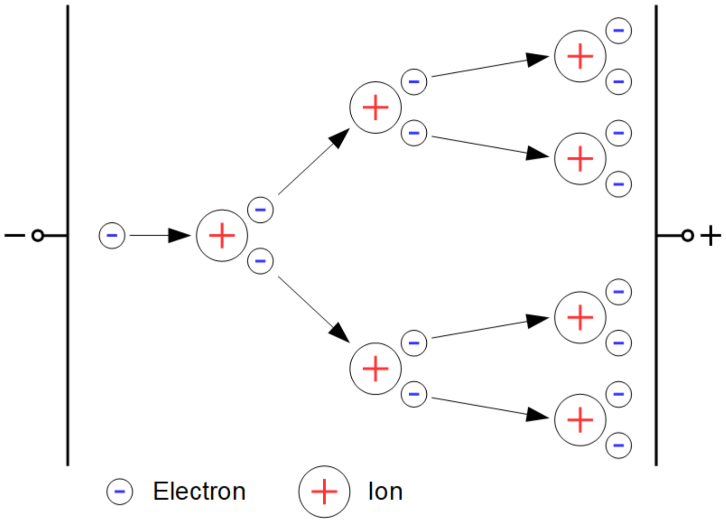

Figure 1.3. Schema of an electron avalanche.

It should be noted that in addition to the impact ionisation, other ionisation mechanisms like thermal ionisation and photo-ionisation, or a superposition of both, may contribute to the exponential increase in electrons [21].

As mentioned above, in a given electric field, the energy acquired by the seed electron is proportional to the travelled distance in the electric field before colliding with a gas atom or molecule. The mean value of this distance is the electron free path λ [21]. Equation (1.4) shows that this distance depends on the collision cross section σ, and on the gas density N:

$$\lambda = \frac{1}{\sigma \cdot N} \tag{1.4}$$

The collision cross section depends on the gas and can be calculated as:

$$\sigma = \pi \cdot (r_1 + r_2)^2 \tag{1.5}$$

where r_1 and r_2 are the radiuses of the particles involved in the collision. If one of the particles is an electron, its radius may be neglected [21]. But it is worth noting that the effective ionisation cross-section by electron impact is dependent on the incident electron energy. Typical values can be found in [26], [27], [28].

The gas density N can be written as:

$$N = \frac{n_V}{V_G} \tag{1.6}$$

where n_v is the number of particles of the gas and V_G the gas volume.

Remark: at this point, it should be highlighted that the symbol n_V is used to designate the number of particles of the gas which should not be confused with the symbol for the number of moles, n.

Introducing the ideal gas law:

$$p \cdot V_G = n_V \cdot k_B \cdot T \Rightarrow \frac{n_V}{V_G} = N = \frac{p}{k_B \cdot T} \tag{1.7}$$

where p is the gas pressure, k_B the Boltzmann constant and T the temperature.

Finally, the equation of the mean free path can be written as:

$$\lambda = \frac{1}{\sigma} \cdot \frac{k_B \cdot T}{p} \tag{1.8}$$

thus showing that the lower the gas pressure, the longer the distance travelled by the seed electron before colliding with a gas atom or molecule. Consequently, at a reduced pressure, the mean free path tends to be very high, thus increasing the electrons energy, but in a finite dimension system, also reducing the number of possible collisions. By contrast, a higher gas pressure leads to a shorter travelling distance of the seed electron, a lower collision energy and a lower probability to ionise gas atoms or molecules. It may also be noted at this point that the temperature has an inverse effect on the mean free path, with higher temperatures leading to a higher mean free path and that it is really the gas density which determines the mean free path between collisions.

For air, the mean free path of an electron amounts under atmospheric standard conditions (T = 293.15 K, p = 1013.25 hPa, absolute humidity: 11 g/m³, relative humidity: 60 %) approximately to 1 µm [29].

1.2.3 Townsend mechanism

The process which leads to an electron avalanche and further potentially to a self-sustaining discharge can be mathematically described by the Townsend mechanism, also called Townsend's ignition condition, first described by the Irish physicist John Sealy Townsend at the beginning of the 20th century [30].

The ignition condition implies that a seed electron released from the cathode must, by means of an electron avalanche and its retroactive effects, generate at least one new electron at the cathode, which can itself provoke an electron avalanche. The mechanism for the creation of new electrons at the cathode can occur via photoemission or from the impact of positive ions on the cathode and is referred to as secondary emission. If this condition is fulfilled, each electron avalanche generates at least one more, leading to a discharge channel and eventually to breakdown between the electrodes. Otherwise, if the number of the new electrons generated is inferior to the number of seed electrons, no discharge channel can be built and no breakdown between electrodes is possible, the process of electron avalanches comes to a halt. Figure 1.4 shows the Townsend mechanism schematically [22].

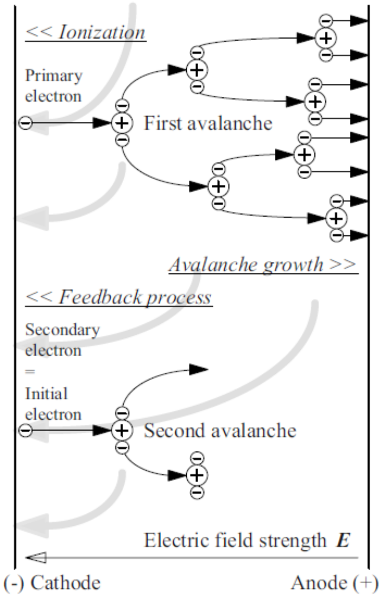

Figure 1.4. Schema of the Townsend mechanism [22].

A more detailed description of the Townsend mechanism including a mathematical examination is given in annex A.1.

1.2.4 Types of electrical discharges

After its initiation, an electrical discharge may develop in different ways, depending on the environment, and on the properties of the external electrical circuit. Figure 1.5 schematically shows as an example a gas discharge characteristic in air for a quasi-homogeneous electric field (sphere electrode configuration) at atmospheric standard conditions [22]. A detailed description of the gas discharge characteristic V/I can be found in the literature, see [22], [23], [31]. A short summary of this description is given hereafter.

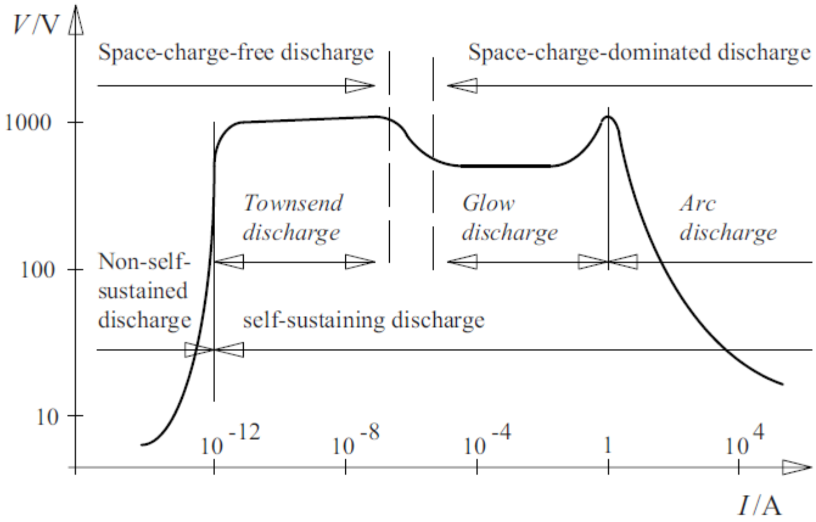

Figure 1.5. Schematical gas discharge characteristic in air for a quasi-homogeneous electric field (sphere electrode configuration) at atmospheric standard conditions [22].

For low electric field strengths, the current is first approximately proportional to the applied voltage. The number of the free charge carriers, which may be generated by ionisation of neutral gas atoms or molecules, provoked by mechanisms such as natural radioactivity or cosmic rays, remains constant (balance between generation and recombination). No additional charge carriers are created.

An increase in electric field strength accelerates the charge carriers in the electric field thus leading, according to the Townsend mechanism, to a Townsend discharge where charge carriers may be created by the discharge itself. This discharge is also called dark discharge since light emission is weak.

With further increase in current, a transition from the dark to a luminescent discharge due to the emission of light during the collision and recombination processes (recombination of charge carriers of different polarity emitting photons) between particles involved in the collisions can be observed. Those to the human eyes visible discharges are called corona or glow discharges. These discharges, which are associated with partial discharges which will be detailed in section 1.3, may be observed when the current is limited by the weak-field region of an inhomogeneous electric field or by a high impedance in series with the electrodes of a quasi-homogeneous electric field (as it is the case for the curve presented in Figure 1.5).

Finally, for a further increase of the current, the generation of charge carriers is characterised by the ohmic losses or rather Joule heat and thermal ionisation generates many charge carriers which results in an arc discharge, usually characterised by an intense emission of light [31], [32].

1.2.5 Paschen's law

The conditions which lead to gas breakdown can be characterised by Paschen's law, named after the German physicist Friedrich Paschen who discovered it empirically in 1889 [33]. Paschen's law gives the inception voltage for electrical breakdown in a gas as a function of the product of the gas pressure and the gas gap distance for an ideal homogeneous electric field between two infinite planar electrodes.

An analytical equation of Paschen's law was eventually established by Townsend, allowing to predict the value of the breakdown voltage for a given pressure, distance, and gas. This equation can be derived from the ignition condition of the Townsend mechanism [34] and the inception voltage V_{BD} for gas breakdown can be expressed as:

$$V_{BD} = \frac{A \cdot p \cdot d_e}{\ln\left(B \cdot p \cdot d_e\right) - \ln\left(ln\left(1 + \frac{1}{\gamma}\right)\right)} \tag{1.9}$$

where p is the gas pressure, d_e the distance between the electrodes and γ Townsend's second or rather secondary emission coefficient (ion bombardment of cathode). The constants A and B can be calculated according to:

$$A = \frac{W_i \cdot \sigma}{e \cdot k_B \cdot T} \tag{1.10}$$

$$B = \frac{\sigma}{k_B \cdot T} \tag{1.11}$$

where W_i is the ionisation energy of the bulk gas atoms or molecules, σ the collision cross section for electron impact – gas ionisation, e the elementary charge, k_B the Boltzmann constant and T the temperature.

As it can be seen in equation (1.9), the breakdown voltage V depends on gas pressure p, and on electrode gap distance d. It may be noted that the pressure parameter is always divided by a factor $k_B \cdot T$, indicating the fact that it is the gas density which is the important physical parameter to be considered in the formation of an electrical discharge.

Figure 1.6 shows the Paschen's curve in nitrogen calculated according to Paschen's law expressed in equation (1.9) as well as an experimentally obtained curve using the mean values of various experimental data obtained with different electrode materials from Dakin *et al.* [35].

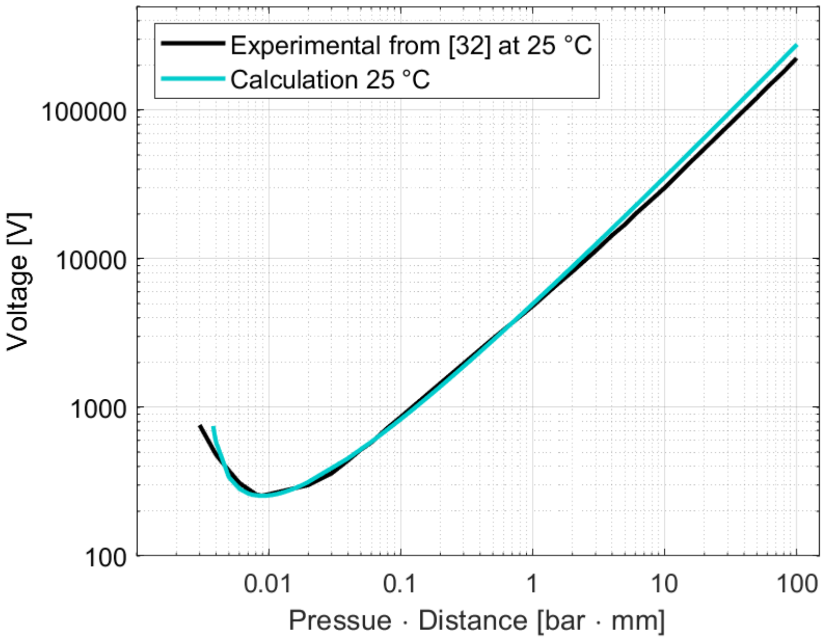

Figure 1.6. Paschen's curve in nitrogen: experimental [35] and calculated curve at 25 °C.

Paschen's curve exhibits a minimum voltage which corresponds at ambient temperature in nitrogen to approximately 250 V at $8.6 \cdot 10^{-3}$ bar · mm [24]. For voltages below the minimum, gas breakdown is assumed not possible. For $p \cdot d$ values below $8.6 \cdot 10^{-3}$ bar · mm (left-hand branch of the curve, i.e., short-distance or low-pressure breakdown) the breakdown voltage increases very strongly. This is due to a small ratio between the interelectrode distance and the electron mean free path, which hinders the development of an avalanche involving a sufficient number of successive collisions to reach the Townsend criterion.

For relatively high values of $p \cdot d$ (right-hand branch of the curve, i.e., long-distance or high-pressure breakdown), the breakdown voltage increases linearly due to a weaker electric field strength caused by increased distance between the electrodes and/or a reduced mean free path and thus to more frequent collisions because of higher gas pressure [21], [22], [36].

1.2.5.1 Influence of gas nature and temperature on Paschen's law

Paschen's law, which has initially been established for air at room temperature [37], may be influenced by several factors such as the gas nature and temperature [31].

The nature of the gas influences Townsend's first and second ionisation coefficient thus leading to different values of constants *A* and *B*, see (1.10) and (1.11). Table 1.2 shows for the gases used in this work (nitrogen and air) the empirically determined values of constants *A* and *B* as well as the range for a reduced electric field *E/p* in which they are considered to be constant [38]. It should be noted that the values are only valid at ambient temperature.

Table 1.2. Empirically determined values of constants *A* and *B* for selected gases [38].

Gas	*A* [V/bar · mm]	*B* [1/bar · mm]	Range of validity for *E/p* [V/bar · mm]
Air	27377	1125	7500 – 60004
N_2	25652	900	7500 – 45003

Breakdown voltage differs for both gases because of differences in ionisation potentials and electron impact – ionisation cross sections. Figure 1.7 shows Paschen's curves for air and nitrogen calculated according to (1.9) considering the values for *A* and *B* given in Table 1.2.

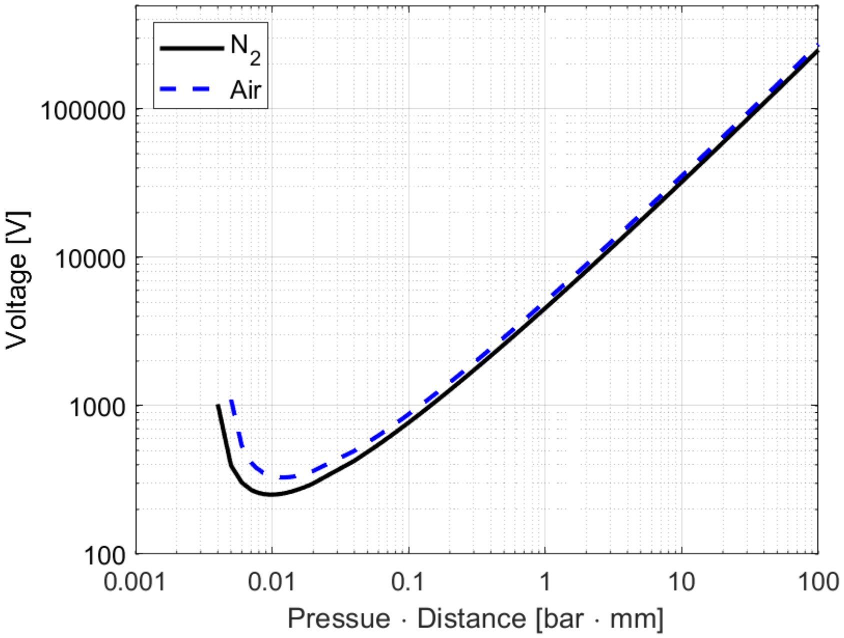

Figure 1.7. Calculated Paschen's curve for air and nitrogen at 25 °C.

Both Paschen's curves are similar regarding their shape but differ depending on the nature of the gas as to their position and the voltage for the curve minimum.

The influence of temperature on the breakdown voltage can be considered using either the correction according to Peek [39] or Dunbar [40], who have separately described the modification of Paschen's curve when temperature changes [41], [42], [43].

The Peek correction, named after the American engineer Frank William Peek Jr., adjusts the breakdown voltage by using a correction factor c_P which can be expressed as:

$$c_P = \frac{p}{p_0} \cdot \frac{T_0}{T} \tag{1.12}$$

where p and T are the values of actual pressure and temperature and p_0 and T_0 the values of pressure and temperature at atmospheric standard conditions.

The resulting breakdown voltage according to Paschen's law can be calculated by multiplying equation (1.9) with (1.12). Given the fact that the resulting breakdown voltage is inversely proportional to the temperature, the Paschen's curves are shifted for a given gas pressure and electrode gap distance downward whereas the minimum p · d remains at the same position on the abscissa.

The Dunbar correction, named after the American engineer William G. Dunbar, assumes a constant gas volume, implying, due to the ideal gas law, that the pressure varies proportionally to the temperature. Considering the pressure p_0 and temperature T_0 at atmospheric standard conditions, the pressure p for a given temperature T can be calculated as:

$$p = p_0 \cdot \frac{T}{T_0} \tag{1.13}$$

Inserting the recalculated value of p in equation (1.9), the result of the Dunbar correction is a shift of Paschen's curve to the right with increased temperature which, on the right part of the curve, leads to a decrease in breakdown voltage.
Figure 1.8 shows the applied Peek and Dunbar corrections on the basis of the calculated Paschen's curves for nitrogen.

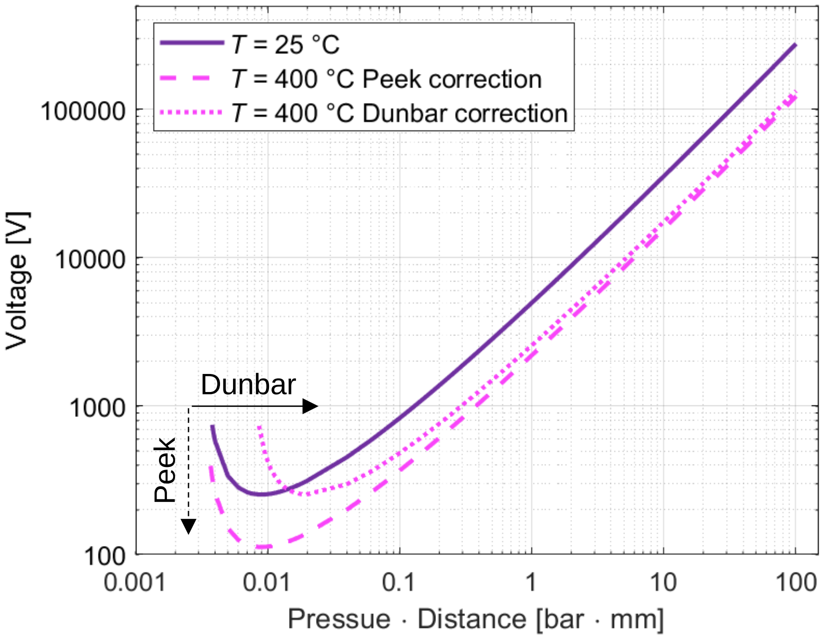

Figure 1.8. Influence of temperature on calculated Paschen's curves for nitrogen applying the Peek and Dunbar corrections.

Both Peek and Dunbar corrections show that an increase in temperature leads to a decrease in breakdown voltage.

The main difference between the corrections is that the Peek correction is more empirically, adjusting the breakdown voltage, whereas the Dunbar correction is based on the ideal gas law adjusting the pressure using equations (1.9), (1.10) and (1.11) reflecting the fact that if the temperature changes at a given pressure, the gas density, and therefore the mean free path for collisions, will also change accordingly. Consequently, by plotting the Paschen's curves as a function of the product $N \cdot d$ instead of $p \cdot d$, all the calculated Paschen's curves merge whatever the temperature, see Figure 1.9.

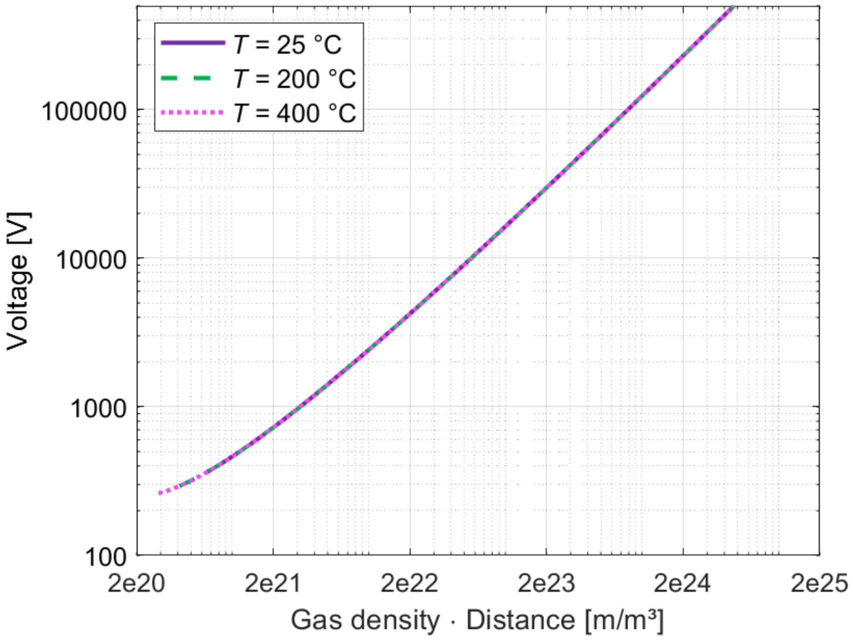

Figure 1.9. Calculated Paschen's curves for nitrogen as a function of the product of gas density and electrode distance applying the Dunbar correction.

1.3 Partial discharges

1.3.1 Definition

The *International Electrotechnical Commission* defines a partial discharge (PD) according to the standard IEC 60270 [44] as a *localised electrical discharge that only partially bridges the insulation between conductors and which can or can not occur adjacent to a conductor*.
PDs are further described as the consequence of a locally enhanced electric field on the surface of the insulation or in the insulation and they *appear as pulses having a duration of much less than 1 µs*. PDs may occur along with emission of light, sound or heat as well as chemical reactions thus allowing to use various methods for their detection [44].

In general, PDs do not lead to an immediate breakdown of the insulation system which separates live parts from the ground. In fact, a persistent appearance of PDs may cause on long-term basis a low-level damage as well as accelerated ageing, thus weakening the insulation system. Finally, the damage provoked by PDs may accumulate and eventually lead in worst case to complete breakdown of the insulation system (dielectric breakdown and/or insulator flashover) [10], [11].

PD activity is always accompanied with various physical phenomena able to damage the insulation system. These include heat generation at the point where PDs occur, leading to thermal degradation of the insulation system, or chemical reactions based on the generation of ions, radicals or other chemically active molecules (ozone, nitric oxides) which in turn could lead to a change in the insulation material properties.
These multiple consequences of PDs make their observation, detection and prevention of great importance [10], [45].

Important criteria for the characterisation of PDs are the partial discharge inception voltage (PDIV) and the partial discharge extinction voltage (PDEV).
According to IEC 60270, the PDIV is defined as the *applied voltage at which repetitive partial discharges are first observed in the test object, when the voltage applied to the test object is gradually increased from a lower value at which no partial discharges are observed* [44]. From a practical point of view, the PDIV can be seen as the lowest voltage at which the magnitude of a PD impulse is at least equal to or higher than a specified value [44]. This specified value for the magnitude of the PD impulse depends on the equipment available for its measurement. Often the integral of the PD current pulse is used and a value of several picocoulombs is fixed as a minimum criterion. This will in turn depend on the electromagnetic environment in which the measurement is taken, and care may be needed to reduce electromagnetic noise in order to be able to measure low down to the picocoulomb level.

The PDEV is defined as the *applied voltage at which repetitive partial discharges cease to occur in the test object, when the voltage applied to the object is gradually decreased from a higher value at which PD pulse quantities are observed* [44]. It can also be seen as the lowest voltage at which the magnitude of a PD impulse is at least equal to or lower than a specified value [44].

The PDEV is always equal to or less than the PDIV because it is measured in the case in which discharges, and therefore seed electrons, are already present. This consideration leads to the idea that the time lag in which seed electrons are available [46] may play a role in the initial measurement of the PDIV and be an important factor in the protocol for the determination of the PDIV.

For the characterisation of PD activity, the apparent charge, the PD magnitude, and PD repetition rate are considered.

The apparent charge is defined as *that charge which, if injected within a very short time between the terminals of the test object in a specific circuit, would give the same reading on the measuring instrument as the PD current pulse itself* [44]. The apparent charge does not correspond to the amount of charge which is locally involved during the discharge because this charge cannot be measured directly. It can be understood as the charge flowing out of the external measurement circuit (e.g. coupling capacitor) after a PD occurred and is usually expressed in picocoulomb (pC) [32], [44].

The PD magnitude, also PD charge magnitude, can be differentiated into the peak and the average PD magnitude. The peak PD magnitude represents the magnitude of the largest measured apparent charge within a defined time interval whereas the average PD magnitude gives the average value of all measured PD magnitudes within a defined time interval [44], [47].

The PD repetition rate in turn is defined as the sum of PD impulses recorded within a defined time interval divided by its duration [44].

1.3.2 Classification of partial discharges

Partial discharges can be classified into internal and external partial discharges [48].

Internal partial discharges include:

- Cavity discharges

Cavity discharges may occur in gas filled cavities of solid insulators or in gas bubbles of liquid insulators. For a given potential difference, the disparity in relative permittivity between the gas-filled cavity (relative permittivity $\varepsilon_r \approx 1$) and the surrounding solid or liquid insulator ($\varepsilon_{r,insulator} >> \varepsilon_{r,cavity}$) leads to an increase in electric field thus facilitating PD activity. Finally, an accumulation of damages in the insulator provoked by PDs within the cavity may accumulate and, in the long term, lead to a failure of the insulation system [48], [49]. The propagation of the cavity may occur in a filamentary fashion, forming a structure called an electrical tree, addressed in the following paragraph.

- Electrical treeing

Electrical treeing for its part may occur when defects as for instance cavities, sharp edges, protrusions on the live electrode, conductive or non-conductive particles are present in the solid insulator [50], [51]. Those defects may lead to a high concentration of the electric field of locally about 100 kV/mm and more [50]. Consequently, PD activity takes place at the local defect degrading the adjacent solid insulator and creating a discharge channel. As the channel building process has a stochastic character, the discharge can occur each time in another direction or in the case of AC applied voltage, even in two different directions at the same time. Finally, the discharge channel with its various ramifications comes to have a filamentary structure resembling a tree [50], [51].

External partial discharges include:

- Corona discharges
- Surface discharges

Since external PD types are of interest in this work, a more detailed description for the corona discharge is given below. A special section is then devoted to the particular topic of surface discharges.

1.3.2.1 Corona discharges

Corona discharges occur at gas-insulated electrode arrangements exhibiting a strong inhomogeneous electric field like a point-plane configuration, see Figure 1.10 [48] in which a model and simplified capacitive equivalent circuit diagram of a corona discharge is shown.

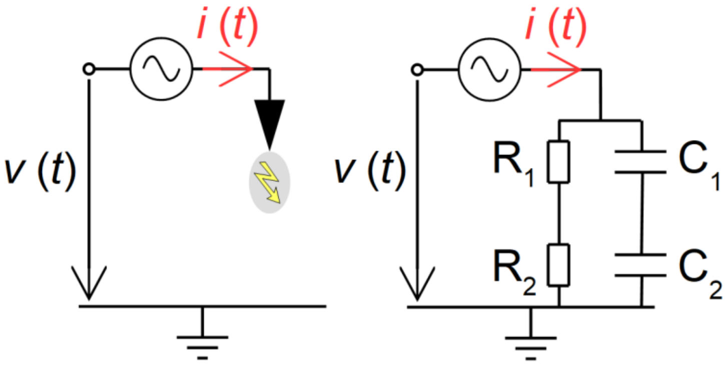

Figure 1.10. Model (left) and simplified equivalent circuit diagram (right) of a corona discharge in a gas under AC voltage [48].

Provided that the applied voltage exceeds the PDIV, local gas ionisation takes place in the vicinity of the smaller radius of curvature electrode (highest electric field), in the above-mentioned geometry the tip. Successive electrons avalanches lead to the multiplications of charged particles of both signs (electrons and positive ions) thus creating a non-equilibrium plasma. The bluish violet sphere observable at the point tip is typical of a corona discharge. This ionisation zone is represented by capacitance C_1 and resistance R_1.

The remaining gap between the electrodes is represented by capacitance C_2 and resistance R_2. This zone is characterised by low electrical field conditions, limited from the ionisation zone by an ionisation boundary which means that the energy of the electrons is beyond this boundary too weak to ionise other gas atoms or molecules. Consequently, no immediate breakdown occurs unless the applied voltage is strongly increased allowing the growth of a discharge channel [22], [49]. In this zone, only ions (positive or negative in air according to the point electrode polarity) are drifting towards the plane electrode. This zone is thus called unipolar ion drift zone.

Under AC voltage, corona discharges first appear in the maximum of a negative half-cycle when the peak electrode is at high voltage potential and the voltage exceeds the PDIV. For a further increase of the applied voltage, discharges appear also in the other half-cycle.

Generally, at atmospheric pressure, corona discharges are characterised by a dense sequence of current pulses characterised by the evacuation of the charges from the capacitance C_2 whereby the repetition frequency of these impulses is defined by the time constant of R_2 multiplied with capacitance C_2. Figure 1.11 shows the voltage characteristic of a corona discharge [22].

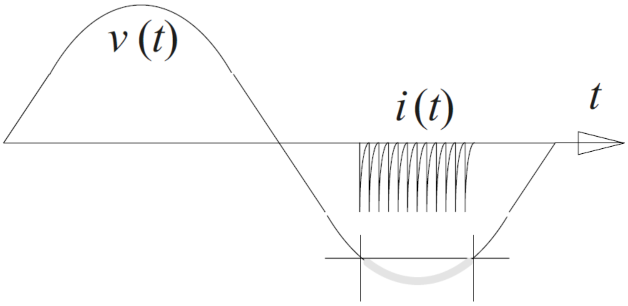

Figure 1.11. Voltage characteristic of a corona discharge; high voltage at the peak electrode [22].

The corona discharge inception and propagation as well as the breakdown voltage depend on the polarity of the applied voltage. Figure 1.12 [22] shows this polarity effect in a strong inhomogeneous electric field (point-plate arrangement) for both negative and positive point electrodes.

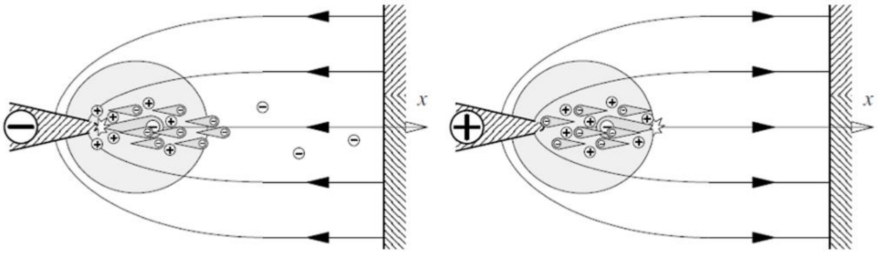

Figure 1.12. Influence of the polarity effect on corona discharges for a negative and a positive point electrode [22].

In the case of a negative point electrode, electrons are accelerated from the cathode to the anode leading to an electron avalanche according to the Townsend mechanism. The initiated discharge propagates towards the anode into the region of the weaker electric field. Beyond the ionisation boundary, the number of electrons is reduced due to attachment to electronegative gas molecules (oxygen) thus leading to a negative ionic space charge. While these negative ions are evacuated towards the anode, the positive ions in the back of the initial discharge drift off more slowly due to their weaker mobility (compared to electrons) thus leading to a positive space charge cloud in front of the negative point electrode. An enhancement of the electric field in the region close to the point electrode and a homogenisation of the electric field towards the anode can therefore be observed. In addition, positive ions impinging the cathode initiate electron emission from the metal. Consequently, the PDIV is relatively low whereas the breakdown inception voltage is relatively high [22].

Since space charges, constituted of negative ions created during the precedent discharge, lead to a decrease of the electric field in front of the negative point electrode, a new discharge can only be initiated when this space charge has recombined or drifted away.

Finally, the time lag between the evacuation of the space charges and the ignition of a new discharge leads to a certain regularity towards the appearance of discharge impulses which are called Trichel-impulses, named after the American scientist G. W. Trichel who discovered them in 1938 [52].

The repetition frequency of these Trichel-impulses is defined by the time needed to transfer the space charges through the gas towards the anode. In this context, it can be observed that the higher the voltage, the higher the ion drift velocity thus leading to an increase in repetition frequency. As soon as the number of generated electrons at the cathode is equal to the number of electrons which have recombined or which are drifted away, a permanent discharge occurs [22].

In the case of a positive point electrode, the electric field at the cathode is weak. On condition that a seed electron is present, the discharge is therefore initiated in the gas volume near the anode. The growth of the electron avalanche is directed towards the point electrode and new electron avalanches are initiated in the gas volume by photo-ionisation when a critical number of electrons is reached. An increase in discharge current can be observed thus leading to a glow discharge.

While the electrons are removed via the anode (positive point), a positive space charge in front of the point electrode remains due to the less mobile positive ions which leads to a reduction of the electric field and thus to a relatively high PDIV (compared to negative corona discharge). The positive space charge tends to grow towards the cathode into the weak field region thus shifting the ionisation boundary towards the cathode. Hence, the field strength towards the cathode increases, the ionisation process takes place ahead of the point in the gap between the electrodes which facilitates the conditions to ignite a streamer discharge leading to breakdown. Consequently, for a positive point, the breakdown inception voltage is relatively low and the breakdown under AC voltage is expected to be at the peak of the positive half cycle [21], [22], [53].

1.3.2.2 Streamer discharges

The behaviour of streamer discharges was first presented and discussed by the works of the German and the American physicists Heinz Raether and Leonard B. Loeb who in 1939 and 1940 independently investigated the discharge behaviour in air using a cloud chamber to visualise the discharge trajectory [54]. Based on these works, Loeb postulated in 1940 together with the physicist John M. Meek the streamer theory emphasising the fact that the streamer growth not only depends on the ionisation of positive ions in the gas and secondary electrons stemming from the cathode but also on the production of electrons by photo-ionisation of the neutral gas atoms or molecules [55], [56].

If an electron avalanche initiated by a seed electron grows up to an important number of electrons, a significant influence on the local electric field near the electron avalanche due to space charges can be observed. The relatively more mobile electrons form a spherical and negative head of the avalanche whereas the relatively fewer mobile ions remain behind the avalanche head forming a positively charged avalanche tail, see Figure 1.13 [21].

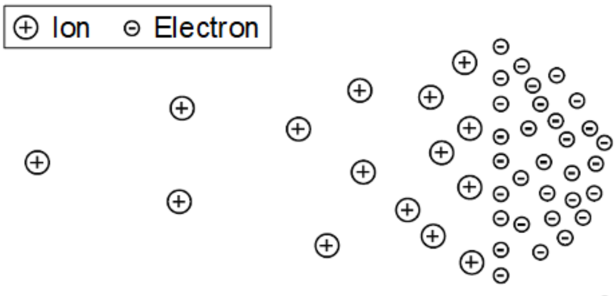

Figure 1.13. Own electric field of the electron avalanche [21].

Because of the space-charge induced enhancement of the electric field at the head of the electron avalanche, the process of inelastic collision increases including an increase of electron excitation process emitting in turn photons.

These emitted photons lead to a photo-ionisation in the gas volume near the initial electron avalanche thus creating seed electrons for new electron avalanches. Finally, the superposition of all created electron avalanches creates a conductive channel, called streamer, which rapidly grows up towards the cathode. The streamer propagation velocity at atmospheric pressure can be estimated to 10^6 m/s in a homogeneous electric field and to 10^5 m/s in an inhomogeneous electric field [22]. For lightning strokes, the streamer propagation can be estimated to 10^7 m/s [57].

The phases of this streamer propagation process are illustrated in Figure 1.14, as an example for a positive streamer [58].

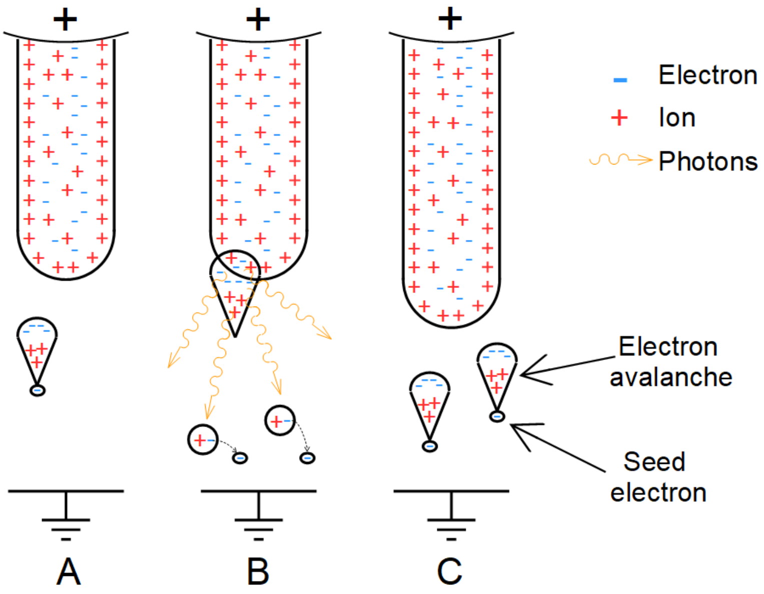

Figure 1.14. Phases of propagation of a positive streamer.
A – Positive space charge and electron avalanche, B – Electron excitation processes and photo-ionisation creating new seed electrons, C – Growth of the streamer channel and new electron avalanches.

The streamer growth can be divided in these phases [58]:

- A – presence of a positive space charge due to an electron avalanche starting from the anode; an adjacent seed electron creates an electron avalanche
- B – growth of the electron avalanche and electron excitation process with release of photons; creation of new seed electrons due to photo-ionisation of other gas atoms or molecules
- C – growth of a new electron avalanches starting from the created seed electrons towards the growing streamer channel

The conditions for streamer ignition are, on the one hand, a positive effective ionisation coefficient (number of created electrons must exceed the number of attached electrons), and, on the other hand, that the number of electrons exceeds a critical value N_c of at least 10^6 to 10^8 electrons [32].
In this context, Raether defined in analogy to Townsend's ignition condition the ignition condition for a streamer [22]:

$$e^{\int_0^d \alpha_e \cdot dx} \geq N_c \tag{1.14}$$

where *d* is the electrode gap distance, α_e the effective ionisation coefficient and N_c the critical value of electrons needed to create a streamer discharge.

If the critical number of electrons is reached, the streamer discharge has created sufficient space charges for a growth towards the cathode. In other words, the streamer discharge becomes self-sustaining and propagates under influence of its own electric field [32].

In general, the streamer can initiate at the anode (positive streamer carrying a positive charge at the streamer head and propagating towards the cathode), at the cathode (negative streamer carrying a negative charge at the streamer head and propagating towards the anode) or in the gas volume between the electrodes. In this case, photo-ionisation leads simultaneously to an anode-directed and a cathode-directed growth of the streamer [22].
For air, the voltage needed for the growth of a positive streamer amounts to approximately 5 kV/cm and of a negative streamer to 10 to 15 kV/cm [21].

1.3.3 Influence of environmental conditions, solid insulator material and gas nature on partial discharge behaviour

Over the years, different studies were made to examine the influence of temperature and/or pressure on PD activity and PDIV. Other studies have been published considering PD activity and PDIV depending on the gas type and also at triple junctions using different solid insulator materials. An overview of the main results is presented in this section.

Various studies have shown that an increase in temperature as well as a decrease in pressure leads to a decrease in PDIV [37], [59], [60], [61], [62]. These results are in accordance with the presented Paschen's curves (see section 1.2.5.1) and the discussed influence of temperature. Based on these facts, focus was on the consequences such as PD activity or insulation lifetime. Since the increase in temperature decreases the gas density thus leading for a given pressure to a longer mean free path, the electrons gain higher energy which results in a lower PDIV, or in a higher PD magnitude for a given applied voltage. In this context, a study [60] showed that the PD became more harmful for the insulating system at higher temperatures which leads to an accelerated ageing and a reduced lifetime. The same effect was observed to have a dependence on pressure: the lower the pressure, the higher the impact of PDs.
Regarding the influence of humidity on PDIV, on the one hand, it was observed that an increase in relative humidity leads to an increase in PDIV nevertheless indicating that the most important influencing factors are pressure and temperature and that the effect of relative humidity is less severe [37], [60]. On the other hand, it was shown that an increase in relative humidity leads to lower PDIV values, especially for high values of relative humidity beyond 60 % [62].

Also, a study combining temperature and humidity was carried out [63]. It was shown that, for low relative humidity, the gas density decreases due to an in increase in temperature, leading to a reduction in PDIV. Increasing relative humidity at constant temperature, PDIV tends to increase. However, above a given humidity threshold, increasing the temperature at a constant level of relative humidity, leads to an increase in PDIV. This is due to the fact that it is the absolute humidity which is responsible for the increase in PDIV. The absolute humidity increases with temperature for a given relative humidity and consequently the electrical breakdown strength of air increases due to electronegativity of water molecules. Hence, the role of both relative humidity (water film on surfaces) and absolute humidity (higher availability of water vapour) must be considered.

In the context of aviation, the influence of low temperatures must also be considered which for example a MEA encounters during its flight. It has been observed [64] that there is only a small impact on PDIV or PD magnitude when the insulation system is exposed for a short time (< 1 h) to temperatures down to - 60 °C. In contrast, for a long exposure time of several hours to a temperature range between - 20 °C and - 60 °C, a large decrease in PDIV and a large increase in PD magnitude was observed. This is due to formation of cavities since the thermo-mechanical stress on the insulator (in this case a silicone gel) provokes cracks inducing a permanent damage of the insulation system.

Another aspect is the PD repetition rate which increases with temperature. The reason behind this is that the solid insulator volume resistivity tends to decrease with temperature, thus reducing the dissipation time of the surface charges accumulated by the discharges [65].
Different results have been observed on the temperature effect on PD magnitude. An increase of the PD magnitude with temperature has been reported in [47], [60] while a decrease – accompanied with higher PD repetition rate – has been observed in [66].

The effect of the pressure has also been analysed on other PD characteristics such as PD pulse rise time (the lower the pressure, the higher the rise time) [67], PD magnitude (the lower the pressure, the higher the magnitude) and PD pulse waveform (the lower the pressure, the larger the pulse width, leading to inaccurate measurements since PD measurement systems are often designed for a PD detection at atmospheric pressure) [68], [69], [70].
It has further been shown that the lower the pressure, the longer the PD duration and the higher the PD intensity (higher PD magnitudes) due to a higher PD inception field at lower pressures thus making the PD activity more harmful to the insulation system [71].

The influence on PDIV of the insulating material permittivity, which is an important factor determining the distribution of the electric field, has also been studied [72]. It has been shown that a higher relative permittivity of the solid insulator reduces the PDIV. This can be explained by the fact that the electric field is concentrated in the gas by an increased polarisation of the solid insulator [10], [62], [73] much as was demonstrated by the simulation presented in section

1.1. This is of particular interest at triple junctions where a further increase of the already enhanced electric field facilitates the ignition of PDs even more.

It has also been shown that PDIV varies depending on the gas nature [10], [74]. For gases with higher electronegativity like SF_6, the PDIV is higher than for gases with lower electronegativity like N_2 or air.

Remark: generally speaking, it may be found that the in the literature presented results for PD activity depending on various environmental conditions are partially contradictory. This may be due to different experimental conditions such as the used experimental setup, solid insulator materials, measuring methods, applied voltage, etc.
It should further be noted that PD activity is, apart from the presented influences, strongly influenced by the voltage parameters such as frequency, voltage waveform, etc. For example, it has been observed [2] that the PD magnitude and number increases with fast voltage rising times, and that the PD magnitude decreases with enhanced frequency, etc.

1.3.4 Partial discharge detection

The occurrence of PDs is accompanied by the emission of electrical and electromagnetic signals, optical, acoustical, and chemical effects as well as heat [44]. It is therefore possible to use various methods for the purpose of PD detection which are divided into conventional and non-conventional detection methods. The first-mentioned include electrical detection whereas the latter include optical, acoustical and chemical detection [75].

1.3.4.1 Electrical detection

The fundamentals of conventional electrical partial discharge detection under AC voltage are described in IEC 60270 in which, among the basic partial discharge test circuits, a unbalanced and a balanced test circuit are presented [44]. The schema of the most widely used (also used in this work) unbalanced test circuit, also called straight test circuit, is shown in Figure 1.15.

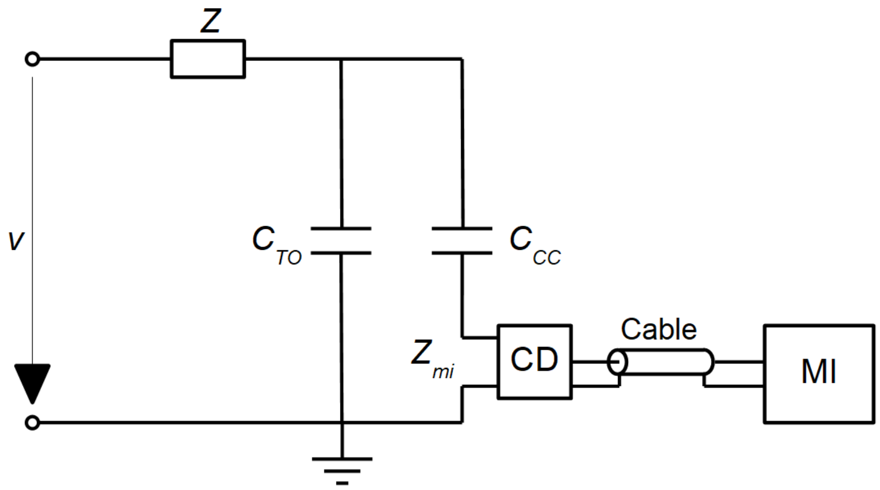

Figure 1.15. Unbalanced test circuit for electrical partial discharge detection [44].
Z – Protection impedance, C_{TO} – Capacitance of the test object, C_{CC} – Capacitance of the coupling capacitance, Z_{mi} – Measuring impedance, CD – Coupling device, MI – Measuring instrument, v – Applied voltage.

The test object C_{TO}, which can be represented as a capacitor, is connected in parallel to a coupling capacitor C_{CC}. The latter should exhibit not only a low inductance and a low PD risk but also approximately the same order of magnitude of capacitance as the test object [50].

A partial discharge event within the test object provokes a fast current pulse on the order of ten to hundred nanoseconds. After passing the coupling capacitor C_{CC}, it reaches the coupling device CD which normally consists of an active or passive four-terminal network (quadripole) and which contains a measuring impedance Z_{mi}. Its output signal is then transmitted via a connecting cable, which as a part of the transmission system should not have any influence on the signal characteristics, to the measuring instrument MI where it is processed.

Narrow-band and wide-band measuring instruments can be distinguished [49]. The narrow-band instruments are characterised by a small bandwidth of 9 kHz to 30 kHz and a midband frequency of 50 kHz to 1 MHz [44]. The most used wide-band instruments have a bandpass characteristic to block low frequency signals and high frequency noise from the network [32]. Their bandwidth is in a range of 100 kHz to 400 kHz, the cut-off frequency of the high pass is between 30 kHz to 100 kHz and the cut-off frequency of the low pass is lower than 500 kHz [44]. In any case, it is recommended to effectuate measurements at a centre frequency of 250 kHz and a bandwidth of 300 kHz [76].

To allow a correct measurement of the partial discharge magnitude the applied voltage v should have a low background noise [44].

The impedance Z is needed to attenuate disturbances provoked by the high voltage supply as well as to increase measurement sensitivity since PD pulses from the test object could otherwise be bypassed by the impedance of the high voltage supply [44]. It is also used to prevent any damage and to limit the current in the case of breakdown of the test object [49].

Although the unbalanced detection method stands out due to its simplicity and its use for routine tests, it is nevertheless not possible to distinguish between discharge signals coming from the test object or from other sources outside of the test circuit. If this is of importance, a balanced test circuit consisting of two identical test objects should be used [44], [48], [49].

Using the circuit shown in Figure 1.15, the measured apparent charge has the opposite polarity to the discharge current since the coupling device is not in series with the test object [77].
If a measurement with high sensitivity is needed, the positions of the coupling capacitor and the test object can be interchanged (test object in series with the coupling device) which avoids a split of the PD signal between the coupling capacitor and the stray capacitances of the test circuit [49]. However, the downside of such an arrangement would be that in the case of breakdown of the test object, the coupling device could be exposed to significant currents and would therefore be less protected than in the circuit pictured in Figure 1.15.

To ensure consistent partial discharge measurements, a charge calibration of the measuring instrument is necessary. Calibration is performed by feeding defined charge pulses by a charge calibrator into the test circuit. The magnitude of the charge pulses should be in the range of the magnitudes expected from the partial discharge measurement to ensure a good exactitude regarding the measurement of the specified partial discharge magnitude.
It is also important to perform a calibration with each new test object due to the influence of the test object’s capacitance on the test circuit.
Finally, to avoid any damage, the calibration system should be removed before starting the experimental procedure using high voltages [32], [44].

Other electrical PD detection methods are based on the detection of electromagnetic radiation which is emitted during a PD event. The most widely used systems for this purpose are high frequency current transformers (HFCT) and ultra-high frequency (UHF) sensors or antennas [78]. The main advantage of using these technologies is the possibility to distinguish between several PD locations. Also, UHF sensors present the advantage that external disturbances can be shielded effectively thus permitting an immunity towards disturbing noises. On the downside, this measurement method does not allow to directly measure the PD charge [49], [79].

1.3.4.2 Optical, acoustical and chemical detection

Optical, acoustical and chemical detection methods are often considered as nonconventional detection methods and are briefly described hereafter.

- Optical detection

Since PDs are accompanied by light emission caused for example by electron impact excitation or recombination processes, an optical detection can be used. The optical systems for the detection of PDs comprise, among others, fibre optics, photodiodes, photomultipliers, night optical devices, low-light enhancers, or ultraviolet corona scopes [80], [81]. Their application depends on the place where PDs occur (inside or outside the test object). Further, the characteristics of the emitted light has to be considered since the optical spectrum of the light emitted during PDs reaches from the ultraviolet up to the visible or infrared range [80].

Optical detection can be more sensitive than the conventional electrical detection, reaching sensitivities down to a charge magnitude of 0.3 pC if a photomultiplier is used [49]. Another advantage is the immunity towards electromagnetic disturbances. On the contrary, no PD charge measurement can be made by default of calibration even though it has been observed that the emitted light is approximately proportional to the apparent charge. Moreover, internal discharges in opaque solid insulators are obviously not detectable [49], [80].

- Acoustical detection

The acoustical detection of PDs, often applied in transformers, switchgears, and gas-insulated systems, is based on the detection of pressure waves provoked by PDs inside the test object. The higher the intensity of the emitted acoustic wave, the higher the PD energy [49], [78]. The detection can be made using for example ultra-sonic detectors to detect external discharges or acoustic sensors placed on the housing surface of the test object to detect internal discharges [48], [78]. Advantages of an acoustical detection are that the sensors are easy to install, immune to electromagnetic interferences and generally associated with low costs. However, this detection method is less sensitive than optical detection, a false location of PD source due to noise interferences with the environment is possible and the measurement depends on several factors such as the location of the PD sensor relative to the PD source or the propagation path of the acoustic wave inside the test object. Further, no PD charge determination can be made [49], [78], [79].

- Chemical detection

Chemical detection of PDs is possible since PD activity is accompanied by the emission of gases such as ozone when the discharge takes place in air. Hence, external discharges can be detected using an ozone detector [77], [79]. Further, chemical detection may be used to detect internal discharges in oil-filled components such as transformers using a dissolved gas analysis since PDs can create new chemical components by reactions with the oil [78].
Despite the possibility of high detection sensitivity via an accumulation of chemical products, chemical detection serves rather for a verification of PD activity since an exact PD source location is not possible. No PD charge can be determined and the detection time is quite long since the detection requires the accumulation of a sufficient amount of gas [78], [79].

1.3.4.3 Identification and interpretation of partial discharges

To avoid damage in high voltage insulation and to ensure functionality and reliability of high voltage equipment, the identification of the PD type is of interest. Every PD type exhibits a specific characteristic which enables its identification and interpretation with the aid of pattern recognition methods. Hence, a relation between the PD pattern and the defect type can be established [82].

The most widely used pattern recognition method under AC voltage is the representation of PD activity in a phase resolved partial discharge (PRPD) diagram [32].

PRPD diagrams are obtained by acquiring PD events using the electrical detection method during a large number of cycles of the applied voltage. They record for each PD the phase position φ in relation to the applied voltage, the PD magnitude Q and accumulate the number N_{PD} of PD events for a given phase and magnitude. The resulting PRPD diagram shows for each detected PD event the PD magnitude (usually displayed using a logarithmic scale) as a function of the phase superposed with the applied voltage. A colour code indicates the total number of PDs for a specific phase position/charge [32], [77], [83]. An example of a PRPD diagram is shown in Figure 1.16.

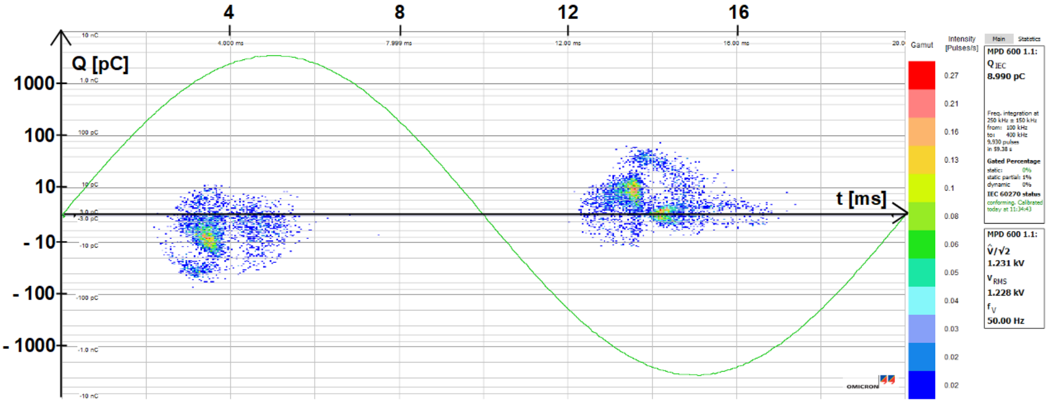

Figure 1.16. Example of a PRPD diagram showing for each PD event the PD magnitude as a function of the phase of the applied AC voltage. A colour code indicates the total number of PDs for a specific phase position/charge.

Every PD type exhibits a typical PRPD diagram thus in principle allowing the identification of the PD source which could be, for example, a defect in insulation leading to PD activity. Figure 1.17 shows schematic representations of PRPD diagrams for selected PD types under AC voltage [22].

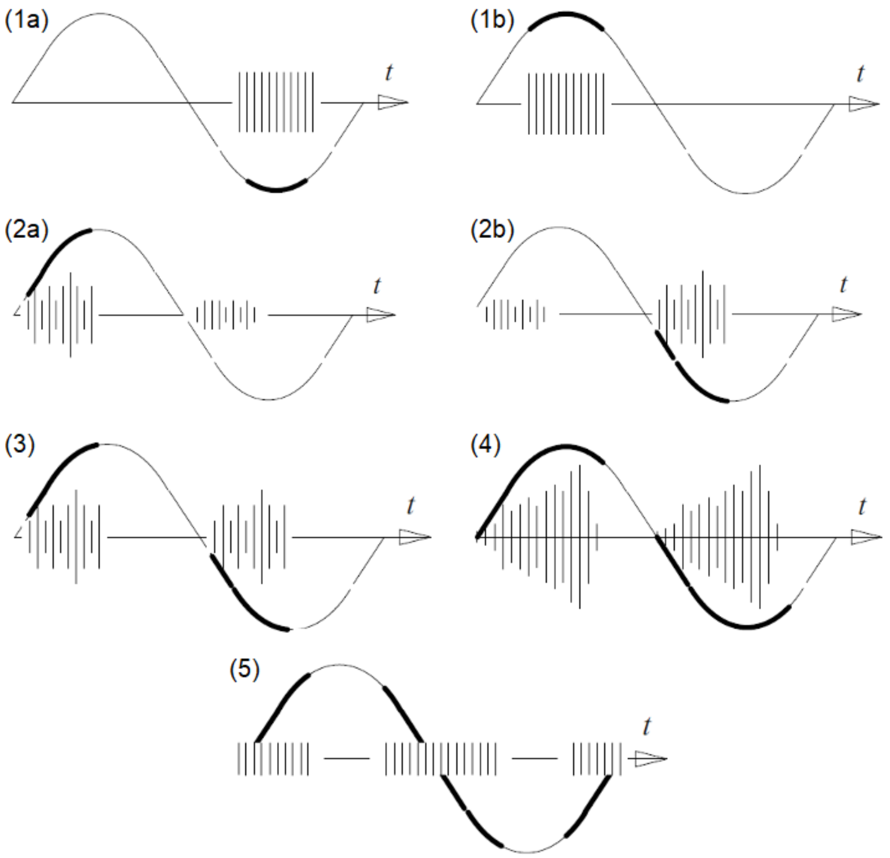

Figure 1.17. Schematic PRPD diagrams for selected PD types under AC voltage [22].
(1a) – Corona discharge in air, negative point, (1b) – Corona discharge in air, positive point, (2a) – Cavity discharge with electrode contact, negative electrode, (2b) – Cavity discharge with electrode contact, positive electrode, (3) – Cavity discharge without electrode contact, (4) – Surface discharge, (5) – Contact noise.

Corona discharges in air (1a)/(1b) (point-plate arrangement, voltage applied at the point) are characterised by bursts of impulses with steady amplitude whose frequency increases with applied voltage. If the applied voltage is further increased, discharges appear also in the opposite half-cycle.

For cavity discharges with contact to the live electrode (2a)/(2b), the impulse amplitude differs by around a factor of 3 between the half cycles whereas cavity discharges without contact to the live electrode (3) exhibit a more uniform amplitude in both half cycles.

Regarding surface discharges (4), an increase in discharge amplitude between voltage zero crossing and voltage maximum can be observed. In general, PD activity for surface and cavity discharges is shifted to the left due to the capacitive effect of the solid insulator. In both cases, charge accumulation on its surface reinforces the electric field thus allowing an ignition of PDs even when the applied AC voltage is low.

PRPD patterns of cavity and surface discharges may be similar and therefore difficult to differentiate. A simple method to do so is, at least in laboratory, to raise the applied voltage thus leading to a change in PRPD pattern for a surface discharge whereas the PRPD pattern for a cavity discharge remain unchanged. Varying the relative humidity (or the gas pressure) can also contribute to a distinction between these PD types since relative humidity only

influences surface discharges [84], [85]. Surface discharges will be analysed in more detail in the next section.
Contact noise (5) occurs due to incorrectly connected conductors and usually around voltage zero crossing where the capacitive current reaches its maximum. However, the contact noise may occur along the entire period [22], [86], [87].

Remark: the schematic PRPD diagrams represented in Figure 1.17 show the most common PD types. Other PD types and the corresponding PRPD diagrams may be found in the literature, see [75], [86], [88], [89].

1.4 Surface discharges

1.4.1 Classification of surface discharges

Two types of surface discharges can be distinguished, depending on the electrode–solid insulator arrangement:

- Live electrode and solid insulator surface, or solid insulators each in contact with an electrode, separated by a gas

In this case, the solid insulator and the surrounding gas are in series between the two electrodes and the discharge first develops in the gas before arriving on the surface of the solid insulator. This type of surface discharges is known as volume dielectric barrier discharges (DBD) [90].

- Electrodes in contact with a common solid insulator

In this instance, both electrodes are in contact with the solid insulator and constitute a triple junction where the discharges are expected to ignite. When the discharges start at the triple junction, they develop for an applied voltage above the PDIV in the gas directly along the surface of the solid insulator and lead to a flashover when the counter electrode is reached.
Since these discharges are of particular interest in this work, they are discussed separately in detail in this section.

1.4.2 Development of surface discharges

A basic description of the surface discharge development along the surface of a solid insulator can be given by the aid of an experimental arrangement developed and first presented at the beginning of the 20th century by the German physicist Maximilian Toepler [91], [92].
This arrangement, whose schema is pictured in Figure 1.18, consists of a rod electrode at high voltage potential (AC) placed on the surface of a glass plate as solid insulator. A thin metallic layer at the back of the glass plate constitutes the counter electrode.

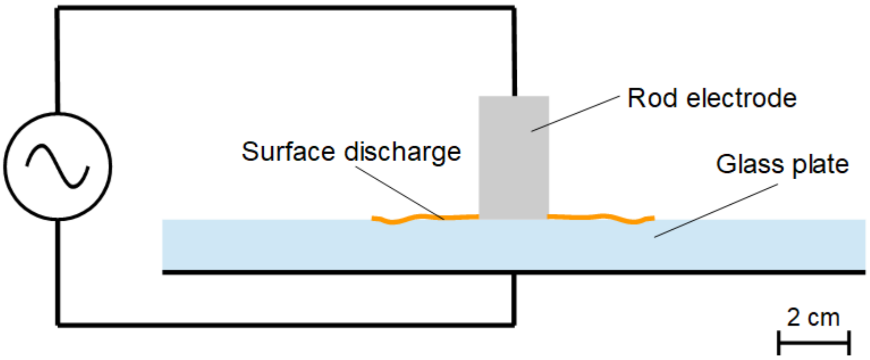

Figure 1.18. Schema of the experimental arrangement for surface discharges according to Toepler [93].

Remark: the arrangement shown in Figure 1.18 is in the original literature, published by *Toepler* [91], [92], described as a sliding discharge arrangement ("*Gleitanordnung*") and the resulting discharges as sliding discharges ("*gleitende Entladungen*"). However, these terms may be confusing since this type of discharges may also describe other mechanisms such as propagating brush discharges [94], [95] which are based on another mechanism.

To provoke a surface discharge along the solid insulator, first a discharge at the triple junction is necessary. Further, the surface discharge can only develop if the surface capacitance exhibits a minimum value. Provided that both conditions are fulfilled, and the applied voltage is increased, a discharge is initiated.
The dielectric strength of the solid insulator is assumed to be sufficiently high so that a dielectric breakdown between the rod and the counter electrode is at this point not considered. The provoked surface discharge occurs rather in the gas guided along the solid insulator surface due to the tangential field component [22], [93].

The surface discharge is induced by mechanisms similar to those for gas discharges in an inhomogeneous electric field. In the case of a rounded electrode edge, it initiates directly by the breakdown of the air gap between the electrode and the solid insulator surface, whereas in the case of a sharp electrode edge, a corona discharge may first be observed [22].
Considering the experimental arrangement according to Toepler, first surface discharges develop radially around the rod electrode which is supplied by an AC voltage, see Figure 1.19 [22], [93].

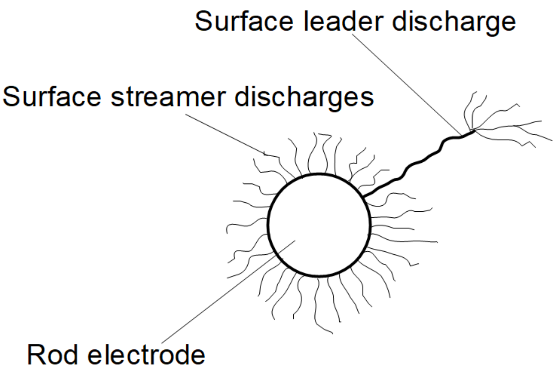

Figure 1.19. Schema of surface discharges for an arrangement according to Toepler, top view [93].

Toepler observed that the radial propagation of the surface discharges is proportional to the applied voltage. Toepler's first law can therefore be expressed as:

$$V_1 = k \cdot r \tag{1.15}$$

where V_1 is the applied voltage, k a constant of proportionality and r the propagation radius of the surface discharge. For a positive surface streamer discharge, k amounts to 5,5 kV/cm and for a negative one to 11,5 kV/cm which shows, on the one hand, that the propagation radius of a positive one is greater than for a negative surface discharge and, on the other hand, that the propagation radius is independent of the geometric (e. g. thickness) or dielectric (e. g. relative permittivity) properties of the solid insulator [11], [90].

Due to the high lateral capacitance of the solid insulator surface together with the capacitance of the solid insulator between the electrodes, the current in the discharge along the surface is much higher than for a streamer discharge in a gas. Hence, thermo-ionisation and the inception of surface leader discharges (also known as creeping discharge or creeping spark) due to high current densities for surface streamer discharge lengths of only a few centimetres is possible whereas in a gas discharge at least a distance of one meter is needed for leader inception [22]. Thus, after a slight increase of the applied voltage, the development of surface leader discharges, which are characterised by a leader channel and streamer discharges at their head (which are similar to bunches), can be observed in addition to the radial surface streamer discharges [22]. The needed voltage V_2 to provoke these surface leader discharges is defined in Toepler's second law:

$$V_2 = k' \cdot \sqrt{\frac{d_i}{\varepsilon_r}} \tag{1}$$

where k' is a constant of proportionality, d_i the thickness of the solid insulator and ε_r the relative permittivity. For a positive surface leader discharge, k' amounts to 110 kV/cm and for a negative one to 119 kV/cm [11]. Hence, in contrast to the first Toepler law, the inception voltage for surface leader discharges is dependent on the properties of the solid insulator whereas the polarity has little influence.

Remark: other sources may be found indicating different values for *k'*. Since this factor depends, among others, on the surface resistance of the solid insulator or the electrode shape, empirically determined values for *k'* are often used [22], [93].

1.4.3 Polarity effect on surface discharges

Similar to discharges in open or bulk gas not affected by a solid insulator, surface discharges propagate differently depending on the polarity of the applied voltage.

Regarding an arrangement as presented in section 1.4.2, a positive surface discharge develops radially on an insulator surface around the high voltage electrode (AC). Since the radially directed electric field at the front of the surface discharge is at the beginning of its propagation uniform, the electric field orthogonally to the discharge path is neutralised thus preventing the formation of ramifications. With further growth of the radially distributed discharge channels, the distance between them and its heads increases. Consequently, the orthogonal electric field distribution between the discharge channels becomes less homogeneous thus allowing the formation of arborescent ramifications. Due to the superposition of the applied electric field with the electric field due to space charges generated by the accumulation of positive ions, the resulting electric field at the front of the surface discharge exceeds the applied one. The positive surface discharge can therefore become self-sustaining [90], [96]

Even though a radial development can also be seen for negative surface discharges, their propagation is different. Because of the lower velocity of positive ions in the back of the electron avalanches, they tend to accumulate near the negative electrode which leads to a positive space charge in front of the negative electrode (the so-called cathode fall) increasing the field strength and therefore the electron emission. Consequently, the further development of negative surface discharges is hindered [90], [96] and the radially propagation distance is smaller than of positive surface discharges what can be seen in Figure 1.20 where a photogram of a positive and a negative discharge on the surface of solid insulator (PMMA) is pictured [57].

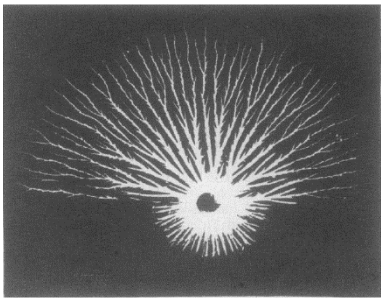

Figure 1.20. Photogram of positive (upper part) and negative (lower part) discharge on the surface of a solid insulator (PMMA) [57].

1.4.4 Interaction of surface discharges with the solid insulator

During the propagation of the surface discharge along the solid insulator surface, interaction between the discharge and the surface may be observed, especially regarding ionisation and attachment phenomena [97], [98]. These interactions are, as an example for a positive surface discharge, schematically presented in Figure 1.21 [98].

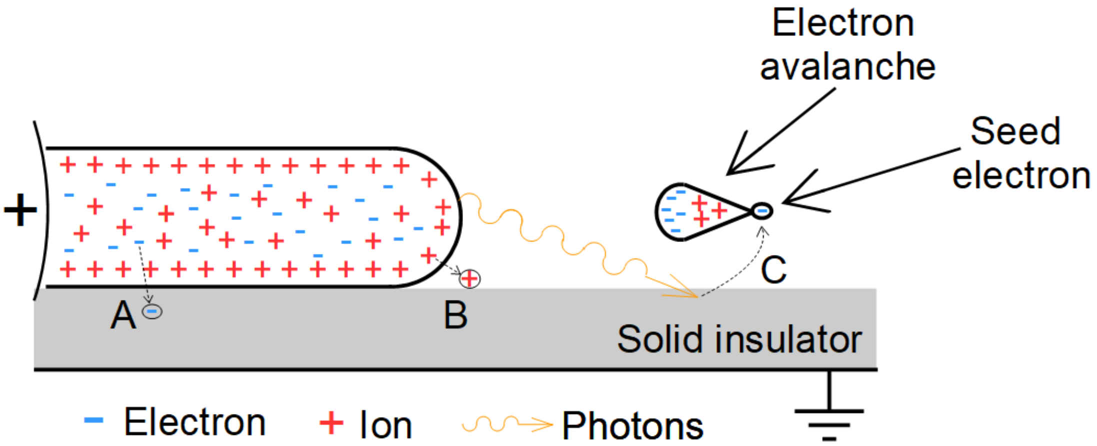

Figure 1.21. Schema showing the interaction between a positive surface discharge and the solid insulator surface. A – Attachment of electrons, B – Attachment of ions, C – Electron emission due to photo-ionisation.

The following interactions between the discharge and the solid insulator surface may occur [97], [98], [99]:

- A – attachment of electrons by trapping on the surface. Depending on the quantity of the trapped electrons, they may modify the electric field on the insulator surface and potentially initiate back discharges.
- B – attachment of ions by electrostatic attraction leading to an accumulation of surface charges and therefore to a reduced electric field between the surface and the discharge.

- C – electron emission due to the impact of photons created by photo-ionisation in the gas. This increases the number of seed electrons leading to more frequent ionisation collisions and electron avalanches.

1.4.5 Influence of different parameters on surface discharge propagation

The mechanisms of the discharge propagation along solid insulator surfaces are quite complex and further research in this field is still necessary. This section gives an overview of some results presented in various studies which were made over the years regarding the influence of different parameters such as dielectric and geometric properties or environmental conditions such as gas pressure or nature of the gas on surface discharge propagation (e. g. propagation velocity and distance).

With regard to the propagation velocity, it has been shown that surface discharges propagate faster along solid insulator surfaces than in open air without any solid insulator [100], [101]. This effect could be explained by the presence of free electrons on the insulator surface, deposed by precedent discharges. Those free electrons may contribute to a fast creation of an ionised discharge channel along the solid insulator surface [102]. Also, the emission of electrons from the insulator surface due to photoemission, which increases the ionisation activity in front of the surface discharge, facilitates a fast propagation [100], [102].
The influence of a high relative permittivity value of the solid insulator may also lead to higher surface discharge velocities [103].
Further, it was observed that the surface discharge velocity is the highest at its starting point before a slight decrease after a few centimetres of propagation down to a constant value occurs. By contrast, the surface discharge velocity in air remains in the absence of a solid insulator regardless of the propagation distance from its starting point nearly constant [100].

Moreover, it was observed that the surface discharge propagates with a fast and a slow component [100], [101], [102], [104]. The fast component is associated to a discharge propagating along the solid insulator surface and the slow component to a discharge propagating in proximity to the surface in ambient air.
The velocity of the fast component is dependent on the material of the solid insulator and increases with the applied electric field. This may be explained by the fact that an increased electric field reduces the electron attachment while enhancing the electron detachment thus leading to a higher ionisation activity.
By contrast, the slow component does not show this dependence since this component propagates in ambient air which is less susceptible to charge attachment processes.
The fast component on the surface has a higher velocity than a streamer discharge in open air in absence of a solid insulator and the slow component. However, the velocity of the latter is slower than a streamer in open air [100], [104].

The made observations are valid for different insulator materials except ceramic [101], [104]. For a surface discharge propagation on a ceramic surface, it has been found that the required electric field as well as the propagation velocity is equal to that in open air, which remains regardless to the applied electric field at a constant level. It has further been shown that in this case, the slow component of the surface discharge is predominant. However, its velocity is higher than the velocity of the slow components of the other insulator materials but nevertheless slower than the velocity of a streamer in air in absence of a solid insulator [101], [104].

Also, the needed electric field for a surface discharge propagation on the ceramic surface is lower than for other materials since the ceramic tends to accumulate less charges on its surface than the other examined materials. Consequently, the electric field is less weakened due to less accumulated surface charges which results in a lower electric field necessary for the surface discharge to propagate. By contrast, a higher electron attachment due to a rougher surface of the aluminium oxide is reported in [101].

A fast component along the ceramic surface only appears if the applied electric field is further increased but even in this case, its velocity is the lowest compared to the other analysed solid insulator materials. This is due to the ionic crystal structure of the ceramic since the chemical bond energy of its ions is large thus requiring photons whose energy is sufficiently high for creating secondary electrons by photoemission. Therefore, the photoemission remains weak for low electric fields whereas sufficiently high electric fields lead to a creation of secondary electrons resulting in an appearance of a, at least low-velocity, fast component.

All these effects were consolidated by analysing the light emission during the surface discharge propagation on the insulator surface [100], [104].

Other studies analysed the influence of the relative permittivity on the surface discharge propagation velocity depending on its polarity [105], [106].

A higher relative permittivity leads to a stronger polarisation of the insulator surface, which results in a stronger attraction of the discharge to the surface, a more rapid increase in electric field, which reaches higher values, as well as an earlier streamer inception [106].

In the case of a negative surface discharge, it has been shown that the propagation velocity decreases with permittivity. Due to the increased electric field, attraction of electrons on the surface is enhanced. The in this way accumulated negative surface charge reduces the electric field at the front of the surface discharge. Simultaneously, the ionisation activity reduces since less electrons are available thus leading to lower propagation velocities [105].

By contrast, only a weak influence on propagation velocity for a positive surface discharge has been observed. This may be explained by the appearance of space charges at the front of the surface discharge which cause high electric fields thus reducing the influence of the insulator material [102], [106].

Another influencing parameter of the propagation velocity is the gas pressure. The higher the gas pressure, the lower the surface discharge velocity due to a shorter mean free path [102].

The surface discharge propagation may also be influenced by the presence of surface charges where their polarity has to be considered. For a negative surface discharge in presence of positive surface charges, the electric field is enhanced thus leading to an accelerated discharge propagation. On the contrary, if the surface charges are negative, the propagation of a negative surface discharge is slowed down or even prevented. However, since these results are based on a numerical simulation, differences to experimental results may be seen showing in some cases a converse result [105]. A self-propagating surface discharge may occur when sufficient surface charges are present [107].

Regarding the propagation distance of surface discharges on insulator surfaces, several parameters may have an influence.
The electronegativity of the gas in which the surface discharge takes place reduces the discharge path due to higher electron attachment. For example, the discharge length in nitrogen is greater than in SF_6 [108].
The propagation distance increases with the applied voltage which is logical since the electric field becomes more important [105], [108], [109].
Concerning the relative permittivity, longer surface discharge channels can be observed with higher relative permittivity due to an increase in electric field [12], [90], [108] whereas an increase in pressure leads to a decrease in propagation distance due to the weaker charge carriers [90], [108], [110].
The propagation distance also depends on the thickness of the solid insulator. Since the capacitance of a thin insulator is higher, the electric field and consequently the surface discharge length increases [108].

1.5 Summary

The objective of this study is to come to a better understanding of discharge phenomena starting at triple junctions under varied pressure and temperature conditions. For this purpose, it was appropriate to present in this chapter the theoretical background on the physical principles for the formation of electrical discharges.
Since pressure and temperature was varied for the experiments carried out in this work, the influence of environmental conditions on Paschen's law, which gives the inception voltage for electrical breakdown in a gas as a function of the product of the gas pressure and the gas gap distance, were discussed.

An overview of partial discharges including a classification, a discussion of several parameters influencing partial discharge activity such as environmental conditions as well as partial discharge detection methods contributed insofar as the study of partial discharge phenomena at triple junctions is the main topic of this work.

Experiments were also carried out for surface discharges starting at a triple junction. For this purpose, several aspects such as the development of discharges along the solid insulator surface are of interest for this work.

In order to contextualise the work, a literature review was made. Regarding the presented studies on the influence of different environmental conditions on partial discharge activity, it can be noted that, despite the interesting results, most of the studies focus on specific applications such as qualification tests, ageing and lifetime of insulation, etc. Therefore, the influence of different temperatures and pressures is often studied separately or limited to a range which is of interest for a specific industrial application such as aviation.
Concerning the studies on discharge propagating on solid insulator surfaces, it has to be mentioned that the presented mechanisms are quite complex and further research has to be done to come to a better understanding of these phenomena.

Considering these aspects, a global study for a wide range of temperatures and pressures is of interest. The aim of this work is therefore to come to a more detailed understanding of the phenomena that occur under these various temperature and pressure conditions, with special attention to the behaviour of the threshold voltage for partial discharge inception and extinction as well as the voltage for breakdown by dielectric flashover mechanism at a triple junction.

Chapter 2

Overview of the experimental work, description of the solid insulators and preliminary results of PDIV measurements

2.1 Introduction

The aim of the present work is to come to a more detailed understanding of discharge phenomena taking place at a triple junction under various temperatures and pressures. For this purpose, measurements of PDIV (Partial Discharge Inception Voltage), PDEV (Partial Discharge Extinction Voltage) and FOV (Flashover Voltage), as well as analyses of the dielectric properties of the solid insulators, were made using a device consisting of a disc-shaped solid insulator placed between two electrodes, one connected to a high voltage AC power supply (50 Hz) and the other one connected to ground. A photograph of a simplified experimental configuration for these experiments is shown in Figure 2.1.

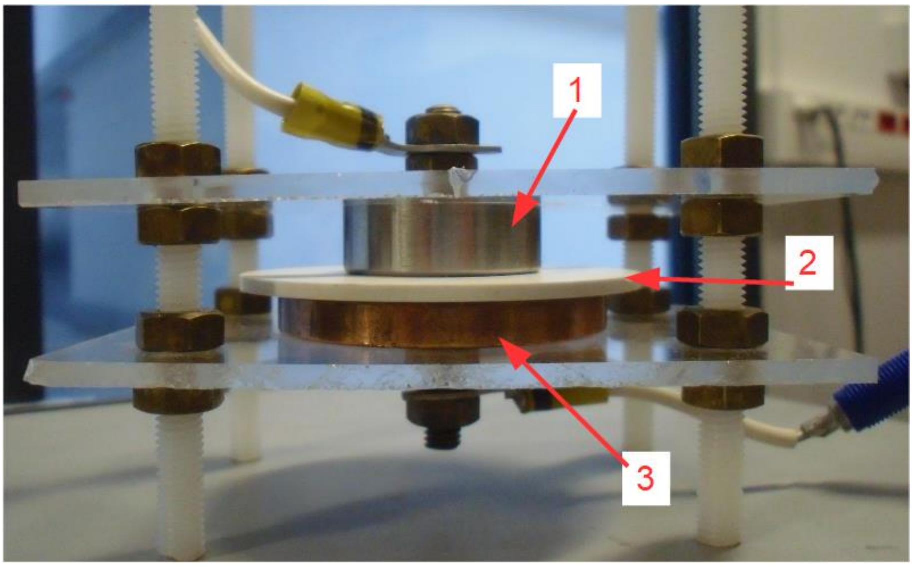

Figure 2.1. Simplified experimental configuration.
1 – Electrode connected to a high voltage power supply (50 Hz AC), 2 – Solid insulator, 3 – Electrode connected to ground.

In this chapter, a description of the experiments is given, starting in section 2.2 with a general overview of the experiments and the test bench including the various experimental equipment.

Section 2.3 describes the solid insulators because their geometrical and dielectric properties play a crucial role for the experiments. Focus is made specifically on aluminium oxide considering that this material was used for most experiments.

Then, section 2.4 presents the experimental setup and its elements which was the basis for all the other experiments carried out in this work. It includes the description of an experimental setup for some preliminary PDIV measurements which were principally made to ensure that the test circuit works properly.

The results obtained during the preliminary PDIV measurements, more precisely the influence on PDIV of several dielectric and geometrical parameters of the solid insulators used for these experiments such as thickness, permittivity, or insulator surface metallisation, are presented and discussed in section 2.5.

While this chapter provides a general overview of the experiments and details about the preliminary setup, more details on experimental arrangements and procedures will also be given in the following chapters which will also present results and analysis of the experimental work.

2.2 General overview of the experimental work and equipment

2.2.1 General overview of the experiments

In the present study, various experiments have been carried out, and the experimental work can be divided into two main categories. On the one hand, experiments concerning the influence of various parameters, such as temperature and pressure, on the values of partial discharge inception voltage (PDIV), partial discharge extinction voltage (PDEV) and flashover voltage (FOV), which constituted the main experimental work, were carried out. On the other hand, experiments regarding the measurements of the dielectric properties of the solid insulators were made. Apart from that, some preliminary PDIV measurements were done in the context of the implementation of the test setup, on which all experiments were based. The experiments performed can be described as follows:

A) PDIV/PDEV & FOV

\- PDIV – Partial Discharge Inception Voltage / PDEV – Partial Discharge Extinction Voltage

- dependence on the properties of the solid insulator (thickness, surface metallisation, relative permittivity)
- dependence on the temperature (20 °C to 400 °C)
- dependence on the gas pressure (50 mbar to atmospheric pressure) and gas density

\- FOV – Flashover Voltage

- dependence on the temperature (20 °C to 400 °C)
- dependence on the gas pressure (50 mbar to atmospheric pressure) and gas density
- dependence on the material of the solid insulator (Al_2O_3, PTFE) and on the gas pressure analysing the spatial flashover behaviour using high-speed imagery

B) Dielectric properties

\- Volume resistivity

- dependence on the temperature (20 °C to 400 °C)

\- Relative permittivity

- dependence on the temperature (20 °C to 500 °C)
- dependence on the frequency (20 Hz to 1 kHz)

Remark: the measurements of the dielectric properties were only made for the aluminium oxide disc which was used in the majority of experiments. The reason for this is that one of the main axes of investigation was the dependence on temperature and only the aluminium oxide disc could be used at higher temperatures.

Some other experiments whose main purpose was to adjust the experimental setup as well as the test procedures are not listed in the above overview but are explained at the appropriate position in this manuscript.

In the following, a general overview of the test bench is given including an enumeration of the experimental equipment which was used for the different experiments.

2.2.2 General overview of the test bench

Figure 2.2 shows a general overview of the test bench which can be divided into five different zones.

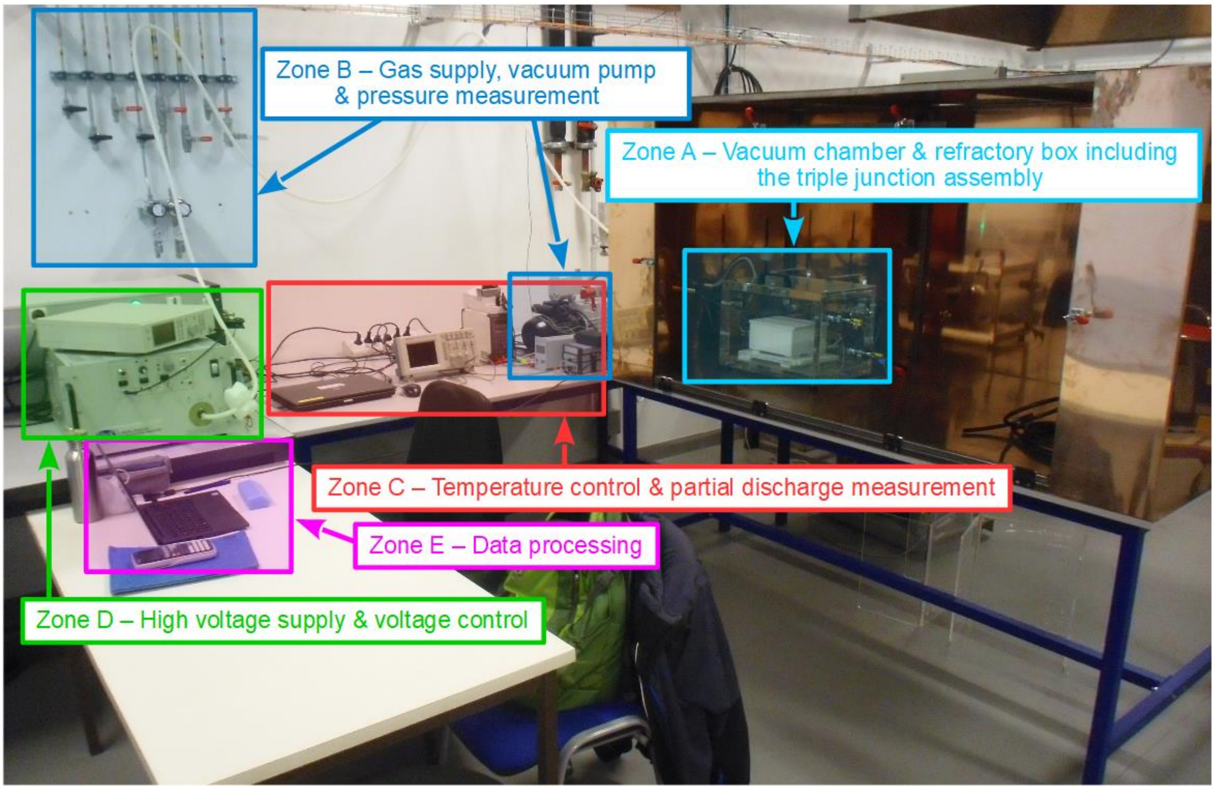

Figure 2.2. Overview of the test bench divided into five different zones.

Each zone consisted of one or more components which were used to realise the experiments mentioned above. Nevertheless, the test setup was adapted for each experiment according to its purpose; these modifications are described for each more precisely in the respective sections in which the experimental work is presented. In the following, the zones pictured in Figure 2.2 are briefly described.

Zone A – Vacuum chamber & refractory box including the triple junction assembly

- This zone is constituted of the vacuum chamber within which a refractory box containing the triple junction assembly and a heating plate is placed. All experiments have been realised within this zone.

Zone B – Gas supply, vacuum pump & pressure measurement

- This zone contains the gas supply and the vacuum pump, both connected to the vacuum chamber in zone A. In addition, the pressure was measured using a pressure gauge.

Zone C – Temperature control & partial discharge measurement

- Within this zone, the temperature of the heating plate inside the refractory box (zone A) was controlled using a LabVIEW interface. Furthermore, the partial discharge measurement using a partial discharge analyser was made in this zone.

Zone D – High voltage supply & voltage control

- In this zone, a high voltage power supply was situated together with a function generator to control its voltage output.

Zone E – Data processing

- The data acquired during the different experiments were processed using a computer. Regarding partial discharge measurement, a software provided by the manufacturer of the partial discharge analyser allowed the visualisation of the partial discharge activity.

As mentioned above, the exact setup of the test bench differed from experiment to experiment and only some components were common to all experiments. Table 2.1 gives an overview of the experimental equipment depending on the experiment.

Table 2.1. Overview of the experimental equipment for the different types of experimentation.

	PDIV/PDEV		**FOV**		**Dielectric measurements**	
	Preliminary PDIV measurements	**Influence of temperature and gas pressure**	**Influence of temperature and gas pressure**	**Discharge location imagery**	**Relative permittivity**	**Volume resistivity**
Solid insulator	✓	✓	✓	✓	✓	✓
High voltage electrode (tungsten)	✓	✓	✓	✓	✓	✓
Grounded counter electrode (inox)	✓	✓	✓	✓	✓	✓
Vacuum chamber	✓	✓	✓	✓	✓	✓
Refractory box	×	✓	✓	×	✓	✓
Vacuum pump	✓	✓	✓	✓	(✓)	(✓)
Pressure gauge	✓	✓	✓	✓	(✓)	(✓)
Gas supply (N_2)	×	✓	✓	✓	✓	✓
High voltage AC power supply	✓	✓	✓	✓	×	×
Function generator	✓	✓	✓	✓	×	×
Resistor (10 MΩ)	✓	✓	×	×	×	×
High voltage cable	✓	✓	✓	✓	×	×
High voltage probe	✓	✓	✓	✓	×	×
CT-2 current probe	×	×	✓	✓	×	×
Heating plate	×	✓	✓	×	✓	✓
DC power supply heating plate	×	✓	✓	×	✓	✓
Thermocouples	×	✓	✓	×	✓	✓
Control heating plate (LabVIEW)	×	✓	✓	×	✓	✓
Partial discharge analyser	✓	✓	×	×	×	×
Oscilloscope	(✓)	(✓)	✓	✓	×	×
DC power supply	×	×	×	×	×	✓
Pico-ammeter	×	×	×	×	×	✓
Guard electrode (copper)	×	×	×	×	×	✓
Counter electrode (copper)	×	×	×	×	×	✓
Insulating aluminium oxide plate	×	×	×	×	×	✓
LCR Meter	×	×	×	×	✓	×
High speed camera	×	×	×	✓	×	×
Computer	✓	✓	×	✓	×	✓

Remarks: the oscilloscope for the experiments regarding the PDIV/PDEV was only used to calibrate the high voltage probe but not during the experiment itself.

Concerning dielectric measurements, the vacuum pump and the pressure gauge were only used during the purging and filling of the vacuum chamber with nitrogen. However, the experiments did not require a special pressure level.

Except for the preliminary PDIV measurements regarding the influence of geometrical and dielectric properties of the solid insulator on PDIV, which were made in air and at ambient temperature, all experiments were realised using nitrogen. This gas was chosen because of its similarity to air with regard to the Paschen's curve minimum and slope at high values of gas pressure/density and inter-electrode distance. The use of an inert gas was needed at high temperature to prevent the oxidation of the metal electrodes inside the refractory box.

The nitrogen used in this work was of type I ("industrial") which means that its purity is ≥ 99.8 %. It was provided by the gas network installed in the laboratory which was supplied by gas bottles. The gas network could be connected directly via a piping equipped with a valve to the vacuum chamber of the test bench.

2.3 Description of the solid insulators

2.3.1 Aluminium oxide

Since most of the experiments about discharge inception and development from a triple junction were done in this work using an aluminium oxide disc, it is of particular interest to characterise its properties to come to a better understanding of the interactions between the discharge activity and the insulator material. This section therefore presents the main properties of aluminium oxide.

Polycrystalline aluminium oxide (alumina, Al_2O_3) is an inorganic solid ceramic often used for electrical insulation. It naturally occurs in bauxite which principally consists of aluminium oxide (in its hydrated form, about 55 %) and other minerals like silica or iron oxide. To extract and purify the aluminium oxide, the Bayer process, named after the Austrian chemist Carl Josef Bayer, who developed this process in 1888 [111], can be used. The product of this process is an aluminium oxide powder. To obtain a solid object, the powder is sintered which means that it is heated to high temperatures. This heating process transforms the powder to solid aluminium oxide. Depending on the sintering method, temperature, time, etc., properties such as purity, density or grain size of the resulting ceramic are determined. Consequently, the sintering process defines the electrical properties of the aluminium oxide.

Different types of aluminium oxide ceramics are distinguished according to their crystal structure, among them the most thermally stable at high temperatures is the α-aluminium oxide, which possesses a rhombic crystal structure and has very low porosity [112]. It is also characterised by its stability at high temperatures, good chemical resistance, high electrical resistivity, good mechanical strength, and reasonable production costs [113]. Therefore, it is used in many fields of application such as electrical engineering (e. g. insulators, packaging material in electronics, substrates in power electronics, capacitors, etc.), chemistry (e. g. membranes, micro-filtration, etc.), mechanical and thermomechanical applications (e. g. motors, turbines, valves, etc.) or the military sector (armouring, etc.) [112]. Table 2.2 shows some dielectric parameters of an α-aluminium oxide [112], [114], [115].

Table 2.2. Dielectric parameters of an α-aluminium oxide [112], [114], [115].

Dielectric constant	**Value**
Relative permittivity [-] (at 25 °C, 1 kHz)	9.3
Volume resistivity [Ω · cm] (at 25 °C)	$> 10^{14}$
Loss factor [-] (at 25 °C, 1 kHz)	0.039
Dielectric strength [kV/mm]	22

Remark: the values indicated in Table 2.2 should be considered as orders of magnitude. They depend on many parameters, such as the purity of the specific aluminium oxide sample considered, measurement method, electrode geometry and material, applied voltage and duration of voltage application, and environmental conditions such as temperature and pressure, etc. [90].

For the experiments realised in this work, several α-aluminium oxide discs were used which differed from each other in shape, size, thickness, purity, and the presence or not of metallisation (aluminium), see Table 2.3.

Table 2.3. Overview of the aluminium oxide discs.

Disc	**Shape**	**Thickness [mm]**	**Size [mm]**	**Purity [%]**	**Metallisation (100 nm aluminium layer)**
(I)	Square	0.127	50.8 x 50.8	96	No
(II)	Circle	1	Ø 50	99.7	No
(III a)	Square	1.016	76.2 x 76.2	96	No
(III b)					Lower surface
(III c)					Lower surface + metallic circle on upper surface (Ø 30 mm)
(IV a)	Square	1.016	101.6 x 101.6	99.6	No
(IV b)					Lower surface
(IV c)					Lower surface + metallic circle on upper surface (Ø 30 mm)
(V)	Circle	2	Ø 60	96	No

During the preliminary PDIV measurements, the influence of parameters like thickness and metallisation on PDIV was analysed and compared. All the aluminium oxide discs were used for these experiments except disc (II).

Then the influence of various temperature and gas pressure/density conditions were explored on discharge phenomena starting at triple junctions, using aluminium oxide discs (II) and (III a) only. Given the critical importance of the insulator properties in this field, a comparison between two aluminium oxide discs with identical nominal properties (geometry, purity) but provided by two different suppliers was made. The results of this comparison are detailed in the following section.

2.3.1.1 Choice of the aluminium oxide disc

For the experiments at different temperature and gas pressure/density conditions, aluminium oxide discs from two different suppliers (situated in France and China) were available. These discs, further named as specimens A and B, were made of 99.7 % pure α-aluminium oxide with identical geometrical dimensions (thickness 1 ± 0.05 mm, diameter of 50 ± 0.1 mm). Figure 2.3 shows photographs of an α-aluminium oxide disc obtained from each supplier. The colours of the two specimens are different. The specimen A is more yellowish or ivory than specimen B which is almost white, but no other macroscopic difference can be discerned. The surface of both specimens is smooth, matte and without any visible defects.

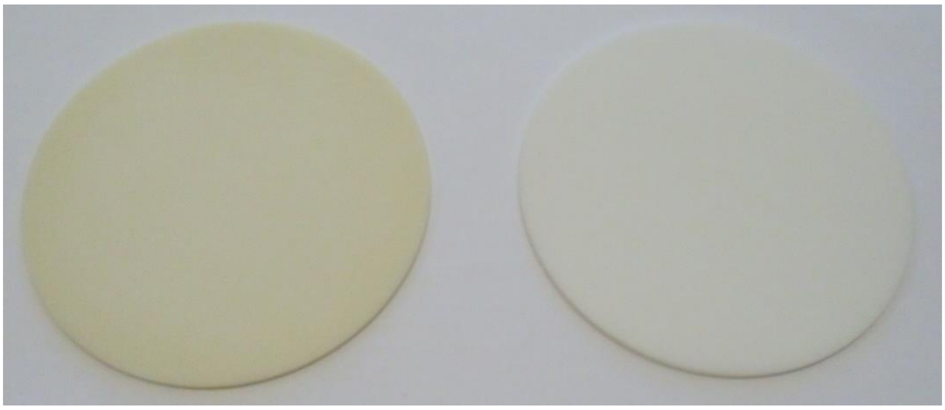

Figure 2.3. α-aluminium oxide disc of supplier A (left) and supplier B (right).

A microscopic analysis of both specimens has been made using a profilometer to have a close look at the surface and to measure its roughness. For this purpose, five zones were chosen on the surface of each specimen, each of a size of 1 mm x 1.3 mm, see Figure 2.4.

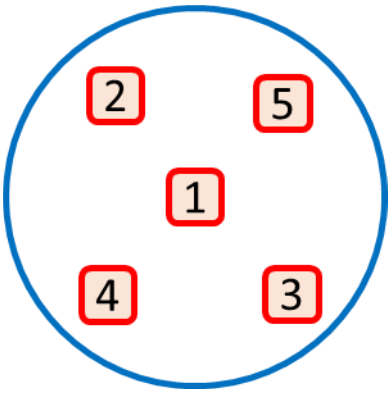

Figure 2.4. Zones of roughness measurement on the surface of each specimen.

For each zone, several parameters of surface roughness, which are described in Table 2.4, were measured.

Table 2.4. Parameters of surface roughness measurement.

Parameter	**Description**
Ra	Arithmetic average of profile height considering deviations (valleys, peaks) from the mean line
Rq	Quadratic mean of profile height considering deviations (valleys, peaks) from the mean line
Rp	Maximum peak height in relation to the mean line
Rv	Maximum valley depth in relation to the mean line
Rt	Maximum valley to peak height, *Rt* = *Rp* + *Rv*

Table 2.5 and Table 2.6 show the measurement results of the analysed zones of specimen A and specimen B including the average values and the 1σ standard deviation for all parameters.

Table 2.5. Measurement results of surface roughness of specimen A.

Zone	**1**	**2**	**3**	**4**	**5**	**Mean value**	**1σ standard deviation**
Ra [µm]	1.853	1.89	1.544	1.496	3.103	**1.977**	0.654
Rq [µm]	2.649	2.555	2.086	2.07	3.917	**2.655**	0.753
Rp [µm]	12.968	11.691	8.704	13.199	8.055	**10.924**	2.403
Rv [µm]	25.889	23.027	21.5	16.897	33.95	**23.253**	6.323
Rt [µm]	38.857	34.718	30.204	30.095	42.006	**35.176**	5.267

Table 2.6. Measurement results of surface roughness of specimen B.

Zone	**1**	**2**	**3**	**4**	**5**	**Mean value**	**1σ standard deviation**
Ra [µm]	2.554	2.41	2.969	3.302	2.536	**2.754**	0.372
Rq [µm]	3.501	3.287	3.932	4.323	3.49	**3.707**	0.417
Rp [µm]	20.306	19.433	23.842	21.145	33.771	**23.669**	5.867
Rv [µm]	12.274	14.52	13.222	11.24	15.399	**13.331**	1.673
Rt [µm]	32.581	33.953	37.064	32.386	49.17	**37.031**	7.039

On the basis of the measurement results presented in Table 2.5 and Table 2.6, it can be established that specimen A has a slightly lower roughness (*Ra*) than specimen B. Regarding the average value of the peak height (*Rp*), specimen A has much lower peaks than specimen B, but this tendency is inverse regarding the average value of the valley depth (*Rv*) which is for specimen A much higher than for specimen B. Nevertheless, even though the average maximum valley to peak height (*Rt*) is less important for specimen A, its value is close for both specimens, especially when the standard deviation is considered.

A clearer picture of the differences in roughness between A and B may appear by considering Figure 2.5 and Figure 2.6 where, as an example, the 3D-map of one of the five zones recorded with the profilometer for both specimens is shown.

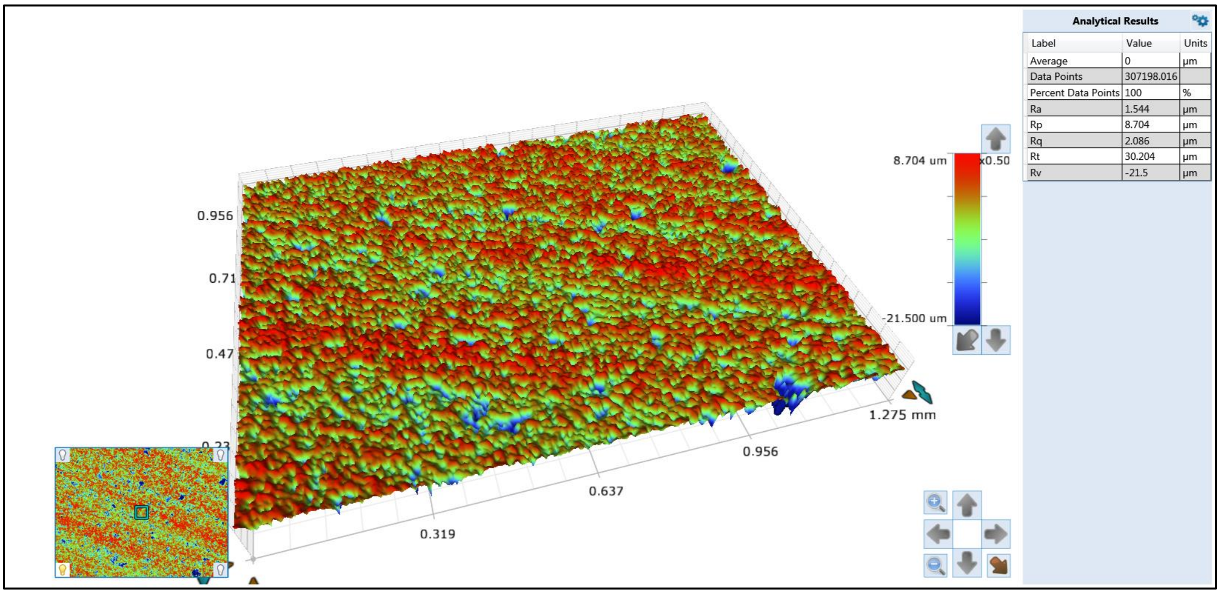

Label	Value	Units
Average	0	µm
Data Points	307198.016	
Percent Data Points	100	%
Ra	1.544	µm
Rp	8.704	µm
Rq	2.086	µm
Rt	30.204	µm
Rv	-21.5	µm

Figure 2.5. 3D-surface map of zone 3 of specimen A.

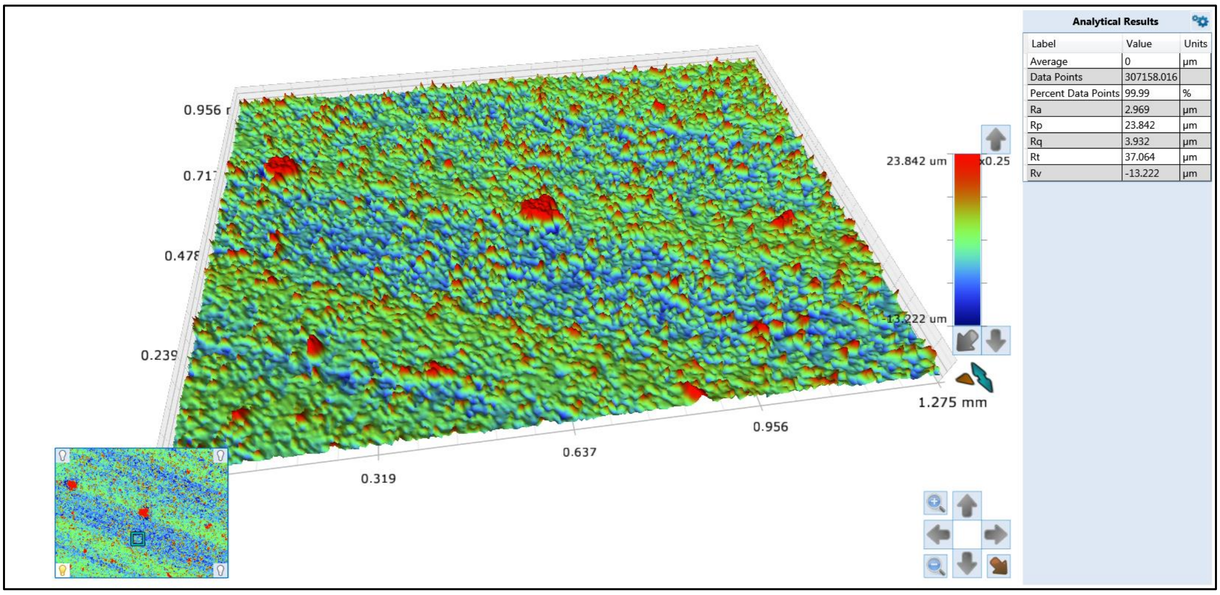

Label	Value	Units
Average	0	µm
Data Points	307158.016	
Percent Data Points	99.99	%
Ra	2.969	µm
Rp	23.842	µm
Rq	3.932	µm
Rt	37.064	µm
Rv	-13.222	µm

Figure 2.6. 3D-surface map of zone 3 of specimen B.

Specimen A has a distribution of peaks interrupted by some deep valleys. The contrary can be seen for specimen B where some peaks stand out. It may be assumed that the valleys and peaks are present due to the limits of the fabrication process whereas some peaks may possibly come from impurities accidentally deposed on the surface. Although each of the specimens presents a characteristic surface (valleys for specimen A, peaks for specimen B), there is a slight advantage for specimen A, especially in light of the average surface roughness which is smaller than for specimen B. Hence, the decision was made to use specimen A as test object for all experiments carried out in this work.

In addition to the surface analysis using the profilometer, an analysis of specimen A using a scanning electron microscope (SEM) including an XPS-analysis (x-ray photoelectron spectroscopy) was made to examine the composition of this aluminium oxide disc. Figure 2.7 shows a SEM-picture of the surface of specimen A including the distribution of aluminium and oxygen according to the XPS-analysis.

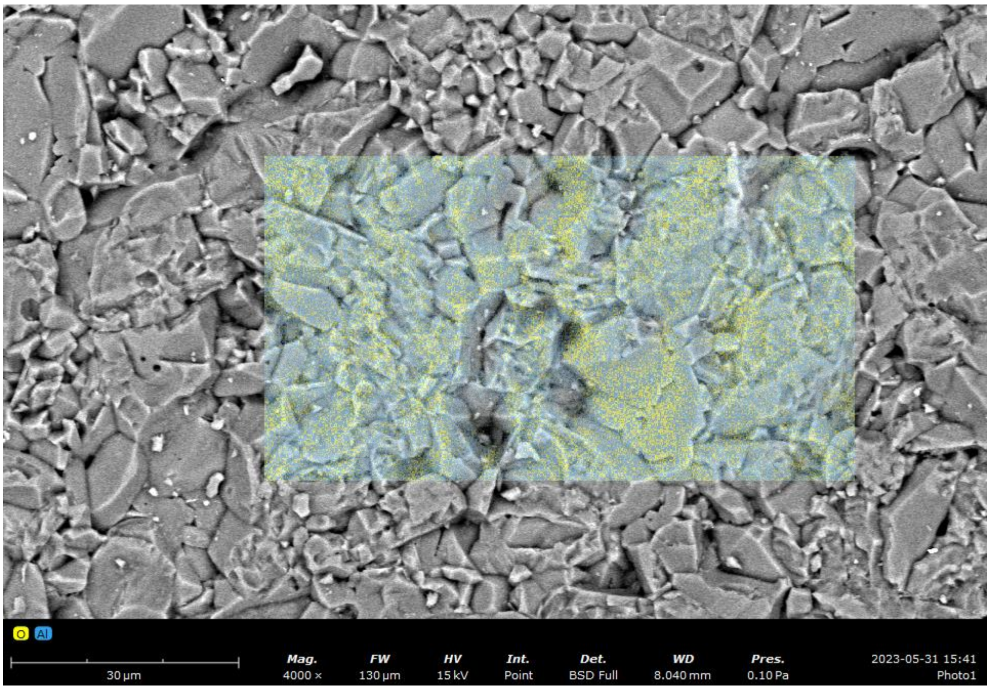

Figure 2.7. Distribution of aluminium (blue-coloured zone) and oxygen (yellow-coloured zone) according to the XPS-analysis of the α-aluminium oxide surface of specimen A.

The aluminium oxide grains are variously shaped, sized and heterogeneously distributed. The average size can be estimated to be in a range from 5 µm to 10 µm.
The results of the XPS-analysis indicate, as expected, the presence of aluminium (blue-coloured areas) and oxygen (yellow-coloured areas) on the surface of the analysed α-aluminium oxide specimen.

2.3.2 PTFE

Some experiments were carried out using PTFE (Polytetrafluorethylene, also known as Teflon) as solid insulator. As shall be seen in section 2.5.3 and section 4.4.2, this was done specifically to examine the influence of the relative permittivity of the solid insulators on PDIV and FOV; PTFE having a drastically different relative permittivity compared to aluminium oxide.

PTFE is a thermoplastic polymer which is obtained by the polymerisation of tetrafluoroethylene (TFE). Owing to this polymerisation, PTFE has excellent insulating properties and is used in many high voltage applications, especially when high temperatures (up to 260 °C) are reached or when fireproof materials are needed. Hence, PTFE may replace a ceramic insulator if the application is exposed to mechanical constraints such as shocks.

Since the intermolecular forces of PTFE are low, the material flows easily even under low mechanical stress. PTFE can therefore be used as a flexible sealing material, e. g. in form of a tape [22].

Because of its regular structure of the molecule, the relative permittivity as well as the loss factor are low and remain at a constant level over a wide range of environmental conditions (heat, cold, UV light) and especially over a wide frequency range since no orientation polarisation (alignment of permanent electric dipoles due to an external electric field) takes place. This allows the use of PTFE in high frequency applications for feedthroughs, connectors, and capacitor dielectrics [22], [116]. PTFE is known to be chemically inert which opens other options for the application of this material [116].

On the contrary, even though PTFE has a high dielectric strength, its continuous dielectric strength amounts only to 2 to 6 kV/mm [22] resulting in a vulnerability to partial discharge activity. Table 2.7 shows some dielectric parameters for PTFE to give an idea of the order of its magnitudes [22], [116].

Table 2.7. Dielectric parameters of PTFE [22], [116].

Dielectric constant	**Value**
Relative permittivity [-]	2.1
Volume resistivity [Ω · cm]	> 10^{18}
Loss factor [-]	0.0004
Dielectric strength [kV/mm]	30

In the present work, two PTFE discs were used, named PTFE disc (I) and PTFE disc (II). Both had the same geometrical dimensions as the α-aluminium oxide disc, a diameter of 50 mm and a thickness of 1 mm. However, PTFE disc (I) was manually cut out of a PTFE sheet whereas PTFE disc (II) was produced by machine out of a PTFE rod which had the exact diameter.

Even if PTFE can be used with temperatures up to 260 °C, it was decided to use the specimens only at ambient temperature.

2.4 Experimental setup and procedure – preliminary PDIV measurements

The purpose of these preliminary PDIV measurements was to develop and qualify a test setup for the experiments carried out in this work. The influence of some dielectric properties of solid insulators such as thickness, surface metallisation or relative permittivity on PDIV at ambient temperature and varied gas pressures was investigated. The experimental results are presented and discussed in section 2.5. This section gives an overview of the test setup with a description of the principal elements.

2.4.1 Test setup

Figure 2.8 shows a schematic of the basic test setup and circuit including a zoom on the triple junction assembly in the right part of the figure.

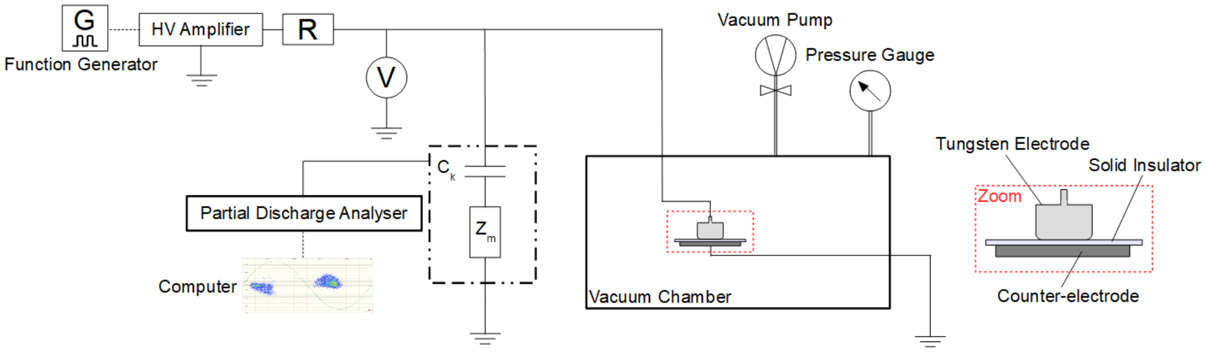

Figure 2.8. Schematic of the test setup and circuit to analyse the influence of different properties of the aluminium oxide test object on PDIV.

The triple junction assembly is constituted of three elements:

- Cylindrical tungsten electrode

The cylindrical tungsten electrode (diameter of 30 mm, height of 10 mm) with Rogowski profile to approach a uniform electrical field was connected to a high voltage source and used for all experiments realised in this work. Tungsten is often used in electrical applications due to its good thermal and electrical conductivity. It is suitable for high temperature applications owing to its high melting point (the highest of all metals) and low thermal expansion coefficient. Since the surface roughness of the electrode may affect the PDIV, the surface of a brand-new and a polished tungsten electrode was analysed in the same manner as presented in section 2.3.1.1 using the profilometer. The polishing procedures – renewed before each experiment – are described section 3.2.2 and were required to remove a visible layer of oxidation which developed at high temperatures over the course of several hours of experimentation.
Five 1 mm x 1.2 mm zones were analysed on the lower surface of the tungsten electrode (which is in contact with the solid insulator). Figure 2.9 shows as an example the 3D-surface

map of one of the analysed zones for the brand-new and Figure 2.10 for the polished tungsten electrode.

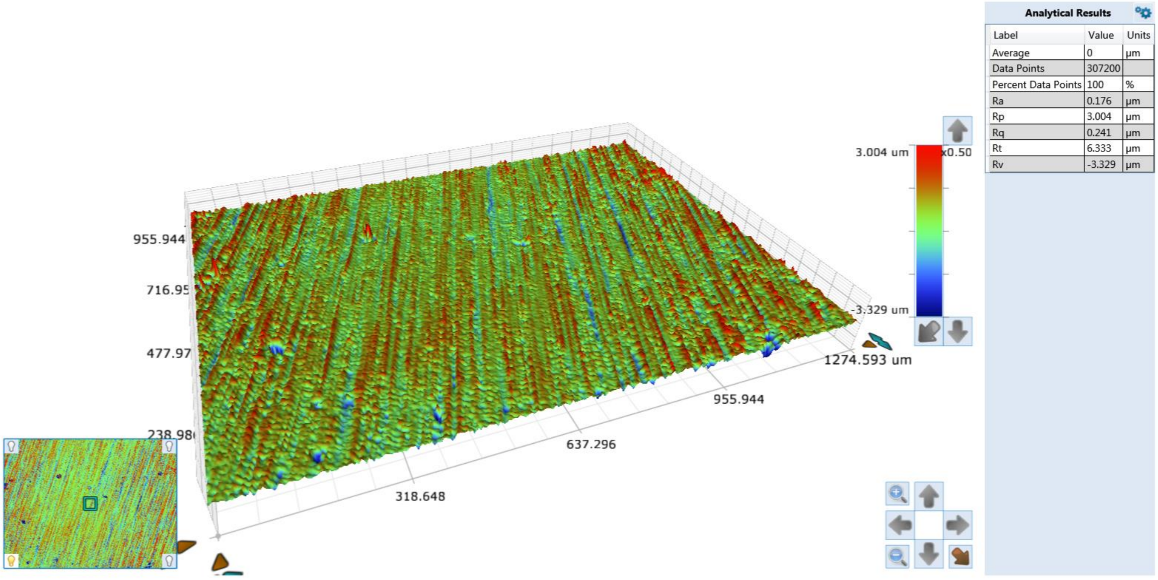

Analytical Results

Label	Value	Units
Average	0	µm
Data Points	307200	
Percent Data Points	100	%
Ra	0.176	µm
Rp	3.004	µm
Rq	0.241	µm
Rt	6.333	µm
Rv	-3.329	µm

Figure 2.9. 3D-surface map of one of the analysed zones of a brand-new tungsten electrode.

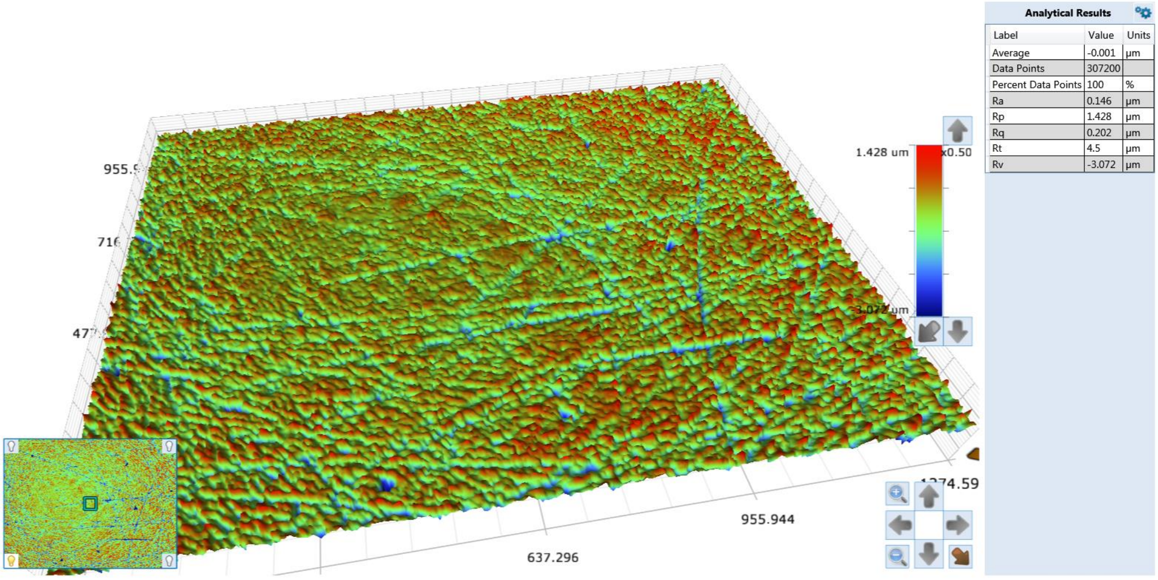

Analytical Results

Label	Value	Units
Average	-0.001	µm
Data Points	307200	
Percent Data Points	100	%
Ra	0.146	µm
Rp	1.428	µm
Rq	0.202	µm
Rt	4.5	µm
Rv	-3.072	µm

Figure 2.10. 3D-surface map of one of the analysed zones of a polished tungsten electrode.

Both 3D-surface maps of the tungsten electrode show the presence of grooves. For the brand-new tungsten electrode, they are systematically parallel to each other whereas on the polished tungsten electrode they are oriented randomly, and the surface has a slightly lower roughness R_a. It could therefore be assumed that the grooves present on the surface of the brand-new tungsten electrode are due to the fabrication process whereas the polishing and cleaning process led to a surface where the initial grooves have nearly disappeared, and the observed grooves were provoked by polishing.

Several parameters of surface roughness (see Table 2.4) were measured for each zone. The results are shown in Table 2.8 and Table 2.9.

Table 2.8. Measurement results of surface roughness of the brand-new tungsten electrode.

Zone	**1**	**2**	**3**	**4**	**5**	**Mean value**	**1σ standard deviation**
Ra [µm]	0.185	0.177	0.188	0.176	0.177	**0.181**	0.006
Rq [µm]	0.248	0.24	0.283	0.241	0.236	**0.25**	0.019
Rp [µm]	2.561	2.412	5.581	3.004	1.471	**3.006**	1.544
Rv [µm]	2.839	2.519	3.572	3.329	1.755	**2.802**	0.716
Rt [µm]	5.4	4.931	9.153	6.333	3.226	**5.808**	2.183

Table 2.9. Measurement results of surface roughness of the polished tungsten electrode.

Zone	**1**	**2**	**3**	**4**	**5**	**Mean value**	**1σ standard deviation**
Ra [µm]	0.159	0.146	0.136	0.147	0.159	**0.149**	0.010
Rq [µm]	0.217	0.202	0.189	0.198	0.226	**0.206**	0.015
Rp [µm]	1.289	1.428	1.981	1.33	1.203	**1.446**	0.310
Rv [µm]	2.345	3.072	2.42	2.669	5.478	**3.197**	1.306
Rt [µm]	3.634	4.5	4.401	3.999	6.681	**4.643**	1.190

These measurements show that the surface roughness of the tungsten electrode decreased after polishing. The polished surface seems to be smoother with less peaks than the brand-new tungsten electrode. The mean valley depth is a bit higher for the polished tungsten electrode but the mean valley to peak height is lower.

Hence, polishing the tungsten electrode surface slightly improves the surface state in comparison to the surface of a brand-new tungsten electrode. This is important since the vast majority of experiments were done using polished electrodes and not new ones. .

- Solid insulator

The solid insulator was either an aluminium oxide disc or a PTFE disc. The properties of the solid insulators were described in section 2.3.

- Counter electrode

The counter electrode used for this experiment was a copper disc electrode (diameter of 49.4 mm, height of 6.5 mm) connected to ground potential.

Apart from that, these components constituted the test setup:

- Vacuum chamber

The vacuum chamber, containing the triple junction assembly, was made of PMMA (poly(methyl methacrylate)). It had inner dimension of 0.39 m x 0.25 m x 0.25 m (length x width x height) corresponding to a volume of approximately 24 litres. The vacuum chamber walls had a thickness of 30 mm and feedthroughs were used to connect the elements inside the vacuum chamber to high voltage potential, ground, etc.

- Vacuum pump

To vary the pressure inside the vacuum chamber, a vacuum pump (Pfeiffer Duo 5M), allowing to reach pressures down to a few millibars, was used. The gas tubing connecting the experimental chamber to the vacuum pump was equipped with a three-way connector, which was in turn connected via a valve to the gas supply. Actioning this valve allowed adjustment of the pressure within the experimental chamber.

- Pressure gauge

The pressure inside the vacuum chamber was measured using a pressure gauge (Pfeiffer PCR 280) which was likewise directly connected to the vacuum chamber via a feedthrough.

- High voltage power amplifier

The triple junction assembly was connected to a high voltage power amplifier, Trek model 20/20C-HS, which had an output voltage range from 0 kV up to ± 20 kV DC or peak AC and an output current range from 0 mA to ± 20 mA DC or 60 mA peak AC for 1 ms.

- Function generator

To control the high voltage power amplifier, a digital function generator (Fluke PM5136) was used. Therefore, the control of the output voltage of the high voltage amplifier was made in steps of approximately 10 V (voltage range from 0 V to 2 kV) or 100 V (voltages above 2 kV) respectively. Its frequency range reached from 0.1 mHz up to 5 MHz and seven different waveform types were available. In this work only a 50 Hz sinusoidal voltage was used.

- 10 MΩ resistor

To prevent any damage in the case of breakdown of the test object, the high voltage power amplifier was placed in series with a 10 MΩ resistor.

- High voltage cable

A high voltage cable was used to ensure the connection between the high voltage power amplifier and the triple junction assembly. The connection traversing the vacuum chamber was made via a feedthrough insulated by PMMA which leads to the presence of a second triple junction in the experiment. However, control experiments at ambient temperature showed no discharge activity up to a voltage of 6.8 kV at atmospheric pressure and up to 1.3 kV (peak values) at 50 mbar.

- High voltage probe

The AC voltage was measured using a high voltage probe (Tektronix P6015A, 1 V:1000 V, 75 MHz bandwidth) connected to an oscilloscope. For PDIV/PDEV measurements, it was primarily used to calibrate the voltage measured with the partial discharge analyser at the beginning of each experiment. For FOV measurements, it was used to determine the FOV value.

- Partial discharge analyser

To detect partial discharges, a commercial discharge analyser based on an electrical detection of partial discharges, OMICRON MPD 600, was used. This analyser was connected in parallel to the triple junction assembly via a 250 pF coupling capacitor. Both the analyser and the high voltage probe were connected directly to the triple junction assembly, e. g. after the 10 MΩ resistor in the circuit as shown in Figure 2.8.

Since the partial discharge measurement depends on the test circuit and the test object, it was necessary to perform a calibration before the partial discharge measurement could be realised. To ensure consistent measurements, charge calibration of the discharge analyser was performed by feeding a defined charge pulse (50 pC) into the measuring circuit by a charge calibrator (OMICRON CAL 542) whereas the voltage was calibrated using the high voltage probe.

Apart from that, it was made sure that the parameters concerning the PD measurement using the partial discharge analyser were in accordance with the standard of IEC 60270 [44] defining the principles of partial discharge measurements.

For all experiments regarding the PDIV/PDEV, a partial discharge detection threshold of 3 pC was achieved.

Finally, the data produced by the discharge analyser were visualised in the form of a PRPD (phase resolved partial discharge) diagram using the software provided by OMICRON. Figure 2.11 shows an example for such a diagram.

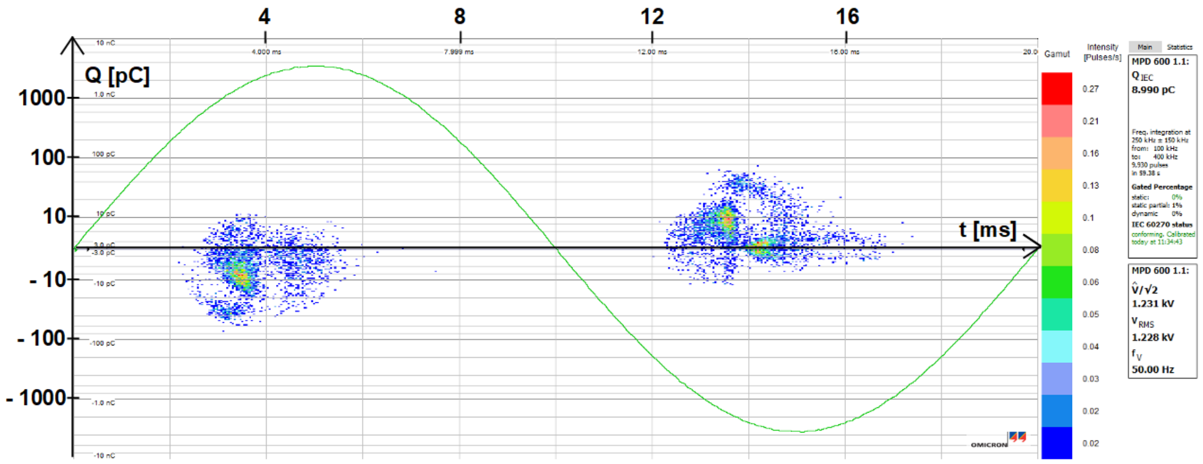

Figure 2.11. Example of a PRPD diagram showing for each PD event the PD magnitude as a function of the phase of the applied AC voltage. A colour code indicates the total number of PDs for a specific phase and magnitude. The PRPD diagram was recorded with the discharge analyser OMICRON MPD 600.

The PRPD diagram shows for each detected partial discharge (PD) event the PD charge magnitude as a function of the phase of the applied voltage in which the PD occurred. A colour code indicates the total number of PDs for a specific phase position/charge.

Although the main purpose of this work was to determine the PDIV/PDEV values, a PRPD diagram was recorded for each experiment.

2.4.2 Experimental procedure

The preliminary experiments were made at ambient temperature and in air. The pressure was varied starting at the highest (atmospheric pressure) and then pumping down gas to reach lower gas pressures (50 mbar).

The PDIV value was determined for different solid insulators (aluminium oxide, PTFE) using the partial discharge analyser. The applied voltage was raised until the occurrence of an established state of repetitive discharges was reached. However, no criterion was yet defined concerning the rate at which the voltage was increased and consequently, the results of these preliminary PDIV measurements may be less consistent than the results for the other experiments presented in this work.

2.5 Experimental results and discussion

This section is dedicated to the influence of different geometric and dielectric properties of the solid insulator such as thickness, surface metallisation or relative permittivity on the partial discharge inception voltage (PDIV). All experiments were made in air at ambient temperature varying pressure in the range of atmospheric pressure down to 50 mbar.

It should be noted that the primary purpose of these experiments was to verify that the elements of the designed test setup were working properly. This was demonstrated by carrying out these experiments, the results of which are in principle scientifically known. Nevertheless, it is worth presenting and discussing them briefly.

2.5.1 Influence of thickness

To analyse the influence of thickness *d* of the aluminium oxide disc on PDIV, three aluminium oxide discs of the same purity (96 %) were used: (I) (d_i = 0.127 mm), (III a) (d_i = 1.016 mm) and (V) (d_i = 2 mm) according to Table 2.3 in section 2.3.1.

Figure 2.12 shows the results for the PDIV (peak value) for each of these discs as a function of gas pressure. Each data point was calculated from the average of three measurements (three repetitions of each pressure). Error bars were calculated for a 1σ standard deviation.

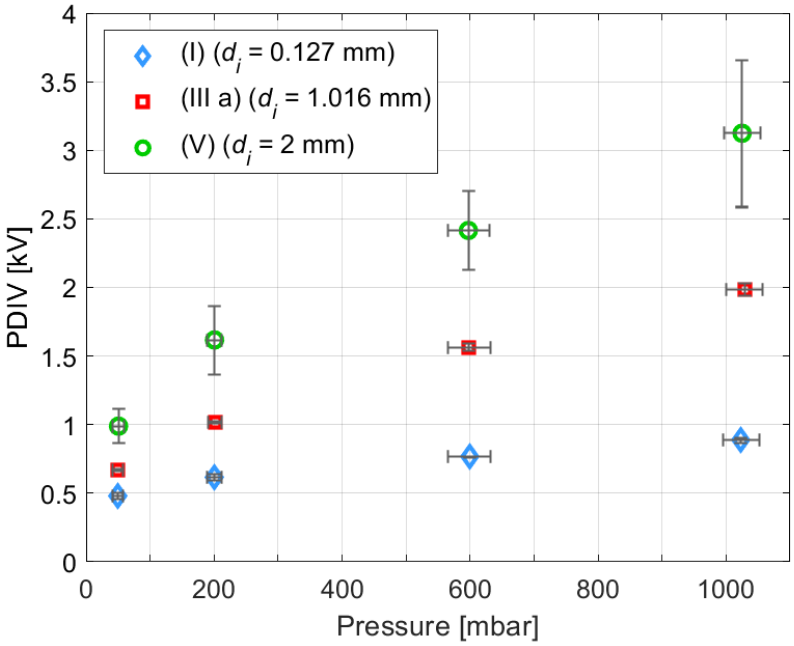

Figure 2.12. PDIV as a function of gas pressure for aluminium oxide discs (I) (d_i = 0.127 mm), (III a) (d_i = 1.016 mm), and (V) (d_i = 2 mm); ambient temperature; air.

The increase in PDIV with pressure is in accordance with Paschen's law. A decrease in PDIV with thickness is also observed. For instance, the PDIV difference between aluminium oxide disc (I) and (V) at atmospheric pressure amounts, under consideration of the mean values, to 2.24 kV.

This can be explained by the fact that the electrode potential, following any field line from the electrode to the ground, in the vicinity of the electrode, is divided between the potential loss in the gas between the electrode and a point on the insulator surface, and the potential remaining on this point of the insulator. This may be viewed as a capacitive voltage divider. Decreasing the insulator thickness or increasing its permittivity will increase its capacitance and obviously lower the potential on its surface, thus leading to an increase of the mean field following the field line in the gas. This will be illustrated in chapter 3.6.1 by a numerical simulation of this field. Consequently, the thinner the aluminium oxide disc, the lower the PDIV.

2.5.2 Influence of metallisation

In the next step, different aluminium oxide discs with and without a metallisation on their surface were compared to investigate the influence on PDIV. The PDIV (peak value) value for different configurations of the metallisation as a function of gas pressure is shown in Figure 2.*13*. The data points are calculated from the average of three measurements (three repetitions of each pressure) and error bars for a 1σ standard deviation.

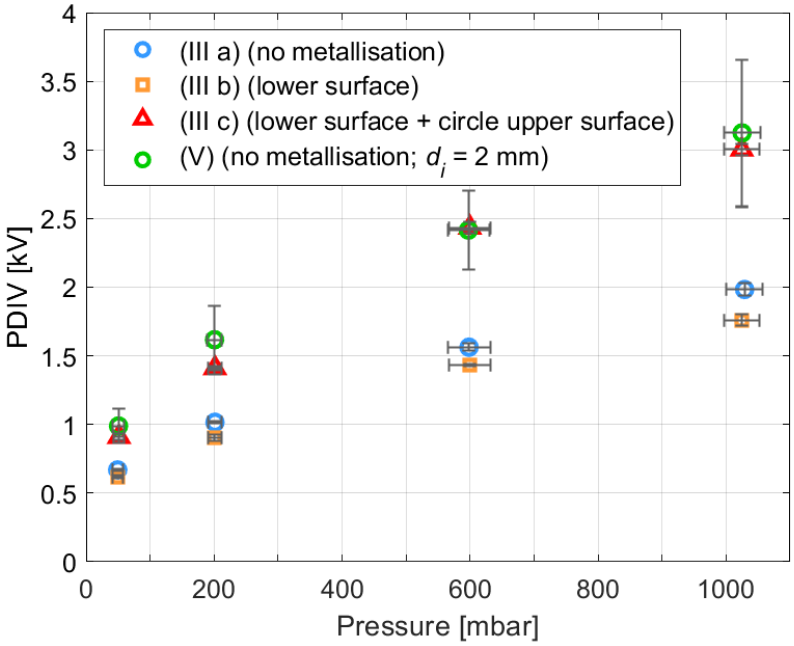

Figure 2.13. PDIV as a function of gas pressure for different aluminium oxide discs of 1.016 mm thickness exhibiting no (discs (III a) and (V) (thickness of d_i = 2 mm)), a one-sided (disc (III b), whole lower surface) or a double-sided (disc (III c)), whole lower surface and circle of approximately 30 mm on the upper surface) metallisation; ambient temperature; air.

The results show that the PDIV for the disc (III a) without metallisation and the discs (III b) with a one-sided metallisation on their lower surface which is in contact with the grounded electrode is for all gas pressures approximately in the same order of magnitude. It can consequently be stated that a metallisation on the counter electrode side does not significantly influence the PDIV.

On the contrary, a metallised disc on the side of the active electrode (III c), leads to a significant increase in PDIV, approximately 1 kV at atmospheric pressure. Hence, it has the same effect as doubling the thickness of the aluminium oxide disc. The same result could be seen when aluminium oxide discs (IV a) to (IV c) were used.

This is due to the fact that the discharge will be initiated on the edge of this thin metallisation, which is a very different geometrical situation compared to a cylindrical electrode with Rogowski profile standing on a bare insulating surface. For the latter, a gaseous gap between the electrode and the aluminium oxide surface up to some millimetres allows the development of a discharge considering that, at atmospheric standard conditions, an electron avalanche requires a space of at least 30 µm [117] to develop. By contrast, as the thickness of the metallisation only amounts approximately to 100 nm, no such gaseous gap is present, and a development of a discharge only is possible when a sufficient high voltage is applied. Consequently, to provoke a discharge on the double-sided metallised aluminium oxide discs, a higher voltage is required than for the one-sided or non-metallised discs which consequently leads to a higher PDIV.

2.5.3 Influence of relative permittivity

The influence of relative permittivity ε_r on the PDIV was investigated using two different insulating materials: an aluminium oxide (disc (II), $\varepsilon_r = 9.6$) and a PTFE disc (disc (I), $\varepsilon_r = 2$), with the same diameter (50 mm) and thickness (1 mm), were compared at ambient temperature and different gas pressures. In contrast to the experiments carried out before, the gas used here was nitrogen. Figure 2.14 shows the results for the PDIV (peak value) dependence on the insulating material as a function of the gas pressure. The data points are calculated from the average of 15 measurements (three repetitions of all pressures whereas for each pressure setpoint five repetitions were made) and the error bars are again calculated on the basis of a 1σ standard deviation.

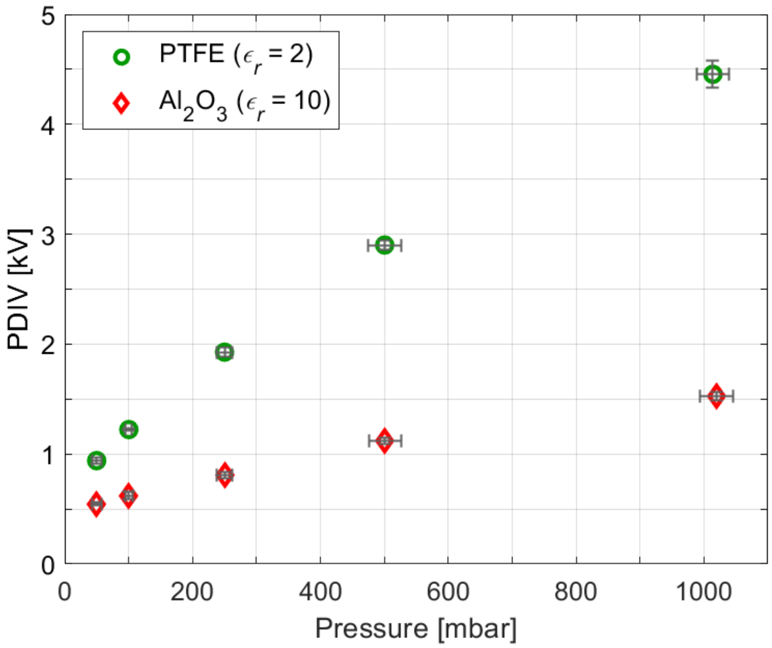

Figure 2.14. PDIV as a function of gas pressure for two different insulating materials (aluminium oxide and PTFE) with same geometry; ambient temperature; nitrogen.

The PDIV for the PTFE disc (I) is for all pressures higher than for the aluminium oxide disc (II). At atmospheric pressure, the difference in PDIV between the two discs amounts to 2.9 kV. This behaviour can be explained by the fact that a higher relative permittivity leads to an increased polarisation of the insulating material, which in turn leads to an increased electric field in the gas near the triple junction. Consequently, it can be stated that a higher relative permittivity leads to a lower PDIV.

Having presented the influence of thickness as well as relative permittivity on PDIV, both results can be combined. As shown by Dakin *et al.* [118], the electric field in the air near the electrode should be proportional to the relative permittivity of the solid insulator, and the PDIV should therefore be a function of the ratio of the thickness d_i of the solid insulator to its relative permittivity ε_r. Consequently, when the PDIV is plotted as a function of this ratio d_i/ε_r, all the data should fall approximately on a single line.

Considering the obtained results, Figure 2.15 shows the PDIV (peak value) as a function of the ratio d_i/ε_r for different aluminium oxide discs ((I), (III a) and (V)) with thicknesses in a range from 0.127 mm to 2 mm and two PTFE discs (thickness of 1 mm and 2 mm – the latter being constituted of two PTFE discs of 1 mm one upon the other with a slight layer of vacuum grease in between).

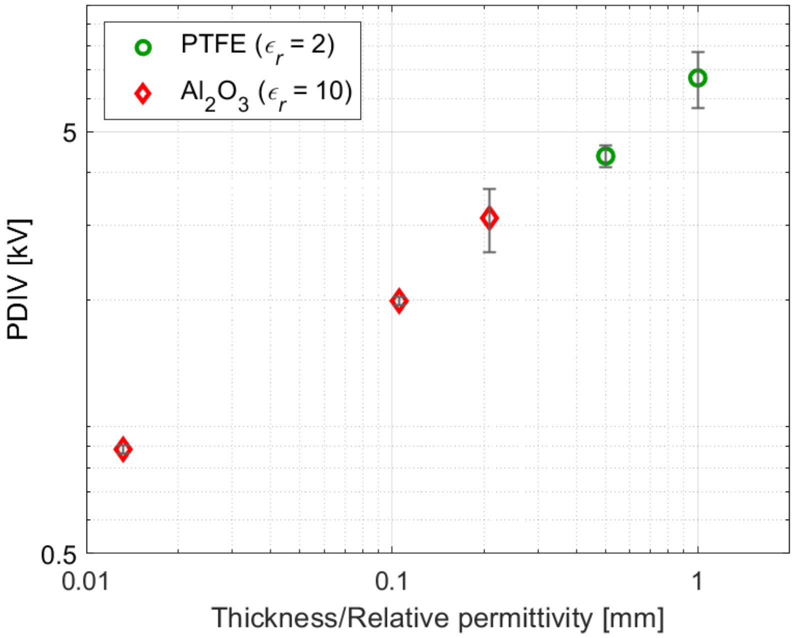

Figure 2.15. PDIV as a function of the ratio between the thickness d_i of the solid insulator to its relative permittivity ε_r for different aluminium oxide and PTFE discs exhibiting different thicknesses; ambient temperature; air.

The obtained results are in accordance with the theory proposed by Dakin *et al.* The PDIV for the different aluminium oxide and PTFE discs conform, depending on the ratio of thickness to relative permittivity, to a single line.

Therefore, based on the experimental results and for given conditions of gas pressure, temperature, and gas type, a trendline can be established which may allow the PDIV to be estimated for known values of thickness and relative permittivity.

2.6 Summary

This chapter first presented an overview of the experiments together with the basic elements of the test bench to reach the objectives of the study which were to come to a better understanding of discharge phenomena at triple junctions under varied conditions of pressure and temperature.

A key element of the triple junction assembly was the solid insulator. Therefore, an overview as well as some dielectric characteristics of the solid insulators used for the experiments, aluminium oxide and PTFE, were presented.

Most of the experiments were made using an aluminium oxide disc. Two aluminium oxide discs provided by different suppliers were available. To choose one of them as to be used for the experiments carried out in this work, a comparison between both on the basis of a geometrical analysis regarding their respective surface structures was made. Finally, the aluminium oxide disc with slightly lower average surface roughness was chosen and in addition, a scanning electron microscope including an XPS analysis was made to know more about its chemical composition.

The experimental setup, on which all experiments presented in this work were based, was then described. Since it was of importance to ensure that this test setup with its components worked properly, some preliminary PDIV measurements were made, regarding the influence of geometrical and dielectric properties of the solid insulators on PDIV.

The main results of these experiments showed that the PDIV increased with thickness of the solid insulator but decreased with relative permittivity what showed that its influence on PDIV was of importance.

Further, a metallisation on the surface of the solid insulator in contact with ground potential did not affect the PDIV. However, a metallic layer in contact with the live electrode showed a distinct increase in PDIV, amounting to a value as if the thickness of the solid insulator was doubled. Reason therefore was the modification of the local electric field and the absence of a gaseous gap between the edge of the metallic layer and the surface of the solid insulator thus resulting in higher required voltages to develop an electron avalanche leading to a discharge.

Chapter 3

Dependence of PDIV/PDEV on various conditions of temperature and gas pressure/density

3.1 Introduction

This chapter presents and discusses the results of the dependence of partial discharge inception voltage (PDIV) and partial discharge extinction voltage (PDEV) on temperature and gas pressure/density. In addition, the influence of different dielectric characteristics of the solid insulator and their dependence on temperature as well as the presence of an oxidation layer on the surface of the tungsten electrode and their influences on PDIV/PDEV are described and discussed.

Section 3.2 first describes the further development of the test setup which was based on that described in chapter 2. Since the experiments were extended to temperatures up to 400 °C, additional elements were required. Moreover, a standardised experimental procedure to ensure consistent measurements of PDIV and PDEV was developed. A subsection on the experimental setup concerning temperature control is presented because of its particular importance in this work.

Section 3.3 then presents the results of experiments carried out to analyse the influence of temperature (starting from ambient temperature up to 400 °C) and gas pressure (50 mbar up to atmospheric pressure) conditions on PDIV and PDEV using two different aluminium oxide discs with different purities. The results are first described and discussed as a function of gas pressure before they are presented as a function of gas density to investigate a possible additional mechanism beyond the well-known effect of gas density.

In sections 3.4 and 3.5, results concerning the influence of temperature on the dielectric properties, more precisely volume resistivity and relative permittivity, of the aluminium oxide discs used in the experiments are presented. The test setup and experimental procedure for these dielectric measurements are described.

The resulting changes in PDIV and PDEV are analysed in section 3.6. A numerical model of the electric field near the triple junction for different conditions of temperature and gas pressure and its influence on PDIV is also presented and discussed.

Finally, a description and discussion of other observations influencing the measurement results related to an oxidation layer on the surface of the tungsten electrode is given in section 3.7.

3.2 Experimental setup and procedure

In this work, focused was made on the influence of various conditions of temperature and gas pressure/density on phenomena taking place at triple junctions. More precisely, the values of PDIV and PDEV had to be determined in a broad range of temperature and pressure. This section presents the test setup and experimental procedure designed for this purpose, as well as considerations concerning the temperature control.

3.2.1 Test setup

To achieve the objective of this study with a broad range of pressures between 50 mbar and atmospheric pressure and temperatures between ambient and 400 °C, it was necessary to modify the basic test setup described in section 2.4. adding several components:

- Heating element

A ceramic (silicon nitride) heating element, situated beneath the counter electrode as depicted in the schematic of Figure 3.2, was used for all experiments in which the influence of temperature was considered. The heating element with a circular heating zone (diameter of 60 mm) could operate at temperatures up to 1000 °C, but in this work the maximum temperature used was 400 °C, as measured close to the triple junction. Higher temperatures led to issues with the tightness of the vacuum chamber.

- DC power supply for the heating element

The heating element was connected to a separate DC power supply, see Figure 3.1, which had an output of 0 V – 64 V/0 – 6 A and could be controlled remotely.

- Heating element control (LabVIEW)

The temperature control of the heating element was ensured using a PI controller realised within LabVIEW, see Figure 3.1. Since the temperature control is of particular importance in this work, a more detailed description of the temperature regulation is given in section 3.2.3.

- Thermocouples

Three thermocouples (type K) were used. One served as input for the control of the separate DC power supply measuring the temperature of the counter electrode in which the thermocouple was located, see Figure 3.2. The two others were installed inside the vacuum chamber to measure and monitor the temperature. They were also used for several measurements regarding the adjustment of the heating element to reach the desired temperature at the triple junction.

The connection to the data acquisition card was made using thermocouple sealed feedthroughs placed in the vacuum chamber walls.

- Counter electrode

Although a counter electrode was already present for the preliminary PDIV measurements, another counter electrode disc, replacing the precedent one, made of stainless steel (diameter of 50 mm, height of 4 mm) was henceforth used for all experiments and placed above the heating element as can be seen in Figure 3.2. One of the above-mentioned thermocouples was placed inside a 1 mm diameter hole drilled about 5 mm into the counter electrode.

- Refractory box

The triple junction assembly was placed together with the heating element in a refractory box, see Figure 3.2, which was constructed using porous aluminium oxide with low thermal conductivity. Its purpose was not only to homogenise the temperature around the triple junction but also to protect the vacuum chamber which was made of PMMA and whose melting point was 160 °C. To avoid any contamination due to dust from the porous aluminium oxide, a protective coat using ceramic adhesive was applied on the inner surfaces of the walls including the lid.

- Nitrogen supply

To avoid undesirable effects because of the oxidation of the metallic materials (tungsten and stainless-steel electrodes) inside the refractory box at high temperature, nitrogen was used (instead of air) for all experiments. Thus, a nitrogen supply was added to the experimental setup, see Figure 3.1, using the gas network installed in the laboratory. The nitrogen was of type I (“industrial”) which means that its purity is ≥ 99.8 %.

- Neoprene gasket

To tighten the vacuum chamber which tended to leak at higher temperatures, a new improved additional neoprene gasket was added between the chamber and its lid.

Apart from these added elements, the same components as for the preliminary PDIV measurements were used. Nevertheless, some minor adjustments were made, e. g. regarding the connection of the wire to the tungsten electrode. First, the wire was soldered but since the electrode was exposed to temperatures up to 400 °C, the soldering tin would have been liquified provoking the risk of a loose contact if a standard soldering were used. Hence, the wire was brazed to ensure a good contact even at high temperatures.

Figure 3.1 shows the schematic of the complete test setup and circuit with the above-listed added elements and Figure 3.2 a schematic of the triple junction assembly including the heating element inside the refractory box.

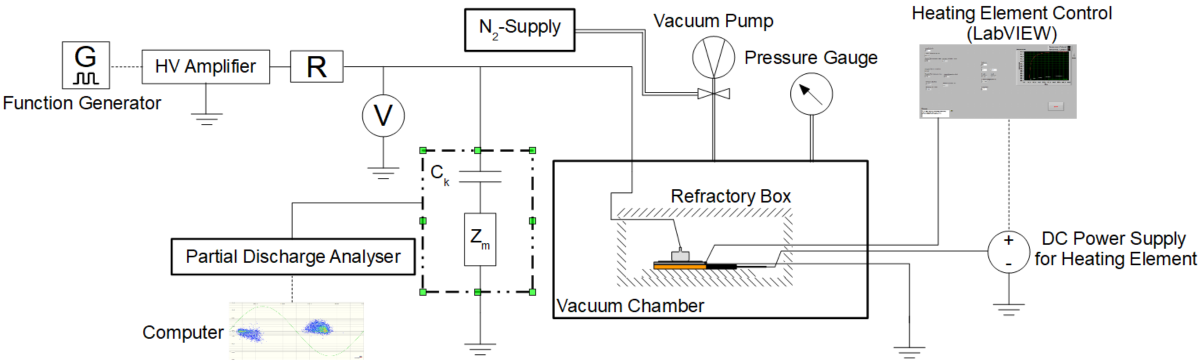

Figure 3.1. Schematic of the test setup and circuit to analyse the influence of various conditions of temperature and gas pressure/density on PDIV/PDEV.

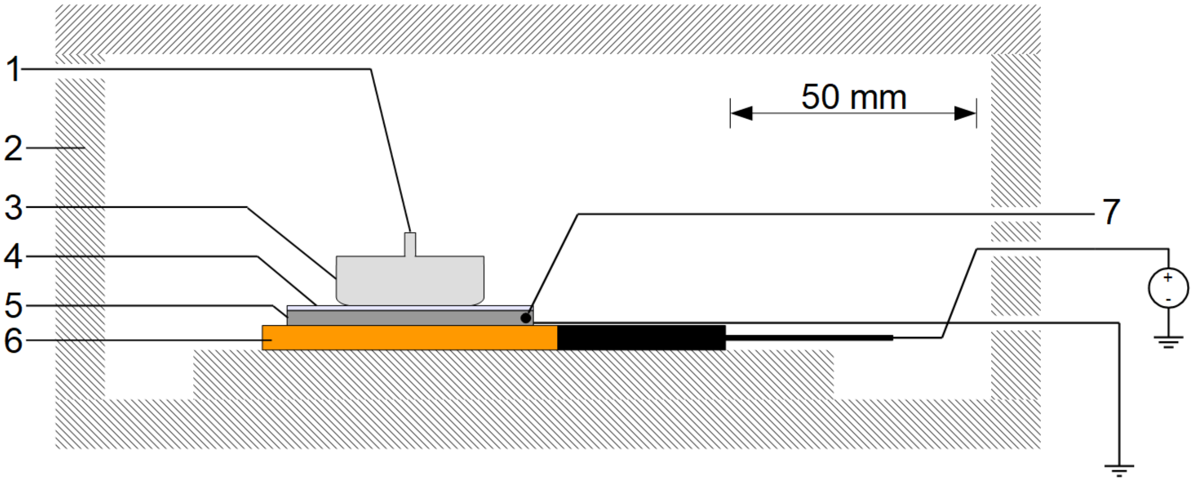

Figure 3.2. Schematic of the triple junction assembly including the heating plate inside the refractory box.
1 – HV-connection, 2 – Refractory box, 3 – Tungsten electrode, 4 – Solid insulator,
5 – Stainless steel disc electrode, 6 – Heating element, 7 – Thermocouple.

The solid insulator was placed between the cylindrical tungsten electrode and the grounded stainless steel disc electrode. The heating element was placed beneath the grounded electrode and connected to its power supply. The thermocouple was connected to the temperature control unit.

The implementation of the vacuum chamber with all its components such as the refractory box and all connections including the feedthroughs for the thermocouples, the power supply of the heating element, the vacuum pump, etc. is pictured in Figure 3.3 and the assembly of the elements inside the refractory box is pictured in Figure 3.4.

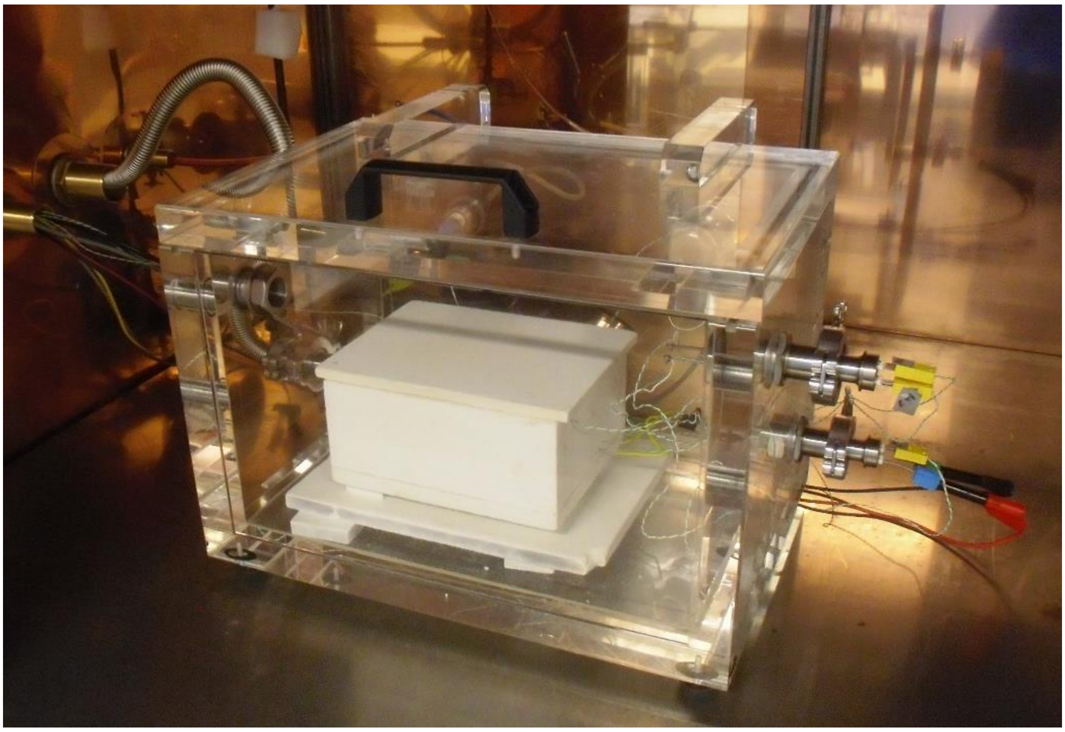

Figure 3.3. Implementation of the vacuum chamber with all its components.

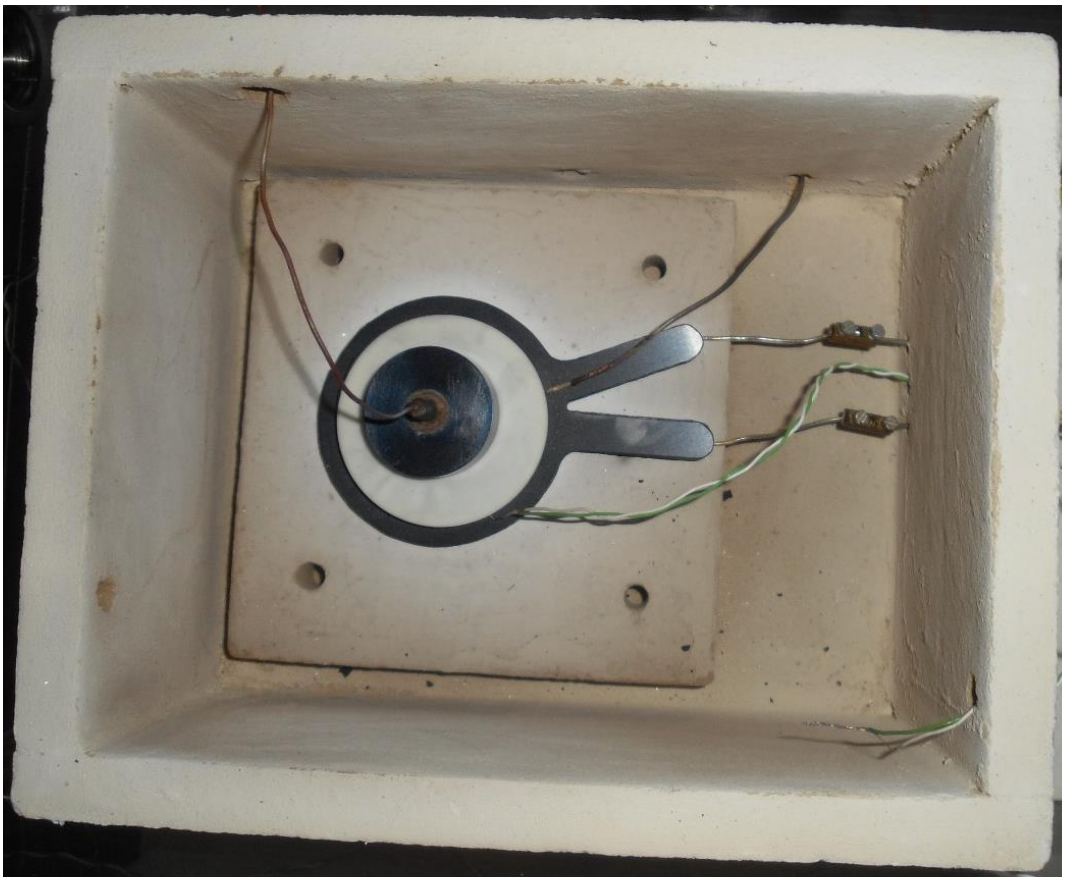

Figure 3.4. Assembly of the elements inside the refractory box.

3.2.2 Experimental procedure

Before each experiment, the tungsten electrode as well as the stainless-steel disc electrode were first polished using a fine sandpaper (grain size of 22 µm/grit 800) and then cleaned with alcohol using a precision wipe (Kimwipe). Cleaning with alcohol in the same manner was done for the solid insulator.

Following this step, all the elements were placed in the refractory box taking care to centre the tungsten electrode on the solid insulator. Then, the refractory box and the vacuum chamber were closed with their respective lids.

To eliminate sources of uncertainty on the composition of the gas inside the vacuum chamber (for example outgassing of materials with elevated temperature), the vacuum chamber was purged three times by pumping down to 3 mbar and then refilled with nitrogen up to atmospheric pressure. This procedure was repeated each time the temperature was changed. Each experiment series was made beginning at the lowest temperature (ambient temperature), and then increasing up to the highest temperature (400 °C). The experiments were carried out for these temperature setpoints:

- Ambient temperature, 80 °C, 150 °C, 200 °C, 250 °C, 300 °C, 350 °C, 400 °C

For each temperature setpoint, the pressure was adjusted, starting at the highest (atmospheric pressure) and then pumping down to the lowest gas pressure (50 mbar). The experiments were carried out for different gas pressures:

- Atmospheric pressure, 500 mbar, 250 mbar, 100 mbar, 50 mbar

To ensure consistent measurement of PDIV and PDEV (electrical detection using a commercial partial discharge analyser, OMICRON MPD 600, see section 2.4.1), a standardised procedure, adapted from FprEn 2591-227 test standard [119], was developed. Figure 3.*5* shows the flowchart of the PDIV determination procedure.

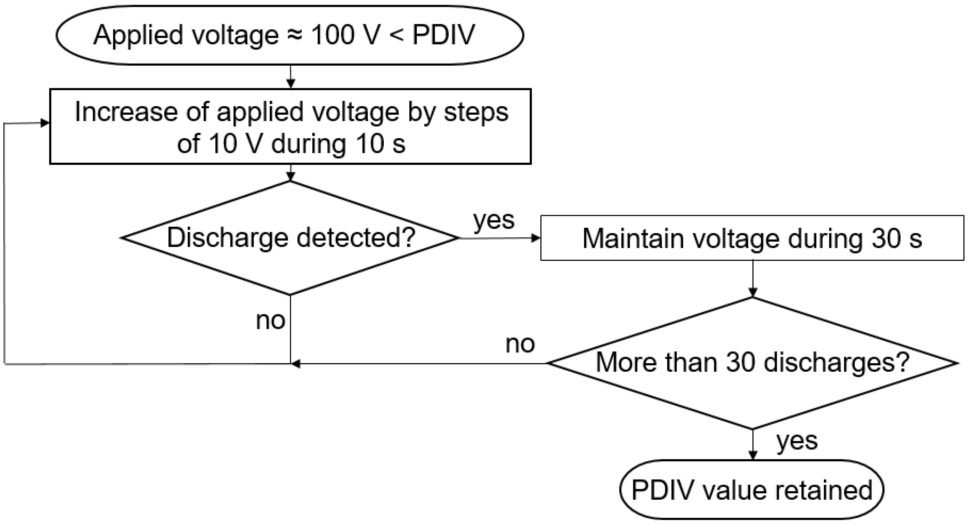

Figure 3.5. Flowchart of the PDIV determination procedure.

The voltage applied to the triple junction assembly was first adjusted approximately 100 V below the expected PDIV (which came from previous measurements). Then, the voltage was raised by steps of 10 V and maintained during 10 s. As long as no discharges were detected (detection threshold: 3 pC), the voltage was raised again by 10 V. Otherwise, the applied voltage was maintained for 30 s. If more than 30 discharge events were detected within this time interval, the PDIV value (peak AC voltage value) was retained. If not, the applied voltage was again raised by 10 V.

Remark: these criteria for the determination of PDIV are the result of a compromise between finding the lowest voltage at which discharges may form while also having a reasonable total experimental time (30 discharges in an interval of 30 s or 10 s without discharge). In other words, if the 10 s waiting was extended, slightly lower PDIV results may have been found, but at the expense of not being able to do as many different pressure and experimental conditions.

Figure 3.6 shows the flowchart of the PDEV determination procedure.

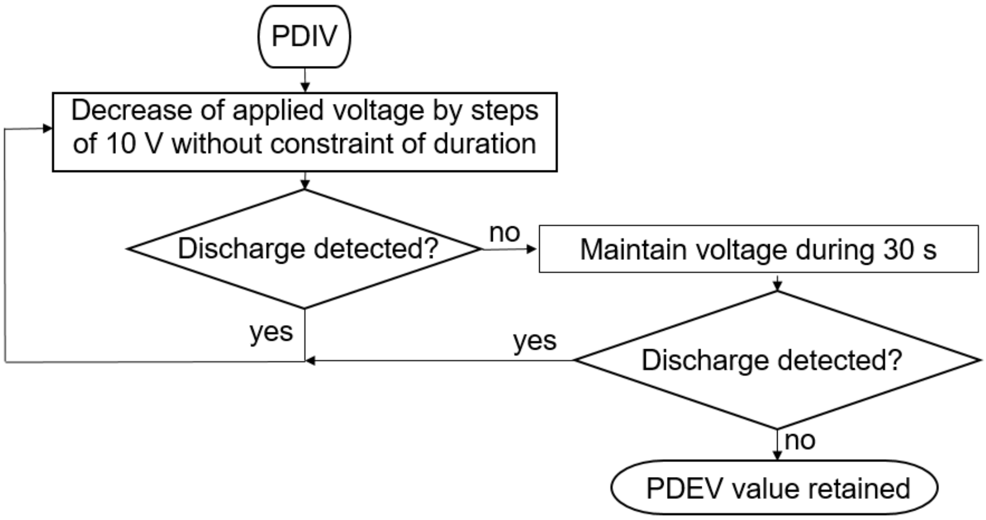

Figure 3.6. Flowchart of the PDEV determination procedure.

The voltage applied to the triple junction assembly, starting from the PDIV, was decreased by steps of 10 V but without a constraint of duration. As long as discharges were detected, the applied voltage was continuously decreased by steps of 10 V. If no more discharges were detected, the applied voltage was maintained during a time interval of 30 s. If no discharge was detected within this time interval, the PDEV value (peak AC voltage value) was retained. Otherwise, the applied voltage was again decreased by 10 V.

Note that the waiting criterion (10 s in the case of PDIV measurement) is no longer retained here. This criterion considered the probability of the presence of seed electrons in the volume of gas subjected to the electric field. Thus, a low probability of presence was associated with a delay. In the case of PDEV measurement, the probability of the presence of seed electrons is no longer a limiting factor. A waiting criterion was therefore no longer necessary.

3.2.3 Temperature control

As already mentioned, the control of the temperature was of particular importance in this work. In this context, it was not only important to determine the heat input necessary to obtain the desired temperature near the triple junction, but also to ensure a temperature regulation without any overshoot as well as a reasonable time for the stabilisation of the temperature during the experimental work.

Further, the temperature of the gas close to the triple junction, the zone where the PD activity is expected to take place, was an important parameter in this study. Hence, this needed a reliable temperature measurement and monitoring.

This section presents the temperature control of the heating element and its adjustment as well as a discussion concerning the temperature gradient in the vicinity of the triple junction.

The temperature control for the heating element basically consisted of five elements:

- PI controller implemented within LabVIEW to control the DC Power supply
- DC Power supply to the heating element
- Thermocouple
- Data acquisition card for thermocouples (NI 9211)
- Data acquisition card to interface between LabVIEW and the DC power supply (NI USB-6008)

A schematic of the heating element control circuit, including the triple junction assembly, is shown in Figure 3.7.

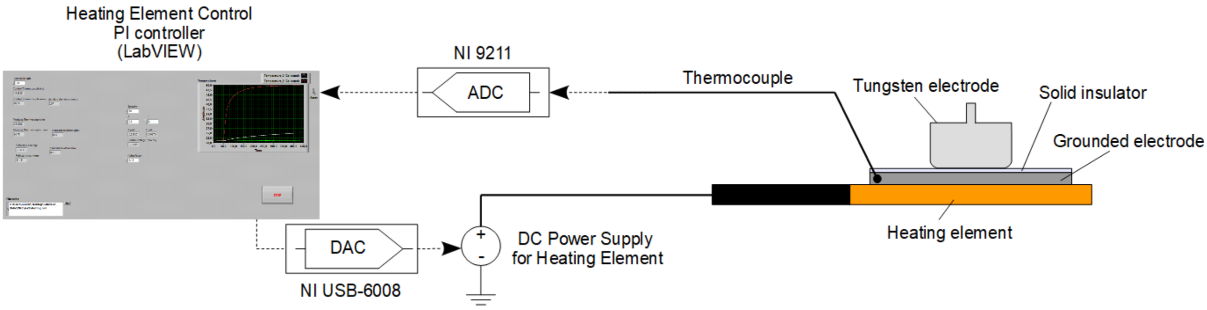

Figure 3.7. Schematic of the heating element control circuit.

The heating element was connected to a DC power supply which was controlled by a PI controller (proportional-integral controller) implemented within LabVIEW. The software LabVIEW (Laboratory Virtual Instrument Engineering Workbench) is a platform allowing the development of measurement and control systems on the basis of a visual programming language.

The thermocouple, which was placed within the grounded stainless-steel electrode just above the heating element, served as input for the heating element control. The temperature measured with the thermocouple was converted using an A-D-converter to be then processed by the PI controller whose signal was thereafter reconverted into an analogue signal as input for the DC power supply of the heating element using a D-A-converter. The implementation of the illustrated schematic is pictured in Figure 3.8, here shown during some preliminary experiments.

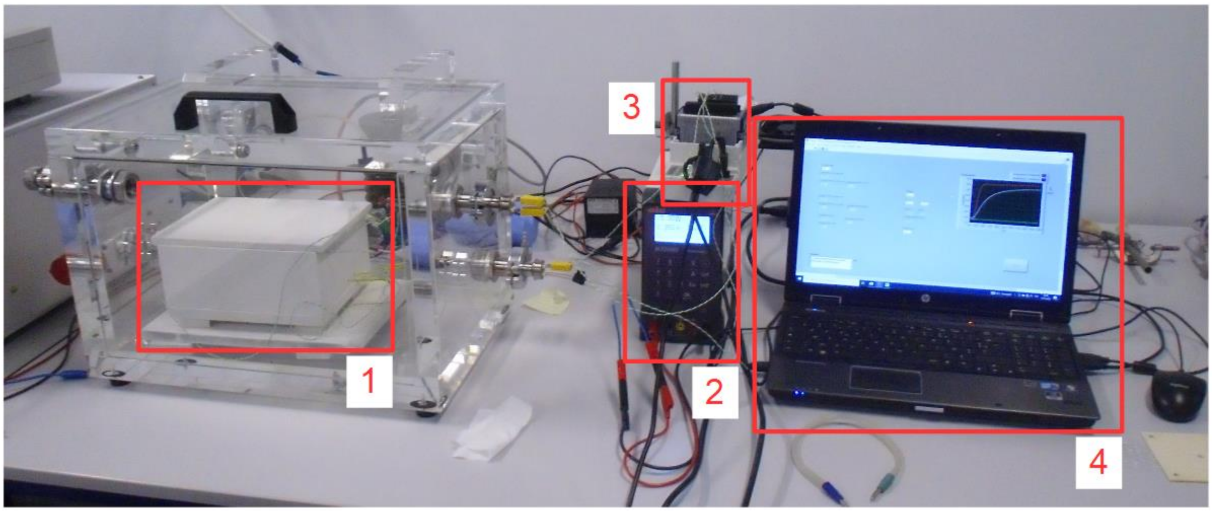

Figure 3.8. Implementation of the heating element control circuit.
1 – Refractory box containing the heating element, 2 – DC power supply,
3 – Data acquisition cards, 4 – Computer (PI controller implemented within LabVIEW).

The PI controller was regulated via the graphical user interface of LabVIEW which allowed to define the temperature setpoint as well as the values of the parameters of the PI controller and to display the measured temperatures of the thermocouples (numerical value and diagram).

In a first step, the terms *P* and *I* of the controller were adjusted to achieve smooth temperature regulation of the heating element without any overshoot and a temperature stabilisation within a reasonable period of time.

To reach the desired temperature at the triple junction, a compensation factor (CF) was added since the temperature of the heating element had to be higher than the temperature setpoint defined in LabVIEW due to the presence of the solid insulator, which was placed above the grounded stainless-steel disc electrode, and to take into account the temperature- and pressure-dependent heat dissipation. To determine the CF, it was necessary to measure the temperature not only within the grounded electrode but also at the triple junction. Therefore, a second thermocouple, which was wedged into the triple junction, was added, and obviously removed before PD measurements were done. Figure 3.9 shows the experimental setup to determine the CF.

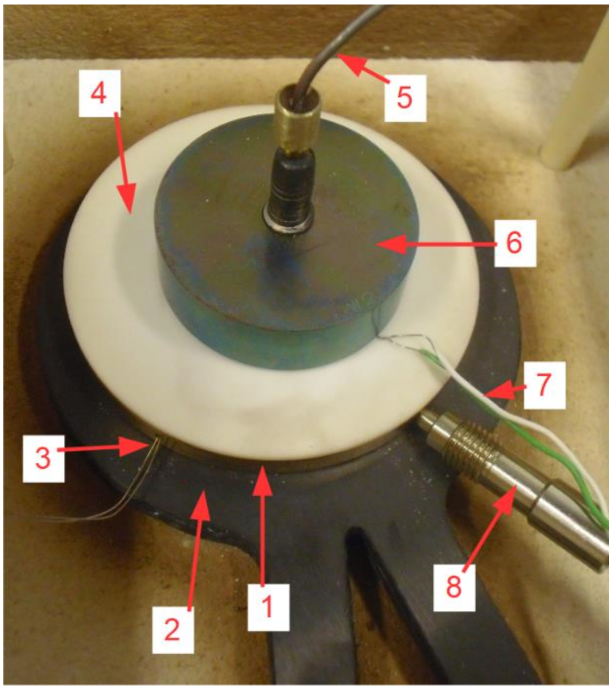

Figure 3.9. Experimental setup to determine the compensation factor.
1 – Grounded electrode, 2 – Heating element, 3 – Thermocouple within the grounded electrode,
4 – Solid insulator, 5 – HV connection, 6 – Tungsten electrode, 7 – Thermocouple wedged into the triple junction,
8 – Connection to ground potential.

The values of the CF were empirically determined varying them for a chosen temperature setpoint and a given gas pressure until the desired and stabilised temperature at the triple junction was reached. They depend on temperature and gas pressure: as the temperature gradient between the heating element and the triple junction slightly increased with temperature, the CF also slightly increased with temperature, while it also decreased with pressure, since at low pressures, the lower density of the gas reduced its cooling influence.

All determined CFs allowed reaching the desired temperature at the triple junction within a precision of the systematic error of the thermocouples (± 1,5 °C). Figure 3.10 shows an example for a temperature profile at the triple junction at atmospheric pressure in air starting at ambient temperature heating up to 500 °C in steps of 50 °C when applying the pre-determined CFs.

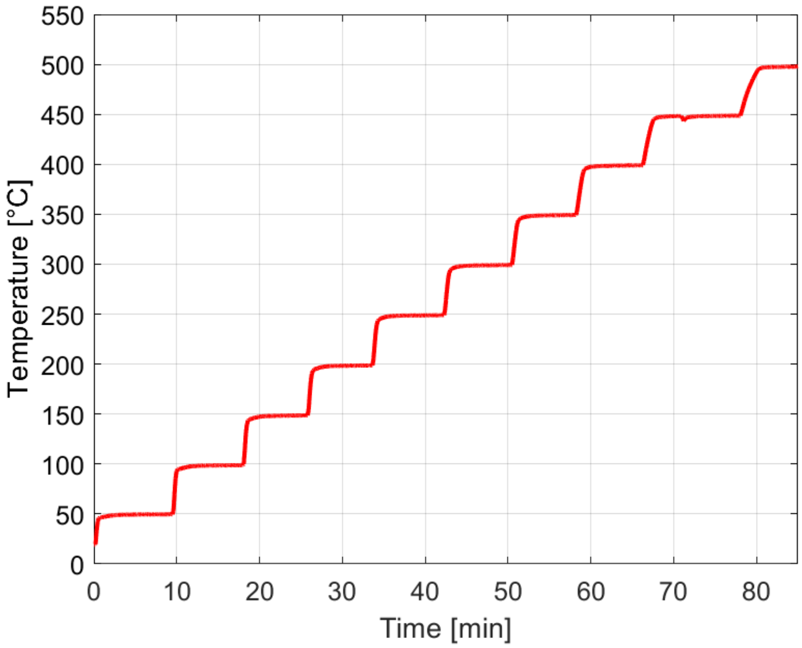

Figure 3.10. Example for a temperature profile as measured at the triple junction when applying the determined compensation factors; air; atmospheric pressure.

The determined CFs were convenient to reach the desired temperature at the triple junction.

Once the CFs were determined, the control of the heating element and the control of the desired temperature at the triple junction were set for the experiments. During experiments, the temperature at the triple junction and therefore the correctness of the previously determined CFs was occasionally verified. Since the same triple junction assembly was used for all experiments, only very slight adjustments of the CFs were ever necessary.

Focus was then made on the temperature of the gas close to the triple junction, which was an important parameter in this work, especially due to the fact that PDs were expected to propagate in the gas close to the triple junction. While the system was designed to have a temperature profile as homogeneous as possible, there remained nevertheless a temperature gradient from the heating element, extending out to the surrounding volume. Therefore, a third thermocouple was placed in the gas near the triple junction (distance of approximately 2 mm) and removed before PD measurements were done. Its purpose was to measure the temperature in the gas for selected triple junction temperatures and gas pressures. The objective of this measurement was to estimate the temperature gradient and thereby its influence on the gas density near the triple junction. Figure 3.11 shows a schematic and Figure 3.12 a photograph of the thermocouple arrangement.

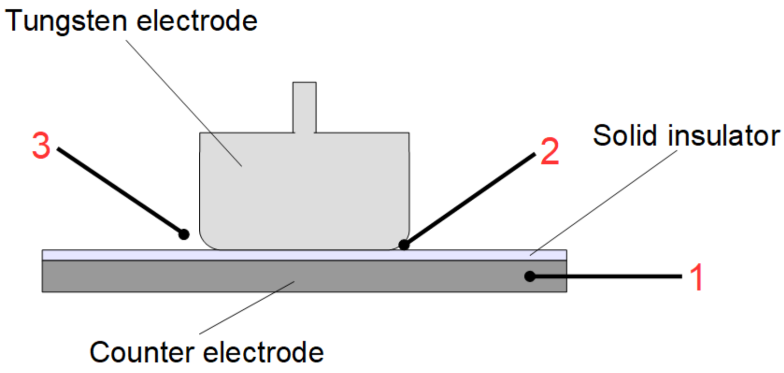

Figure 3.11. Schematic of the thermocouple arrangement to estimate the temperature gradient near the triple junction. 1 – Thermocouple inside the grounded electrode, 2 – Thermocouple wedged into the triple junction, 3 – Thermocouple in the gas (≈ 2 mm from the triple junction).

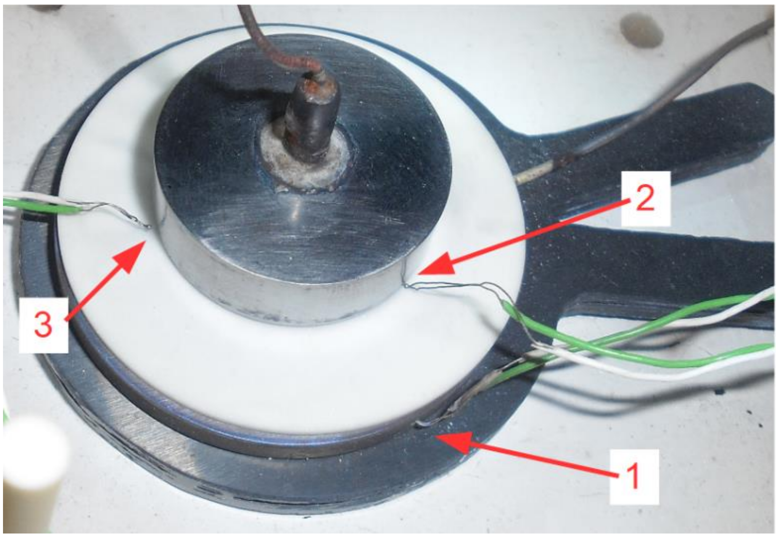

Figure 3.12. Photograph of the thermocouple arrangement to estimate the temperature gradient near the triple junction.1 – Thermocouple inside the grounded electrode, 2 – Thermocouple wedged into the triple junction, 3 – Thermocouple in the gas (≈ 2 mm from the triple junction).

Figure 3.13 shows for each temperature setpoint for the triple junction the measured temperatures inside the grounded electrode above the heating element, at the triple junction, and in the gas in near proximity of the triple junction for nitrogen at atmospheric pressure.

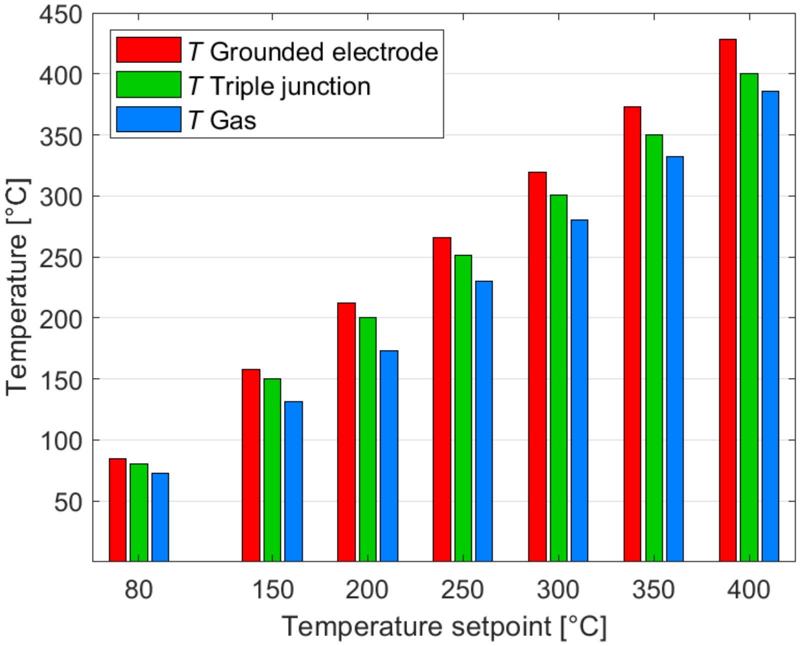

Figure 3.13. Comparison of measured temperatures inside the grounded electrode, at the triple junction, and in the gas in its near proximity for nitrogen at atmospheric pressure.

The temperature inside the grounded electrode was always the highest of the three measured temperatures to reach the desired temperature at the triple junction which was the control variable.

The temperature difference between the triple junction and the temperature measured approximately 2 mm away in the gas was about 8 °C for a setpoint of 80 °C and 15 °C for a setpoint of 400 °C. This difference in temperature led only to a small difference in gas density of approximately $2.489 \cdot 10^{23}$ 1/m³ which is smaller than the gas density fluctuation corresponding to the measurement error of the pressure gauge according to the manufacturer. Additional experiments were also made for other pressure values and their difference in temperature between the triple junction and the gas in its close vicinity had a similar order of magnitude.

Furthermore, the lower the gas pressure, the lower the absolute difference in gas density between the triple junction and the gas in its near proximity although the temperature gradient had approximately the same order of magnitude for the different temperatures, see Figure 3.*14*.

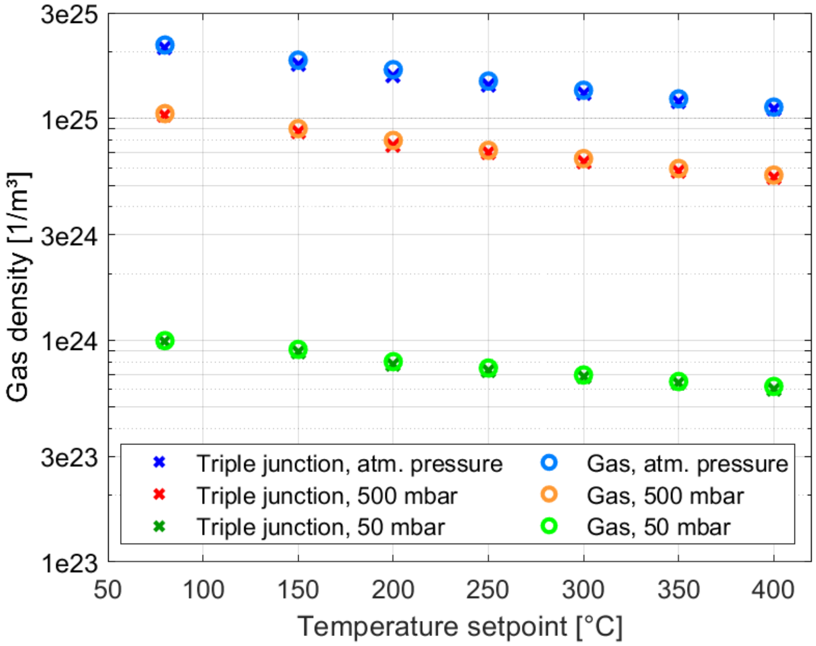

Figure 3.14. Comparison of gas density at the triple junction and in its near proximity for nitrogen at different temperatures and gas pressures.

For a gas pressure of 50 mbar, the absolute difference in gas density between the two measurement points was almost negligible.

Remark: the temperature measurement in the gas near the triple junction could only give an approximative value of the gas temperature. The main reason for this is that the temperature measured by the thermocouple corresponded to the temperature of the thermocouple itself but not to the “real” gas temperature. This is why the temperature measurements were performed in steady state conditions (3 min after changing the temperature setpoint) for which it was assumed that the gas temperature was equilibrated with the thermocouple temperature. In this context, it has to be noted that also a heat conduction along the thermocouple wires may influence the measurement leading to a measured temperature which is equal to or slightly below the real gas temperature. Consequently, the gas temperature may be underestimated what means that the already little difference in gas density between the two measurement points is slightly overestimated and therefore negligible. Further, the thermocouple position in the gas was controlled at the beginning of the measurement at ambient temperature. Due to influencing factors such as dilatation with temperature, unintended movements of the thermocouple during pumping, etc., its position in relation to the triple junction can be estimated to be approximately 2 mm to 4 mm.

Hence, based on these observations, the gas densities at the triple junction and its near proximity can be considered as virtually the same and a presentation of the obtained results of the experiments regarding the PDIV/PDEV and FOV (see chapter 4) is made using the gas density as calculated when using the temperature at the triple junction (as opposed to the temperature which had been measured in the gas in proximity to the triple junction).

Finally, it was chosen to present PDIV/PDEV and FOV results only as a function of pressure/density and not as a function of the product pressure/density by distance (cf. Paschen's curves), since in the case of the triple junction under study, the notion of distance would not be pertinent (in contrast to a well-defined gas gap situation and therefore representable in the form of a Paschen curve). Furthermore, the geometry of the system at the triple junction remained unchanged, while pressure and temperature were the study variables.

3.3 Experimental results

This section deals with the influence of various conditions of temperature and gas pressure/density on partial discharge inception voltage (PDIV) and partial discharge extinction voltage (PDEV). As the PDIV/PDEV were obtained using AC voltage, the values that will appear in the manuscript are peak values. The results of the experiments, which were made in a temperature range from ambient temperature up to 400 °C and for gas (nitrogen) pressures between 50 mbar and atmospheric pressure, are first presented and discussed as a function of gas pressure. Influences other than the well-known effect of the change in the gas density with temperature are shown presenting the results as a function of gas density. Results are presented for aluminium oxide discs (II) and (III a) which have different purities.

3.3.1 PDIV & PDEV – dependence on temperature as a function of gas pressure

3.3.1.1 Aluminium oxide disc (II) – purity of 99.7 % – PDIV

First, the influence of temperature on PDIV and PDEV was analysed. For this purpose, both PDIV and PDEV were measured according to the procedure as presented in section 3.2.2 using an aluminium oxide disc (II) which had a diameter of 50 mm, a thickness of 1 mm and a purity of 99.7 %.

Figure 3.15 shows the results for the PDIV for several values of the temperature as a function of gas pressure. Each data point was calculated from the average of 15 measurements: the PDIV was measured five times consecutively for each pressure setpoint during a given temperature and each temperature was repeated three times. All error bars were calculated for a 1σ standard deviation from the 15 data points. For the measured pressure values, the uncertainty of the pressure gauge, which depends on the pressure range according to the manufacturer, was represented by x-axis error bars.

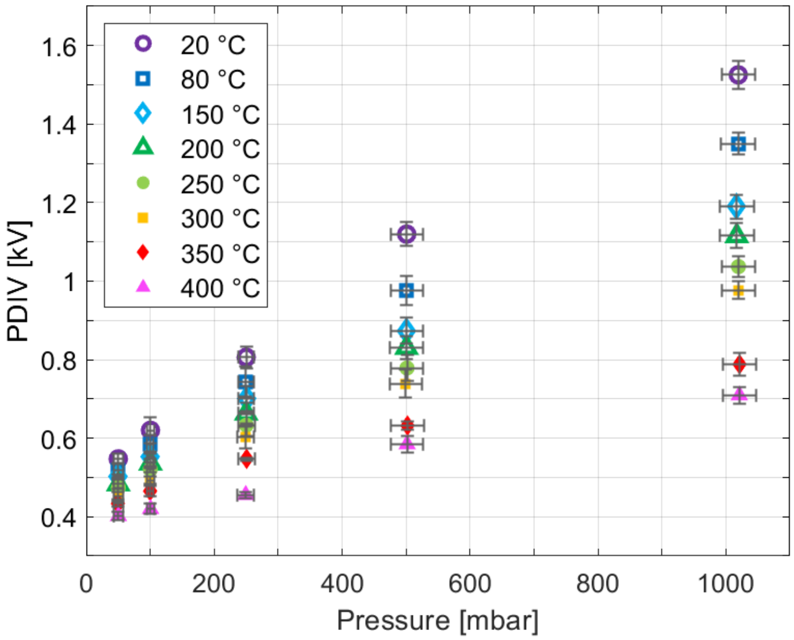

Figure 3.15. Aluminium oxide disc (II): PDIV as a function of gas pressure for different temperatures; nitrogen.

The PDIV increases for all temperatures with gas pressure in accordance with Paschen's law. An increase in temperature also leads to a decrease in PDIV consistent with the theory proposed by Townsend and thus the data correction method recommended by Dunbar. Assuming that the ideal gas law can be applied here, an increase in temperature *T* leads for a given gas pressure *p* and considering the Boltzmann constant k_B to a decrease in gas density *N*:

$$N = \frac{p}{k_B \cdot T} \tag{3.1}$$

This leads in turn to a greater value of the free mean path λ:

$$\lambda = \frac{1}{\sigma \cdot N} \tag{3.2}$$

where σ is the collision cross section for electron impact – gas ionisation.

Consequently, for a given ionisation potential W_i, the electric field strength *E,* and thus the voltage *V* (corresponding in this case to the PDIV) required to trigger a discharge, decrease:

$$E = \frac{W_i}{e \cdot \lambda} \propto \frac{V}{d} \tag{3.3}$$

with *e* the elementary charge and *d* the distance between the electrodes.

Figure 3.16 shows, as a function of temperature for all the gas pressures considered, the difference in PDIV between ambient and imposed temperatures. To ease the lecture, only the mean values without error bars are displayed.

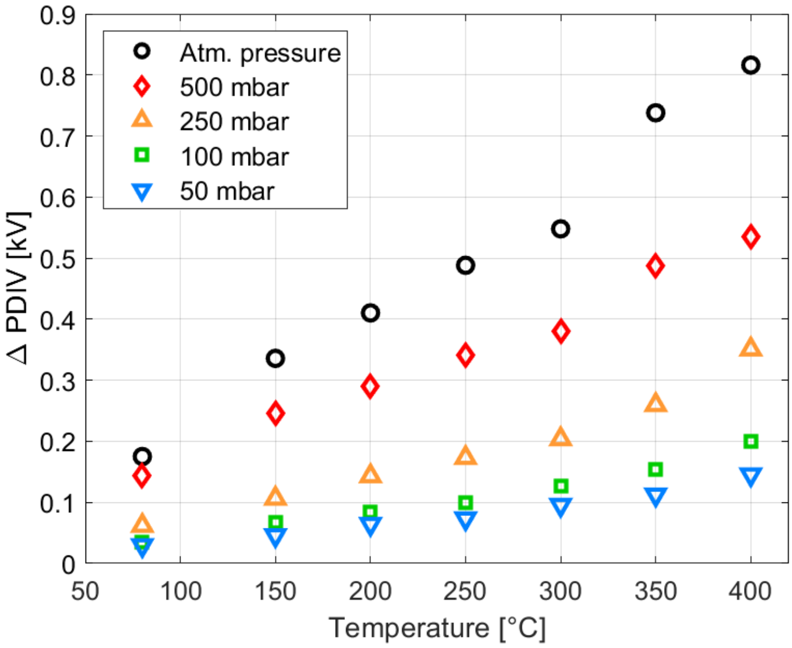

Figure 3.16. Difference in PDIV between ambient and imposed temperatures for different gas pressures as a function of temperature.

The difference in PDIV increases regularly with pressure and with temperature in the range of 80 °C to 300 °C before a steeper increase in the absolute value of the PDIV difference is visible from 350 °C onwards. The reason therefore will be explained in section 3.6.

According to the measurement results, it can be stated that the difference in PDIV between 20 °C and 400 °C at atmospheric pressure amounts approximately to 820 V and at 50 mbar to 145 V.

Based on the difference in PDIV as shown in Figure 3.16, a relative difference in PDIV can be calculated, see Table 3.1.

Table 3.1. Relative difference in PDIV in % compared to the PDIV at ambient temperature.

		T [°C]						
		80	**150**	**200**	**250**	**300**	**350**	**400**
p [mbar]	**1000**	- 11	- 22	- 27	- 32	- 36	- 48	- 54
	500	- 13	- 22	- 26	- 30	- 34	- 43	- 48
	250	- 8	- 13	- 18	- 21	- 25	- 32	- 44
	100	- 6	- 11	- 14	- 16	- 21	- 25	- 32
	50	- 5	- 8	- 12	- 13	- 17	- 21	- 27

At atmospheric pressure, the PDIV is reduced by nearly 50 % at 350 °C and is even less than half its value at ambient temperature when the temperature is increased up to 400 °C. In general, the relative difference in PDIV decreases with lower gas pressures but increases with temperature.

3.3.1.2 Aluminium oxide disc (II) – purity of 99.7 % – PDEV and comparison with PDIV

A similar behaviour was observed regarding the PDEV which is shown in Figure 3.17 as a function of gas pressure and for different temperatures. The data points and the error bars were calculated in the same manner as for the PDIV.

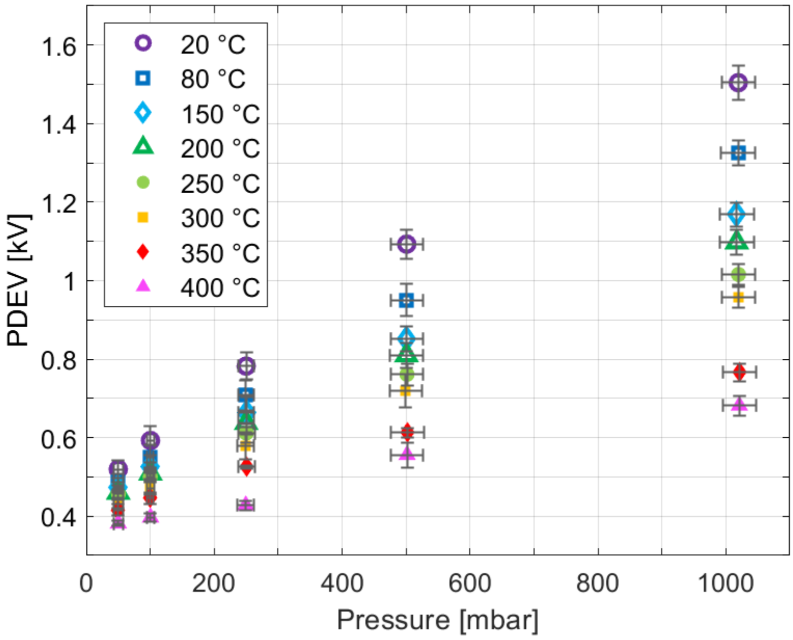

Figure 3.17. Aluminium oxide disc (II): PDEV as a function of gas pressure for different temperatures; nitrogen.

The difference in PDEV between 20 °C and 400 °C is similar to the difference in PDIV, it amounts at atmospheric pressure to 820 V and at 50 mbar to 140 V.

A comparison between the PDIV and PDEV values and their dependence on temperature as a function of gas pressure is shown in Figure 3.18. To ease the lecture, no error bars were added.

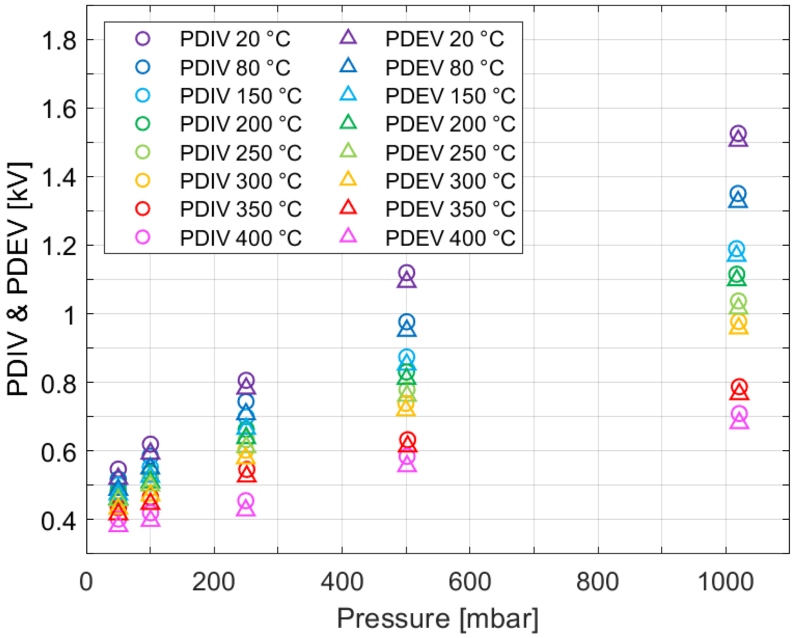

Figure 3.18. PDIV and PDEV as a function of gas pressure for different temperatures; nitrogen.

The PDIV is, as expected, for all pressures and all temperatures higher than the PDEV. Further, the difference between PDIV and PDEV is for all pressures and temperatures in a constant range of approximately 15 V to 40 V. Hence, when plotting the PDEV as a function of PDIV, all values should fall on the same line. Figure 3.19 shows this relation as an example for atmospheric pressure.

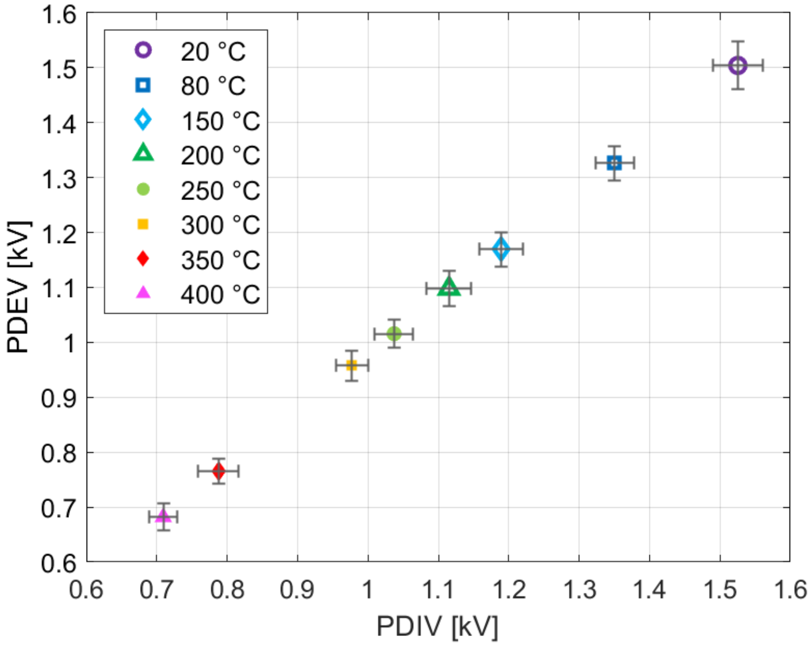

Figure 3.19. PDEV as a function of PDIV for different temperatures at atmospheric pressure; nitrogen.

However, no clear tendency of an increase or a decrease in difference between PDIV and PDEV with pressure or temperature could be noted. It should be mentioned that the difference between PDIV and PDEV in the indicated range is quite small compared to the measured values of PDIV and PDEV as well as in comparison to the error bars which are greater than the mentioned difference. Since the behaviour of PDEV is similar to that of PDIV and since the latter is of main interest in this work, a detailed analysis of the absolute and relative difference in PDEV will be omitted.

For each pressure setpoint at a given temperature, the PDIV and PDEV values were determined by five consecutive repetitions. In other words, the voltage was applied five times consecutively and the time between subsequent voltage applications can be estimated to an average of 2½ min.

The question may thus be raised whether the succession of several discharges could influence the results, for example by charge trapping on the surface of the aluminium oxide disc provoked by previous discharges. However, the experimental results do not show any clear sign of an influence of previous discharge activity on subsequent measurements, neither during the five successive PDIV/PDEV measurements at fixed temperature and pressure, nor along the three temperature cycles (20 °C to 400 °C, each including pressures in a range of 50 mbar to atmospheric pressure). A given experimental series was accomplished over the course of a few days and the subsequent two repetitions were made within a couple of weeks. Repeatability of the measurements on this time scale supports the idea of a steady behaviour of the system. The average of three experimental series led to repeatable results and reasonable error bars based on a 1σ standard deviation as can be seen in Figure 3.15 and Figure 3.17.

3.3.1.3 Aluminium oxide disc (III a) – purity of 96 % – PDIV

Complementary PDIV measurements were also made for aluminium oxide disc (III a), at ambient temperature and 400 °C. Aluminium oxide disc (III a) had a lower purity of 96 %. It had a square shape (76.2 mm x 76.2 mm) and a thickness of 1.016 mm.

Figure 3.20 shows the PDIV as a function of gas pressure for ambient temperature and 400 °C. Here the data points were calculated from the average of 10 measurements: the PDIV was measured five times consecutively for each pressure setpoint during a given temperature and each temperature was repeated twice. The error bars are again calculated for a 1σ standard deviation.

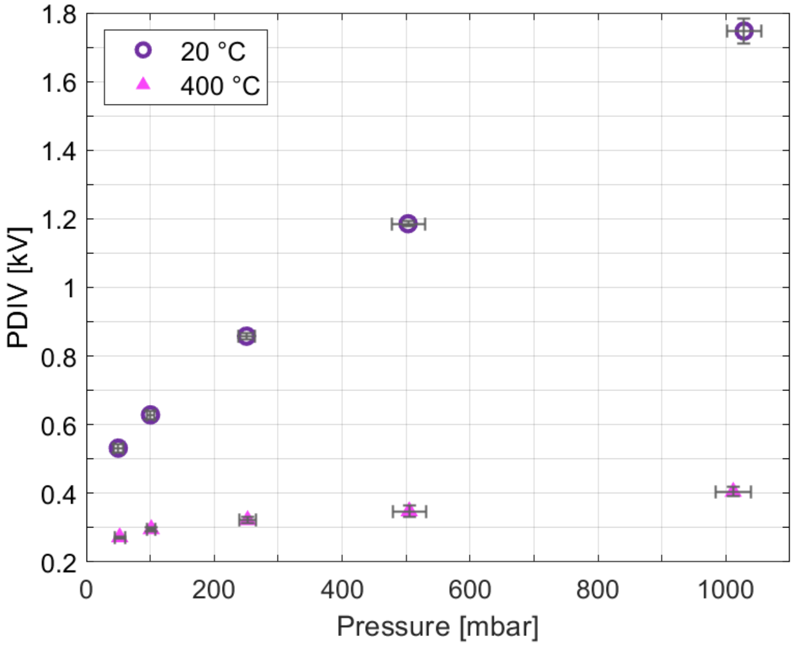

Figure 3.20. Aluminium oxide disc (III a): PDIV as a function of gas pressure at ambient temperature and 400 °C; nitrogen.

The results present the same general behaviour (PDIV increases with pressure but decreases with temperature for a given pressure) as when using aluminium oxide disc (II), but different PDIV values and temperature dependence, see Table 3.2.

Table 3.2. Comparison of PDIV and of decrease in PDIV between ambient temperature and 400 °C for aluminium oxides discs (II – purity of 99.7 %) and (III a – purity of 96 %).

Aluminium oxide disc	**Atmospheric pressure**			
	PDIV 20 °C [V]	**PDIV 400 °C [V]**	**Δ PDIV [V]**	**Δ PDIV [%]**
(II)	1530	710	820	- 54
(III a)	1745	405	1340	- 77
	50 mbar			
(II)	545	400	145	- 27
(III a)	530	270	260	- 49

The decrease in PDIV with temperature is significantly greater for the lower purity aluminium oxide disc. This fact combined with the observation of the way the PDIV decreased with temperature for the aluminium oxide disc (II), led to the idea that something more than simply an effect of gas density was playing a role. Therefore, the data were analysed as a function of density to better discern such effect; this is the subject of the following section.

3.3.2 PDIV – dependence on temperature as a function of gas density

In this section, the same results as in section 3.3.1 are presented, but now as a function of the calculated gas density. Since the results for PDEV were similar to those for PDIV, only PDIV will be considered from hereon.

3.3.2.1 Aluminium oxide disc (II) – purity of 99.7 %

Figure 3.21 shows the results for the PDIV (peak value) of aluminium oxide disc (II) and their dependence on temperature as a function of gas density. As the values of PDIV are the same as in section 3.3.1.1 (see Figure 3.15), the calculation of the data points (average of 15 measurements) is the same. The error bars are again calculated based on a 1σ standard deviation. For the gas density, only the uncertainty of the pressure gauge according to the manufacturer, depending on the pressure range, was considered whereas the uncertainty of the thermocouples was negligible.

For ease of reading, a trend line (second-degree polynomial) has been added to the experimental points for each temperature.

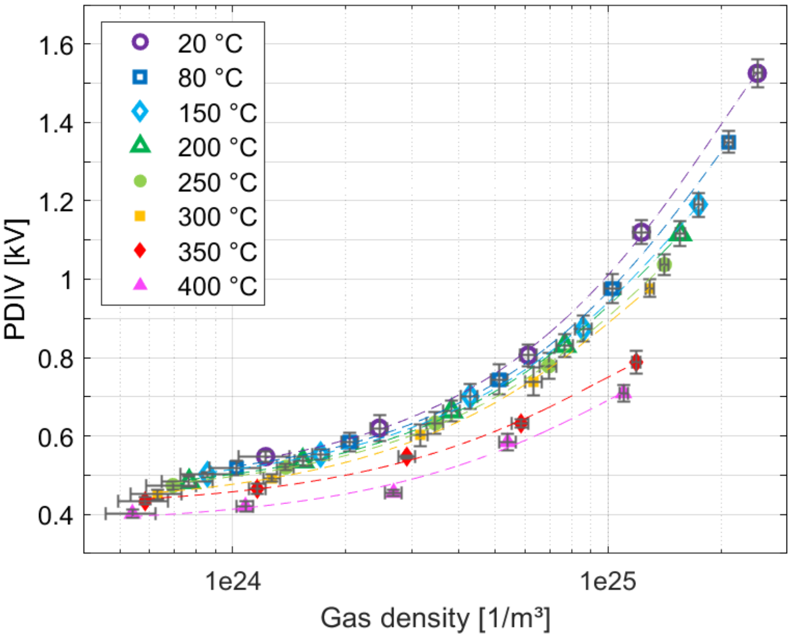

Figure 3.21. Aluminium oxide disc (II): PDIV as a function of gas density for different temperatures; nitrogen.

According to the theory proposed by Dunbar [40], see section 1.2.5.1, and assuming that the gas density in vicinity of the triple junction is homogeneous, it should be expected that all trendlines merge together when plotted as a function of gas density.

However, with increasing temperature up to 400 °C, all the curves are slightly below their precedent ones whereas a bigger gap between 300 °C and 350 °C can be observed. This behaviour was already rudimentarily seen in Figure 3.16, where the increase in difference in PDIV appears to be steeper for temperatures above 300 °C than for lower temperatures.

3.3.2.2 Aluminium oxide disc (III a) – purity of 96 %

In addition to aluminium oxide disc (II), the results of PDIV for aluminium oxide disc (III a) at ambient temperature and 400 °C are also presented as a function of gas density. The data points are again calculated from the average of 10 measurements and for a 1σ standard deviation, see Figure 3.22.

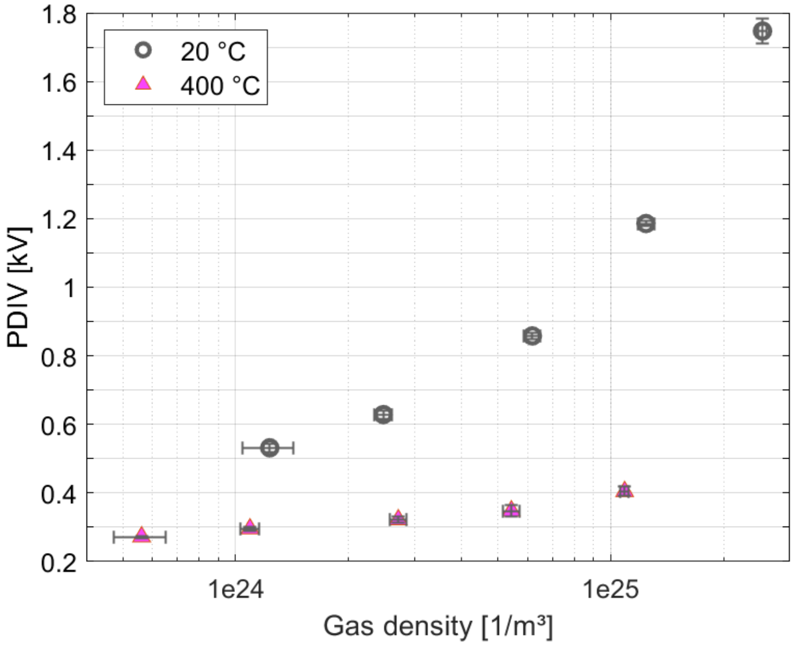

Figure 3.22. Aluminium oxide disc (III a): PDIV as a function of gas density at ambient temperature and 400 °C; nitrogen.

Figure 3.22 demonstrates a noticeable drop in PDIV, even though the theory suggests that both curves should merge independently of temperature.

These results suggest that, for a given pressure, the increase in the mean free path due to the increase in temperature does not alone explain the decrease in PDIV with temperature. An additional effect, especially at temperatures above 300 °C, influences PDIV in a manner that the decrease becomes even more important.

To explain this phenomenon, attention was directed towards the role that the aluminium oxide disc could play on the PDIV (and PDEV) as a function of temperature. It is well known that temperature may have a strong influence on the dielectric properties of solid insulators, such as volume resistivity or relative permittivity [90], [113]. Hence, dielectric measurements were realised on aluminium oxide discs (II) and (III a); these measurements are presented in the next section.

3.4 Influence of temperature on volume resistivity of the aluminium oxide disc

In a first step, volume resistivity (DC) of the aluminium oxide disc (II) was measured depending on temperature, from ambient temperature up to 400 °C. The gas pressure/density was not of importance for this experiment and remained at 500 mbar simply to ensure that the vacuum chamber was airtight and thus maintained a low level of oxygen in order to avoid oxidation of the electrodes at high temperature.

This section describes the test setup and the experimental procedure as well as the obtained results.

3.4.1 Test setup

The test setup for the measurement of the volume resistivity was designed on the same basis as the one used for PDIV/PDEV measurement. However, the composition of the counter electrode of the triple junction assembly had to be modified and some components for the measurement to be added. Figure 3.23 shows the schematic of the test setup and circuit and Figure 3.24 the enlarged schematic of the triple junction assembly.

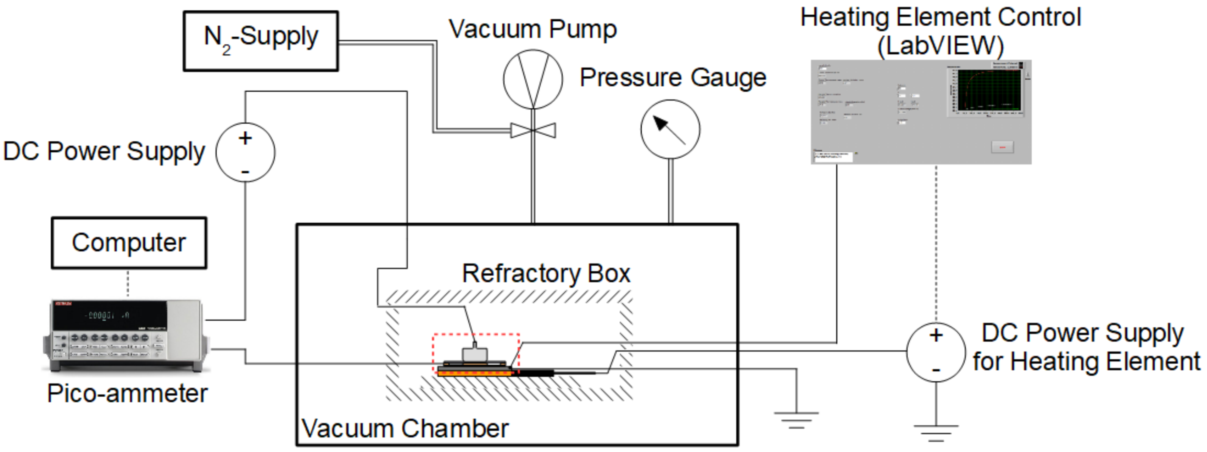

Figure 3.23. Schematic of the test setup and circuit to analyse the influence of temperature on volume resistivity.

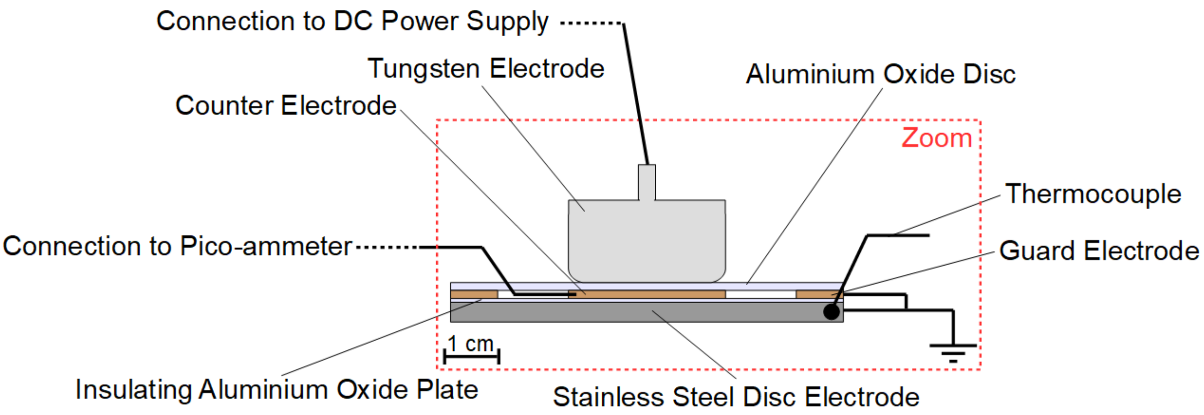

Figure 3.24. Schematic of the triple junction assembly for volume resistivity measurement.

The tungsten electrode was connected to a DC power supply, also connected to the pico-ammeter. For a correct volume resistivity measurement, a circular copper counter electrode (thickness of 60 µm) was placed opposite to the tungsten electrode beneath the aluminium oxide disc and connected to the pico-ammeter. The surface of this counter electrode corresponded to that of the tungsten electrode. Additionally, an annular copper guard electrode (thickness of 60 µm) was placed around the copper counter electrode and connected to ground potential. To isolate the grounded stainless steel disc electrode from the copper counter electrodes (measurement and guard electrodes), a thin (thickness of 127 µm) aluminium oxide plate (aluminium oxide disc (I)) was used. The heating plate (not shown in Figure 3.24) was placed beneath the described assembly.

The volume resistivity of the aluminium oxide disc was determined using a commercial pico-ammeter (Keithley Model 6485 Picoammeter) allowing current measurements in a range of 20 mA down to 20 fA. The measurements were acquired via a RS-232 serial computer interface. A control software for the pico-ammeter based on an add-in for Excel (ExcelLINX) to configure and control the measurement procedure and collect the data was used.

3.4.2 Experimental procedure

Apart from the usual preparations regarding the polishing/cleaning of the tungsten electrode as described in section 3.2.2, a zero check or rather a zero correct of the pico-ammeter was made first and the measurement was configured (measurement range (20 nA), sampling rate) using the Excel add-in ExcelLINX.

Absorption current was measured during 20 min after application of a 30 V voltage step, then resorption current in short circuit (realised by setting the applied voltage to 0 V) was measured during another 20 min. This measurement was made twice for a temperature range from ambient temperature up to 400 °C according to the defined temperature setpoints in section 3.2.2.

The volume resistivity ρ was calculated from the applied voltage V, the tungsten electrode surface A_S, the measured current I and the thickness d_i of the aluminium oxide disc according to:

$$\rho = \frac{V \cdot A_S}{I \cdot d_i} \tag{3.4}$$

Remarks: the current value used for the calculation of the volume resistivity corresponded to its mean value over the last five minutes when a voltage of 30 V was applied and assuming that the current has reached a constant level. The calculated value of the volume resistivity is time dependent, but the data allow comparisons to be made between different temperatures. It may also be affected by a slight overestimate due to the fact that, despite all the care taken to assemble the setup, it could not be guaranteed that the counter electrode was placed exactly opposite to the tungsten electrode. This again is not a problem for comparisons at different temperatures, given that the same setup was used.

3.4.3 Experimental results – volume resistivity as a function of temperature

Figure 3.25 shows the measured absorption and resorption currents for the eight considered values of the temperature as a function of time.

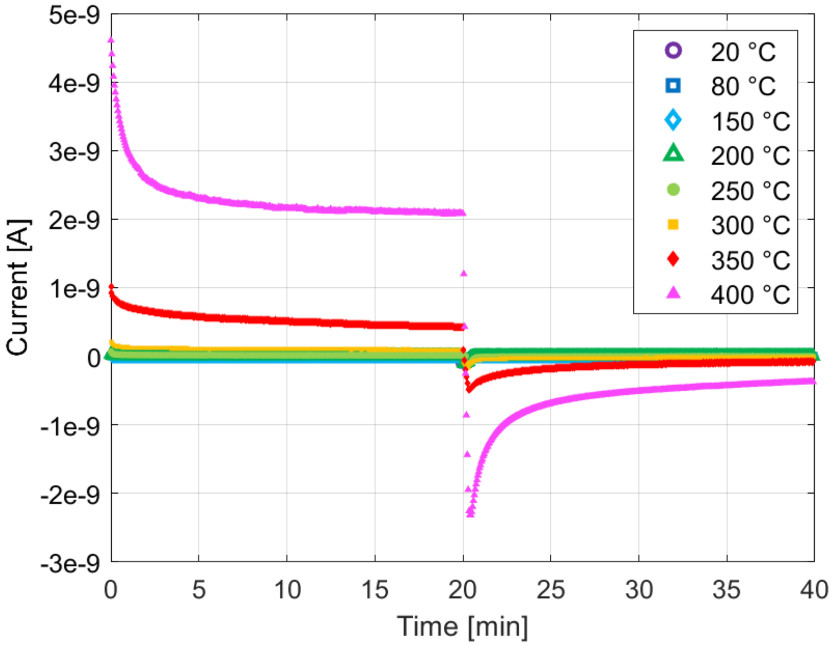

Figure 3.25. Aluminium oxide disc (II): measured absorption (t < 20 min) and resorption (t > 20 min) currents for different temperatures as a function of time.

A current peak occurred when the voltage was applied or switched off before the current decreased towards to a stabilised value. However, the currents measured at 350 °C and

400 °C may not have stabilised completely, as a slight decrease can be seen by end of the 20-minute measurement period. A longer measurement would have been interesting but for the sake of comparability, the same measurement procedure was used for all temperatures, with two 20-minute measurement periods at 30 V and 0 V respectively.

Further, a noticeable increase in current up to some nanoamperes is only visible for temperatures greater than 300 °C. For lower temperatures, the measured current only increases up to some hundreds of picoamperes and is in Figure 3.25 hardly distinguishable. Hence, to better show the behaviour of the absorption currents at temperatures below 300 °C during the first 20 minutes of measurement, a zoom was made using a logarithmic scale, as can be seen in Figure 3.26. It should be noted that for the currents obtained at a temperature below 250 °C, a filter was applied to allow a better distinguishability between the relevant currents and the measurement noise.

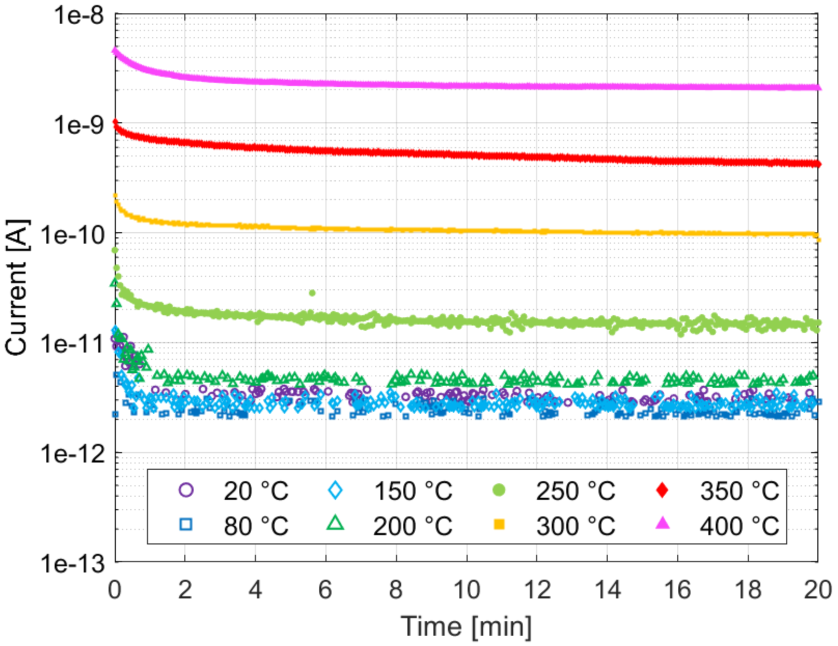

Figure 3.26. Aluminium oxide disc (II): absorption currents during the first 20 minutes of measurement for different temperatures as a function of time.

Only the polarisation currents obtained for a temperature at or above 250 °C exhibit a smooth curve shape. For temperatures below 250 °C, acquired data are more influenced by the measurement noise.

Nevertheless, the volume resistivity for different temperatures was calculated considering the average value of the polarisation current measured during the last five minutes when a voltage of 30 V was applied. Figure 3.27 shows the calculated volume resistivity as a function of temperature. As indicated, the data points were calculated on the basis of two measurements and the error bars for a 1σ standard deviation considering the uncertainty of the pico-ammeter according to the manufacturer.

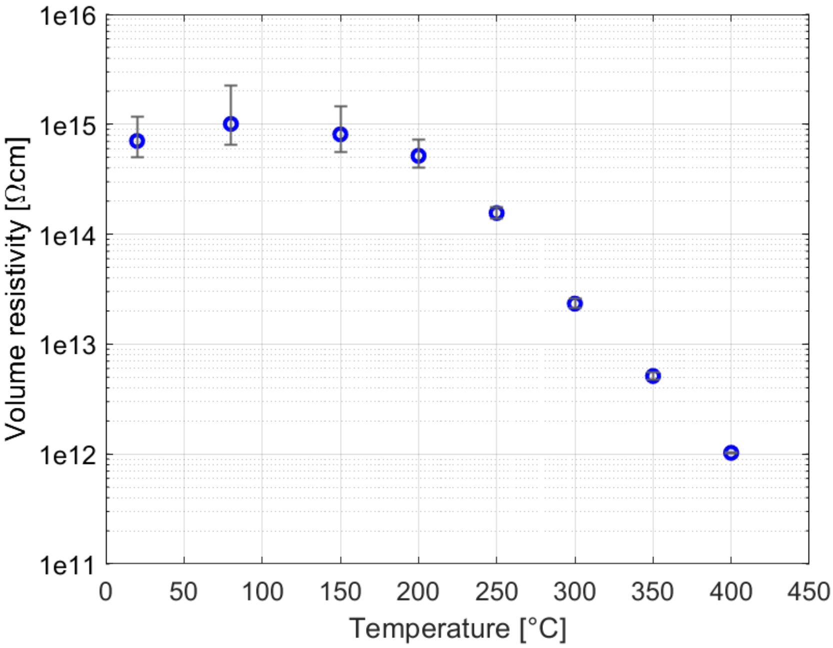

Figure 3.27. Aluminium oxide disc (II): volume resistivity as a function of temperature.

As expected, the volume resistivity decreases with temperature. A three-order-of-magnitude decrease was observed (from 10^{15} Ω·cm to 10^{12} Ω·cm) when the temperature rose from ambient to 400 °C. These experimental results are in good accordance with data from the literature [115].

However, the volume resistivity between ambient temperature and 80 °C is not expected to increase. The trend observed over this temperature range is not significant, given the size of the error bars.

3.5 Influence of temperature on relative permittivity of the aluminium oxide disc

The relative permittivity of aluminium oxide is also known to increase with temperature [113], [120], [121], [122], [123]. To quantify this influence, it was measured in a range from 20 Hz up to 1 kHz over a temperature range of ambient to 500 °C. The temperature and frequency range of this measurement has been extended compared to the previous experiments, making it possible to show the behaviour of the relative permittivity with increasing temperature in more detail.
This section presents, in analogy to the measurements of the volume resistivity, the test setup, the experimental procedure as well as the experimental results for these measurements.

3.5.1 Test setup

The setup is based on the one presented in section 3.2.1., using the same triple junction assembly, heating element and peripheral equipment. Figure 3.28 depicts the schematic of the test setup and circuit.

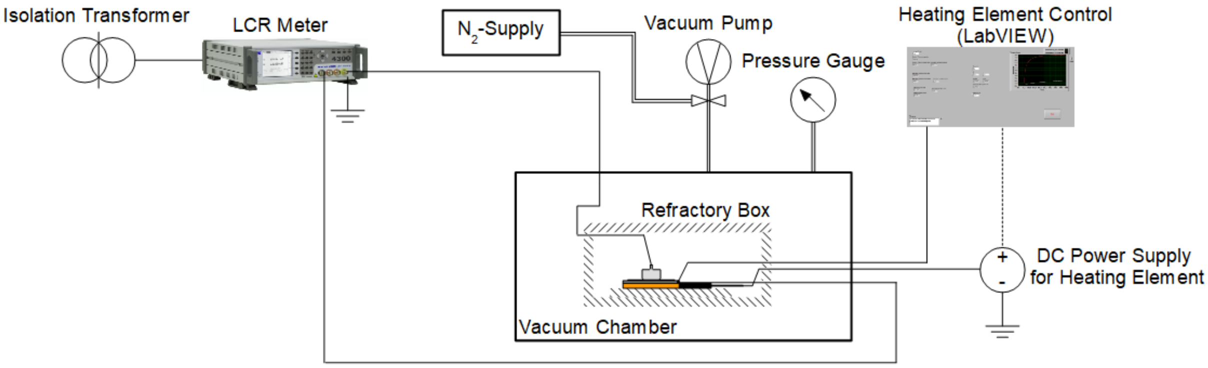

Figure 3.28. Schematic of the test setup and circuit to analyse the influence of temperature on relative permittivity.

To prevent oxidation, the vacuum chamber was purged three times and then filled with nitrogen. As the gas pressure/density inside the vacuum chamber was not of importance for this experiment, the vacuum pump and the pressure gauge were only used for the purpose of purging, and the experiments were made at a gas pressure inferior to atmospheric pressure (500 mbar).

The relative permittivity of the aluminium oxide disc was determined using a commercial LCR meter (Wayne Kerr LCR Meter 4300). In general, this device was designed to measure passive components over a frequency range from 20 Hz to 1 MHz.
The tungsten electrode and stainless-steel disc electrode were respectively connected via a wire to the supplied Kelvin clips which are, for their part, connected to the 4-terminal BNC-input of the LCR meter. To limit the noise in the measurements caused by electrical

perturbations from the environment such as harmonics, an isolation transformer was used separating the LCR meter from the grid.

3.5.2 Experimental procedure

The capacitance *C* of the aluminium oxide disc was measured for these frequencies:

- 20 Hz, 40 Hz, 50 Hz, 60 Hz, 100 Hz, 1 kHz

The same polishing/cleaning of the tungsten electrode and purging of the vacuum chamber was realised before the experiment as described in section 3.2.2. Besides, to eliminate the effects of series impedance and stray capacitance in the leads used to connect the LCR meter to the test object, a calibration in open and short circuit as well as for DC was done before the measurement for each applied frequency.

For the same temperature setpoints as defined in section 3.2.2, five consecutive measurements at each frequency were made and the capacitance value was calculated from their average.

The relative permittivity ε_r was subsequently calculated using the thickness d_i of the aluminium oxide disc, the tungsten electrode surface A_S as well as the vacuum permittivity ε_0 according to:

$$\varepsilon_r = \frac{C \cdot d_i}{\varepsilon_0 \cdot A_S} \tag{3.5}$$

Remark: although an isolation transformer was used, the measurement for frequencies of 50 Hz and 100 Hz (as a multiple of 50 Hz) were occasionally affected by electrical perturbations from the environment; other frequencies were not significantly affected by these perturbations.

3.5.3 Experimental results – relative permittivity as a function of temperature

Figure 3.29 shows the relative permittivity calculated from capacitance measurements on aluminium oxide disc (II) for different temperatures at the six chosen frequencies. The error bars were calculated for a 1σ standard deviation. The 50 Hz case, also used for the PDIV experiments, is highlighted by a solid line.

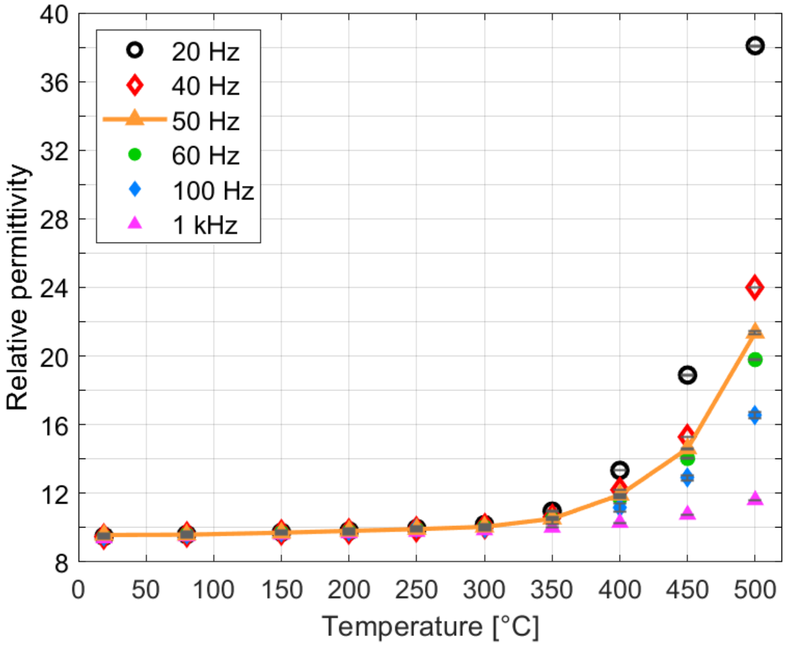

Figure 3.29. Aluminium oxide disc (II): relative permittivity for different frequencies as a function of temperature. A solid line is highlighting the 50 Hz case.

The relative permittivity remains nearly constant up to 300 °C regardless of frequency. For temperatures beyond 300 °C, an increase of relative permittivity with temperature can be observed, which is more important at low frequencies.

The higher relative permittivity at increased temperatures can be explained by the presence of mobile charge carriers which derive from dopants used to control the grain size of the aluminium oxide or from impurities. With higher temperature, these mobile charge carriers are excited and respond to the external electric field to produce a polarisation current [113]. This displacement of mobile charge carriers is responsible for the increase of the aluminium oxide DC conductivity with temperature studied in section 3.4, as well as for this permittivity increase. Since the charge quantity carried by conduction is approximately proportional to the duration of the applied voltage, this increase in relative permittivity should also be inversely proportional to the signal frequency, which is indeed what is observed.

The relative permittivity was also determined for aluminium oxide disc (III a) which had a lower purity (96 %). Figure 3.30 shows the relative permittivity as a function of temperature for the same frequency values.

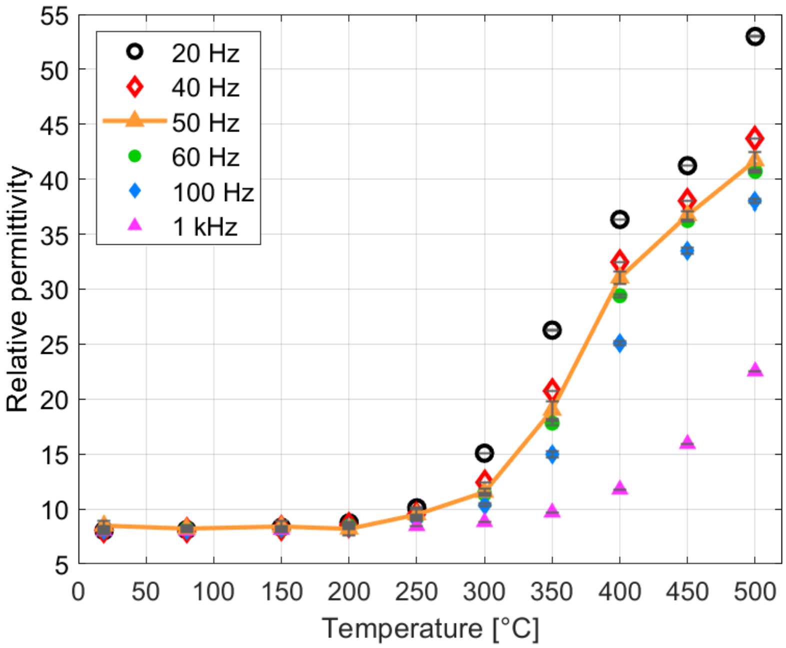

Figure 3.30. Aluminium oxide disc (III a): relative permittivity for different frequencies as a function of temperature. A solid line is highlighting the 50 Hz case.

The value of relative permittivity at ambient temperature is for this aluminium oxide disc lower than for higher purity aluminium oxide disc (II). However, the increase in permittivity with temperature occurs here for a lower value, and the relative permittivity for temperatures above 350 °C becomes higher for 96 % (III a) than for 99.7 % (II) aluminium oxide disc. This is in accordance with the assumption that the increase in relative permittivity with temperature is due to mobile charge carriers stemming from impurities.

Another effect is also observed, which is the change of slope in the increase of the relative permittivity above 300 °C. A possible explanation for this may be an internal space charge effect, for instance charge retention at the internal interfaces of this polycrystalline material, which may affect the current only when the charge motion integrated over one signal demi-period is enough for significant charge accumulation on these interfaces.

However, it should be noted that the measurement of the relative permittivity in this case is less smooth than it was for the results as shown in Figure 3.29, especially for lower frequencies and temperatures above 350 °C where the increase in relative permittivity seems to flatten. A reason may be influences provoked by electrical perturbations from the environment during the measurement which affected especially the lower frequencies since the results for 1 kHz don’t seem to be affected.

Nevertheless, it can be seen that the increase in relative permittivity is much more important for a lower purity aluminium oxide disc than for a higher purity aluminium oxide disc, see Figure 3.*31* which plots the relative permittivity of both aluminium oxide discs for a frequency of 50 Hz as a function of temperature.

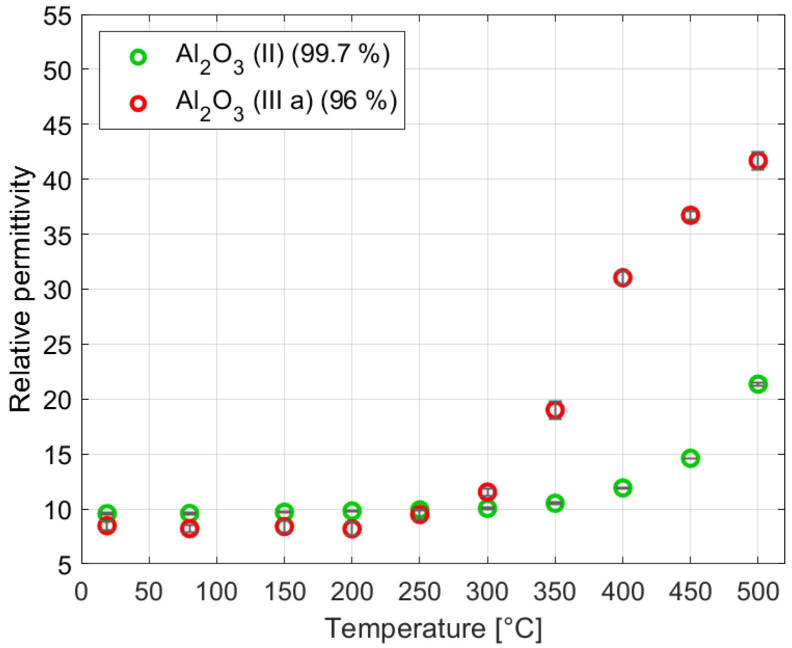

Figure 3.31. Aluminium oxide discs (II) and (III a): relative permittivity for 50 Hz as a function of temperature.

For the sake of clarity, no further comparison of the relative permittivity of both 96 % and 99.7 % aluminium oxide discs within the same diagram as a function of temperature for different frequencies was made. Instead, Table 3.3 compares relative permittivity of both aluminium oxide discs for selected temperatures and frequencies.

Table 3.3. Comparison between aluminium oxide discs (II) and (III a) towards relative permittivity for selected temperatures and frequencies.

Temperature [°C]	**Aluminium oxide disc (II)**				**Aluminium oxide disc (III a)**			
	Frequency [Hz]							
	20	**50**	**100**	**1000**	**20**	**50**	**100**	**1000**
20	9.5	9.6	9.5	9.4	8.0	8.5	8.1	8.0
80	9.6	9.6	9.6	9.5	8.1	8.2	8.1	8.0
200	9.8	9.8	9.8	9.7	8.7	8.2	8.3	8.2
300	10.2	10.1	10.0	9.9	15.1	11.5	10.4	8.8
400	13.3	11.9	11.2	10.3	36.3	31.0	25.1	11.8
500	38.1	21.4	16.6	11.6	53.0	41.7	38.0	22.5

Considering the temperature range from ambient temperature up to 400 °C in which the experiments of PDIV and PDEV were carried out, it can be stated that the relative permittivity is a least twice for all frequencies – except 1 kHz – when the lower purity aluminium oxide disc (III a) is used. For 20 Hz and 50 Hz, almost a tripling can be observed.

Remark: It should be noted that the same relative permittivity was measured during a control measurement at ambient temperature after exposure of the aluminium oxide disc to temperatures up to 400 °C. This demonstrates that exposure of the aluminium oxide disc to elevated temperatures did not irreversibly change its dielectric properties.

3.6 Discussion of influences on PDIV due to modification of the dielectric properties of the aluminium oxide disc

As presented in section 3.3.2, the results of the PDIV measurements depending on temperature as a function of gas density showed that other effects than the well-known gas density effect contribute to a supplementary decrease in PDIV.

Attention was then directed towards the changes in relative permittivity and volume resistivity with temperature. It has been shown that as temperature increases, the volume resistivity falls while the relative permittivity increases, and for the latter, the lower the purity of the aluminium oxide disc the higher the relative permittivity rises. The consequences of these modifications on PDIV (and PDEV) will be discussed in this section.

3.6.1 Influence of changes in relative permittivity on PDIV – numerical simulation

According to the results, it could be noted that the relative permittivity increases with temperature which leads, for given gas density and voltage applied across the system, to an increase in the local electric field in the gas close to the triple junction. Consequently, this increase in electric field facilitates the inception of partial discharges and it is therefore logical that the PDIV (and PDEV) drop with temperature even more than may be expected simply due to the decrease in gas density.

It has been observed that this increase in relative permittivity with temperature is more pronounced starting from 300 °C, see Figure 3.29. This profile therefore justifies the fact that in Figure 3.21, the PDIV curve corresponding to 350 °C is clearly detached from that obtained at 300 °C and lower temperatures. It is also logical that in Figure 3.16, a steeper increase in the difference of PDIV relative to that measured at ambient temperature can be seen for temperatures above 300 °C.

Apart from that, the higher PDIV at ambient temperature of aluminium oxide disc (III a) in comparison to disc (II), see Table 3.2 in section 3.3.1.3, can also be explained by the difference in relative permittivity at this temperature. Since it is slightly lower for the less pure aluminium oxide disc (III a), it is also logical that a higher PDIV can be measured at ambient temperature than for aluminium oxide disc (II).

In the next sections, these observations are further analysed by a numerical simulation of the electric field in the gas near the triple junction using finite element modelling (COMSOL Multiphysics).

3.6.1.1 Objective of the simulation

It has been shown in the literature that the PDs at triple junctions do not start at the contact point of all three materials (metal/solid insulator/gas) where the electric field is the highest because of a lack of space for an electron avalanche to propagate [10], [13], [59], [74]. The point at which PDs initiate also depends on pressure and temperature, parameters that were only considered partially or not at all in these studies from the literature.

Here, a calculation allowing an evaluation of the location of the partial discharges at their inception voltage condition is presented. This may be helpful to check whether the hypothesis that the PDs occur within a zone near the triple junction, in which the gas density is supposed to be homogeneous, see section 3.2.3, is correct. Besides, further calculations regarding the change in electric field near the triple junction will be made, which would be more precise when the approximate position where the PD takes place is known.

3.6.1.2 Calculation of the voltage difference between the solid insulator surface and the electrode at PDIV along an electric field line

Figure 3.32 shows the numerical simulation (2D axisymmetric, mesh size of the finite elements of 10 µm, Neumann boundary conditions) of the electric field near the triple junction for an applied voltage of 1 V. The counter electrode at position 0 mm and at a potential of 0 V is not depicted in the figure in which electric field lines for the zone around the triple junction were included.

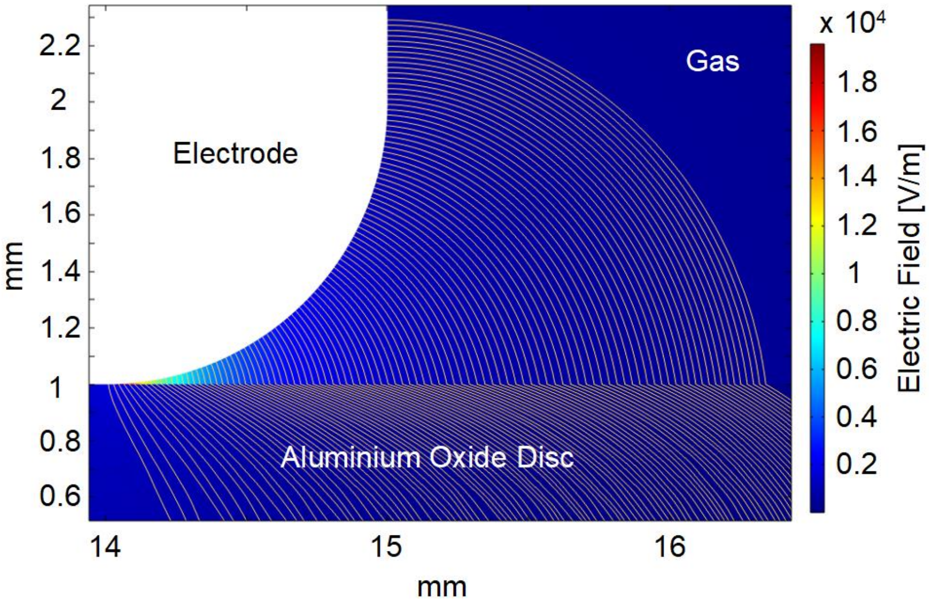

Figure 3.32. Numerical simulation of the electric field near the triple junction for an applied voltage of 1 V including the electric field lines for the zone around the triple junction.

Considering that the PDIV is applied to the electrode, from this simulation, a calculation of the voltage loss in the gas separating the electrode and the aluminium oxide disc surface becomes possible by integrating the electric field along each field line bridging the gas gap. In the simulation, it is assumed that there is no residual charge at the aluminium oxide disc.
Hence, at a given temperature and a given pressure, knowing the PDIV and the value of the aluminium oxide disc permittivity, a plot may be drawn of the voltage across the gas gap as a function of the product of pressure by distance in the interval. The distance considered here is the length of an electric field line, which can be seen as the "PD trajectory" assuming that the PDs follow the electric field line without branching.

Remark: to come to a more precise result, more electric field lines (500) than displayed in Figure 3.32 were used in the numerical simulation.

3.6.1.3 Comparison with Paschen's curves and determination of the partial discharge trajectory/initiation point at PDIV

This simulation was made for the extreme values of the whole temperature and pressure range used in the experiments as well as for both aluminium oxide discs (II) and (III a). Table 3.4 shows the parameters for which the simulation was carried out, including the pressure and temperature ranges, the corresponding relative permittivities, as well as the PDIV values which were considered as applied to the electrode.

Table 3.4. Simulation parameters for the determination of the PD trajectory/PD initiation point as a function of temperature and pressure.

Aluminium oxide disc	**(II) (99.7 %)**		**(III a) (96 %)**	
Temperature [°C]	20	400	20	400
Pressure [mbar]	1019	50	1021	50
Relative permittivity [-]	9.6	11.9	8.5	31
PDIV [V]	1530	400	1745	270

Figure 3.33 and Figure 3.34 show the calculated potential differences along the electric field lines for aluminium oxide disc (II – purity of 99,7 %) and aluminium oxide disc (III a – purity of 96 %) at 20 °C/1019 mbar and 400 °C/50 mbar together with the Paschen's curves at 20 °C and 400 °C under consideration of the Dunbar correction as a function of the product of gas pressure and inter-electrode distance.

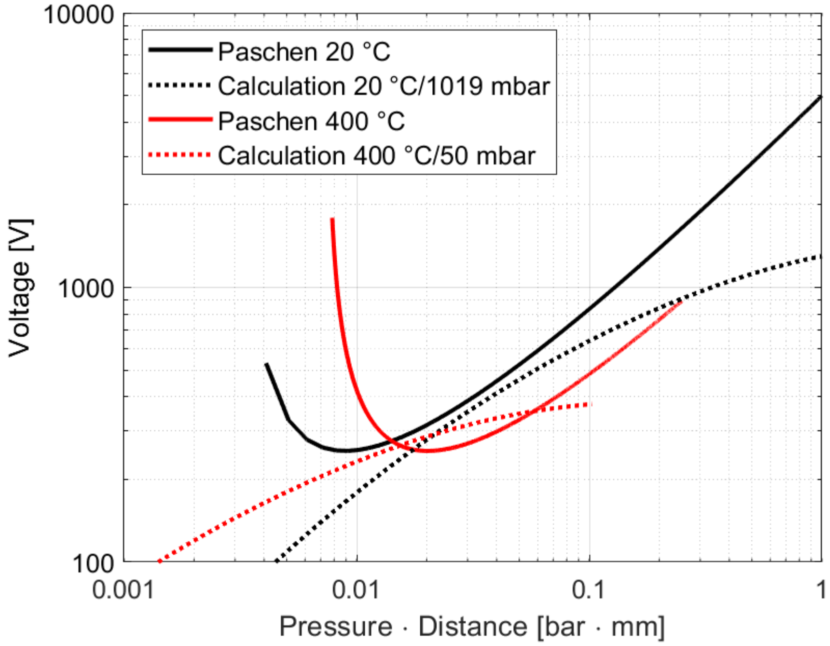

Figure 3.33. Aluminium oxide disc (II): calculated potential differences at 20 °C/1019 mbar and 400 °C/50 mbar in comparison with Paschen's curves at 20 °C and 400 °C; nitrogen.

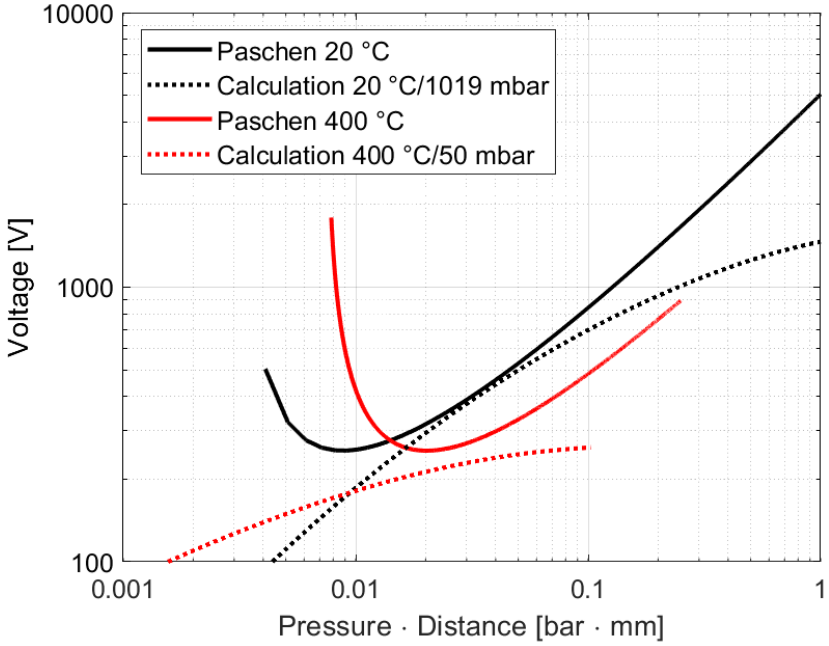

Figure 3.34. Calculated potential differences at 20 °C/1021 mbar and 400 °C/50 mbar in comparison with Paschen's curves at 20 °C and 400 °C; aluminium oxide disc (III a); nitrogen.

The discharge length at PDIV should be given by the intersection of the Paschen's curves with the calculated potentials along the field lines. However, on three of the four situations, the calculated potentials remain below the Paschen's curves, with no intersection. This contrast between the measured, repeatable PDIV values and the simulation results may have various causes:

- surfaces of the electrode and the aluminium oxide disc in the simulation exhibit no imperfections while their real surfaces (see sections 2.3.1.1 and 2.4.1.) present imperfections, such as micro-scratches, peaks, etc., that lead to local enhancements of the electric field and a lower PDIV. Without any imperfections and a more homogeneous electric field, a higher PDIV would be needed to come to an intersection between the calculated and Paschen's curves.
  Further, the voltage applied to the electrode in the simulation corresponds to the mean value of the measured PDIV taking into account these imperfections although the geometry in the simulation exhibited no imperfections.

- the error bars of the measured PDIV were not taken into account. Since the applied voltage may differ by some tens of volts, the position of the calculated curves relative to the Paschen's curves may therefore slightly change.

- the simulation was carried out for an electrode with a geometry of an ideally shaped rounded edge with a radius of 1 mm, which does not exactly reflect the real Rogowski profile of the used electrode. However, as the Rogowski profile seeks to render the electric field more homogeneous, the electric field lines may even be shorter and the field in the air gap lower.

- no residual charges on the surface of the aluminium oxide disc were taken into account thus leading to a less important PDIV than for the measured PDIV since PD activity is not impeded by the presence of charges of the same polarity as the applied voltage.

Despite these discussed differences between the results of the numerical simulation and the measured PDIV, an estimation of the length of the PDs and the zone where the PDs are expected to take place remains possible. For the cases without interception, the closest point between the calculated and the Paschen's curve was used. Table 3.5 shows the results for both aluminium oxide discs (II) and (III a).

Table 3.5. Calculated length of PD trajectory and distance from the triple junction according to the numerical simulation.

Aluminium oxide disc	**(II) (99.7 %)**		**(III a) (96 %)**	
Temperature [°C]	20	400	20	400
Pressure [mbar]	1019	50	1021	50
Length of PD trajectory [µm]	32	307 – 1159	32	489
Distance from triple junction [µm]	252	824 – 1719	256	1062

The PD trajectory length increases with temperature and lower pressure conditions. Hence, at ambient temperature and atmospheric pressure, the PDs initiate closer to the triple junction than at 400 °C/50 mbar. As expected, and shown in previous studies [10], [13], [59], [74], the PDs do not initiate directly at the triple junction where the electric field has its maximum because the discharge trajectory is too short for an electron avalanche to develop.

No difference between aluminium oxide discs (II) and (III a) can be observed. At ambient temperature/atmospheric pressure, the same PD trajectory was calculated leading to almost the same distance from the triple junction. At 400 °C/50 mbar, the values for aluminium oxide disc (III a) are within the range calculated for aluminium oxide disc (II) at these temperature and gas pressure conditions.

Knowing that in the simulation an ideal electrode geometry was used, it can nevertheless be estimated that the PDs are expected to occur within a distance from approximately 250 µm to 1700 µm from the triple junction. Consequently, the assumption made that the gas density at and in the vicinity of the triple junction (2 mm, as measured and discussed in section 3.2.3) is estimated to be virtually the same can be maintained since the PDs are expected to occur within this distance.

Remark: according to the discussion concerning the results of the numerical simulation, the values indicated in Table 3.5 should rather be seen as a rough estimation of the order of magnitude where the PDs are expected to initiate. Even though it is possible to calculate exact numerical values, the simulation is too idealised to directly transfer the obtained data to the actual geometry under study.

3.6.1.4 Simulation of the increase in electric field in the gas as a function of relative permittivity

A simulation of the increase in electric field in the gas near the triple junction due to the rise of relative permittivity of the aluminium oxide disc with higher temperatures was also made. For this purpose, four points in the gas close to the surface of the aluminium oxide disc in the region where the PDs are supposed to occur were defined, see Figure 3.35.

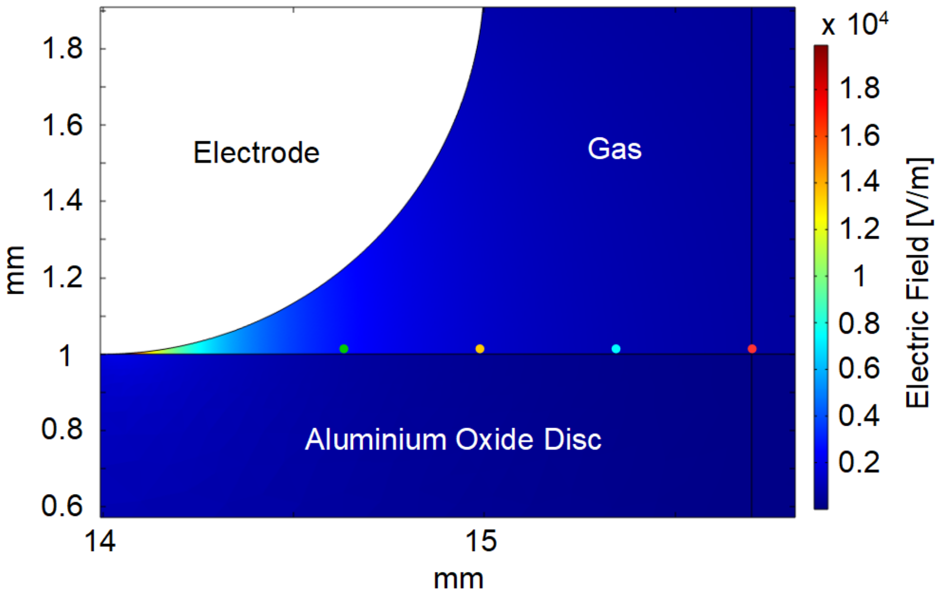

Figure 3.35. Defined points in the gas near the triple junction for the calculation of the increase in electric field in the gas as a function of relative permittivity.

For the points displayed, a calculation of the electric field as a function of relative permittivity, when 1 V is applied on the electrode, is given in Figure 3.38 for aluminium oxide disc (II) and in Figure 3.39 for aluminium oxide disc (III a). The relative permittivity was varied for aluminium oxide disc (II) between $\varepsilon_r = 9.6$ and $\varepsilon_r = 11.9$, and for aluminium oxide disc (III a) between $\varepsilon_r = 8.5$ and $\varepsilon_r = 31$.

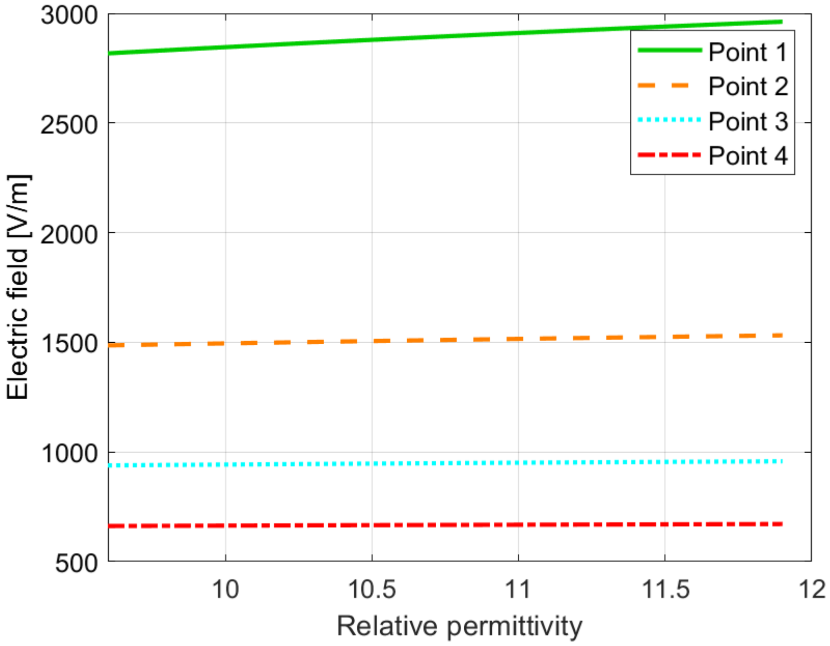

Figure 3.36. Aluminium oxide disc (II): numerical calculation of the electric field for different points in the gas in the zone where PDs are expected to occur as a function of relative permittivity; applied voltage of 1 V.

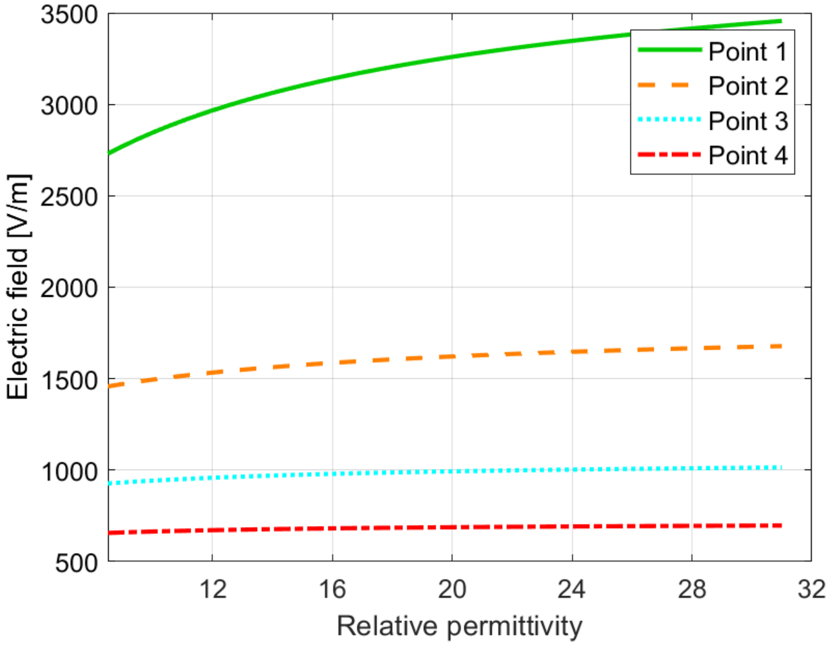

Figure 3.37. Aluminium oxide disc (III a): numerical calculation of the electric field for different points in the gas in the zone where PDs are expected to occur as a function of relative permittivity; applied voltage of 1 V.

The electric field is the higher, the closer the point is situated to the triple junction. However, the calculated values should only be seen as a rough estimate since simulation parameters such as mesh size influence the calculation.

On the basis of these results, a calculation of the percentage increase in electric field with relative permittivity was made for each of the defined points, see Figure 3.38 and Figure 3.39.

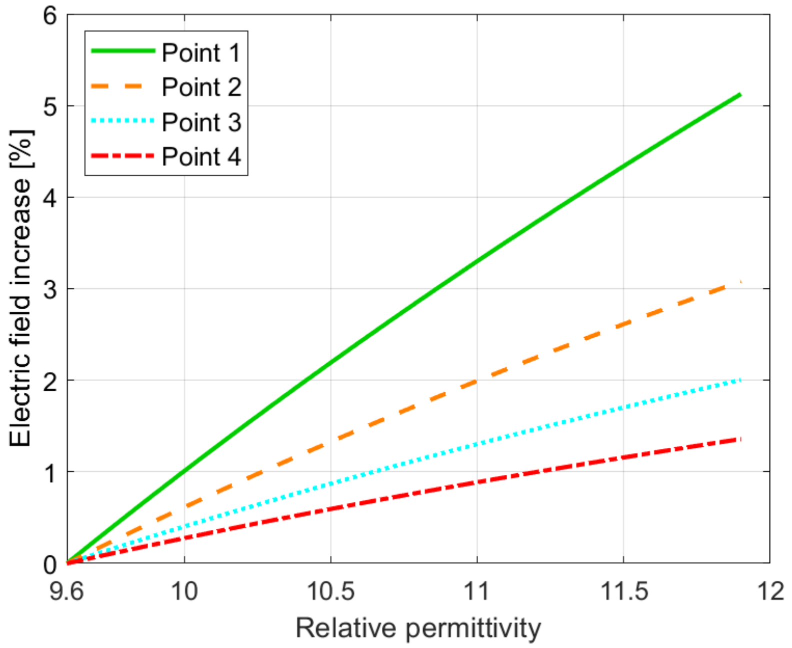

Figure 3.38. Aluminium oxide disc (II): numerical calculation of the percentage increase in electric field for different points in the gas in the zone where PDs are expected to occur as a function of relative permittivity; applied voltage of 1 V.

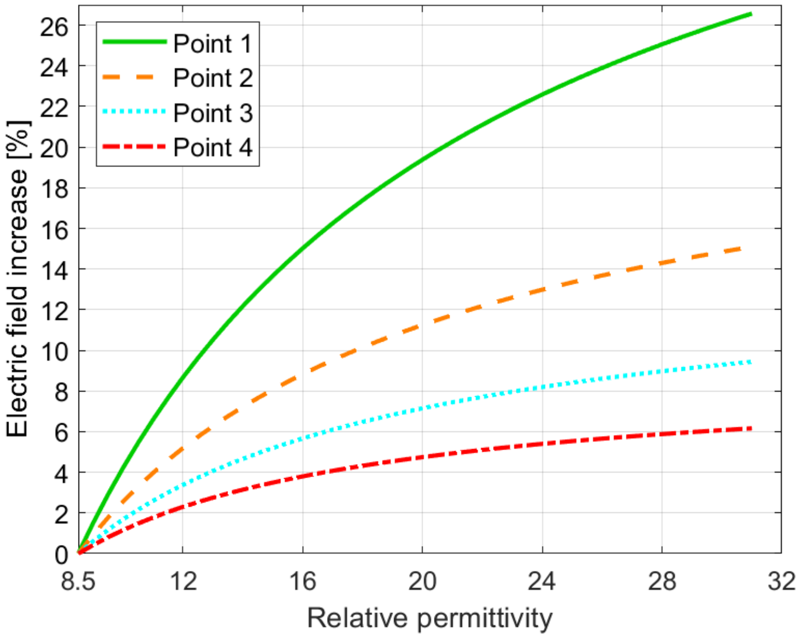

Figure 3.39. Aluminium oxide disc (III a): numerical calculation of the percentage increase in electric field for different points in the gas in the zone where PDs are expected to occur as a function of relative permittivity; applied voltage of 1 V.

The electric field in the gas increases with relative permittivity for both aluminium oxide discs, and the increase is, as expected, higher for the point closest to the triple junction. The much larger range of relative permittivity values considered for the aluminium oxide disc (III a) explains both the much stronger maximal reinforcement of the electric field using this material, and also the non-linear shape of the curve. This non-linear shape is due to the fact that, for large values of the relative permittivity, the main part of the voltage loss tends to be concentrated in the gas, so that the influence of variations of the relative permittivity are influencing only a minor part of it. It may also be considered that the curve for aluminium oxide disc (II) corresponds to the first part of the curve for disc (III a).

The percentage increase in electric field for both points on the right (blue and red) seems to be quite small, especially for aluminium oxide disc (II) (Figure 3.38). Although the calculations based on the numerical simulation predict that the PDs take place up to 1700 µm away from the triple junction, it seems to be unlikely that this is really the case since the increase in electric field at this position even at high temperatures up to 400 °C is low. Consequently, it may be assumed that the PDs rather take place in a zone closer to the triple junction than at the end of the calculated zone.

Despite the qualitative character of the calculations based on these numerical simulations, it can clearly be seen that an increase in relative permittivity leads to a reinforcement of the electric field in the gas near the triple junction thus facilitating PD activity. Hence, the changes in relative permittivity are mainly responsible for the decrease in PDIV (and PDEV) with temperature beyond the effect of gas density.

3.6.2 Influence of changes in volume resistivity on PDIV

According to the results shown in Figure 3.27, the volume resistivity decreases with temperature thus leading to a quicker charge evacuation at elevated temperatures. This effect can be illustrated by the reduction of the stability time constant t of the charge deposited on the solid insulator surface, which is equal to the product of the volume resistivity ρ by the permittivity $\varepsilon_r \cdot \varepsilon_0$ of the insulator:

$$t = \rho \cdot \varepsilon_r \cdot \varepsilon_0 \tag{3.6}$$

The stability time constant varies depending on the moment when the current, which is used to calculate the volume resistivity, is measured. Table 3.6 shows for different temperatures the calculated stability time constants based on different current measurement moments (which result in different volume resistivities): after 10 ms (current value estimated based on the slope of the measured current over a few seconds after applying the voltage; this value is of interest since an important quantity of charge may evacuate in this time span), after 3 s (first measurement point) and after 20 min (stabilised current value; mean value over the last five minutes when voltage is applied). For each temperature, the corresponding relative permittivity at a frequency of 50 Hz is considered.

Table 3.6. Stability time constant *t* of the charge deposited on the solid insulator surface for different temperatures and different current measurement moments.

***T* [°C]**	***t* [s] (*I* after 10 ms)**	***t* [s] (*I* after 3 s)**	***t* [s] (*I* after 20 min)**
20	112.35	194.63	600.57
80	90.06	351.41	855.91
150	28.48	151.26	697.66
200	19.2	81.65	449.31
250	7.27	38.79	137.64
300	3.69	9.79	20.93
350	1.52	2.14	4.80
400	0.3	0.51	1.08

The decreasing stability time constant leads to an enhanced partial discharge activity. In context with the PDIV detection procedure, as presented in section 3.2.2, it was defined that, if a discharge was detected over a 10 s time period at a given voltage, the voltage was maintained during 30 s, expecting 30 discharge events detected to assess a PDIV value. Hence, with enhanced partial discharge activity, it is more likely to detect a discharge within 10 s. Therefore, the voltage is more often applied during 30 s which consequently increases the probability to reach the criteria to retain the applied voltage as the PDIV. This finally leads to a reduction of the observed PDIV.

Although the presented values of the stability time constant indeed support the idea of a higher partial discharge activity thus leading to a lower PDIV with temperature, the main effect therefore remains the increase in relative permittivity. The calculated values of the volume resistivity and consequently of the stability time constants rather include already the effect of increased relative permittivity with temperature. Further, the stability time constants were calculated for a relative permittivity at a frequency of 50 Hz although the measurement of the volume resistivity was carried out at an applied DC voltage. Consequently, the shown values only support qualitatively the idea of an increase in partial discharge activity.

The not expected increase of the stability time constant between ambient temperature and 80 °C is due to a measurement incertitude in this temperature range.

3.7 Influence of oxidation

It is clear from the former sections that the increase in relative permittivity with temperature is an important factor to account for the decrease in PDIV (and PDEV) at elevated temperatures. For instance, the more pronounced increase in relative permittivity with temperature starting from 300 °C (see Figure 3.30) may explain that in Figure 3.21, the PDIV curve corresponding to 350 °C is clearly detached from that obtained at 300 °C. However, a greater difference between the curve at 350 °C and that at 400 °C should have been expected, given the strong corresponding increase in relative permittivity.

To explain, at least partly, this discrepancy, the oxidation of the surface of the tungsten electrode used for the experiments can be evoked, since it must be taken into account that some air leaked in during the experiments. This was observed during some preliminary tests regarding the gas-tightness of the vacuum chamber before the measurement series of PDIV and PDEV were started and before the neoprene gasket was added. Figure 3.40 shows as an example the temperature of the heating element and the gas pressure inside the vacuum chamber as a function of time before any measures were taken to improve the gas-tightness of the vacuum chamber.

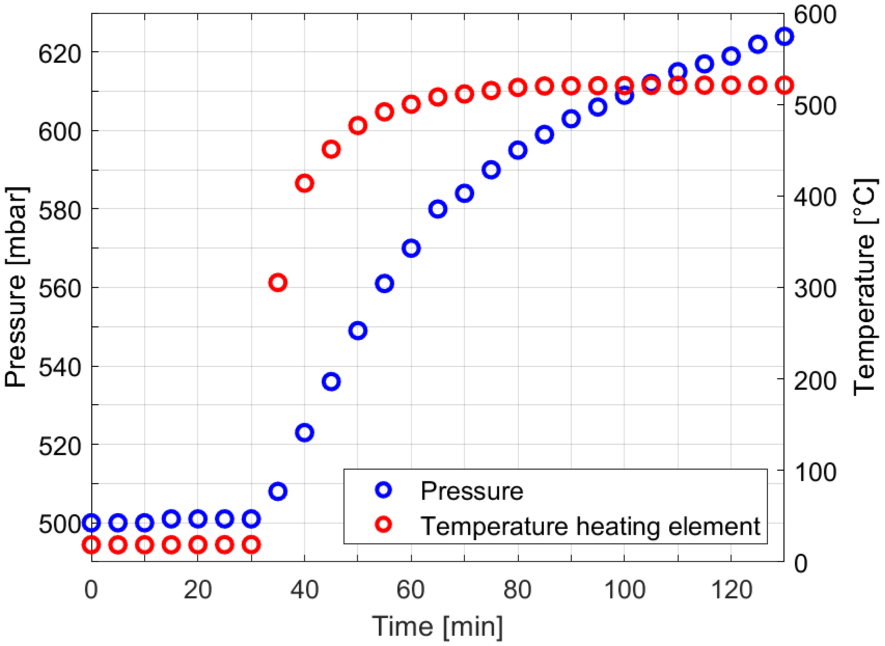

Figure 3.40. Gas pressure and temperature of the heating element as a function of time during a gas-tightness test of the vacuum chamber.

The heating element was heated from ambient temperature up to 500 °C and during the heating time, the gas pressure was measured. Over the first 30 minutes without heating, the gas pressure inside the vacuum chamber, which was set to 500 mbar, remained almost constant. An increase of only 1 mbar during 30 min at ambient temperature was observed thus demonstrating gas-tightness under these conditions. During the heating time (approximately 50 minutes, in Figure 3.40 between minute 30 and 80) from ambient temperature up to 500 °C, the gas pressure increased according to the ideal gas law. However, after the heating element reached a constant temperature, the increase in gas pressure continued linearly over time since atmospheric air leaked in the vacuum chamber.

Although the vacuum chamber was purged with nitrogen three times before each experiment to eliminate sources of uncertainty on the composition of the gas such as outgassing of materials with elevated temperature, the gas-tightness default of the vacuum chamber at elevated temperatures resulted in a formation of a tungsten oxide layer on the surface of the tungsten electrode. Figure 3.41 shows the lower surface of the tungsten electrode, which is in contact with the aluminium oxide disc, at its initial state (a), after one (b), and several (c) heating cycles up to 500 °C at 500 mbar.

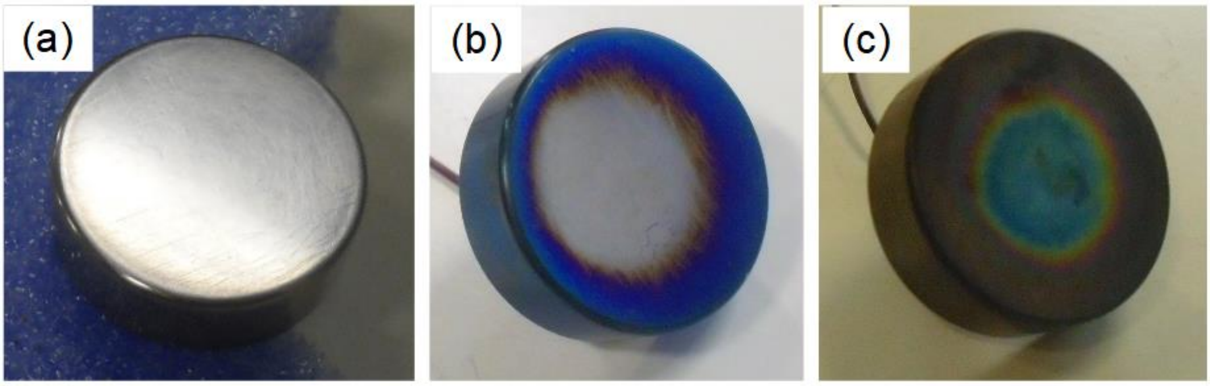

Figure 3.41. Lower surface of the tungsten electrode at its initial state (a) and after one (b) and several (c) heating cycles up to 500 °C at 500 mbar.

A bluish tungsten oxide layer is visible on the surface of the tungsten electrode after exposure to 500 °C, covering almost the entire electrode except a zone on the lower surface which was protected from oxidation and therefore retained its silverly colour as in the initial, non-oxidised state. After several heating cycles up to 500 °C, the oxidation has increased, and the previously protected zone was covered with the bluish tungsten oxide layer whereas the oxide layer on the remaining surface had a brownish colour.

Based on the observation that the vacuum chamber at high temperatures was not perfectly gastight, thus leading to the described oxidation, several measures were adopted to make the vacuum chamber more gastight. For example, the high vacuum grease on the gasket of the vacuum chamber as well as on the feedthroughs was renewed, a weight was put on the lid of the vacuum chamber, the feedthroughs were better screwed, and PTFE tape was added at critical points where possibly atmospheric air could leak in, etc. Despite all these measures, no real improvement of the gas-tightness was reached. Finally, a supplementary, large gasket made of neoprene was added beneath the lid of the vacuum chamber which made it in effect more gastight; the pressure in the vacuum chamber increased by only a few millibars at a stable, elevated temperature. Nevertheless, oxidation could not be avoided completely (after one temperature cycle up to 400 °C, the surface state of the tungsten electrode resembled to picture (b) in Figure 3.41 thus having it made necessary to clean the electrodes after each temperature cycle according to the procedure described in section 3.2.2. It was further decided to limit the temperature range for the experiments to 400 °C at its maximum even though the initial objective was to carry out the experiments up to 500 °C.

Apart from the visible effect of the oxidation, an XPS-analysis to characterise the composition of the tungsten electrode surface of a brand-new and an oxidised (in this case exposed to a temperature up to 400 °C during approximately three hours; corresponding to the surface state as shown in picture (b) in Figure 3.41) tungsten electrode was made. Table 3.7 shows the measured atomic concentration of tungsten and oxygen on the surface of the tungsten electrode before and after heating.

Table 3.7. Atomic concentration of tungsten and oxygen on the surface of the tungsten electrode before and after heating (3 h at 400 °C).

Tungsten electrode	Before heating	After heating
Tungsten	84,2 %	45,3 %
Oxygen	15,8 %	54,7 %

The values clearly indicate that the bluish coloured surface of the tungsten electrode after heating showed a higher atomic concentration of oxygen than of tungsten whereas tungsten largely predominated for the surface of the tungsten electrode before heating.

Remark: the hypothesis was made that the surface state of the electrode before heating corresponds to that of a polished/cleaned electrode which was used for the experiments carried out in this work.

Finally, these results of the analysis support the assumption that it may be possible that the tungsten oxide layer has an influence on the secondary emission processes through the increase of the electron work function (from 4.5 - 5 eV to 6 - 7 eV) of the electrode material [124], [125], resulting in an increase in PDIV.

This hypothesis is supported by results presented in Figure 3.42 where the PDIV of aluminium oxide disc (II) at 400 °C is plotted as a function of pressure. Three series of results are presented, corresponding to three increasing exposure times of the electrode to temperatures above 300 °C (350 °C and 400 °C) since oxidation effects were only observed for temperatures above 300 °C. At this point, it should be noted that the presented values in Figure 3.42 do not correspond to the results presented in section 3.3.

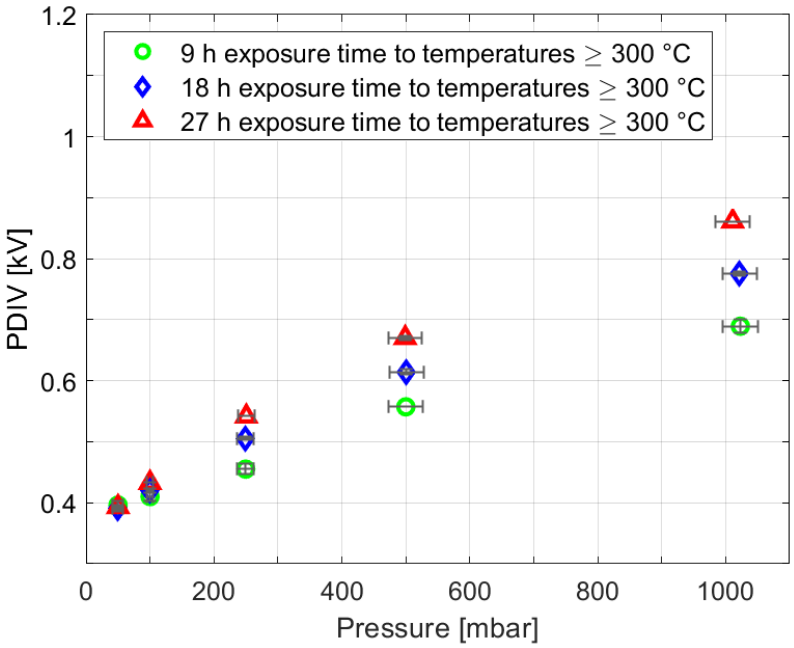

Figure 3.42. Aluminium oxide disc (II): PDIV at 400 °C as a function of gas pressure for increasing exposure time of the tungsten electrode to temperatures above 300 °C; nitrogen.

With increasing exposure time to high temperature (≥ 300 °C), the PDIV measured at 400 °C tends to increase. From 9 h to 27 h, a rise of 170 V in PDIV was observed at atmospheric pressure.

Therefore, the PDIV values of aluminium oxide disc (II) presented in Figure 3.15 and Figure 3.21 for temperatures above 300 °C are potentially overestimated even though the electrode surface was polished using a fine sandpaper (grain size of 22 µm) and then cleaned with alcohol using a precision wipe after each temperature cycle, so resulting in a 9 h maximum exposure time to temperature above 300 °C. The PDIV values therefore are shown in Figure 3.43.

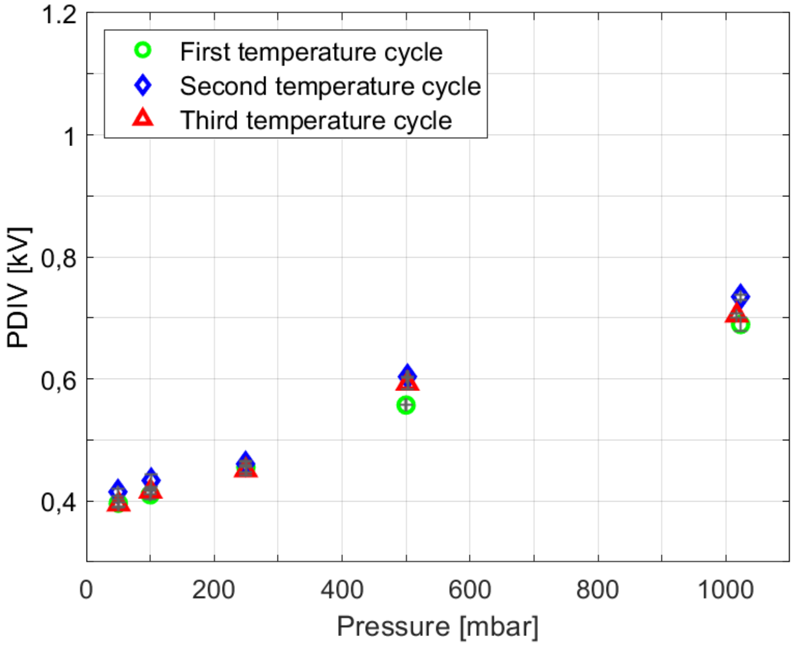

Figure 3.43. Aluminium oxide disc (II): PDIV at 400 °C as a function of gas pressure for three temperature cycles up to 400 °C and with polishing/cleaning the surface of the tungsten electrode after each temperature cycle; nitrogen.

When the tungsten electrode is polished/cleaned after each temperature cycle, there is no longer any difference in the PDIV value at 400 °C. On the one hand, this result should be expected since the exposure time of the tungsten electrode to temperatures above 300 °C is equal for all temperature cycles. On the other hand, this result does not mean that the oxidation is not at all present for shorter exposure times. The shown PDIV values, which correspond to that presented in section 3.3, rather include the effect of oxidation but owing to the polishing/cleaning after each temperature cycle, no difference in PDIV at 400 °C can be seen since the surface state of the tungsten electrode was approximately the same for all temperature cycles.

Remarks: at this point, it should be emphasised that the effect of oxidation, which happens increasingly at high temperature, is to increase the PDIV, whereas the goal of this work is to explain the *reduction* of PDIV at high temperatures in excess of what is expected simply due to reduced gas density. The oxidation phenomenon therefore is contrary to the proposed mechanism which is that the increased relative permittivity of the aluminium oxide insulator at higher temperatures results in higher local electric fields at a given applied voltage.

It should further be noted that the counter electrode was also affected by the oxidation. However, since it was located beneath the aluminium oxide disc, its surface was better protected and consequently, the effect of oxidation was less important than for the tungsten electrode. Nevertheless, the counter electrode was as well polished and cleaned after each temperature cycle to ensure the same experimental conditions for each experiment.

3.8 Summary

In this chapter, the influence of various temperature (ambient temperature up to 400 °C) and pressure (atmospheric pressure down to 50 mbar) conditions on partial discharge inception voltage (PDIV) and, to a lesser extent partial discharge extinction voltage (PDEV), for two different aluminium oxide discs of different purity was analysed.

For this purpose, the in chapter 2 presented experimental setup used for preliminary PDIV measurements was further developed and an experimental procedure including a standardised method for the PDIV/PDEV detection was defined to ensure consistent measurements.
Since the temperature was an important parameter in this work, the temperature control was detailly described. A discussion of the temperature gradient at the triple junction and its influence on gas density in the gas near the triple junction, where the discharges were expected to take place, was given. It has been shown that the gas density at the triple junction and in its near proximity in the gas could be considered as virtually the same which allowed a presentation of the obtained results only as a function of the gas density especially since the notion of distance became for the geometry under study meaningless.

The results of PDIV and PDEV were first presented for different temperatures as a function of pressure. It has been shown that both PDIV and PDEV increased with pressure and decreased with temperature which is in accordance with Paschen’s law and the gas density effect. The behaviour for both aluminium oxide discs was principally similar but the PDIV and PDEV for the less pure aluminium oxide disc varied in a larger range. Additionally, a steeper decrease in difference of PDIV has been observed for temperatures above 300 °C.
When plotted as a function of gas density, it became visible that, in contrast to the theory proposed by Dunbar which would expect that all curves of PDIV merge together, each series of temperature exhibited its own curve which was measured to be below the precedent one for the PDIV of a lower temperature. Both aluminium oxide disc types showed the same behaviour.

To explain the observed phenomenon, attention was then directed towards the role that the aluminium oxide disc could play when temperature was increased. For this purpose, influence of temperature on volume resistivity and relative permittivity was investigated.
It has been observed that, as expected, volume resistivity decreased with temperature while relative permittivity increased, especially for temperatures above 300 °C and whereby a more distinct increase was observed for low frequencies. Also, the increase in relative permittivity was observed to be much stronger for the aluminium oxide disc with lower purity grade.

Based on these results, the influences due to the changes in the dielectric properties with temperature on PDIV and PDEV were analysed. It could be stated that, on the one hand, the increase in relative permittivity leads to an increase of the local electric field in the gas near the triple junction thus lowering the PDIV. Consequently, this increase in electric field facilitates the inception of partial discharges and it is therefore logical that the PDIV (and PDEV) drop with temperature even more than may be expected simply due to the decrease in gas density. This result was further supported by a numerical simulation showing that the increase in relative permittivity led to an increase in the electric field in the zone where PDs are expected to initiate. Although the simulation supports the described phenomenon, it was discussed that it nevertheless remains qualitative. On the other hand, the decrease in volume resistivity enhances the PD activity thus making a PD detection more probable, which results in a lower measured PDIV.

Finally, the influence of oxidation on the measurement results was analysed. Although the experiments were carried out in nitrogen, an oxidation layer on the surface of the tungsten electrode was observed since air leaked in the vacuum chamber during the experiments at elevated temperatures. After an optical and an XPS-analysis of the tungsten electrode surface, the influence of the oxidation layer was discussed. It is suggested that its presence raises the electron work function; the PDIV consequently increases and for the presented results in this work, at least for the temperatures above 300 °C, PDIV values are potentially overestimated.

Chapter 4

Dependence of flashover voltage on various conditions of temperature and gas pressure/density

4.1 Introduction

The aim of this chapter is to analyse the influence of various temperature and gas pressure/density conditions on the flashover voltage (FOV) of the triple junction assembly studied in chapter 3. In this situation, the flashover does not result from a dielectric breakdown of the solid insulator, but from a discharge connecting the high voltage and the counter electrode by propagating along the surface of the solid insulator, as seen in Figure 4.1.

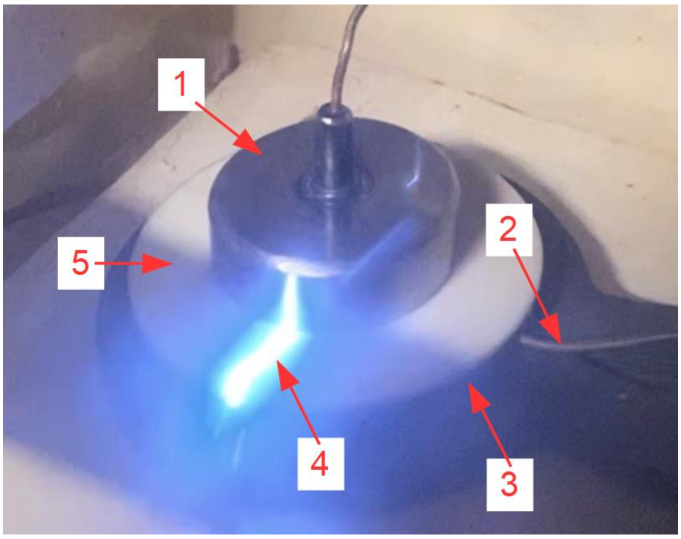

Figure 4.1. Experimental setup for the determination of FOV.
1 – Electrode connected to high voltage power supply (50 Hz AC), 2 – Wire connecting the counter electrode to ground potential, 3 – Counter electrode, 4 – Flashover, 5 – Solid insulator.

The minimum length of the discharge path leading to flashover can be evaluated assuming that the discharge propagates on the insulator surface to reach the counter electrode at ground potential. This pathway, using the same experimental setup as in the experiments presented in chapter 3, corresponds to a distance of 1.1 cm.

This chapter is not intended to be a complete and comprehensive study of the flashover phenomena. This was not possible due to lack of time, not all experiments could be repeated, and the experimental setup was not exploited in the same extensive manner as it was the case for the experiments presented in chapter 3. The aim was rather to observe the conditions under which the flashover phenomenon is established, and to propose mechanisms for interpreting these observations.

Section 4.2 gives an overview of the test setup as well as the experimental procedure for the determination of the FOV under varied conditions of temperature (ambient temperature up to 400 °C) and pressure (atmospheric pressure down to 50 mbar). A standardised procedure for FOV detection is given to ensure consistent measurements.

The results in chapter 3 have shown that the changes in the dielectric properties of aluminium oxide with temperature, in particular the increase in relative permittivity and the decrease in volume resistivity, lead in addition to the gas density effect to a supplementary decrease in PDIV. In this context, this chapter presents in section 4.3 the results for the FOV dependence on temperature and gas pressure/density using two aluminium oxide discs with different purities and two PTFE discs (the latter only at ambient temperature). The results are presented and briefly discussed as a function of gas pressure, including an analysis of other factors such as electrode oxidation, to verify whether they may affect the results. Then, the results are presented as a function of gas density.

Section 4.4 consists of a critical discussion of the obtained results. A comparison between the results of FOV and PDIV is made as well as between FOV for aluminium oxide and PTFE. Thereafter, considerations regarding Toepler’s first law as well as observations of flashover location at ambient temperature and varied pressures are presented and discussed, using a high-speed camera in combination with an oscilloscope recording current and voltage signals.

4.2 Experimental setup and procedure – FOV

This section describes the experimental setup and procedure. Just like the experiments regarding PDIV/PDEV, the purpose of these experiments was to analyse the influence of various conditions of temperature and gas pressure/density on FOV. Focus was also made on the flashover behaviour at the triple junction assembly.

4.2.1 Test setup

Since the experiments concerning the FOV were to a certain degree a further development of the PDIV/PDEV experiments presented in section 3.2, the same basic test setup could be used. The discharge analyser and the resistor in series with the high voltage amplifier were removed, and an oscilloscope, a CT-2 current probe (Tektronix current transformer CT-2: 1 mV/mA, < 0.5 ns rise time, approximately 6 ns delay time when connected to a P6041 probe cable) and a high-speed camera were added. Figure 4.2 depicts a schematic of the test setup and circuit.

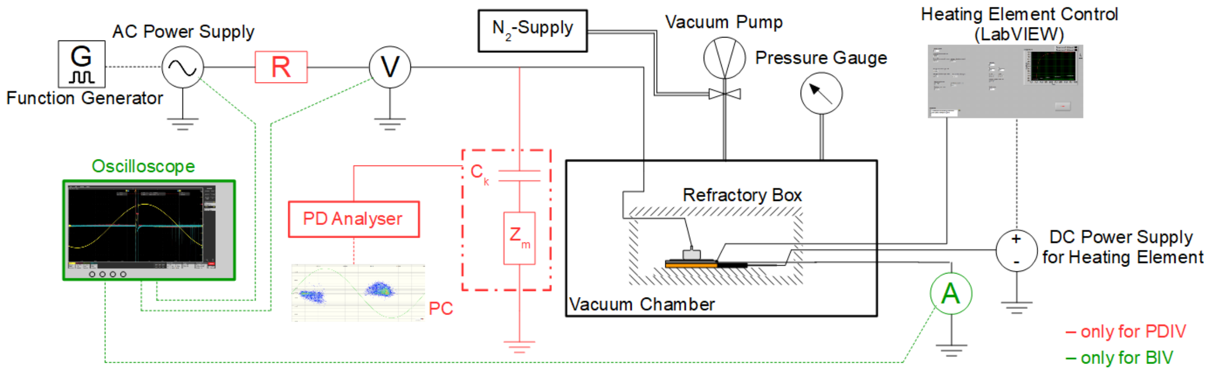

Figure 4.2. Schematic of the test setup and circuit to analyse the influence of various conditions of temperature and gas pressure/density on FOV.

The measurement of the FOV was made using the high voltage probe, the CT-2 current probe, and the current output of the high voltage power amplifier. All these components were connected to an oscilloscope.

First, the detection of the flashover was made by triggering the oscilloscope on the current signal of the CT-2 current probe. Since the discharge intensity changed with lower gas pressure/density values and with increase of temperature, the trigger level needed to be adapted for each pressure/density and temperature setpoint.

To avoid this reoccurring adjustment of the trigger level and to assure a correct and repeatable measurement, the triggering was changed to the signal of the load current of the high voltage power amplifier. This device featured a current trip mode which means that, as soon as a predefined peak current was reached, the high voltage power amplifier was interrupted. The peak current was adjusted with a potentiometer (0 % to 100 % of peak current, corresponding to 0 mA to 60 mA AC peak current) and here limited to 10 % (6 mA). Henceforth, this trigger method was used for FOV determination. Since the flashover could appear within both the positive and negative half cycle, the load current signal was split using a BNC T-connector and the trigger type was set to “logic” to trigger the oscilloscope either on the positive or the negative current value. In Figure 4.3, a screenshot from the oscilloscope shows an example for the flashover detection including the signals of the voltage, the current measured by the CT-2 probe (partial discharge current pulses visible before flashover), and the load current of the high voltage power amplifier.

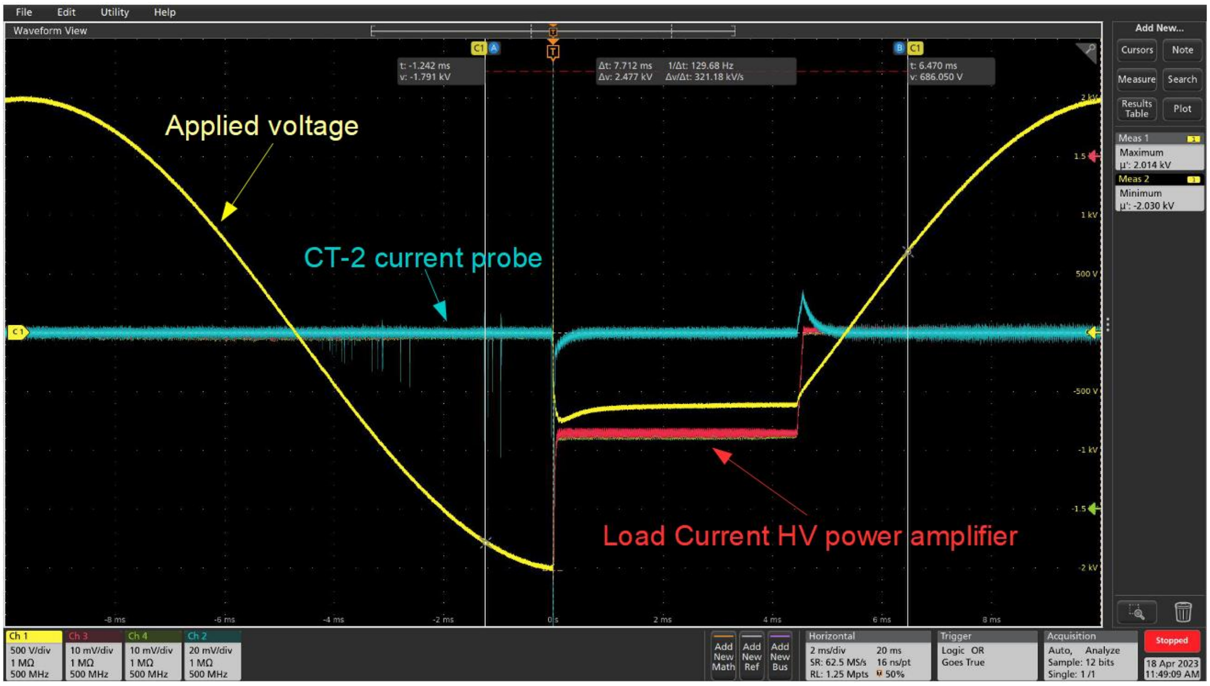

t: -1.242 ms
v: -1.791 kV

Δt: 7.712 ms 1/Δt: 129.68 Hz
Δv: 2.477 kV Δv/Δt: 321.18 kV/s

t: 6.470 ms
v: 686.050 V

Meas 1
Maximum
µ': 2.014 kV

Meas 2
Minimum
µ': -2.030 kV

Ch 1
500 V/div
1 MΩ
500 MHz

Ch 3
10 mV/div
1 MΩ
500 MHz

Ch 4
10 mV/div
1 MΩ
500 MHz

Ch 2
20 mV/div
1 MΩ
500 MHz

Horizontal
2 ms/div 20 ms
SR: 62.5 MS/s 16 ns/pt
RL: 1.25 Mpts 50%

Trigger
Logic OR
Goes True

Acquisition
Auto, Analyze
Sample: 12 bits
Single: 1 /1

18 Apr 2023
11:49:09 AM

Figure 4.3. Example for flashover detection - screenshot from the oscilloscope; 100 mbar; ambient temperature; nitrogen.

Figure 4.4 shows screenshots from the oscilloscope illustrating a typical situation observed during the FOV determination, here as an example for atmospheric pressure and ambient temperature, where the flashover duration is shorter than for lower pressure conditions.

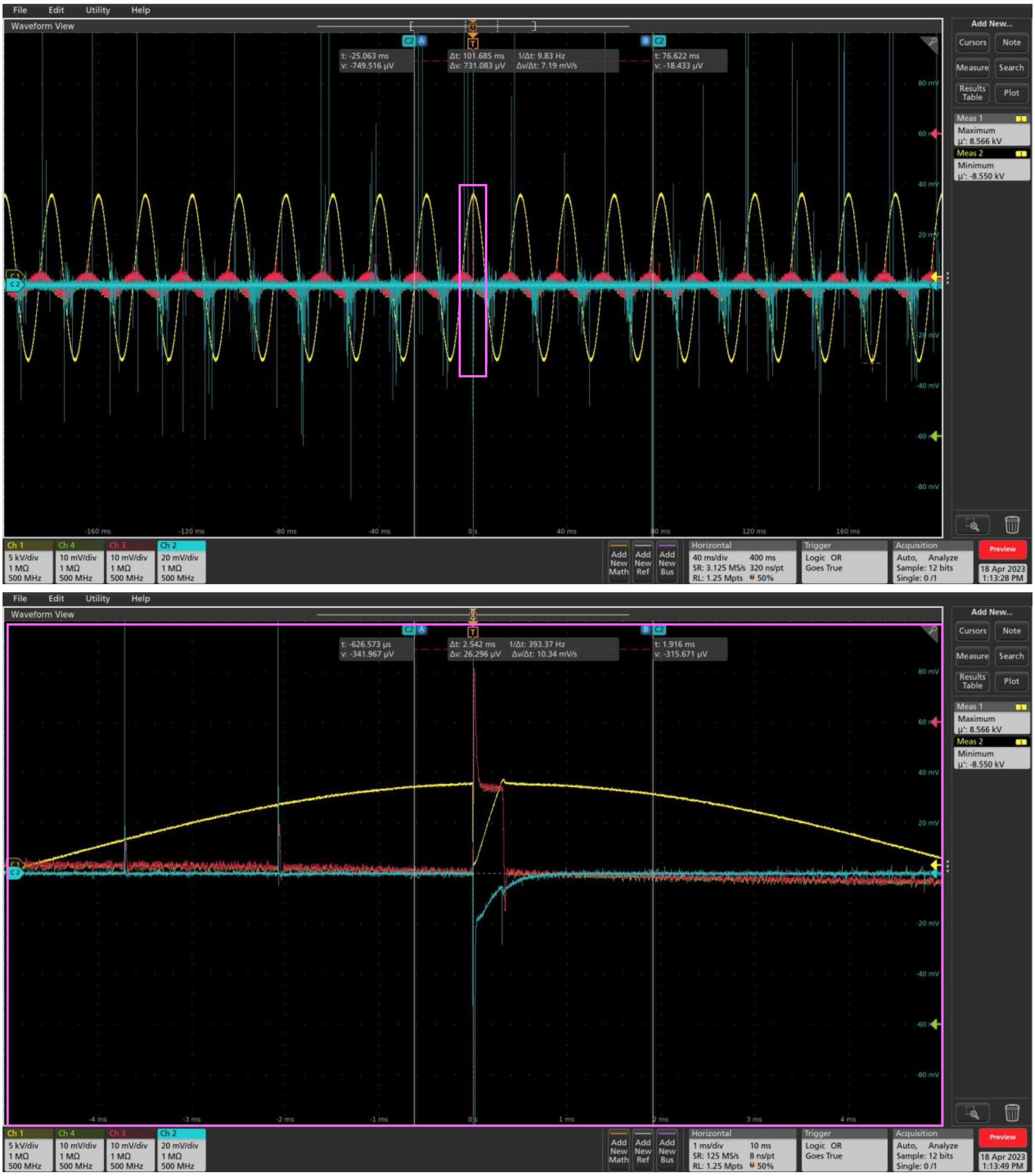

t: -25.063 ms
v: -749.516 μV
Δt: 101.685 ms 1/Δt: 9.83 Hz
Δv: 731.083 μV Δv/Δt: 7.19 mV/s
t: 76.622 ms
v: -18.433 μV

Meas 1
Maximum
μ': 8.566 kV
Meas 2
Minimum
μ': -8.550 kV

Ch 1
5 kV/div
1 MΩ
500 MHz
Ch 4
10 mV/div
1 MΩ
500 MHz
Ch 3
10 mV/div
1 MΩ
500 MHz
Ch 2
20 mV/div
1 MΩ
500 MHz

Horizontal
40 ms/div 400 ms
SR: 3.125 MS/s 320 ns/pt
RL: 1.25 Mpts 50%
Trigger
Logic OR
Goes True
Acquisition
Auto, Analyze
Sample: 12 bits
Single: 0 /1
18 Apr 2023
1:13:28 PM

t: -626.573 μs
v: -341.967 μV
Δt: 2.542 ms 1/Δt: 393.37 Hz
Δv: 26.296 μV Δv/Δt: 10.34 mV/s
t: 1.916 ms
v: -315.671 μV

Meas 1
Maximum
μ': 8.566 kV
Meas 2
Minimum
μ': -8.550 kV

Ch 1
5 kV/div
1 MΩ
500 MHz
Ch 4
10 mV/div
1 MΩ
500 MHz
Ch 3
10 mV/div
1 MΩ
500 MHz
Ch 2
20 mV/div
1 MΩ
500 MHz

Horizontal
1 ms/div 10 ms
SR: 125 MS/s 8 ns/pt
RL: 1.25 Mpts 50%
Trigger
Logic OR
Goes True
Acquisition
Auto, Analyze
Sample: 12 bits
Single: 0 /1
18 Apr 2023
1:13:49 PM

Figure 4.4. Example for flashover detection - screenshots from the oscilloscope; atmospheric pressure; ambient temperature; nitrogen. The lower screenshot shows a zoom of the flashover.

Before the flashover takes place, partial discharges, detected by the CT-2 current probe, can be seen. The load current of the high voltage power amplifier is relative to the applied voltage phase-shifted and exhibits, exactly like the current measured by the CT-2 current probe, a peak when the flashover takes place.

For a correct determination of the FOV, the 10 MΩ resistor in series with the high voltage power amplifier had to be removed, because the voltage drop across the resistor prevented the propagation of surface discharge to reach the grounded counter electrode and therefore increased the applied voltage necessary for the observation of a full flashover. It was verified that the high voltage power amplifier was able to withstand the FOV current, being protected against over-voltage and over-current conditions. The current trip mode had a delay to switch off the high voltage power amplifier 500 ms after the defined current value was exceeded.

Attempts were made to determine the arc's pathway between the electrodes. For this purpose, a high-speed camera (Photron Fastcam SA1.1) was installed in front of the vacuum chamber. The opaque refractory box was removed and only the triple junction assembly without the heating element remained inside the vacuum chamber. Consequently, for these experiments, only gas pressure was varied.

The high-speed camera could record up to 675000 images per second depending on image size; in this work, a frame rate of 3000 images per second was chosen so as to have an image size sufficient to record the entire flashover distance. The high-speed camera was manually triggered as soon as a discharge occurred, using “end mode” triggering, thus recording only the content directly before the trigger event. In the present instance, a time interval of 1.819 s before the trigger event was recorded which corresponded to 5457 images.

The control of the high-speed camera including the processing of the recorded images was done using the supplied software.

4.2.2 Experimental procedure

The same temperature and pressure setpoints were used as for the measurements of the PDIV/PDEV described in section 3.2.2. The same polishing/cleaning procedure of the tungsten electrode as well as purging of the vacuum chamber was also followed.

Since the distance between the cylindrical tungsten electrode and the grounded electrode is of importance to ensure repeatable measurements, the tungsten electrode was carefully placed in the centre of the solid insulator using an epoxy resin annulus with the same outer diameter as the solid insulator and the same inner diameter as the tungsten electrode. After centring the tungsten electrode, the annulus was removed.

To ensure consistent measurement of FOV, a standardised procedure, based on that which was applied for PDIV/PDEV determination, was defined but since the voltage range for FOV is higher than for PDIV/PDEV measurements, the step width was increased. Figure 4.5 shows the flowchart of the FOV determination procedure.

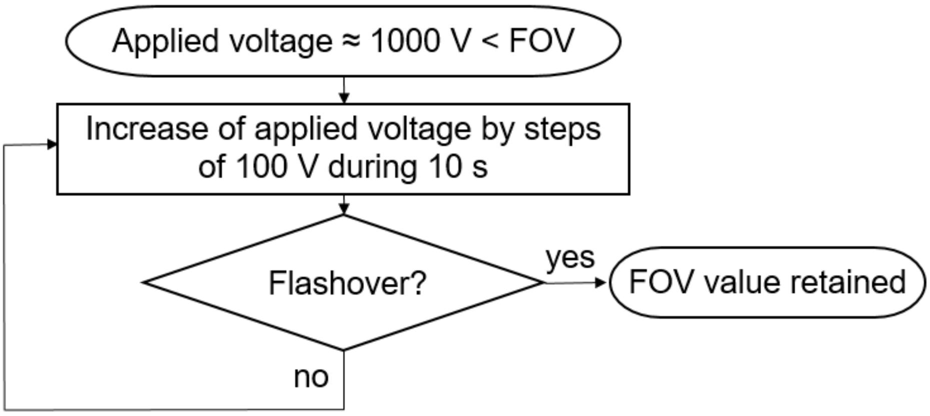

Figure 4.5. Flowchart of the FOV determination procedure.

The voltage applied to the triple junction assembly was first adjusted approximately 1000 V below the expected FOV (which came from previous measurements). Then, the voltage was raised by steps of 100 V and maintained during 10 s. As long as no flashover was detected, the voltage was raised again by 100 V. If the rise in voltage led to a flashover, the FOV was retained. Two voltages were noted: the AC voltage peak value of the last half cycle before the flashover occurred and the instantaneous value of the voltage at the flashover.

It was also defined that the FOV value was only retained when the applied voltage dropped by at least 80 % of its initial value. This criterion was necessary since the oscilloscope occasionally triggered before a “real” flashover occurred. In this case, a small voltage drop, which can be interpreted as a high-intensity discharge, was visible but the limit of the defined peak current to switch off the high voltage power amplifier was not exceeded.

In some cases, the defined peak current limit of the high voltage power amplifier was exceeded although the oscilloscope did not record a discharge. In this case, the measurement had to be repeated. It should be noted that this specific case occurred rarely.

4.3 Influence of various conditions of temperature and gas pressure/density on FOV

In this section, the experimental results, which were again made in a temperature range from ambient temperature up to 400 °C and for gas (nitrogen) pressures between 50 mbar and atmospheric pressure, are first presented as a function of gas pressure and then as a function of gas density for aluminium oxide discs (II), purity of 99.7 %, and (III a), purity of 96 %, as well as for PTFE discs (I) and (II) (at ambient temperature only).

4.3.1 FOV – dependence on temperature as a function of gas pressure

4.3.1.1 Aluminium oxide disc (II) – purity of 99.7 %

The influence of temperature on FOV was first measured according to the procedure defined in section 4.2.2 using aluminium oxide disc (II) which has a diameter of 50 mm, a thickness of 1 mm and a purity of 99.7 %.
All experiments were made starting at ambient temperature, and then increasing up to 400 °C. For each temperature setpoint, the pressure was varied starting at atmospheric pressure and then pumping down gas to reach lower gas pressure values down to 50 mbar.

In Figure 4.6, the results for the FOV (peak value of the last half cycle of the applied AC voltage before flashover occurred) of aluminium oxide disc (II) and its dependence on temperature as a function of gas pressure are shown. Each data point was calculated from the average of 10 measurements: the FOV was measured five times consecutively for each pressure setpoint during a given temperature and each temperature was repeated twice. All error bars were calculated for a 1σ standard deviation. For the measured pressure values, the uncertainty of the pressure gauge, which depends on the pressure range, according to the manufacturer was additionally taken into account using horizontal error bars.

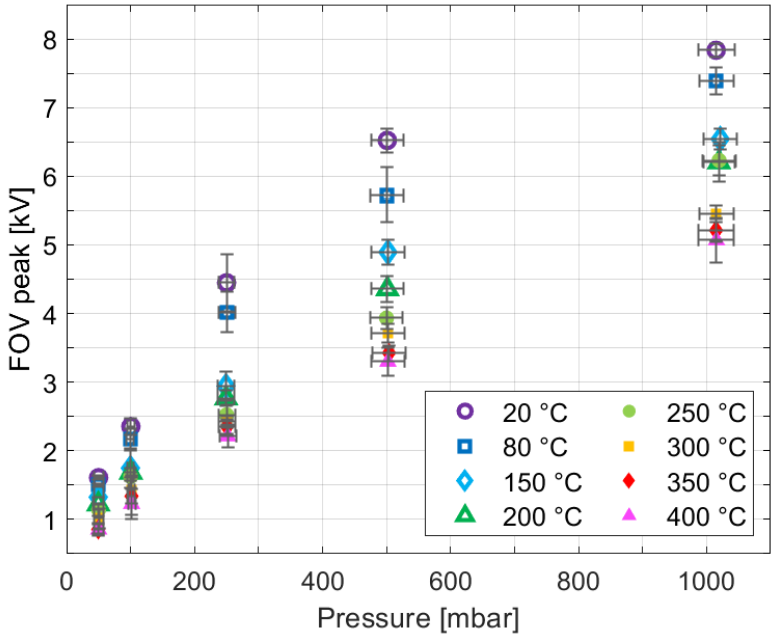

Figure 4.6. Aluminium oxide disc (II): FOV as a function of gas pressure for different temperatures; nitrogen.

FOV increases for all temperatures with gas pressure which is in accordance with Paschen's law. The results also show that an increase in temperature leads to a decrease in FOV which is logical according to the theory proposed by Townsend and thus the data correction method recommended by Dunbar as discussed in section 3.3.1.1.

However, the observed results are different than the results presented for the PDIV in section 3.3.1.1. On the one hand, the FOV curves seem to flatten with increased pressure. An explanation might be that the high voltage power amplifier triggered on a high-intensity discharge, which fulfilled the criterion to be considered as a flashover, without being a "real" flashover. Hence, the FOV at atmospheric pressure, where flashovers were observed with higher peak currents than at lower pressures, might be underestimated.

On the other hand, the difference between FOV at ambient temperature and at elevated temperatures differs for each pressure setpoint, see Figure 4.7 in which the drop in FOV at a given temperature compared to FOV at ambient temperature depending on gas pressure is shown as a function of temperature. To ease the lecture, only the mean values without error bars are displayed.

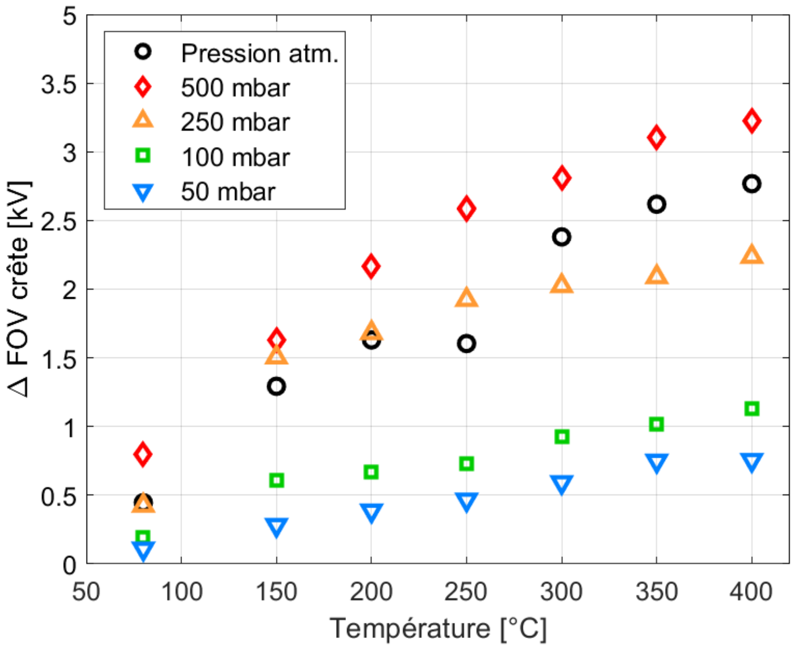

Figure 4.7. Drop in FOV compared to FOV at ambient temperature for different gas pressures as a function of temperature.

As it is the case for the PDIV, the drop in FOV increases with temperature and with pressure in the pressure range between 50 mbar to 500 mbar. However, the FOV drop is for all temperatures lower at atmospheric pressure than at 500 mbar and for 150 °C to 250 °C also lower than at 250 mbar. In other words, the range of FOV values at 500 mbar, and for several temperatures at 250 mbar, is larger than at atmospheric pressure. This can also be seen in Table 4.1 where the drop in FOV compared to ambient temperature is shown.

Table 4.1. Relative difference in FOV in % compared to the FOV at ambient temperature.

		Temperature [°C]						
		80	**150**	**200**	**250**	**300**	**350**	**400**
Pressure [mbar]	**1000**	- 6	- 17	- 21	- 20	- 30	- 33	- 35
	500	- 12	- 25	- 33	- 40	- 43	- 48	- 49
	250	- 10	- 34	- 38	- 43	- 46	- 47	- 50
	100	- 8	- 26	- 28	- 31	- 39	- 43	- 48
	50	- 7	- 18	- 24	- 29	- 37	- 47	- 47

For example, at 250 mbar, the value of the FOV at 400 °C is halved compared to the FOV at ambient temperature. However, at atmospheric pressure, the decrease only amounts to 35 %.

Remark: it should be noted that the presented results might be less reliable than the PDIV measurements. As described above, the results are based on the average of 10 measurements obtained during two experimental series, but the detection method was not exactly the same for both series. For the first one, the current signal recorded with a CT-2 current probe was triggered to obtain the FOV. Since a change in the flashover intensity with lower pressure was observed, which is also reported in [126], the trigger level needed to be adapted for each temperature and pressure setpoint which was not convenient regarding the repeatability of the experiments when both temperature and pressure were changed. To improve the reliability of the FOV determination, the signal of the load current of the high voltage power amplifier was used for triggering during the second temperature series, thus allowing to maintain the same trigger level for almost all temperature and pressure setpoints. Therefore, it may be assumed that this led to a higher reliability of the measurements when temperature and pressure were changed. However, each series, and hence each detection method, was made once without repetition. The results presented therefore show the average value of the FOV detected for two temperature series using different detection methods, each performed only once. Nevertheless, it should be noted that the two detection methods gave comparable results.

To verify if other factors may have influenced the results, two complementary experiments were carried out.

Concerning the results of the PDIV experiments, it has been shown that consecutive partial discharges (PDs) do not influence each other. However, this may not be the case for this experiment since the flashovers are more energetic than PDs. Therefore, a repetition of 30 flashovers in a row at ambient temperature and atmospheric pressure was made. The results of the obtained FOV (peak values) as well as its average value (dashed line) are shown in Figure 4.8.

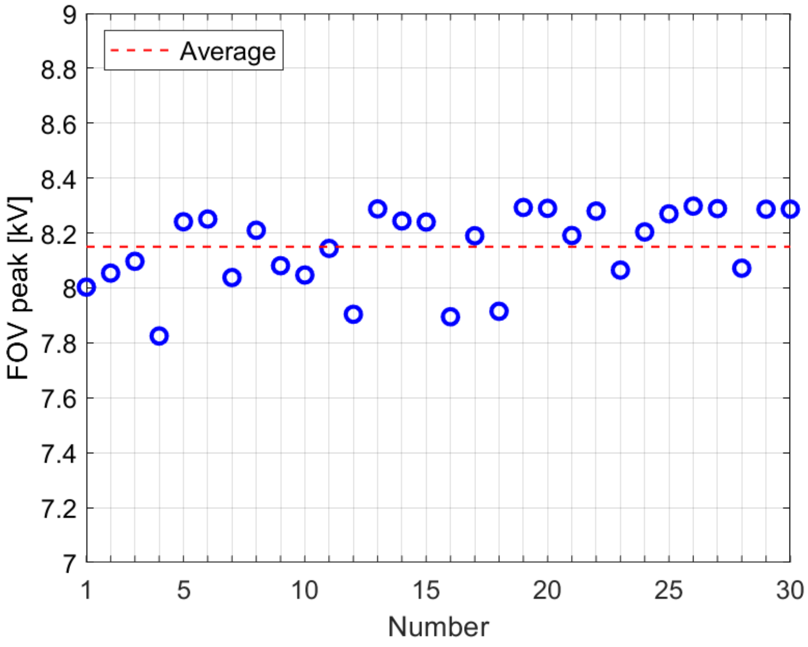

Figure 4.8. FOV values of 30 consecutive flashovers at ambient temperature and atmospheric in nitrogen; red dashed line: calculated average value.

No clear tendency towards an increase or a decrease in FOV over 30 consecutive flashovers can be seen. Consequently, it can be stated that the flashovers do not influence each other. Moreover, 26 out of 30 measured FOV values are situated within a range of approximately

± 140 V around the average value, corresponding to a 1σ standard deviation. This standard deviation is of the same order of magnitude of the standard deviation as for the results shown in Figure 4.6.

Apart from that, it has been shown that the oxidation of the tungsten electrode, especially at temperatures above 300 °C, may lead to an increase in PDIV, see section 3.7. To check whether a similar effect could be observed for the FOV, the latter was measured every 20 minutes for four hours at 400 °C first at atmospheric pressure and then in another experiment at 50 mbar. The surface of the electrodes was polished/cleaned between these two cycles. The results for the FOV (peak value) are shown in Figure 4.9 and are calculated as the average of three repetitions at each measurement time point. The error bars were calculated according to a 1σ standard deviation.

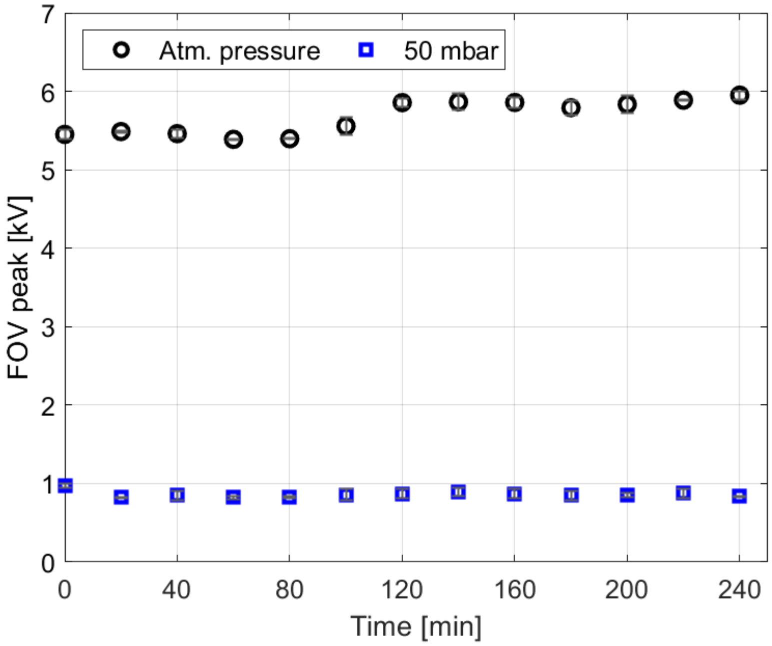

Figure 4.9. Repetitive FOV measurements at 400 °C for different pressures during a period of four hours; nitrogen.

It can be observed that the FOV at atmospheric pressure first remained nearly constant before an increase after 100 minutes became visible. In the following, the FOV remained at a constant level until the end of the experiment but was on average approximately 300 V higher than during the first 80 minutes.

In contrast, such an effect wasn't observed at 50 mbar: the FOV remained at a constant level over the entire four hours.

After the experiment at atmospheric pressure, a slight tungsten oxide layer on the surface of the tungsten electrode was visible which was not the case after the experiment at 50 mbar. Consequently, the influence of oxidation may, for this experiment, again explain the increase in FOV after a certain exposure time to elevated temperature. The absence of the oxidation layer at 50 mbar and the resulting unchanged FOV may be due to the fact that the lid of the vacuum chamber is sealed with a greater force exerted by the pressure difference with the exterior atmospheric pressure thus hindering the intrusion of air. Another possibility is simply that at 50 mbar there is about 20 times less oxygen available in the system even for equivalent levels of contamination from outside air.

Based on these observations, and taking into account the duration of one experiment at a given temperature was approximately two hours including five repetitions at each of the five pressure setpoints, the influence of oxidation should not be crucial for the measurement results presented in Figure 4.6. Since the experiment is carried out for various pressures starting at atmospheric pressure, the critical exposure time to see an influence of oxidation at elevated temperatures was not reached during these shorter experiments.

4.3.1.2 Aluminium oxide disc (III a) – purity of 96 %

The FOV was also determined using the less pure (96 %) aluminium oxide disc (III a), at ambient temperature and at 400 °C. The results for the FOV (peak value) are shown in Figure 4.*10* for both temperatures as a function of gas pressure. In contrast to aluminium oxide disc (II), each temperature cycle was made only once, and the data points are therefore calculated from the average of five consecutive measurements at each pressure setpoint. The error bars are again calculated for a 1σ standard deviation.

It should be noted that the geometry of aluminium oxide disc (III a) is different to that of aluminium oxide disc (II). It has a square shape (76.2 mm x 76.2 mm) which means that the creepage distance between the tungsten electrode and the counter electrode is higher which consequently leads to a higher FOV than for aluminium oxide disc (II).

The same detection method as for the second temperature cycle of aluminium oxide disc (II) (triggering using the load current of the high voltage power amplifier) was employed.

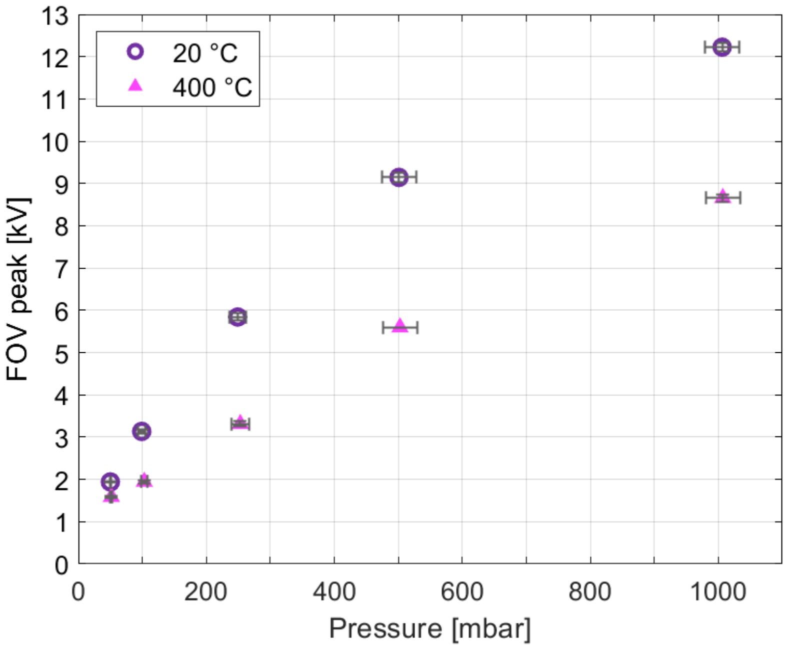

Figure 4.10. Aluminium oxide disc (III a): FOV as a function of gas pressure at ambient temperature and 400 °C; nitrogen.

The same behaviour as for aluminium oxide disc (II) can be seen, the FOV increases with pressure but decreases with temperature. A tendency towards a flatter curve at atmospheric pressure can also be seen but may be less distinct.

Since only one temperature cycle was made, the error bars concerning the FOV values are quite small.

4.3.1.3 PTFE discs (I) and (II)

The FOV was also determined using PTFE discs (I) and (II) which had the same geometrical dimensions as aluminium oxide disc (II). However, PTFE disc (I) was manually cut out of a PTFE sheet whereas PTFE disc (II) was produced by machine from a PTFE rod which had the same diameter.

The results for the FOV (peak value) at ambient temperature as a function of pressure for both PTFE discs can be seen in Figure 4.11. The error bars are calculated for a 1σ standard deviation, and the same detection conditions as for aluminium oxide disc (III a) (load current of the high voltage power amplifier as trigger for the FOV; only one series for each disc) were employed.

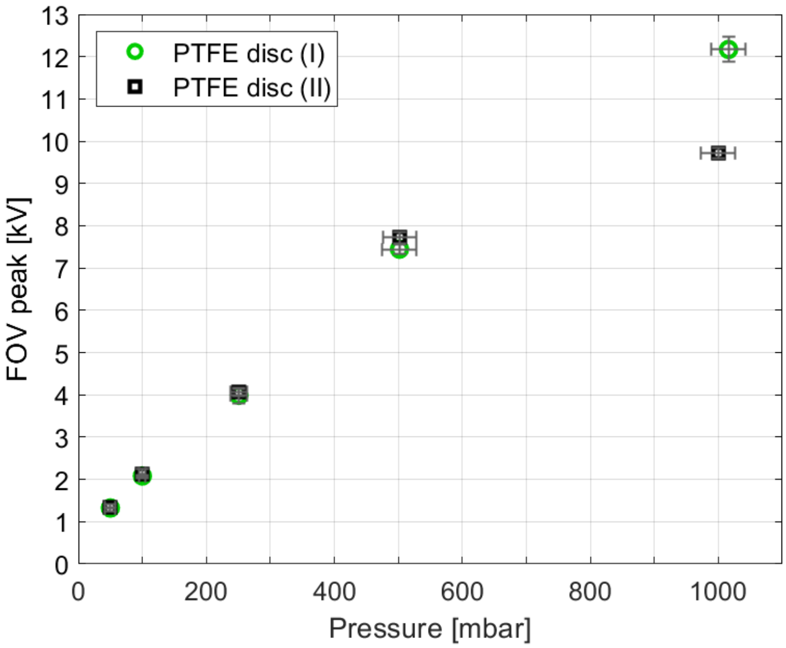

Figure 4.11. PTFE discs (I) and (II): FOV as a function of gas pressure at ambient temperature; nitrogen.

The data for both PTFE discs are in the pressure range of 50 mbar up to 500 mbar close to each other or rather identical which suggests a good repeatability of the FOV results of the same insulator material although two different discs were used.
However, the result at atmospheric pressure contrasts with this behaviour. As seen previously, the FOV flattens at atmospheric pressure for PTFE disc (II) whereas this is much less the case for PTFE disc (I).

4.3.2 FOV – dependence on temperature as a function of gas density

As presented and discussed in chapter 3, plotting the results of PDIV as a function of gas density allowed to differentiate between the influences due to the gas density effect and those due to the changes in the properties of the aluminium oxide with temperature. Therefore, the results of FOV are plotted in this section as a function of gas density.

Since the distance between the tungsten electrode and the counter electrode and therefore the length of the discharge path is known, it would be possible to plot the FOV as a function of the product of gas density *N* and inter-electrode distance *d*. However, for the sake of comparability between PDIV and FOV measurements, the results for FOV are still plotted only as a function of gas density.

4.3.2.1 Aluminium oxide disc (II) – purity of 99.7 %

Figure 4.12 presents the results for the FOV (peak value) of aluminium oxide disc (II) depending on temperature and as a function of gas density. Since the FOV values are the same as in section 4.3.1.1, the calculation of the data points (based on the average of 10 measurements) as well as the error bars (1σ standard deviation) is the same. For ease of reading, all the points belonging to the same temperature are connected with a trendline (second-degree polynomial).

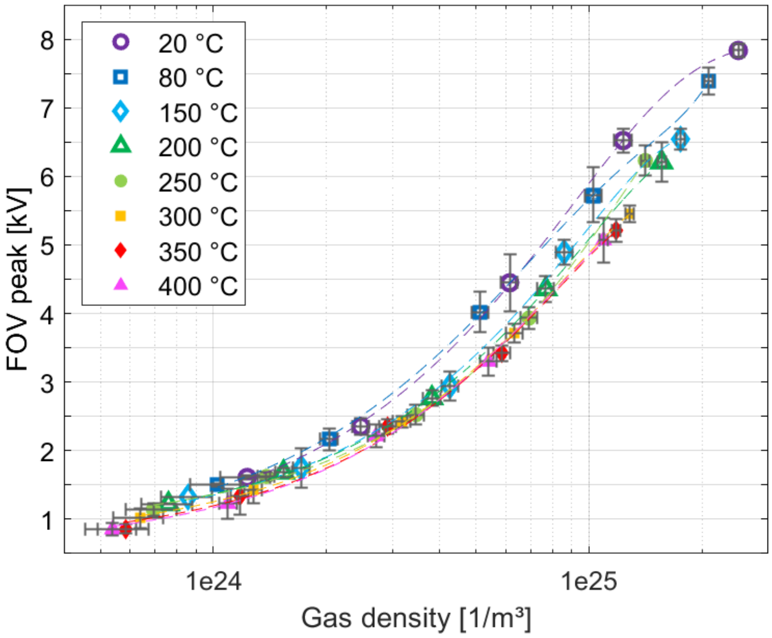

Figure 4.12. Aluminium oxide disc (II): FOV as a function of gas density for different temperatures; nitrogen.

A gap between the curves for the FOV at 20 °C and 80 °C and the other curves can be observed whereby this gap is more important for higher gas densities. This behaviour was already seen in Figure 4.6 and Figure 4.7 in terms of a high difference in FOV or rather a larger range of FOV for some pressures at these temperatures.

All the other data in the range of 150 °C to 400 °C, fall along the same curve (in particular when the error bars are considered), and the gap above 300 °C, as seen for the PDIV, is not observed.

4.3.2.2 Aluminium oxide disc (III a) – purity of 96 %

As for aluminium oxide disc (II), the results of FOV (peak value) for the less pure aluminium oxide disc (III a) at ambient temperature and 400 °C are also presented as a function of gas density. According to the obtained results, the data points are calculated on the average of five measurements and the error bars again for a 1σ standard deviation. Figure 4.13 shows the results.

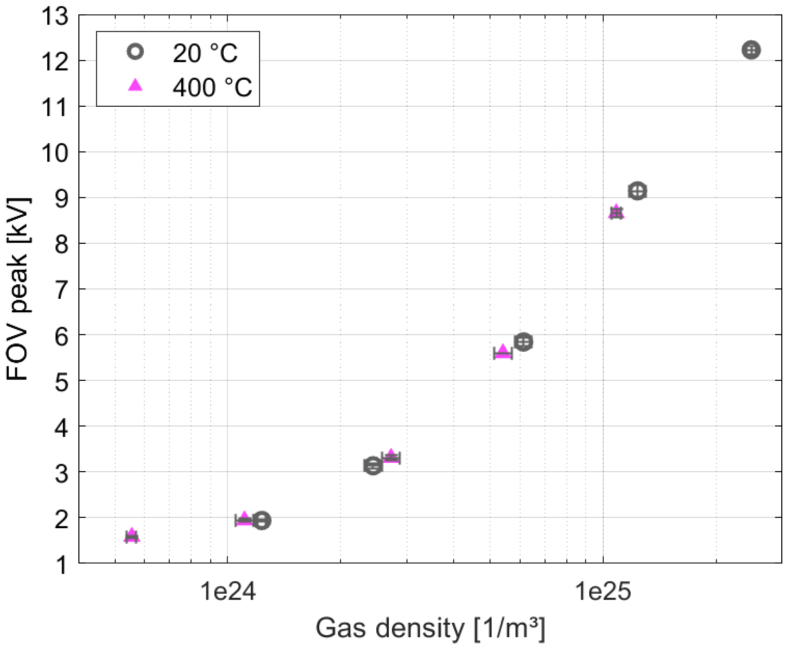

Figure 4.13. Aluminium oxide disc (III a): FOV as a function of gas density at ambient temperature and 400 °C; nitrogen.

The effect that both series coincide regardless of the temperature is even more obvious when only two temperatures are displayed. In contrast to Figure 4.12, a gap between the temperatures is no longer visible.

Remark: since the experiments for the PTFE discs were only carried out at ambient temperature, no presentation of those results as a function of gas density is pertinent.

4.4 Discussion of the results

In this section, the observed results are compared with those obtained for the PDIV and the influence or not of the changes in the dielectric properties of the aluminium oxide disc with temperature on FOV, as presented in chapter 3, are discussed.

In addition, a comparison of the FOV between the geometrically identical aluminium oxide disc (II) and the PTFE discs (I) and (II) is presented. Thereafter, an analysis of the flashover behaviour on the solid insulator surface is made.

4.4.1 Comparison between PDIV and FOV for aluminium oxide disc (II)

FOV shows the same trends as PDIV when plotted as a function of gas pressure. FOV decreases with temperature at a given gas pressure which is in accordance with the theory proposed by Dunbar. However, when the results for the FOV are plotted as a function of gas density, no difference between the curves for temperatures above 150 °C can be observed whereas for PDIV each temperature has its own curve (cf. Figure 3.21), see Figure 4.14, which compares both PDIV and FOV (peak values) along with their trendlines for each temperature.

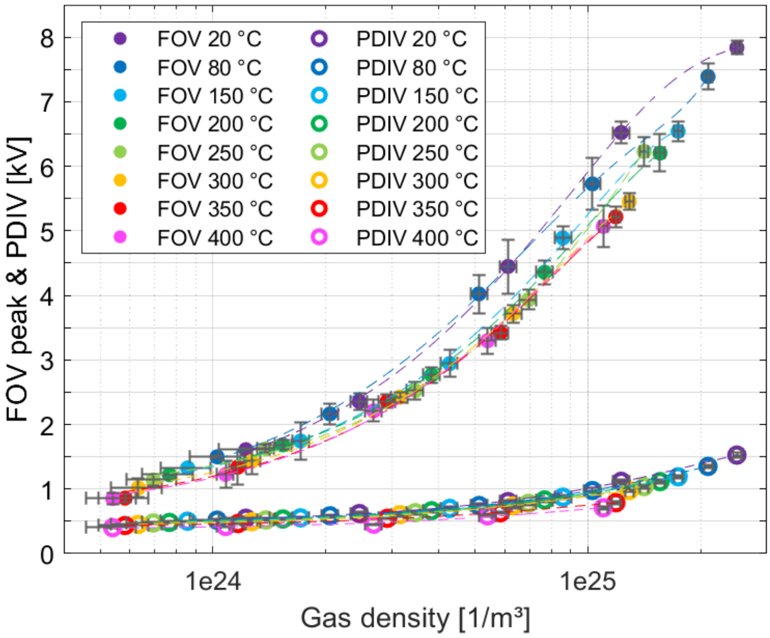

Figure 4.14. Aluminium oxide disc (II): FOV and PDIV for different temperatures as a function of gas density; nitrogen.

Figure 4.15 shows the average values of the difference FOV – PDIV (peak values), representing the intermediate case between partial discharge activity and flashover as discussed in section 1.4.2; this representation of the data appears to increase the merge of the curves for temperatures above 150 °C.

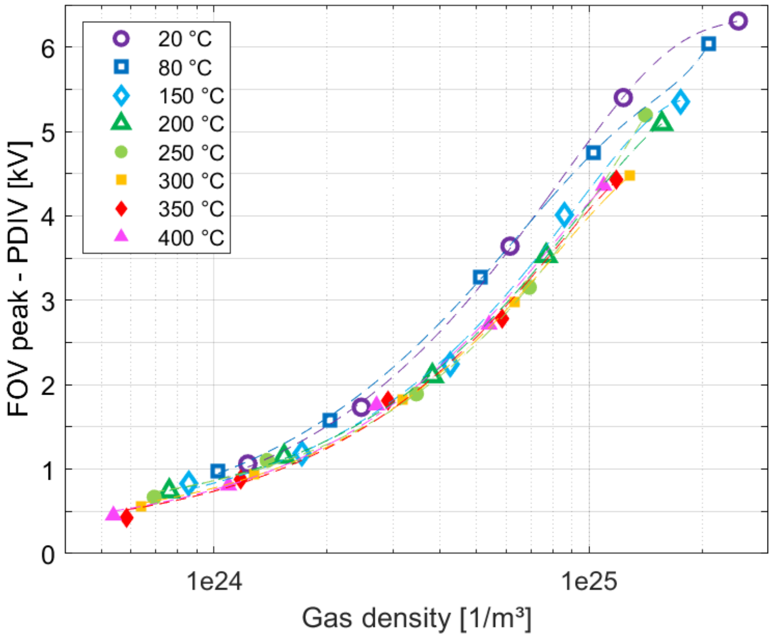

Figure 4.15. Aluminium oxide disc (II): difference of FOV – PDIV for different temperatures as a function of gas density; nitrogen.

It can be concluded that the changes in the dielectric properties of the aluminium oxide disc, especially the increase in relative permittivity with temperature thus leading to an enhancement of the electric field in the gas near the triple junction, do not affect the FOV. In particular, the trendlines above 150 °C fall along the same curve. This was not only seen using aluminium oxide disc (II), but also for aluminium oxide disc (III a), see Figure 4.13, where no difference between the curves at ambient temperature and 400 °C is visible even though the increase in relative permittivity for this aluminium oxide disc is even greater than for aluminium oxide disc (II).

At this point, it should be remembered that PDIV is correlated to the local electric field conditions (imposed by the 50 Hz AC power supply at the triple junction). If these conditions are compatible with a self-sustained discharge, detectable with the used instrumentation (with a threshold that depends, of course, on the experimental conditions), the corresponding applied voltage was retained as PDIV.

For FOV, the main point is that it is the propagation of discharges across the dielectric surface which leads to a transition to a flashover. In other words, it is the discharge that creates the local electric field at a distance far removed from the triple junction, with a dynamic corresponding to its propagation speed (and no longer simply the local field at the triple junction imposed by the 50 Hz AC voltage and the properties of the dielectric).

In the case of the FOV, assuming a mechanism involving the propagation of discharges on the surface of the insulator, the local electric field is created by the ionisation front (whereas at a distance from the triple junction, the imposed electric field is relatively weak). In the streamer model, the propagation velocity of this ionisation front is at atmospheric pressure in the order of 10^5 m/s [22]. Since the distance between the edge of the high voltage tungsten electrode and the grounded counter electrode amounts to 1.1 cm (for aluminium oxide disc (II) and PTFE discs), it can be estimated that this distance is covered by the discharge within 10^{-7} s which corresponds to a frequency of 10 MHz. As was shown in Figure 3.29 of section 3.5.3 and is found in the literature, the relative permittivity at or above 1 kHz remains relatively stable with respect to temperature. Hence, it can be assumed that there is no important increase in relative permittivity for the considered frequency which means that the relative permittivity does not influence the discharges leading to flashover (FOV). From this perspective, it is logical to observe a merging of the FOV curves at varying temperature.

However, curves for ambient temperature and 80 °C do not merge with the curves measured at higher temperatures. An explanation of this behaviour may be to assume another transition in the polarisation behaviour of the aluminium oxide, with a time constant in the order of 10^{-7} s below 80 °C. At a frequency of 50 Hz, it would follow the field and therefore would be included in the value of the permittivity, as well as at 10 MHz for temperatures above 100 °C, assuming a thermal activation of this process. According to this interpretation, the fact that, for the less pure aluminium oxide disc (III a), FOV curves coincide regardless the temperature, may also be correlated with the lower value of relative permittivity for this material at temperatures below 200 °C and frequencies below 1 kHz (8 - 8.7 versus 9.4 - 9.8 for aluminium oxide disc (II), see Table 3.3). At temperatures below 200 °C, this transition which is included in the permittivity at moderate frequencies for the purest sample, may be blocked by the impurities in a less pure material. These hypotheses need to be proven experimentally and are subject of future work.

4.4.2 FOV comparison between aluminium oxide disc (II) and PTFE discs

To confirm these hypotheses, FOV measurements were carried out at ambient temperature using a material whose relative permittivity differed significantly from that of aluminium oxide: PTFE. It was shown in section 2.5.3 that the PDIV for PTFE was higher than that of aluminium oxide and the aim of this section is to verify whether this is also the case for FOV. Figure 4.16 shows the results.

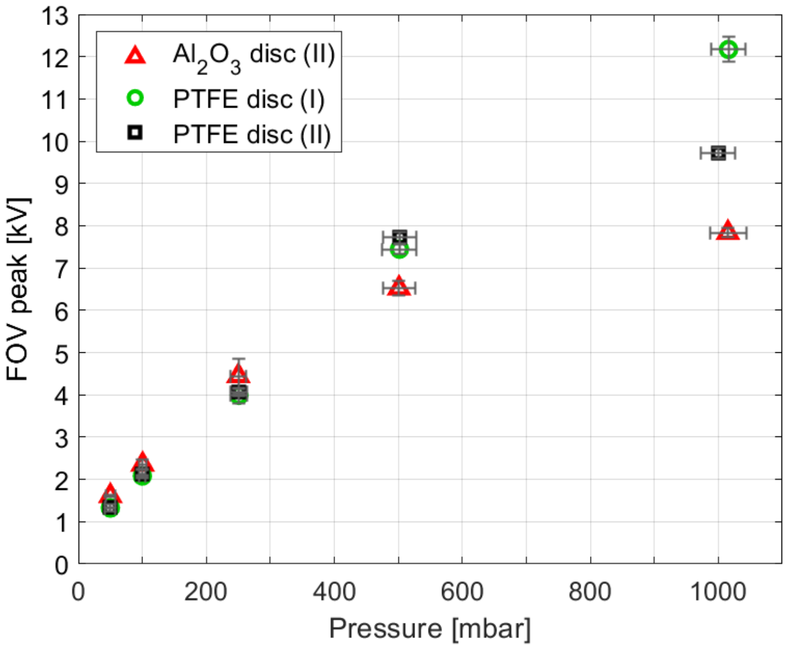

Figure 4.16. FOV as a function of pressure for two different insulating materials (PTFE and aluminium oxide) with same geometry; ambient temperature; nitrogen.

FOV for both PTFE discs is at 500 mbar and atmospheric pressure higher than for the aluminium oxide disc (II). However, for the other pressure setpoints, the FOV values are close to each other and for PTFE even inferior to those of aluminium oxide which is in contrast to the results observed for PDIV. In other words, an important difference in the solid insulator's relative permittivity does not lead to a clear difference in FOV. It should be noted that another study of FOV in air at and above atmospheric pressure using different electrode geometries and solid insulators with a relative permittivity range from $\varepsilon_r = 2$ to $\varepsilon_r = 9$ [127] showed that, independently of the electrode geometry (point parallel to the solid insulator, sphere electrode in contact with the solid insulator thus constituting a triple junction), the FOV tends to decrease with increased relative permittivity.

4.4.3 Consideration of Toepler's 1st law

According to the model of Toepler as presented in section 1.4.2, surface discharges first develop as surface streamer discharges propagating radially around the electrode circumference. Toepler observed that their radial propagation is proportional to the applied voltage and independent of geometrical and dielectric properties of the solid insulator. Consequently, a constant of proportionality *k* (see equation (1.15)) between the applied voltage for surface streamer discharges and their propagation length can be defined. For a positive surface streamer discharge, *k* amounts to 5.5 kV/cm and for a negative one to 11.5 kV/cm [11].

Assuming that the discharges for which FOV was determined were surface streamer discharges leading to flashover as soon as the counter electrode was reached, this constant of proportionality *k* can be calculated. This was made for ambient temperature and different pressure conditions and for the geometrically identical solid insulators (aluminium oxide disc (II) and PTFE discs). The distance *r* between the high voltage and the counter electrode corresponded to the shortest discharge path between both electrodes (1.1 cm).

It has to be specified that for this calculation, the difference between the absolute mean value of the instantaneous FOV and the PDIV was considered instead of the FOV peak value; with this approach, the distance over which discharges propagate from the high-voltage triple junction to the counter electrode is evaluated in relation to the voltage:

$$k = \frac{FOV_{instantaneous} - PDIV}{r} \tag{4.1}$$

The results are presented in Figure 4.17 showing *k* as a function of pressure. Error bars, based on a 1σ standard deviation, are added for PTFE since this series is based on the mean values of PTFE discs (I) and (II).

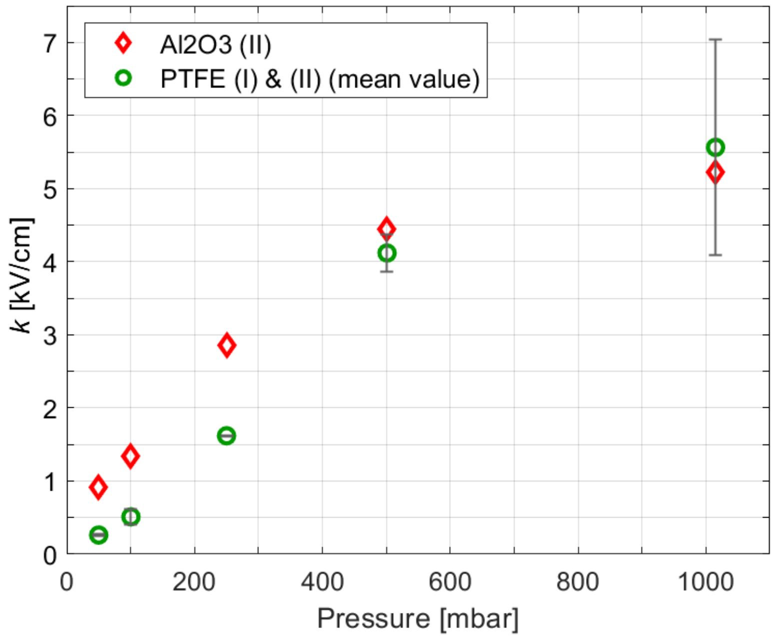

Figure 4.17. Calculated constant of proportionality *k* on the basis of Toepler's first law as a function of pressure for different solid insulator materials.

In comparison to *k* for a positive surface streamer discharge (5.5 kV/cm), the calculated mean values for aluminium oxide disc (II) (*k* = 5.23) and the PTFE discs (*k* = 5.56) at atmospheric pressure are similar (although with a high degree of measurement dispersion, as shown by the error bar) and compatible with Toepler's first law thus supporting the hypothesis that the flashover mechanism involves the propagation of discharges on the solid insulator surface. At 500 mbar, *k* values are lower than those at atmospheric pressure, but with a much smaller measurement dispersion. However, the assumption of discharge surface propagation remains a hypothesis and further calculation showed that the values of *k* tend to diverge for pressures below 500 mbar which may further question the hypothesis made insofar as for these pressures another mechanism may take place (e.g. Toepler's 2nd law). Further, Toepler's 1st law was only established for atmospheric pressure thus making further work for other pressure values necessary.

4.4.4 Analysis of the flashover using a high-speed camera depending on pressure

The results for FOV depending on temperature and gas density seem to be unaffected by the changes in the dielectric properties of the aluminium oxide disc with temperature. One hypothesis as mentioned in the previous section therefore is that the streamer propagation velocity is too fast to be influenced by these changes. However, since the comparison of the FOV between an aluminium oxide and a PTFE disc showed that there is no clear distinction between them although they have a different relative permittivity, other reasons than the propagation velocity of the streamer discharge may play a role. One reason for this behaviour might be the fact that the flashover does not propagate along the surface of the solid insulator but in the ambient gas. Further, the starting point of the flashover may not be at the triple junction.

To come to a better understanding of the flashover behaviour, a high-speed camera was used to obtain an image of the flashover. To obtain this image of the flashover, the opaque refractory box, in which the triple junction assembly was placed, had to be removed. Consequently, the experiments could only be made at ambient temperature but nevertheless for different pressure setpoints. The tungsten electrode was also slightly moved, to increase the probability of the flashover to occur always in the same zone, where the distance between the tungsten electrode and the counter electrode is the shortest. The displacement of the tungsten electrode was made in a way that allows a lateral view of the flashover.

Note that only the full flashover was detected with the high-speed camera but not its propagation. Hence, it could only be verified where the flashover ignited and if it propagated along the surface of the solid insulator or rather in the ambient gas.

Images were made in a range of atmospheric pressure down to 50 mbar using the aluminium oxide disc (II) and PTFE disc (II) with the same geometrical properties. A screenshot from the oscilloscope including the corresponding signals of voltage and current was also recorded.

It was observed that the flashovers showed similar behaviours regardless of the solid insulator used. Therefore, the following observations can be considered as valid for both aluminium oxide and PTFE discs. Several observations were made.

First, it was observed that, independently of the pressure setpoint, the flashover takes place in the first instance on the solid insulator surface, connecting the tungsten electrode/gas/solid insulator triple junction to the counter electrode/gas/solid insulator triple junction. This can be seen in Figure 4.18, where as an example an image of the flashover on the aluminium oxide disc at 500 mbar is shown.

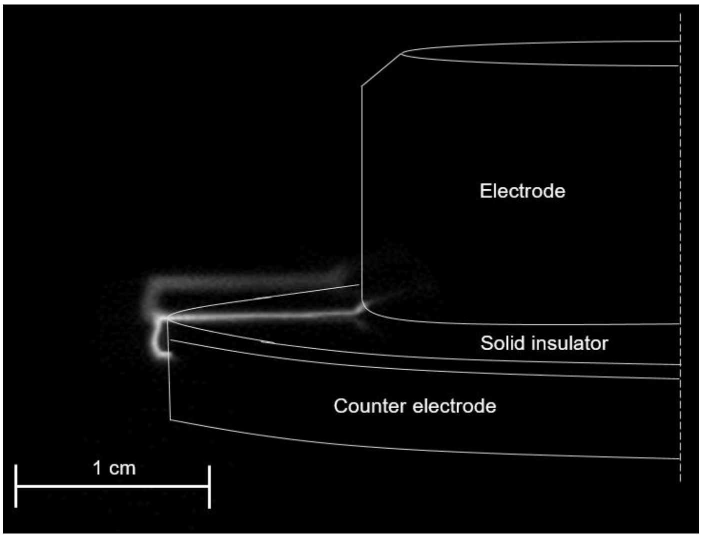

Figure 4.18. Flashover on the surface of aluminium oxide disc (II); 500 mbar; ambient temperature; nitrogen. Note: a reflexion of the flashover in the PMMA vacuum chamber can be seen behind the principal image.

Figure 4.19 shows the voltage drop and the increase in current (measured by the CT-2 current probe and the load current of the high voltage power amplifier) during the appearance of the flashover shown in Figure 4.18. The peak value of the voltage of the half cycle preceding the flashover is retained as the FOV.

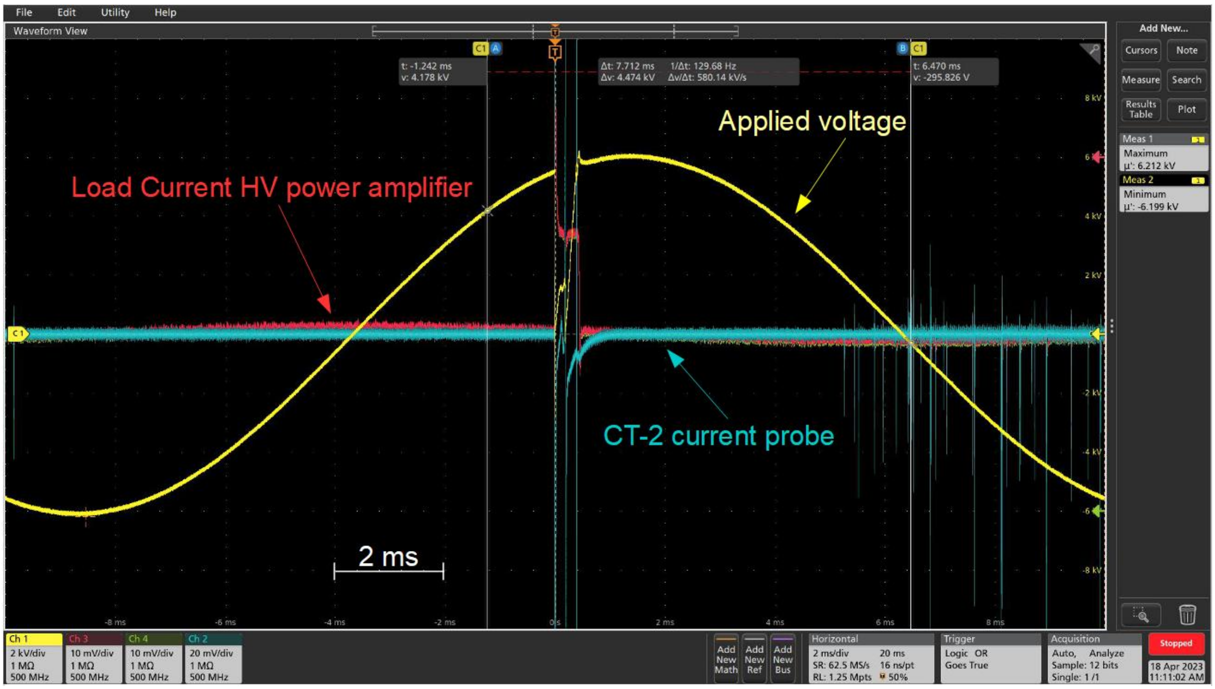

t: -1.242 ms
v: 4.178 kV

Δt: 7.712 ms 1/Δt: 129.68 Hz
Δv: 4.474 kV Δv/Δt: 580.14 kV/s

t: 6.470 ms
v: -295.826 V

Meas 1
Maximum
µ': 6.212 kV

Meas 2
Minimum
µ': -6.199 kV

Ch 1
2 kV/div
1 MΩ
500 MHz

Ch 3
10 mV/div
1 MΩ
500 MHz

Ch 4
10 mV/div
1 MΩ
500 MHz

Ch 2
20 mV/div
1 MΩ
500 MHz

Horizontal
2 ms/div 20 ms
SR: 62.5 MS/s 16 ns/pt
RL: 1.25 Mpts 50%

Trigger
Logic OR
Goes True

Acquisition
Auto, Analyze
Sample: 12 bits
Single: 1 /1

18 Apr 2023
11:11:02 AM

Figure 4.19. Voltage and current signals as displayed on the oscilloscope corresponding to the flashover showed in Figure 4.18.

Since this behaviour was seen for almost all flashovers independently of the pressure or the solid insulator material, these observations support the mechanism proposed in 4.4.2, suggesting that flashover results from the propagation of discharges along the surface of the insulator.

Although the flashover takes place in the first instance on the solid insulator surface, connecting the tungsten/gas/solid insulator triple junction to the counter electrode/gas/solid insulator triple junction, it has been observed that the point of connection with the tungsten electrode tends to rise over time, see Figure 4.20.

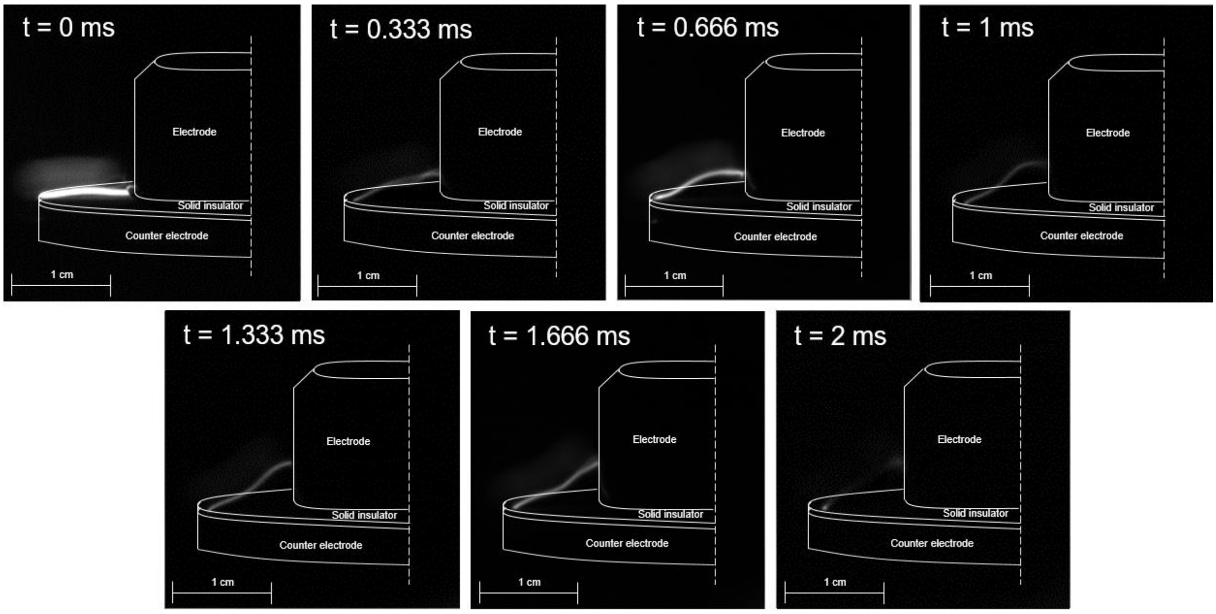

Figure 4.20. Flashover at the triple junction, rise of its base point; PTFE disc (II); 500 mbar; ambient temperature; nitrogen.

In the series of images, the flashover is observed to be initiated between the triple junctions of the high voltage electrode and the counter electrode on the surface of the solid insulator (first image, t = 0 s). However, in the following images (t = 0.333 ms to 2 ms), it can be seen that the base point of the flashover rises. This behaviour could be observed over the whole pressure range and regardless of the solid insulator material. This rise of the base point may already be seen in Figure 4.1, where, under consideration of the camera angle, a reflection of the discharge in the tungsten electrode should be seen. Since this is not the case and the used camera integrated several discharges, the assumed starting point at the top of the electrode and not at the triple junction may be ascribed to this effect.

This observation was made more often at pressures below 500 mbar since the flashover duration tended to increase with lower pressures. Hence, it became easier for the high-speed camera to record more images than at higher pressure. This does nevertheless not mean that this behaviour is exclusively present at low pressures, it could rather be stated that the used settings of the high-speed camera were less able to record this phenomenon at atmospheric pressure.

It may be conceivable that the rise of the base point is due to the accumulation of charges on the surface of the solid insulator. The charges deposited on the solid insulator surface during the first instant (see Figure 4.20, t = 0 s) may with further duration repel the discharge channel whose charges are of the same polarity as the charges on the solid insulator surface. It may also be possible that the rise of the base point is provoked by local thermal effects.

It has also been observed that the flashover duration increases as the pressure decreases. This can be seen in Figure 4.21, where, as an example, the voltage and the current signals for atmospheric pressure and 50 mbar are compared.

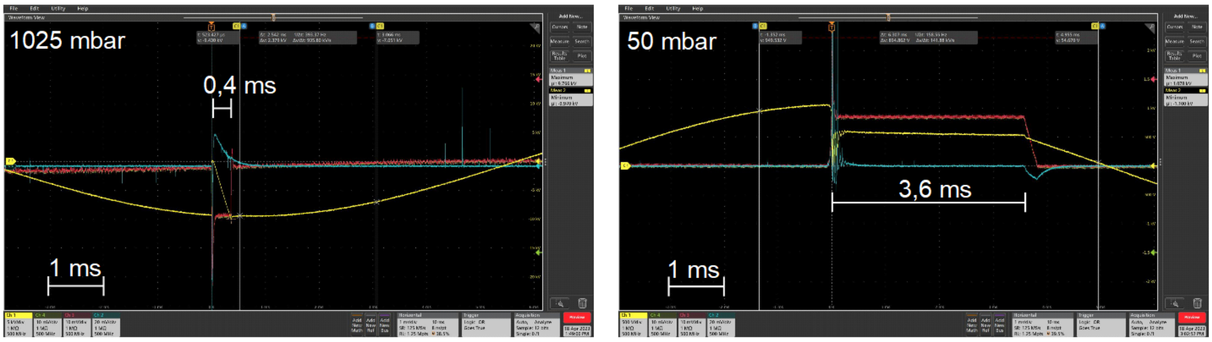

Figure 4.21. Comparison of the flashover duration at atmospheric pressure (1025 mbar; left) and 50 mbar (right); PTFE disc; ambient temperature; nitrogen.

The difference between the two pressures is evident. Both oscilloscope screenshots have the same time scale. The duration of the flashover at 1025 mbar amounts approximately to 0.4 ms whereas that of the flashover at 50 mbar approximately to 3.6 ms. Note that the duration was estimated by the aid of the load current of the high voltage power amplifier (measured current) since the CT-2 current probe is a current transformer thus suppressing the DC component. Table 4.2 shows the mean values of the flashover durations for several pressures.

Table 4.2. Mean value of the flashover duration depending on pressure.

Pressure [mbar]	**Mean value of flashover duration [ms]**
50	4.20
100	4.44
250	5.30
500	3.61
1000	1.36

The mean value of the flashover duration slightly increases from 50 mbar to 250 mbar before its duration clearly decrease with further increased pressure. This is consistent with the observations concerning PD where longer PD durations and pulse widths with lower pressure are reported [70], [71].

Remark: since for each pressure setpoint a different number of flashovers was recorded, the sample size is not the same. Therefore, the indicated durations of the flashovers should rather be seen as a rough order of magnitude than as an exact value. Nevertheless, the tendency towards a shorter flashover duration with higher pressure is noticeable.

Finally, it has also been observed that at the same pressure setpoint more than one flashover can take place, see Figure 4.22, which shows, as an example, the screenshot from the oscilloscope containing the voltage and current signals for two flashovers at the same pressure setpoint.

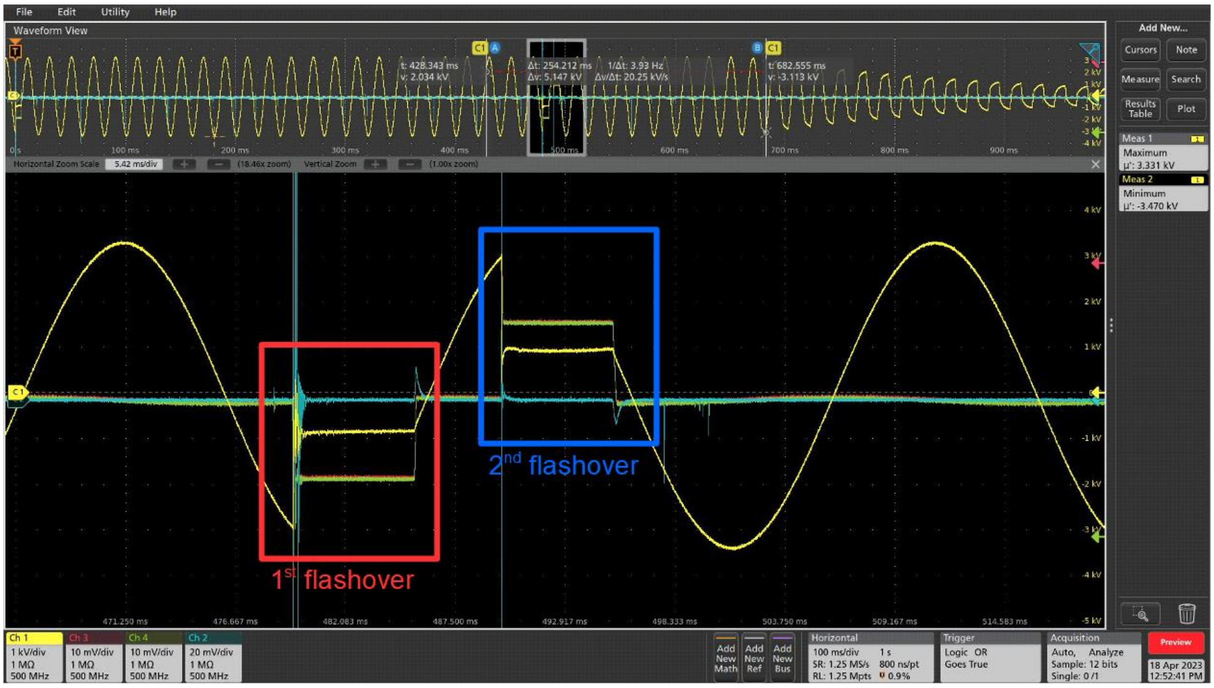

t: 428.343 ms
v: 2.034 kV

Δt: 254.212 ms
Δv: 5.147 kV

1/Δt: 3.93 Hz
Δv/Δt: 20.25 kV/s

t: 682.555 ms
v: -3.113 kV

Horizontal Zoom Scale 5.42 ms/div (18.46x zoom)
Vertical Zoom (1.00x zoom)

Meas 1
Maximum
μ': 3.331 kV

Meas 2
Minimum
μ': -3.470 kV

Ch 1
1 kV/div
1 MΩ
500 MHz

Ch 3
10 mV/div
1 MΩ
500 MHz

Ch 4
10 mV/div
1 MΩ
500 MHz

Ch 2
20 mV/div
1 MΩ
500 MHz

Horizontal
100 ms/div 1 s
SR: 1.25 MS/s 800 ns/pt
RL: 1.25 Mpts 0.9%

Trigger
Logic OR
Goes True

Acquisition
Auto, Analyze
Sample: 12 bits
Single: 0 /1

18 Apr 2023
12:52:41 PM

Figure 4.22. Screenshot from the oscilloscope containing the voltage and current signals for two flashovers at the same pressure setpoint; aluminium oxide disc (II); 250 mbar; ambient temperature; nitrogen.

This behaviour can be explained by the operating principle of the high voltage power amplifier. As soon as a flashover is detected, the voltage is switched off within 500 ms. In this period of time, the voltage first remains at a constant level and further flashovers can occur before the voltage is gradually switched off (see the declining amplitude of the applied voltage at the top on the right of Figure 4.22).

4.5 Summary

This chapter reported on the influence of various conditions of temperature (ambient temperature up to 400 °C) and gas pressure/density (atmospheric pressure down to 50 mbar) on the flashover voltage, FOV. This FOV corresponds to the inception voltage of a flashover taking place between the high voltage tungsten electrode and the stainless-steel counter electrode.

The results for FOV were first presented as a function of gas pressure. It has been shown that for both solid insulator materials (aluminium oxide and PTFE) the FOV increased with pressure and decreased with temperature (only investigated for aluminium oxide discs) which is in accordance with Paschen’s law and the gas density effect.
It has further been shown that consecutive flashovers did not significantly influence the FOV and that the effect of oxidation should not play a crucial role for the results since the critical exposure time, at which an influence may become visible, was not reached.

As shown in chapter 3, in addition to the gas density effect, the changes in the dielectric properties of the aluminium oxide cause the PDIV to decrease with temperature. In contrast, the FOV seems to be unaffected. When plotting the results for the FOV as a function of gas density, it was observed that, in contrast to the PDIV, the curves tended to merge, especially at temperatures above 150 °C. This effect was seen for both aluminium oxide discs, independently of their purity grade. Therefore, it has been proposed that the establishment of flashover relies on a mechanism of streamer-type discharge propagation on the solid insulator surface. This propagation, at a distance from the triple junction and therefore under relatively low imposed electric field conditions, would take place under the action of the gaseous space charge field at the head of the streamer. Given the streamer's velocity of propagation (and therefore the ionisation front), the corresponding frequency is of the order of 10 MHz, which would explain why changes in the dielectric properties of the aluminium oxide disc (for rising temperatures at high frequency) have no influence. Moreover, a comparison of the results for the FOV between the aluminium oxide disc and PTFE discs was made. It was expected that, according to the large difference in relative permittivity of these two materials, the FOV should be strongly different. Experimental results showed, especially for pressures below 500 mbar, FOV values close to each other for the two solid insulators. According to Toepler’s first law, a proportionality constant (homogeneous with an average electric field in the streamer column) was calculated for different solid insulators of identical geometry. Even though the calculated values were close to each other in a range from atmospheric pressure to 500 mbar, a difference was visible for lower pressures thus questioning the assumption of discharge surface propagation at these pressure conditions.

Finally, the behaviour of the flashover at ambient temperature and for different pressures in a range from atmospheric pressure down to 50 mbar was analysed using a high-speed camera in combination with the current and voltage signals recorded by an oscilloscope. It was observed that, independently of the pressure setpoint, the first flashover always established between the high voltage triple junction and the counter electrode triple junction along the surface of the solid insulator. When successive flashover events were accumulated, the point of connection to the high potential electrode tended to rise from the triple junction up along the side of the electrode. These observations have been made for both the aluminium oxide and PTFE discs and are independent of the pressure. Hence, the assumption that the flashover might propagate in the gas rather than on the solid insulator surface, thus reducing the likelihood of a difference in FOV between aluminium oxide and PTFE, could not be supported. At this point it can be concluded that the mechanism is based on the propagation of streamer discharges incepting at the triple junction and leading to a flashover after propagation along the solid insulator surface.

As already mentioned, the results presented in this chapter may not be as reliable as the results for the observations made on the PDIV. The main reason for this is that some series of measurements were only made once, such as the FOV of aluminium oxide disc (III a) or the influence of 30 consecutive flashovers on aluminium oxide disc (II), or twice, but with slightly different detection methods, as in the case of the aluminium oxide disc (II), or on two different samples of the same material, as in the case of the FOV for the PTFE discs. Hence, the results presented, and the assumptions made to explain them, may not be fully conclusive.

In addition, an analysis and a discussion of the polarity of the flashovers depending on temperature and pressure was made, see annex A.2.

Chapter 5

Conclusions and outlook

In the present work, an investigation of partial discharge and gas breakdown phenomena at a triple junction (gas/solid insulator/conductor) under various pressure and temperature conditions was made. The main objective was to come to a better understanding of these phenomena; focus was made on partial discharge inception voltage (PDIV) and, to a lesser extent, partial discharge extinction voltage (PDEV), as well as flashover voltage (FOV) in a gas pressure range from 50 mbar to atmospheric pressure and a temperature range from ambient temperature to 400 °C. Particular attention was paid to a solid dielectric material that could be used in this temperature range: aluminium oxide.
The results may be of interest for industrial applications featuring triple junctions exposed to severe environmental conditions such as high temperatures (e. g. nuclear sector) or low pressures (e. g. aeronautical sector).

In the first chapter, an introduction to the context as well as to the theoretical background relevant for the studies carried out in this work was given: physical mechanisms of the formation of electrical discharges including Paschen’s law, definition and classification of partial discharges and their detection methods, development of surface discharges including Toepler’s laws. For both partial discharges and surface discharges, a literature review discussing the influence of various parameters, such as pressure and temperature on partial discharges or insulator material on surface discharge propagation, was made. It is worth noting that most publications found in the literature on this subject concerned specific applications, and parameters such as pressure or temperature were in most cases considered separately or in a range limited to the specific requirements of the investigated application. Therefore, a more fundamental study including a wide range of temperature and pressure, as carried out in the present work, was of interest.

The second chapter first presented a general overview of the experimental setups necessary to reach the objectives of this study. The dielectric properties of the solid insulator materials (aluminium oxide, PTFE) were presented as well as the selection process of the aluminium oxide disc, which was used for many experiments, based on a comparison between two aluminium oxide discs from different suppliers regarding their surface roughness.
A functional test of the experimental setup forming the basis for all experiments, ensuring that its components worked properly, was used to carry out several preliminary PDIV measurements regarding the influence of geometrical and dielectric properties of the solid insulators on PDIV. The main results of these measurements, made at ambient temperature but with variable gas pressures, were:

- the PDIV increases with thickness of the solid insulator but decreases with relative permittivity.
- the presence of a metallic layer on the surface of the solid insulator in contact with ground potential does not affect PDIV whereas a noticeable increase in PDIV can be observed when the metallic layer is in contact with the high voltage electrode. This was due to the absence of a gaseous gap between the edge of the metallic layer and

the surface of the solid insulator thus resulting in higher required voltages to develop an electron avalanche leading to a discharge.

The third chapter presented the main results of this work: the dependence of PDIV/PDEV on various conditions of temperature and gas pressure.
To obtain consistent measurements, a standardised experimental procedure for the determination of PDIV/PDEV was defined, and a precise temperature control system for the further developed experimental setup was conceived. Considering that in the case of a triple junction the distance parameter was not pertinent (in contrast to a well-defined gas gap situation representable in the form of a Paschen curve), a presentation of the obtained results as a function of gas pressure only was found to be relevant.

The results of PDIV and PDEV for both examined aluminium oxide discs (purity of 96 % and 99.7 %) were first presented as a function of gas pressure. It has been shown that:

- PDIV and PDEV increased with pressure and decreased with temperature which is in accordance with Paschen’s law and the gas density effect.
- the behaviour of both aluminium oxide discs was similar but PDIV and PDEV for the less pure aluminium oxide disc varied in a larger range.
- above 300 °C, a larger difference in PDIV compared to that at ambient temperature was visible.

In the context of the existence of a temperature gradient between the triple junction and the gas in its proximity, where discharges are expected to take place, the temperature at the triple junction and approximately 2 mm away in the gas were measured and compared in steady state conditions. Little difference was observed, resulting in a negligible uncertainty in the calculated gas density. Hence, the gas density at the triple junction and in its near proximity were assumed to be the same. When plotted as a function of gas density, a decrease in PDIV for higher temperatures could be observed for both aluminium oxide discs, which is in contrast with the Townsend mechanism. This experimental result shows that the increase in electron mean free path does not alone explain the decrease in PDIV in the gas subjected to an increase in temperature at constant pressure. The insulator dielectric properties dependence with temperature had to be taken into account.

For this purpose, different dielectric measurements (volume resistivity, relative permittivity) were carried out. It has been observed that with temperature increase:

- volume resistivity decreased, especially above 200 °C.
- relative permittivity increased, especially above 300 °C.
- the increase in relative permittivity was more distinct for low frequencies.
- the increase in relative permittivity was much stronger for the less pure aluminium oxide disc (96 % purity compared to 99.7 % purity).

Using a numerical simulation of the electric field in the gas in proximity to the triple junction, it was shown that the increase in relative permittivity led to an enhancement of the local electric field in the gas near the triple junction, thus lowering the PDIV (and PDEV). In addition to the predominant influence of increased relative permittivity, the decrease in volume resistivity adds its influence by enhancing partial discharge activity.

Another phenomenon was also observed: the decrease in PDIV between 350 °C and 400 °C was smaller than between 300 °C and 350 °C although the increase in relative permittivity was higher. Formation of an oxidation layer on the surface of the tungsten electrode at temperatures above 300 °C, thus increasing electron work function, was invoked to explain this behaviour, and confirmed by optical as well as XPS analysis of the electrode surface. As a result, PDIV values for temperatures greater than 300 °C could potentially be overestimated compared to what should have been observed for an electrode with a unoxidized surface condition.

The fourth chapter dealt with study of the flashover voltage between the high voltage electrode and the grounded counter electrode (FOV) under temperature and pressure conditions identical to those used for the PDIV (PDEV) investigations. It was shown that FOV measurements exhibited rather stables values for the examined sold insulators. When plotted as a function of gas density, FOV measured for different temperatures (ambient to 400 °C) tended to merge, in particular for temperatures greater than 150 °C. This trend was observed for both aluminium oxide discs regardless of purity (96 % and 99.7 %) and is contradictory to the results obtained for the PDIV/PDEV. FOV seems to be unaffected by the changes in the dielectric properties of the aluminium oxide with temperature. At this point, it was hypothesised that flashover was actually a surface breakdown, involving a steamer-type surface discharge mechanism from the triple junction at high voltage potential. At atmospheric pressure, the propagation speed of the ionisation front (which locally and transiently creates the electric field responsible for the streamer propagation) corresponds to a frequency of approximately 10 MHz. At this frequency, the absence of any measurable influence of the solid insulator's change in permittivity is therefore not surprising.

At ambient temperature, when replacing the aluminium oxide by a lower permittivity PTFE disc, as expected, FOV was higher at 500 mbar and atmospheric pressure, but at lower pressures it was slightly inferior to FOV values obtained on aluminium oxide. In other words, strong difference in material relative permittivity again did not lead to a clear difference in FOV. In this context, Toepler's first law was considered, and the constants of proportionality *k* (kV/cm) were calculated for different solid insulators with the same geometry. For atmospheric pressure and 500 mbar, proportionality constants were close to each other thus supporting the assumption that the flashover mechanism involved the propagation of discharges on the solid insulator surface. Nevertheless, for lower pressures, this result was no longer confirmed, thus questioning the validity of this law for these pressure conditions.

In addition, the behaviour of the flashover at ambient temperature and at different pressures in a range from 50 mbar to atmospheric pressure was analysed using a high-speed camera in combination with the current and voltage signals recorded by an oscilloscope. Independently of the solid insulator material, it was observed that for all investigated pressure setpoints, the first flashover always ignited between the high voltage electrode and the grounded counter electrode along the surface of the solid insulator. This result supports the hypothesis of a mechanism based on discharge propagation on the solid insulator surface. Note that in the case of successive events, the point at which the flashover connected to the high voltage electrode tended to rise which may have been provoked by surface charges repelling the discharge or local thermal effects.

The overall objective of the present work was to come to a better understanding of discharge phenomena taking place at triple junctions under varied conditions of pressure and temperature.

The investigations made for PDIV (and PDEV) led to the main results of this work. In contrast, the presented results for FOV are much less distinct and reliable. The main reason for this is that, due to lack of time, the experimental setup was not exploited in the same extensive manner as it was the case for the experiments regarding PDIV/PDEV. Consequently, uncertainties remain concerning the proposed mechanisms which were, as well as the hypothesis, not fully conclusive.

Hence, future work is needed to come to a better understanding of these flashover phenomena.

In the first instance, systematic experiments should be carried out to refine the results for FOV as a function of dielectric material (aluminium oxide and PTFE) at ambient temperature, enabling a more robust statistical study, especially to explain the results obtained at ambient and 80 °C. Other materials could also be considered (such as glass or quartz). In addition, optical study of flashover in high temperature conditions shall be performed (not only at ambient temperature, as it the case in this work). For that purpose, the opaque material of the refractory box (porous aluminium oxide) could be replaced by a heat-insulating transparent material such as quartz.

In addition to resolving the uncertainties of the work presented here, a more physical approach should be adopted. Instead of using a cylindrical electrode, as was the case in the present work thus allowing a large degree of freedom in terms of the possibility for the surface discharges to develop in all directions, two point electrodes could be used. In this case, the streamer discharge would be expected to develop between the two points, thus fixing the electrode gap. It may further be envisaged to modify the location of the point electrodes towards the solid insulator. For example, the influence of the solid insulator on surface discharges or rather the FOV could be investigated by varying the distance of the point electrode from the solid insulator surface as it was shown by [102], but in addition to this with varied temperature conditions. Another possibility would be to vary the angle of the point electrode on the surface of the solid insulator to investigate if this influences the streamer propagation or the FOV. In these situations, the propagation of discharges along the surface of the solid insulator up to flashover, could be studied using fast optical emission spectroscopy to measure propagation velocities and access quantities such as electron density and nitrogen rotational temperature.

In a more general point of view, the range of pressure and temperature may further be enlarged. For example, high temperature fission chambers work in a pressure range of several bars [4]. Apart from that, the influence of voltage parameters, still in combination with varied temperature and pressure conditions, may be of interest since power electronic devices with high commutation frequencies are increasingly used, as for example in the “More Electrical Aircraft” application [2].

Annex

A.1 Mathematical description of the Townsend mechanism

For the purpose of a mathematical description of the Townsend mechanism, two coefficients were introduced:

- Townsend’s first ionisation coefficient *α* (also Townsend’s first avalanche coefficient)
- Townsend‘s second ionisation coefficient *γ* (also surface ionisation coefficient)

A.1.1 Townsend’s first ionisation coefficient *α*

Townsend’s first ionisation coefficient *α* describes the number of electrons that are generated by a single electron during an ionising collision with a gas atom or molecule per unit of length. It depends on the nature of the gas (ionisation energy, collision cross section), the electrical field strength (relative velocity while collision between the gas atoms or molecules) and the pressure (gas density, mean free path) [21], [22].
A mathematical description of Townsend’s first ionisation coefficient can be given considering the aspects presented hereafter [21], [22], [23], [31].

Due to the acceleration in an electric field, the seed electron travels a distance *dx*. Within this distance, it either collides with another gas atom or molecule, or it travels the distance without a collision. The probabilities for the first case, P_c, and complementary for the second case, P_{nc}, can be expressed as:

$$P_c\,(dx) = \frac{dx}{\lambda} \tag{A.1}$$

$$P_{nc}\,(dx) = 1 - \frac{dx}{\lambda} \tag{A.2}$$

For an ionising collision, the seed electron must acquire sufficient energy within its travelled distance *dx*. The condition for this is that no collision takes place. Therefore, equation (A.2) can for n_d travelled distances *dx* be written as:

$$P_{nc}\,(dx) = \left(1 - \frac{dx}{\lambda}\right)^{n_d} \tag{A.3}$$

With the total travelled distance *x*:

$$x = n_d \cdot dx \tag{A.4}$$

equation (A.3) becomes:

$$P_{nc}\,(dx) = \left(1 - \frac{x}{n_d \cdot \lambda}\right)^{n_d} \tag{A.5}$$

If the number n_d of travelled distances dx tends to be infinite, it follows:

$$P_{nc}\,(dx) = e^{-\frac{x}{\lambda}} \tag{A.6}$$

Finally, the probability P_i of an ionising collision can be calculated as the product of the two probabilities P_c and P_{nc}:

$$P_i = P_c\,(dx) \cdot P_{nc}\,(dx) = \frac{dx}{\lambda} \cdot e^{-\frac{x}{\lambda}} \tag{A.7}$$

Considering that Townsend's first ionisation coefficient α describes the number of electrons dN_E which are created during an electron avalanche by N_{SE} seed electrons along the distance dx:

$$dN_E = N_{SE} \cdot \alpha \cdot dx \tag{A.8}$$

equation (A.7) can be expressed as:

$$dN_E = N_{SE} \cdot \alpha \cdot dx = N_{SE} \cdot \frac{dx}{\lambda} \cdot e^{-\frac{x}{\lambda}} \tag{A.9}$$

Consequently, α can be defined as:

$$\alpha = \frac{1}{\lambda} \cdot e^{-\frac{x}{\lambda}} \tag{A.10}$$

In due consideration of the equations for the ionisation energy W_i (1.2), the mean free path λ (1.4), and the ideal gas law (1.7), the expression for α in equation (A.10) can be rewritten as:

$$\alpha = \frac{\sigma \cdot p}{k_B \cdot T} \cdot e^{-\frac{W_i \cdot \sigma \cdot p}{e \cdot E \cdot k_B \cdot T}} \tag{A.11}$$

In the case of a homogeneous electric field, the electric field strength E can be expressed as:

$$E = \frac{V}{d} \tag{A.12}$$

where V is the voltage and d the electrode gap distance thus leading for equation (A.11) to:

$$\alpha = \frac{\sigma}{k_B \cdot T} \cdot p \cdot e^{-\frac{W_i \cdot \sigma}{e \cdot V \cdot k_B \cdot T} \cdot p \cdot d} \quad \text{(A.13)}$$

The exponential increase of the electrons within the electric field during an electron avalanche can be illustrated considering equation (A.8) [21], [22]. With N_{SE} equal to N_1 seed electrons and assuming that α is in a homogeneous electric field constant, it can be written:

$$N_E = N_1 \cdot e^{\alpha \cdot x} \quad \text{(A.14)}$$

The term $e^{\alpha \cdot x}$ thus consolidates the exponential increase of the electron avalanche. Townsend's first ionisation coefficient α is usually expressed in cm^{-1}. For example, $\alpha = 3\ cm^{-1}$ can be interpreted as an average of three collisions per centimetre of electron travel leading to ionisation [34].

Remark: the ionisation coefficient α does not take into account attachment processes of electrons during the collision with less mobile molecules. This effect occurs especially in the presence of electronegative gases such as oxygen or sulphur hexafluoride (SF_6) and leads to a higher breakdown strength. The attachment may be described using an attachment coefficient η equal to the relative decrease of the number of free electrons per unit length. This coefficient depends on the nature of the gas, the pressure, and the electric field strength. An effective ionisation coefficient α_e may be defined to merge the ionisation and attachment processes:

$$\alpha_e = \alpha - \eta \quad \text{(A.15)}$$

The number of electrons after an electron avalanche can finally be written as:

$$N_E = N_1 \cdot e^{\alpha_e \cdot x} \quad \text{(A.16)}$$

Consequently, the formation of an electron avalanche is only possible when the effective ionisation coefficient is positive [21], [22].

A.1.2 Townsend's second ionisation coefficient γ

Considering N_1 seed electrons at the cathode (distance $x = 0$), an electron avalanche grows exponentially towards the anode ($x = d$ (electrode gap distance)) generating a number of electrons N_{1-} which can, under consideration of equation (A.14), be expressed as:

$$N_{1-} = N_1 \cdot e^{\alpha \cdot d} \quad \text{(A.17)}$$

Simultaneously, positive ions are generated whose number N_{1+} can be calculated as:

$$N_{1+} = N_{1-} - N_1 = N_1 \cdot e^{\alpha \cdot d} - N_1 = N_1 \cdot (e^{\alpha \cdot d} - 1) \qquad \text{(A.18)}$$

They are accelerated towards the cathode. Those having a kinetic energy superior to the work function of the cathode material will be able to release new seed electrons from it by energy transfer on the metal surface. Townsend's second ionisation coefficient γ, also known as surface ionisation coefficient, is defined as the mean number of secondary electrons generated by the impact of one single positive ion. Beside of the cathode material, it depends on the kinetic energy of the positive ions, the nature of the gas, its pressure, and the electrical field strength on the cathode. The order of magnitude for γ is typically taken to be in a range of 10^{-5} to 10^{-1} [22]. This can be interpreted as the probability that one positive ion releases one electron from the cathode or in other words, that on average 10^1 to 10^5 positive ions are needed to release one electron from the cathode [21].

Remark: beside this mechanism, the generation of secondary electrons can also be provoked by photo-ionisation [21].

After the impact of positive ions on the cathode, new seed electrons, which lead to another electron avalanche, are generated. With due regard to the second emission coefficient γ, the number N_2 of seed electrons at the cathode for the second electron avalanche can be calculated as follows:

$$N_2 = N_{1+} \cdot \gamma = N_1 \cdot \left(e^{\alpha \cdot d} - 1\right) \cdot \gamma \qquad \text{(A.19)}$$

Under consideration of the exponential increase of the electron number during the electron avalanche which is taken into account by the avalanche factor $e^{a \cdot d}$, the generated number N_{2-} of electrons during the second electron avalanche can be expressed as:

$$N_{2-} = N_2 \cdot e^{\alpha \cdot d} = N_1 \cdot \left(e^{\alpha \cdot d} - 1\right) \cdot e^{\alpha \cdot d} \cdot \gamma \qquad \text{(A.20)}$$

and the generated number N_{2+} of ions is calculated by subtraction of the number of seed electrons:

$$N_{2+} = N_1 \cdot \left(e^{\alpha \cdot d} - 1\right) \cdot \gamma \cdot (e^{\alpha \cdot d} - 1) = N_1 \cdot \left(e^{\alpha \cdot d} - 1\right)^2 \cdot \gamma \qquad \text{(A.21)}$$

The same calculation is repeated for the following electron avalanches. Thus, for the n^{th} electron avalanche, the number of seed electrons N_n, of generated electrons N_{n-}, and ions N_{n+} can be calculated as:

$$N_n = N_1 \cdot \left(e^{\alpha \cdot d} - 1\right)^{(n-1)} \cdot \gamma^{(n-1)} \tag{A.22}$$

$$N_{n-} = N_n \cdot \left(e^{\alpha \cdot d} - 1\right) \cdot e^{\alpha \cdot d_e} \cdot \gamma^{(n-1)} \tag{A.23}$$

$$N_{n+} = N_n \cdot \left(e^{\alpha \cdot d} - 1\right)^n \cdot \gamma^{(n-1)} \tag{A.24}$$

As can be seen in (A.22), the number of seed electrons for the n^{th} electron avalanche is described by a geometrical series. In the case of convergence,

$$\left(e^{\alpha \cdot d} - 1\right) \cdot \gamma < 1 \tag{A.25}$$

the number of electrons decreases with each electron avalanche and thus, a finite sum of charges will be reached which does not lead to breakdown, a non-self-sustaining discharge takes place.
However, the number of charge carriers increases due to collision ionisation and electron avalanches. This leads to a temporary increase in current which can be noticed in form of current impulse.

By contrast, in the case of divergence,

$$\left(e^{\alpha \cdot d} - 1\right) \cdot \gamma \geq 1 \tag{A.26}$$

the number of electrons increases with each electron avalanche and therefore, a self-sustaining discharge occurs. Hence, equation (A.26) represents the ignition condition for the above presented Townsend mechanism. Consequently, the number of secondary electrons released from the cathode has at least to be equal to or greater than one to initiate at least one consecutive electron avalanche [21], [22].

Since the number of produced electrons at the anode is much bigger than one [31], it can be written:

$$e^{\alpha \cdot d} \gg 1 \tag{A.27}$$

thus reducing the ignition condition to

$$e^{\alpha \cdot d} \cdot \gamma \geq 1 \tag{A.28}$$

Remark: it should be noted that the considerations made are only valid for the case of a homogeneous field. For an inhomogeneous field, the integral along the electric field lines has to be considered [22]. Therefore, the ignition condition can be expressed as:

$$\left(e^{\int_0^d \alpha \cdot dx} - 1\right) \cdot \gamma \geq 1 \tag{A.29}$$

A.2 Polarity of the flashover for aluminium oxide disc (II)

Beside the results concerning the FOV and its comparison with those of the PDIV, an analysis of the dependence of the number of flashovers on polarity, more precisely the half cycle of the applied AC voltage in which the flashover occurred, was made. This could be of interest since a tendency towards more positive or negative flashovers depending on pressure and temperature may be seen. The analysis was only made for aluminium oxide disc (II) since for that specimen data were available for a temperature range of ambient temperature up to 400 °C. Figure A2.1 shows the number of flashovers for different temperatures and Figure A2.2 the number of flashovers for different pressures, each separated into polarity respectively.

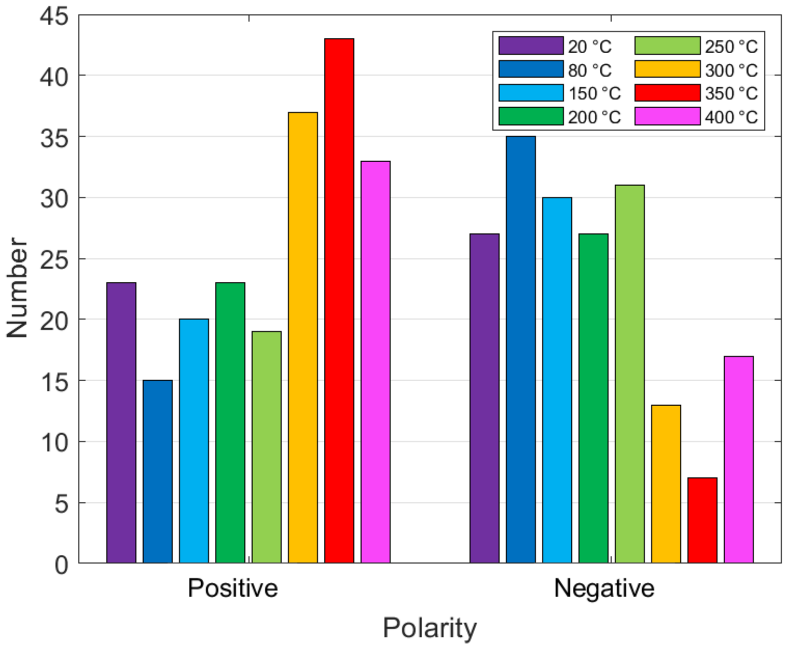

Figure A2.1. Number of flashovers as a function of polarity for different temperatures.

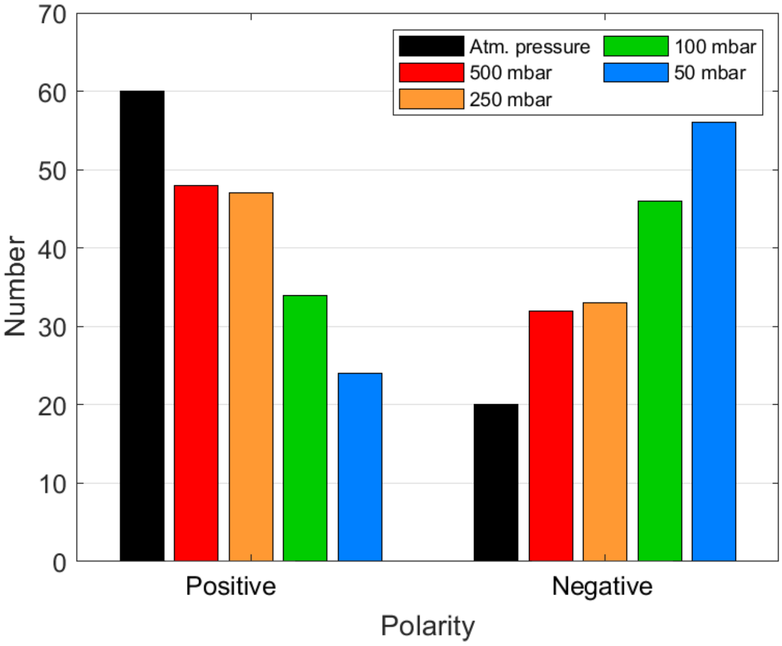

Figure A2.2. Number of flashovers as a function of polarity for different pressures.

For a range of ambient temperature up to 250 °C, flashover occurs mainly in the negative half cycle of the applied voltage. Nevertheless, positive flashovers were also observed in this temperature range albeit they are slightly less frequent than negative flashovers. For temperatures above 300 °C, this tendency changes in favour of the positive half cycle, where significantly more flashovers occur than in the negative half cycle.

Regarding the dependence of the number of flashovers on pressure, see Figure A2.2, it can be observed that flashover occurs for pressures in a range of 250 mbar up to atmospheric pressure mainly in the positive half cycle whereas for pressures below 100 mbar this tendency is inversed with more flashovers in the negative half cycle than in the positive one.

Combining these results, it can be stated that flashovers in the positive half cycle occur more often at higher pressures (≥ 250 mbar) and temperatures above 300 °C and flashovers in the negative half cycle more often at lower pressures (≤ 100 mbar) and temperatures below 300 °C.

The obtained results might be discussed under the aspect of the polarity effect. As presented in section 1.3.2.1, it is more likely to reach breakdown for a positive than for a negative voltage. On the one hand, it has been seen that for higher pressures more positive flashovers occur. Since all experiments were started at atmospheric pressure before pumping down to reach lower pressures, it may therefore be logical to first observe predominantly positive flashovers. On the other hand, more negative flashovers were observed at lower pressures. However, the reason therefore does not necessarily have to be the influence of pressure but possibly the fact that consecutive positive flashovers may lead to an accumulation of positive charges on the surface of the aluminium oxide disc. This potentially hinders the further development of new positive in favour of negative flashovers. Figure A2.3, in which the polarity of the 30 subsequent flashovers, corresponding to the results shown in Figure 4.8, is displayed, may support this hypothesis.

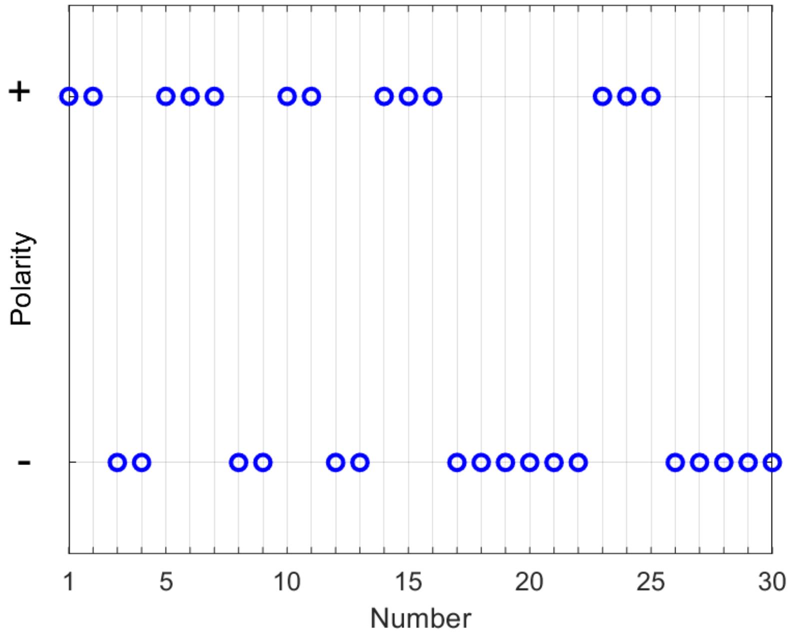

Figure A2.3. Aluminium oxide disc (II): polarity of 30 consecutive flashovers; ambient temperature; atmospheric pressure; nitrogen.

For approximately the first half of the 30 repetitions, positive flashovers predominate before more negative flashovers occur. As this experiment was carried out at constant, atmospheric pressure, it seems that the change from positive to negative flashovers is due to the successive flashovers influencing each other rather than to a pressure effect. In addition, the negative flashovers predominately occur in this experiment after 16 flashovers. This is in accordance with the observations made which showed that negative flashovers predominate at pressures below 250 mbar knowing that the first three pressure setpoints (atmospheric pressure, 500 mbar, 250 mbar) include in total exactly 15 repetitions of flashover. Nevertheless, the change in polarity does not seem to influence the FOV value, see Figure 4.8.

However, at elevated temperatures above 250 °C, the positive flashovers are much more frequent than the negative ones. This effect was also seen during the experiments analysing the influence of oxidation at 400 °C (Figure 4.9) where nearly all flashovers were positive. This may be explained by the fact that with higher temperature, the volume (and probably surface) resistivity decreases thus leading to an enhanced mobility of surface charges. Hence, the accumulation of charges on the solid insulators surface is less important. Consequently, the easier to provoke positive flashovers occur more frequently and are not hindered by the accumulation of positive surface charges stemming from previous positive flashovers.

Remark: these results only concern the aluminium oxide disc (II) and are inconclusive since the same tendency could not be observed for the aluminium oxide disc (III a) and the two PTFE discs. However, the data for the latter specimens are too few to draw any conclusions. Further, the data presented in Figure A2.3 are based only on one repetition so that those conclusions made may neither be completely conclusive.

References

References

[1] M. Karadjian, N. Imbert, C. Munier, M. Kirkpatrick, and E. Odic, ‘Partial Discharge Detection in an Aeronautical Power Cable’, in *2018 AIAA/IEEE Electric Aircraft Technologies Symposium*, Cincinnati, Ohio: American Institute of Aeronautics and Astronautics, Jul. 2018. doi: 10.2514/6.2018-5033.

[2] J. Jiang *et al.*, ‘A review on insulation challenges towards electrification of aircraft’, *High Voltage*, vol. 8, no. 2, pp. 209–230, 2023, doi: 10.1049/hve2.12304.

[3] M. Borghei and M. Ghassemi, ‘Insulation Materials and Systems for More- And All-Electric Aircraft: A Review Identifying Challenges and Future Research Needs’, *IEEE Transactions on Transportation Electrification*, vol. 7, pp. 1930–1953, Sep. 2021, doi: 10.1109/TTE.2021.3050269.

[4] G. Galli *et al.*, ‘Characterization and localization of partial-discharge-induced pulses in fission chambers designed for sodium-cooled fast reactors’, in *The European Physical Journal Conferences*, Liège: EPJ Web of Conferences, 2017, p. 03002. doi: 10.1051/epjconf/201817003002.

[5] M. Dulian, ‘Nuclear energy in the European Union’. EPRS | European Parliamentary Research Service, Sep. 2023.

[6] C. Cordina, ‘Nuclear energy | Fact Sheets on the European Union | European Parliament’. Accessed: Oct. 13, 2023. [Online]. Available: https://www.europarl.europa.eu/factsheets/en/sheet/62/nuclear-energy

[7] K. Krohn, ‘Ausbau erneuerbarer Energien: EU setzt sich ehrgeizige Ziele bis 2030’, *Der Tagesspiegel Online*, Mar. 30, 2023. Accessed: Sep. 26, 2023. [Online]. Available: https://www.tagesspiegel.de/wirtschaft/ausbau-erneuerbarer-energien-eu-setzt-sich-ehrgeizige-ziele-bis-2030-9588470.html

[8] D. Gremillet and S. Primas, ‘L’essentiel sur le projet de loi nouveau nucléaire | https://www.senat.fr/lessentiel/pjl22-100.pdf’. Commission des Affaires Économiques, May 2023.

[9] Légifrance, ‘LOI n° 2023-491 du 22 juin 2023 relative à l’accélération des procédures liées à la construction de nouvelles installations nucléaires à proximité de sites nucléaires existants et au fonctionnement des installations existantes’, Légifrance. Accessed: Oct. 13, 2023. [Online]. Available: https://www.legifrance.gouv.fr/jorf/id/JORFTEXT000047715784

[10] C. Tran Duy *et al.*, ‘Partial discharges at a triple junction metal/solid insulator/gas and simulation of inception voltage’, *Journal of Electrostatics*, vol. 66, no. 5, pp. 319–327, May 2008, doi: 10.1016/j.elstat.2008.01.011.

[11] E. Odic, A. Goldman, M. Goldman, M. Dhainaut, and R. Dussart, ‘Current distribution of AC surface discharges and associated chemistry’, *Journal of Electrostatics*, vol. 64, no. 7, pp. 477–484, Jul. 2006, doi: 10.1016/j.elstat.2005.10.026.

[12] M. Michelarakis, P. Widger, A. Beroual, and A. (Manu) Haddad, ‘Electrical Detection of Creeping Discharges over Insulator Surfaces in Atmospheric Gases under AC Voltage Application’, *Energies*, vol. 12, no. 2970, p. 15, Aug. 2019, doi: 10.3390/en12152970.

[13] J.-H. Song, J.-Y. Kim, B.-Y. Seok, and Y.-C. Choi, ‘Evaluation of discharge characteristics on the triple junction for development of the Gas-Insulated Switchgear’, in *15th International Conference on Electrical Machines and Systems (ICEMS)*, Sapporo: IEEE, 2012, p. 5.

[14] M. S. Naidu, *Gas insulated substations*. New Delhi: I.K. International Pub. House, 2008.

[15] A. Simonin *et al.*, ‘R&D around a photoneutralizer-based NBI system (Siphore) in view of a DEMO Tokamak steady state fusion reactor’, *Nucl. Fusion*, vol. 55, no. 12, p. 123020, Nov. 2015, doi: 10.1088/0029-5515/55/12/123020.

[16] J. Jiang *et al.*, ‘Partial Discharge Detection and Diagnosis of Transformer Bushing Based on UHF Method’, *IEEE Sensors J.*, vol. 21, no. 15, pp. 16798–16806, Aug. 2021, doi: 10.1109/JSEN.2021.3066809.

[17] M. E. Banda, D. Malec, and J.-P. Cambronne, ‘Simulation of Space Charge Impact on Partial Discharge Inception Voltage in Power Busbars Dedicated to Future Hybrid Aircrafts’, *CS*, vol. 09, no. 11, pp. 196–212, 2018, doi: 10.4236/cs.2018.911018.

[18] I. Langmuir, ‘Oscillations in Ionized Gases’, *Phys. Rev.*, vol. 33, no. 2, pp. 195–210, Feb. 1929, doi: 10.1103/PhysRev.33.195.

[19] L. Rezeau and G. Belmont, ‘Quelques propriétés des plasmas’. LPP - Laboratoire de Physique des Plasmas, 2007. [Online]. Available: https://www.lpp.polytechnique.fr/IMG/pdf_Intro_plasmas.pdf

[20] C. Tendero, C. Dublanche-Tixier, P. Tristant, J. Desmaison, and P. Leprince, ‘Atmospheric Pressure Plasmas: A Review’, *Spectrochimica Acta Part B-atomic Spectroscopy - SPECTROCHIM ACTA PT B-AT SPEC*, vol. 61, pp. 2–30, Jan. 2006, doi: 10.1016/j.sab.2005.10.003.

[21] W. Schufft, *Taschenbuch der elektrischen Energietechnik*, 1st ed. München: Fachbuchverlag Leipzig im Carl Hanser Verlag, 2007.

[22] A. Küchler, *High Voltage Engineering: Fundamentals - Technology - Applications*, 1st ed. in VDI-Buch. Heidelberg: Springer Vieweg, Berlin, 2018. doi: 10.1007/978-3-642-11993-4.

[23] J.-M. Rax, *Physique des plasmas. Cours et applications*, 1st ed. Paris: Dunod, 2005. Accessed: Jul. 07, 2023. [Online]. Available: https://www.decitre.fr/ebooks/physique-des-plasmas-cours-et-applications-9782100527878_9782100527878_9.html

[24] M. Beyer, W. Boeck, K. Möller, and W. Zaengl, *Hochspannungstechnik: Theoretische und praktische Grundlagen*. Berlin, Heidelberg: Springer Berlin Heidelberg, 1986. doi: 10.1007/978-3-642-61633-4.

[25] D. R. Lide, Ed., *CRC Handbook of Chemistry and Physics*, Internet Version 2005. Boca Raton, FL: CRC Press, 2005. [Online]. Available: http://www.hbcpnetbase.com

[26] National Institute of Standards and Technology, ‘Electron-Impact Cross Section Database - Table of molecules’. Accessed: Dec. 02, 2023. [Online]. Available: https://physics.nist.gov/PhysRefData/Ionization/molTable.html

[27] Y. Itikawa *et al.*, ‘Cross Sections for Collisions of Electrons and Photons with Nitrogen Molecules’, *Journal of Physical and Chemical Reference Data*, vol. 15, no. 3, pp. 985–1010, Jul. 1986, doi: 10.1063/1.555762.

[28] H. C. Straub, P. Renault, B. G. Lindsay, K. A. Smith, and R. F. Stebbings, ‘Absolute partial cross sections for electron-impact ionization of H 2 , N 2 , and O 2 from threshold to 1000 eV’, *Phys. Rev. A*, vol. 54, no. 3, pp. 2146–2153, Sep. 1996, doi: 10.1103/PhysRevA.54.2146.

[29] P. Ryder, *Einführung in die Elektrodynamik und die spezielle Relativitätstheorie*, 1st ed. Aachen: Shaker Verlag, 2004.

[30] A. von Engel, ‘John Sealy Edward Townsend. 1868-1957’, *Biographical Memoirs of Fellows of the Royal Society*, vol. 3, pp. 257–272, 1957.

[31] D. Xiao, ‘Fundamental Theory of Townsend Discharge’, in *Gas Discharge and Gas Insulation*, vol. 6, in Energy and Environment Research in China, vol. 6. , Berlin, Heidelberg: Springer Berlin Heidelberg, 2016, pp. 47–88. doi: 10.1007/978-3-662-48041-0_3.

[32] A. Küchler, *Hochspannungstechnik: Grundlagen - Technologie - Anwendungen*, 3rd ed. in VDI-Buch. Berlin Heidelberg: Springer-Verlag, 2009. doi: 10.1007/978-3-540-78413-5.

[33] F. Paschen, ‘Ueber die zum Funkenübergang in Luft, Wasserstoff und Kohlensäure bei verschiedenen Drucken erforderliche Potentialdifferenz’, *Ann. Phys.*, vol. 273, no. 5, pp. 69–96, 1889, doi: 10.1002/andp.18892730505.

[34] A. Dominguez, ‘Derivation of the Paschen curve law’. ALPhA Advanced Laboratories, 2014.

[35] Dakin et al., ‘Breakdown of Gases in Uniform Fields Paschen Curves for Nitrogen, Air and Sulfur Hexafluoride’, *Cigre 32*, p. 22, Jan. 1974.

[36] F. Koliatene, ‘Contribution à l’étude de l’existence des décharges dans les systèmes de l’avionique’, Thesis, Université de Toulouse, Université Toulouse III - Paul Sabatier, Toulouse, 2009. Accessed: May 14, 2021. [Online]. Available: http://thesesups.ups-tlse.fr/496/

[37] F. Koliatene, T. Lebey, J. P. Cambronne, and S. Dinculescu, ‘Impact of the aeronautic environment on the Partial Discharges Ignition: A basic study’, in *Conference Record of the 2008 IEEE International Symposium on Electrical Insulation*, Vancouver, BC: IEEE, Jun. 2008, pp. 603–606. doi: 10.1109/ELINSL.2008.4570404.

[38] E. Bădăreu and I. Popescu, *Gaz ionisés*. Paris, Bucarest: Dunod, 1968.

[39] F. W. Peek, *Dielectric phenomena in high-voltage engineering*, 2nd ed. New York, London: McGraw-Hill Book Company Inc, 1920.

[40] W. G. Dunbar and J. W. Seabrook, ‘High Voltage Design Guide for Airborne Equipment’, Boeing Aerospace Company, Seattle, Jun. 1976. Accessed: Sep. 08, 2022. [Online]. Available: https://apps.dtic.mil/sti/citations/ADA029268

[41] G. Galli *et al.*, ‘Paschen’s Law in Extreme Pressure and Temperature Conditions’, *IEEE Trans. Plasma Sci.*, vol. 47, no. 3, pp. 1641–1647, Mar. 2019, doi: 10.1109/TPS.2019.2896352.

[42] E. Sili, ‘Etude et caractérisation des décharges partielles et du vieillissement du polyimide en environnement aéronautique’, Thesis, Université de Toulouse, Université Toulouse III - Paul Sabatier, Toulouse, 2012. Accessed: May 14, 2021. [Online]. Available: http://thesesups.ups-tlse.fr/1922/

[43] E. Sili and J. P. Cambronne, ‘A New Empirical Expression of the Breakdown Voltage for Combined Variations of Temperature and Pressure’, *International Journal of Aerospace and Mechanical Engineering*, vol. 6, no. 3, pp. 611–616, Mar. 2012.

[44] International Electrotechnical Commission, ‘IEC 60270: High-Voltage Test Techniques - Partial Discharge Measurements’. IEC, 2000.

[45] K. Hencken and Y. Maret, ‘Teilentladungen in Mittelspannungsanlagen - Phänomene, Messtechniken, Trends’, presented at the ABB Kundentag, Zuzwil, Jan. 18, 2017.

[46] Ö. Altay, Ö. Kalenderli, A. Merev, S. Dedeoglu, and K. Gulnihar, ‘Preliminary partial discharge measurements with a computer aided partial discharge detection system’, in *2009 International Conference on Electrical and Electronics Engineering - ELECO 2009*, Bursa: IEEE, Nov. 2009, p. I-345-I–348. doi: 10.1109/ELECO.2009.5355233.

[47] R. H. Khawaja and T. R. Blackburn, ‘Partial Discharge Patterns in Oil-Impregnated Paper and Pressboard Insulation at High Temperature’, in *Australasian Universities Power Engineering Conference*, Sydney: IEEE, 2008, p. 6.

[48] F. H. Kreuger, *Industrial High Voltage - 4. Coordinating, 5. Testing, 6. Measuring*. Delft: Delft University Press, 1992. Accessed: May 14, 2021. [Online]. Available: https://repository.tudelft.nl/islandora/object/uuid%3A7c7bc501-c84a-4e55-a058-12971b360447

[49] F. Alrumayan, I. Cotton, and A. Nelms, ‘Partial Discharge Testing of Aerospace Electrical Systems’, *IEEE Trans. Aerosp. Electron. Syst.*, vol. 46, no. 2, pp. 848–863, Apr. 2010, doi: 10.1109/TAES.2010.5461661.

[50] F. H. Kreuger, *Industrial High DC Voltage - 1. Fields, 2. Breakdowns, 3. Tests*. Delft: Delft University Press, 1995. Accessed: May 14, 2021. [Online]. Available: https://repository.tudelft.nl/islandora/object/uuid%3Abf4186ec-d67a-4438-871b-ecadf7c59531

[51] M. G. Danikas and T. Tanaka, ‘Nanocomposites-a review of electrical treeing and breakdown’, *IEEE Electrical Insulation Magazine*, vol. 25, no. 4, pp. 19–25, Jul. 2009, doi: 10.1109/MEI.2009.5191413.

[52] G. W. Trichel, ‘The Mechanism of the Negative Point to Plane Corona Near Onset’, *Phys. Rev.*, vol. 54, no. 12, pp. 1078–1084, Dec. 1938, doi: 10.1103/PhysRev.54.1078.

[53] A. Csernátory-Hoffer, A., ‘Über den Mechanismus des Polaritätseffektes in der Durchschlagspannung von Gasen’, *Archiv für Elektrotechnik*, vol. 47, pp. 207–218, Mar. 1961.

[54] H. Raether, ‘Die Entwicklung der Elektronenlawine in den Funkenkanal’, *Zeitschrift für Physik*, vol. 112, no. 7, pp. 464–489, Jul. 1939, doi: 10.1007/BF01340229.

[55] J. M. Meek, ‘A Theory of Spark Discharge’, *Phys. Rev.*, vol. 57, no. 8, pp. 722–728, Apr. 1940, doi: 10.1103/PhysRev.57.722.

[56] L. B. Loeb and J. M. Meek, ‘The Mechanism of Spark Discharge in Air at Atmospheric Pressure. I’, *Journal of Applied Physics*, vol. 11, no. 6, pp. 438–447, 1940, doi: 10.1063/1.1712792.

[57] J. Mason, ‘Disharges’, *IEEE Trans. Elect. Insul.*, vol. EI-13, no. 4, pp. 211–238, Aug. 1978, doi: 10.1109/TEI.1978.298074.

[58] S. Nijdam, J. Teunissen, and U. Ebert, ‘The physics of streamer discharge phenomena’, *Plasma Sources Sci. Technol.*, vol. 29, no. 10, p. 103001, Nov. 2020, doi: 10.1088/1361-6595/abaa05.

[59] V. Madonna, P. Giangrande, W. Zhao, H. Zhang, C. Gerada, and M. Galea, ‘Electrical Machines for the More Electric Aircraft: Partial Discharges Investigation’, *IEEE Transactions on Industry Applications*, vol. 57, no. 2, pp. 1389–1398, Mar. 2021, doi: 10.1109/TIA.2020.3046434.

[60] E. Sili, J. P. Cambronne, N. Naude, and R. Khazaka, ‘Polyimide lifetime under partial discharge aging: effects of temperature, pressure and humidity’, *IEEE Trans. Dielect. Electr. Insul.*, vol. 20, no. 2, pp. 435–442, Apr. 2013, doi: 10.1109/TDEI.2013.6508745.

[61] W. Hassan, G. A. Hussain, F. Mahmood, M. Shafiq, and G. C. Montanari, ‘Effects of Temperature and Pressure on Failure Risk of Electric Motors based on Partial Discharge Measurements’, *IEEE Transactions on Aerospace and Electronic Systems*, pp. 1–9, 2023, doi: 10.1109/TAES.2023.3262622.

[62] N. Driendl, F. Pauli, and K. Hameyer, ‘Influence of Ambient Conditions on the Qualification Tests of the Interturn Insulation in Low-Voltage Electrical Machines’, *IEEE Transactions on Industrial Electronics*, vol. 69, no. 8, pp. 7807–7816, Aug. 2022, doi: 10.1109/TIE.2021.3108721.

[63] Y. Ji *et al.*, ‘Investigation on combined effect of humidity–temperature on partial discharge through dielectric performance evaluation’, *IET Science, Measurement & Technology*, vol. 17, no. 1, pp. 37–46, 2023, doi: 10.1049/smt2.12128.

[64] T. A. T. Vu, J.-L. Augé, and O. Lesaint, ‘Low temperature partial discharge properties of silicone gels used to encapsulate power semiconductors’, in *2009 IEEE Conference on Electrical Insulation and Dielectric Phenomena*, Virginia Beach: IEEE, Oct. 2009, pp. 421–424. doi: 10.1109/CEIDP.2009.5377750.

[65] Y. Li, Qiaogen Zhang, Yi Zhao, Tonglei Wang, Guangqi Liu, and Ke Wang, ‘The influence of temperature on Partial Discharges and wormhole effect of oil-paper insulation under DC voltage’, in *2017 IEEE Electrical Insulation Conference (EIC)*, Baltimore, MD, USA: IEEE, Jun. 2017, pp. 100–103. doi: 10.1109/EIC.2017.8004704.

[66] L. Bao, J. Li, J. Zhang, X. Li, and X. Li, ‘Influences of temperature on partial discharge behavior in oil-paper bounded gas cavity under pulsating DC voltage’, *IEEE Transactions on Dielectrics and Electrical Insulation*, vol. 23, no. 3, pp. 1482–1490, Jun. 2016, doi: 10.1109/TDEI.2016.005567.

[67] T. Billard, C. Abadie, and T. Lebey, ‘Partial discharge testing in aeronautic environment on magnet wire and feeder cables’, in *2016 IEEE Electrical Insulation Conference (EIC)*, Montreal, QC, Canada: IEEE, Jun. 2016, pp. 101–104. doi: 10.1109/EIC.2016.7548577.

[68] D. G. Kasten, Xin Liu, S. A. Sebo, D. F. Grosjean, and D. L. Schweickart, ‘Partial discharge measurements in air and argon at low pressures with and without a dielectric barrier’, *IEEE Trans. Dielect. Electr. Insul.*, vol. 12, no. 2, pp. 362–373, Apr. 2005, doi: 10.1109/TDEI.2005.1430404.

[69] D. L. Schweickart, D. F. Grosjean, D. G. Kasten, X. Liu, and S. A. Sebo, ‘Partial discharge measurements at low pressures with and without a dielectric barrier’, in *The 17th Annual Meeting of the IEEE Lasers and Electro-Optics Society, 2004. LEOS 2004.*, Rio Grande: IEEE, Oct. 2004, pp. 462–465. doi: 10.1109/CEIDP.2004.1364287.

[70] D. L. Schweickart, D. F. Grosjean, D. G. Kasten, S. A. Sebo, and X. Liu, 'Low-Pressure Partial-Discharge Measurements: Monitoring the Insulation Integrity of Aircraft Power Wiring Systems', in *2008 IEEE International Power Modulators and High-Voltage Conference*, Las Vegas, NV, USA: IEEE, May 2008, pp. 568–571. doi: 10.1109/IPMC.2008.4743722.

[71] M. Borghei and M. Ghassemi, 'Effects of Low–Pressure Condition on Partial Discharges in WBG Power Electronics Modules', in *2020 Electrical Insulation Conference (EIC)*, Knoxville: IEEE, Jun. 2020, p. 4. doi: 10.1109/EIC47619.2020.9158715.

[72] C. Park, 'Electret: An Entirely New Approach of Solving Partial Discharge Caused by Triple Points, Sharp Edges, Bubbles, and Airgaps', *IEEE Access*, vol. 8, pp. 78354–78366, 2020, doi: 10.1109/ACCESS.2020.2990310.

[73] A. Boubakeur, S. Mokhnache, A. Feliachi, and S. Boukhtache, 'Theoretical investigation on barrier effect on point-plane air gap breakdown voltage based on streamers criterion', *IEE Proceedings - Science, Measurement and Technology*, vol. 151, no. 3, pp. 167–174, May 2004, doi: 10.1049/ip-smt:20040155.

[74] M. Hara, T. Kurihara, S. Kozuru, J. Suehiro, and N. Hayashi, 'Estimation of partial discharge onset characteristics in gases around a triple junction', *Elect. Eng. Jpn.*, vol. 144, no. 1, pp. 1–11, Jul. 2003, doi: 10.1002/eej.10175.

[75] J. Fuhr, *Partial Discharges in Transformers*. in Technical Brochures, no. 676. Paris: Cigré, 2017.

[76] Omicron, 'MPD 600 Benutzerhandbuch - Version MPD600.GE.4'. OMICRON electronics, 2013.

[77] R. Boukadoum, 'Étude des décharges partielles et de leur transition à l'arc dans la connectique aéronautique du futur', Thesis, Université Paris Saclay, Gif-sur-Yvette, 2018. Accessed: May 14, 2021. [Online]. Available: https://tel.archives-ouvertes.fr/tel-02463942

[78] M. Wu, H. Cao, J. Cao, H.-L. Nguyen, J. B. Gomes, and S. P. Krishnaswamy, 'An overview of state-of-the-art partial discharge analysis techniques for condition monitoring', *IEEE Electrical Insulation Magazine*, vol. 31, no. 6, pp. 22–35, Nov. 2015, doi: 10.1109/MEI.2015.7303259.

[79] A. Darwish, S. S. Refaat, H. A. Toliyat, and H. Abu-Rub, 'On the Electromagnetic Wave Behavior Due to Partial Discharge in Gas Insulated Switchgears: State-of-Art Review', *IEEE Access*, vol. 7, pp. 75822–75836, 2019, doi: 10.1109/ACCESS.2019.2921089.

[80] M. Muhr and R. Schwarz, 'Experience with optical partial discharge detection', in *nternational Conference on Advances in Processing, Testing and Application of Dielectric Materials*, Wroclaw, 2007, pp. 26–29.

[81] S. Behrend, ‘Optische und elektrische Untersuchungen zu Teilentladungen in transparenten Silikonelastomeren’, Thesis, TU Berlin, Berlin, 2015. Accessed: May 14, 2021. [Online]. Available: https://depositonce.tu-berlin.de/handle/11303/4786

[82] P. M. Kothoke, N. R. Bhosale, A. Despande, N, and Cheeran, ‘Analysis of Partial Discharge using Phase-Resolved (nq) Statistical Techniques’, *International Journal of Engineering Research and Applications (IJERA)*, vol. 3, no. 3, pp. 1317–1323, Jun. 2013.

[83] A. Strotmann, *Bewertung von Mustererkennungsverfahren für die elektrische Teilentladungsmessung an Leistungstransformatoren*, 1. Auflage. in Schriftenreihe des Instituts für Energieübertragung und Hochspannungstechnik, IEH, no. Band 15. Göttingen: Sierke Verlag, 2016.

[84] L. Chang-Hsing, C. Min-Yen, H. Chih-Hsien, and Y. Shih-Shong, ‘The Sustained Property of Partial Discharge Signal Observed by Partial Discharge Monitoring’. Power Diagnostic Service, 2016. Accessed: Jul. 31, 2023. [Online]. Available: https://www.pdservice.com/publications/26/

[85] H. Q. Niu, A. Cavallini, and G. C. Montanari, ‘Identification of Partial Discharge Phenomena in HVDC Apparatus’, in *Conference Record of the 2008 IEEE International Symposium on Electrical Insulation*, Vancouver: IEEE, Jun. 2008, pp. 373–376. doi: 10.1109/ELINSL.2008.4570352.

[86] J. Fuhr, ‘Procedure for identification and localization of dangerous PD sources in power transformers’, *IEEE Trans. Dielect. Electr. Insul.*, vol. 12, no. 5, pp. 1005–1014, Oct. 2005, doi: 10.1109/TDEI.2005.1522193.

[87] M. Jenny, ‘Präzise Zustandsbewertung von Kabelanlagen mittels phasen- und ortsaufgelöster TE- Messung’, presented at the BAUR Prüf- und Messtechnik GmbH, May 16, 2013.

[88] E. Gulski and F. H. Kreuger, ‘Computer-aided recognition of discharge sources’, *IEEE Trans. Elect. Insul.*, vol. 27, no. 1, pp. 82–92, Feb. 1992, doi: 10.1109/14.123443.

[89] M. Ghaffarian Niasar, ‘Partial discharge signatures of defects in insulation systems consisting of oil and oil-impregnated paper’, Licentiate Thesis, KTH School of Electrical Engineering, Stockholm, 2012.

[90] M.-A. Handala, ‘Etude de la décharge de surface sous tension alternative 50 Hz - Effets sur une interface isolante air /solide’, Thesis, Université Mouloud Mammeri, Tizi-Ouzou, 2007. Accessed: Jan. 19, 2023. [Online]. Available: https://www.ummto.dz/dspace/handle/ummto/1259

[91] M. Toepler, ‘Über die physikalischen Grundgesetze der in der Isolatorentechnik auftretenden elektrischen Gleiterscheinungen’, *Archiv f. Elektrotechnik*, vol. 10, no. 5, pp. 157–185, May 1921, doi: 10.1007/BF01656612.

[92] M. Toepler, ‘Zur Kenntnis der Gesetze der Gleitfunkenbildung’, in *Annalen der Physik*, vol. 21, in Annalen der Physik, no. 4, vol. 21. , Leipzig: Verlag von Johann Ambrosius Barth, 1906, pp. 193–122. Accessed: Jul. 19, 2023. [Online]. Available: https://gallica.bnf.fr/ark:/12148/bpt6k15328k

[93] V. Hinrichsen, ‘Oberflächenentladungen’. TU Darmstadt, 2009. Accessed: May 14, 2021. [Online]. Available: https://www.yumpu.com/de/document/read/5257716/10-oberflachenentladungen-fachgebiet-hochspannungstechnik

[94] I. Pavey, ‘Practical Guide - Industrial Electrostatics - hazards, Problems and Applications’. DEKRA Process Safety, 2018.

[95] N. Berger, M. Deonzière, J.-C. Gilet, D. Guionnet, and H. Romat, ‘Électricité statique’. INRS. Paris, Jul. 2004.

[96] Y. Murooka, T. Takada, and K. Hiddaka, ‘Nanosecond surface discharge and charge density evaluation Part I: review and experiments’, *IEEE Electr. Insul. Mag.*, vol. 17, no. 2, pp. 6–16, Mar. 2001, doi: 10.1109/57.917527.

[97] V. Bloshchitsyn, ‘Review of surface discharge experiments’, *Plasma Physics*, p. 10, May 2010.

[98] M. L. Coulibaly, ‘Caractérisation des décharges électriques se propageant aux interfaces gaz/solide – Relation entre propriétés des matériaux et dimension fractale’, Thesis, École Céntrale de Lyon, Lyon, 2009.

[99] S. Kumara, Bin Ma, Y. V. Serdyuk, and S. M. Gubanski, ‘Surface charge decay on HTV silicone rubber: effect of material treatment by corona discharges’, *IEEE Trans. Dielect. Electr. Insul.*, vol. 19, no. 6, pp. 2189–2195, Dec. 2012, doi: 10.1109/TDEI.2012.6410223.

[100] N. L. Allen and P. N. Mikropoulos, ‘Streamer propagation along insulating surfaces’, *IEEE Transactions on Dielectrics and Electrical Insulation*, vol. 6, no. 3, pp. 357–362, Jun. 1999, doi: 10.1109/94.775623.

[101] V. V. Timatkov, G. J. Pietsch, A. B. Saveliev, M. V. Sokolova, and A. G. Temnikov, ‘Influence of solid dielectric on the impulse discharge behaviour in a needle-to-plane air gap’, *J. Phys. D: Appl. Phys.*, vol. 38, no. 6, pp. 877–886, Mar. 2005, doi: 10.1088/0022-3727/38/6/016.

[102] A. Sobota *et al.*, ‘Speed of streamers in argon over a flat surface of a dielectric’, *J. Phys. D: Appl. Phys.*, vol. 42, no. 1, p. 015211, Jan. 2009, doi: 10.1088/0022-3727/42/1/015211.

[103] M. Akyuz, L. Gao, V. Cooray, T. G. Gustavsson, S. M. Gubanski, and A. Larsson, ‘Positive streamer discharges along insulating surfaces’, *IEEE Trans. Dielect. Electr. Insul.*, vol. 8, no. 6, pp. 902–910, Dec. 2001, doi: 10.1109/94.971444.

[104] X. Meng, H. Mei, C. Chen, L. Wang, Z. Guan, and J. Zhou, ‘Characteristics of streamer propagation along the insulation surface: influence of dielectric material’, *IEEE Trans. Dielect. Electr. Insul.*, vol. 22, no. 2, pp. 1193–1203, Apr. 2015, doi: 10.1109/TDEI.2015.7076822.

[105] X. Li, A. Sun, and J. Teunissen, ‘A computational study of negative surface discharges: Characteristics of surface streamers and surface charges’, *IEEE Transactions on Dielectrics and Electrical Insulation*, vol. 27, no. 4, pp. 1178–1186, Aug. 2020, doi: 10.1109/TDEI.2020.008880.

[106]X. Li, A. Sun, G. Zhang, and J. Teunissen, ‘A computational study of positive streamers interacting with dielectrics’, *Plasma Sources Sci. Technol.*, vol. 29, no. 6, p. 065004, Jun. 2020, doi: 10.1088/1361-6595/ab8f75.

[107] R. A. Fouracre, E. Santos, I. Timoshkin, M. J. Given, and S. J. Macgregor, ‘Surface Discharge Propagation: The Influence Of Surface Charge’, in *Conference Record of the 2006 Twenty-Seventh International Power Modulator Symposium*, Arlington: IEEE, May 2006, pp. 39–42. doi: 10.1109/MODSYM.2006.365178.

[108] F. Sadaoui and A. Beroual, ‘DC creeping discharges over insulating surfaces in different gases and mixtures’, *IEEE Transactions on Dielectrics and Electrical Insulation*, vol. 21, no. 5, pp. 2088–2094, Oct. 2014, doi: 10.1109/TDEI.2014.004486.

[109] N. Sakamoto, Y. Kuninaka, H. Ueno, and H. Nakayama, ‘Local corona behavior and creeping discharge on (needle-dielectric, semiconductor) composite electrodes’, *Elect. Eng. Jpn.*, vol. 145, no. 1, pp. 1–9, Oct. 2003, doi: 10.1002/eej.10208.

[110] A. Beroual, M. L. Coulibaly, O. Aitken, and A. Girodet, ‘Investigation on creeping discharges propagating over epoxy resin and glass insulators in the presence of different gases and mixtures’, *European Physical Journal: Applied Physics*, vol. 56, no. 3, p. 30802 (8 pages), Dec. 2011, doi: 10.1051/epjap/2011110122.

[111] A. R. Hind, S. K. Bhargava, and S. C. Grocott, ‘The surface chemistry of Bayer process solids: a review’, *Colloids and Surfaces A: Physicochemical and Engineering Aspects*, vol. 146, no. 1–3, pp. 359–374, Jan. 1999, doi: 10.1016/S0927-7757(98)00798-5.

[112] M. Decup, ‘Impact des procédés industriels de traitement sur les propriétés diélectriques des substrats d’alumine utilisés dans les modules de commutation haute tension’, Thesis, Université de Toulouse, Université Toulouse III - Paul Sabatier, Toulouse, 2010. Accessed: Apr. 25, 2023. [Online]. Available: http://thesesups.ups-tlse.fr/1077/

[113] L.-Y. Chen and G. W. Hunter, ‘Temperature Dependent Dielectric Properties of Polycrystalline 96 % Al_2O_3’, *MRS Proc.*, vol. 833, pp. 228–233, 2004, doi: 10.1557/PROC-833-G7.6.

[114] P. T. B. Shaffer, *Plenum Press Handbooks of High-Temperature Materials - No. 1 - Materials Index*, 1st ed. New York: Springer US, 1963. doi: 10.1007/978-1-4899-6405-2.

[115] J. F. Shackelford and W. Alexander, Eds., *CRC Materials Science and Engineering Handbook*, 3rd ed. Boca Raton, FL: CRC Press, 2001.

[116] DuPont Fluoroproducts, *Teflon PTFE Fluoropolymer Resin: Properties Handbook*. Wilmington: DuPont Fluoroproducts, 1996.

[117] Meek J. M. and Craggs J.D., *Electrical Breakdown Of Gases*. Oxford: Oxford University Press, 1953. Accessed: Jul. 18, 2023. [Online]. Available: http://archive.org/details/electricalbreakd031039mbp

[118] T. W. Dakin, H. M. Philofsky, and W. C. Divens, 'Effect of electric discharges on the breakdown of solid insulation', *Electrical Engineering*, vol. 73, no. 9, pp. 812–817, 1954, doi: 10.1109/EE.1954.6438979.

[119] CEN - European Committee for Standardization, 'FprEN 2591-227 - Aerospace Series - Elements of electrical ond optical connection - Test methods - Part 227 Partial discharges test'. CEN, 2014.

[120] L.-Y. Chen, 'Dielectric Performance of a High Purity HTCC Alumina at High Temperatures - A Comparison Study with other Polycrystalline Alumina', *Additional Conferences (Device Packaging, HiTEC, HiTEN, and CICMT)*, vol. 2014, no. HITEC, pp. 000271–000277, Jan. 2014, doi: 10.4071/HITEC-WP26.

[121] M. Park, H.-N. Kim, S. Baek, E. Kang, Y. Baek, and D. K. Kim, 'Dielectric Properties of Alumina Ceramics in the Microwave Frequency at High Temperature', *Solid State Phenomena*, vol. 124–126, Jun. 2007, doi: 10.4028/www.scientific.net/SSP.124-126.743.

[122] A. H. Seltzman and S. Wukitch, 'Precision measurement of relative permittivity of aluminum oxide for a high power resonant waveguide window with low return loss', *Fusion Engineering and Design*, vol. 147, p. 9, Oct. 2019, doi: 10.1016/j.fusengdes.2019.05.045.

[123] L. Gauckler, 'Ingenieurkeramik III - Funktionskeramik'. ETH Zürich - Professur für nichtmetallische Werkstoffe, 2001. doi: 10.13140/RG.2.2.34595.81443.

[124] P. Reinicke, 'Herstellung und Untersuchung gesputterter transparenter Seilberelektroden für organische Solarzellen', Thesis, Albert-Ludwigs-Universität, Freiburg, 2016.

[125] M. T. Greiner, L. Chai, M. G. Helander, W.-M. Tang, and Z.-H. Lu, 'Transition Metal Oxide Work Functions: The Influence of Cation Oxidation State and Oxygen Vacancies', *Advanced Functional Materials*, vol. 22, no. 21, pp. 4557–4568, 2012, doi: 10.1002/adfm.201200615.

[126] A. V. Chvyreva, A. J. M. Pemen, and T. Christen, 'Investigation of streamer propagation along insulating surfaces', *Proceedings of the 31st International Conference on Phenomena in Ionized Gases (ICPIG 2013), 14 - 19 July 2013, Granada, Spain*, p. 3, 2013.

[127] L. Tremas, ‘Pre-breakdown and breakdown phenomena in air along insulating solids’, These de doctorat, Université Grenoble Alpes (ComUE), Grenoble, 2017. Accessed: Sep. 21, 2023. [Online]. Available: https://www.theses.fr/2017GREAT117

List of publications

- R. Szilágyi, Ph. Molinié, M. J. Kirkpatrick, E. Odic, G. Galli, Ph. Dessante, ‘Role of Temperature in Partial Discharge Inception Voltage at Triple Junctions’, IEEE Transactions on Dielectrics and Electrical Insulation, vol. 30, no. 6, pp. 2809-2818, December 2023, doi: 10.1109/TDEI.2023.3315686.

- R. Szilágyi, Ph. Molinié, M. J. Kirkpatrick, E. Odic, G. Galli, Ph. Dessante, ‘Étude des phénomènes de décharges partielles à partir d’un point triple sous conditions variées de pression et de température’, $12^{\text{ème}}$ conférence de la Société Française d’Électrostatique, 4-6 juillet 2023, Cherbourg-en-Cotentin, France.

- R. Szilágyi, Ph. Molinié, M. J. Kirkpatrick, E. Odic, G. Galli, Ph. Dessante, ‘Study of partial discharge and breakdown phenomena at triple junctions under various conditions of pressure and temperature’, IOP Electrostatics 2023, 4-7 September 2023, Brunel University, Uxbridge, United Kingdom.

Résumé en français

Dans de nombreuses applications industrielles, la présence d'une jonction entre un isolant solide, un conducteur, et le gaz environnant constitue un point triple comme illustré par la Figure 1.

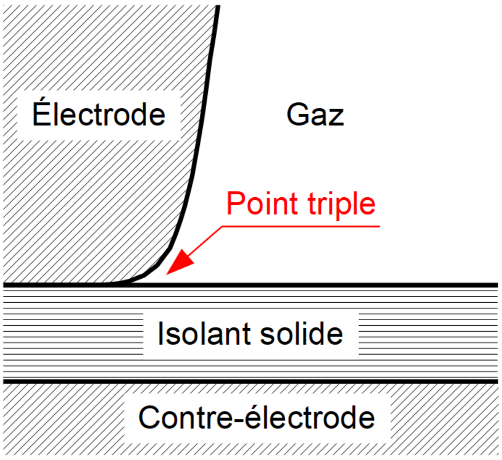

Figure 1. Schéma d'un point triple.

Même si une attention est portée à la géométrie de la jonction pour contrôler le champ électrique local, ce dernier est renforcé en raison de la courbure de l'électrode et de la différence de permittivité relative des isolants solide et gazeux. Cette situation peut favoriser le déclenchement des phénomènes de décharges tels que des décharges partielles (DP), ou, pour des tensions plus élevées, des décharges de surface du type streamer. Les DP sont susceptibles de contribuer à une dégradation progressive du système d'isolation et, à terme, de conduire à une défaillance (claquage diélectrique, contournement de l'isolant solide),

Des points triples sont souvent présents dans des applications industrielles dans lesquelles les isolants solides sont utilisés pour isoler des conducteurs haute tension d'autres composants du système ou du potentiel de terre. Ils peuvent être exposés à des conditions environnementales (température, pression) parfois extrêmes, par exemple dans le secteur aéronautique (pressions jusqu'à 100 mbar) ou nucléaire (températures jusqu'à 650 °C).

L'objectif de cette étude est de parvenir à une meilleure compréhension des phénomènes de décharge survenant au niveau d'un point triple dans des conditions variées de température et de pression. Pour cela, des mesures des tensions-seuil d'amorçage de DP (*Partial Discharge Inception Voltage*, PDIV) et d'extinction de DP (*Partial Discharge Extinction Voltage*, PDEV) ainsi que de la tension de claquage par contournement diélectrique (*Flashover Voltage*, FOV) ont été réalisées sur un dispositif constitué d'un disque d'alumine (Al_2O_3) inséré entre un disque d'inox connecté à la masse et d'une électrode cylindrique de tungstène alimentée en haute tension (50 Hz AC) dans des conditions de pression de gaz (N_2) comprises entre 50 mbar et la pression atmosphérique et de température comprises entre l'ambiante et 400 °C.

Une décharge gazeuse peut être initiée sous la condition que des électrons germes (provenant du rayonnement cosmique, de la radioactivité naturelle, etc.) soient accélérés par un champ électrique externe. Si les électrons acquièrent une énergie suffisante lors de leur libre parcours moyen et s'ils entrent en collision ionisante avec les atomes / molécules de gaz, une avalanche électronique peut se former et initier une décharge auto-entretenue dans des conditions impliquant un mécanisme d'émission secondaire permettant de renouveler les électrons germes initiaux.

L'effet de la température sur l'initiation des décharges peut être décrit en utilisant les équations de la loi des gaz parfaits (1), du libre parcours moyen (2), et du champ électrique qui est ici supposé être homogène (3) :

$$N = \frac{p}{k_B \cdot T} \quad (1) \qquad \lambda = \frac{1}{\sigma \cdot N} \quad (2) \qquad E = \frac{W_i}{e \cdot \lambda} \propto \frac{V}{d} \quad (3)$$

dans celles-ci, N représente la densité du gaz, p la pression, k_B la constante de Boltzmann, T la température, λ le libre parcours moyen, σ la section efficace de collision ionisante, E le champ électrique, W_i le potentiel d'ionisation de gaz, e la charge élémentaire, V la tension et d la distance inter-électrodes.

Ces équations montrent qu'une augmentation de la température entraîne une diminution de la densité du gaz, ce qui implique une augmentation du libre parcours moyen. Par conséquent, pour un potentiel d'ionisation donné, l'intensité du champ électrique et donc la tension nécessaire pour provoquer une décharge diminuent.

Pour pouvoir étudier le point triple à température élevée et à différentes pressions / densités du gaz, un dispositif expérimental, conçu pour cette étude et décrit par la Figure 2, a été placé dans une chambre étanche.

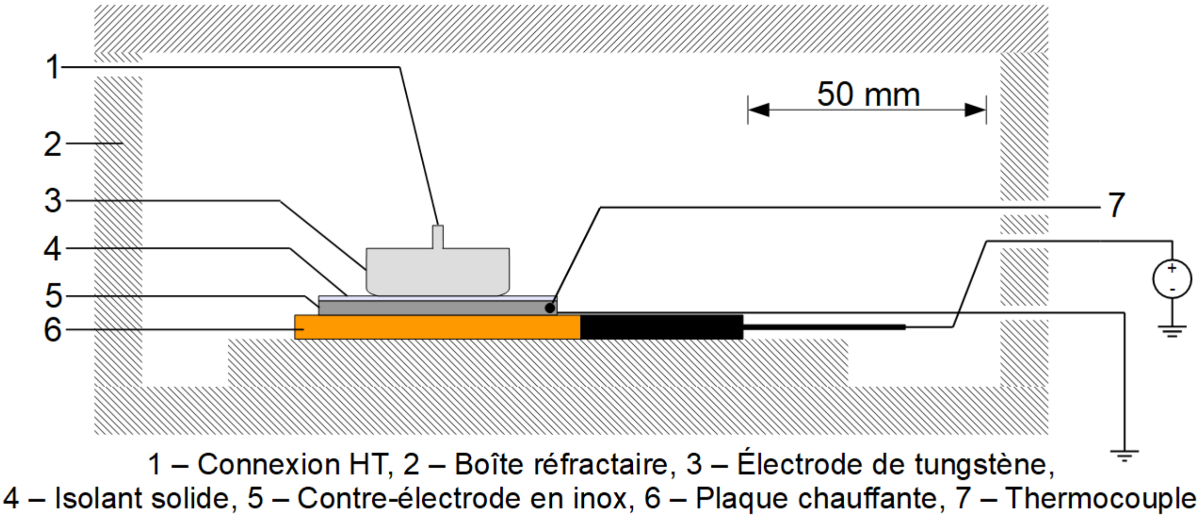

Figure 2. Schéma de l'arrangement du point triple comprenant la plaque chauffante à l'intérieur de la boîte réfractaire.

L’arrangement du point triple est constitué d’une électrode cylindrique de tungstène (30 mm de diamètre) ayant un profil de Rogowski (3) et alimentée en haute tension 50 Hz AC (1), d’un disque d’alumine (Al_2O_3, 99,7 % de pureté, 50 mm de diamètre, 1 mm d’épaisseur) (4) en tant qu’isolant solide, et d’un disque d’inox (50 mm de diamètre) (5) connecté à la masse. Ce système repose sur une plaque chauffante en céramique (nitrure de silicium) (6), alimentée séparément en DC (0-64 V, 0-6 A), qui a été exploitée jusqu’à une température de 400 °C (mesurée près du point triple). La température du disque d’inox a été mesurée par un thermocouple (type K) (7) et cette mesure a été utilisée comme entrée pour le réglage de la plaque chauffante réalisé par LabVIEW en utilisant un régulateur PI. L’arrangement du point triple a été placé dans une boîte réfractaire (2) constituée d’une alumine poreuse à faible conductivité thermique pour homogénéiser la température autour du point triple et pour protéger la chambre étanche en PMMA (poly(méthacrylate de méthyle)) dans laquelle se trouvait la boîte réfractaire.

La Figure 3 montre le schéma du dispositif expérimental contenant la boîte réfractaire avec l’arrangement du point triple.

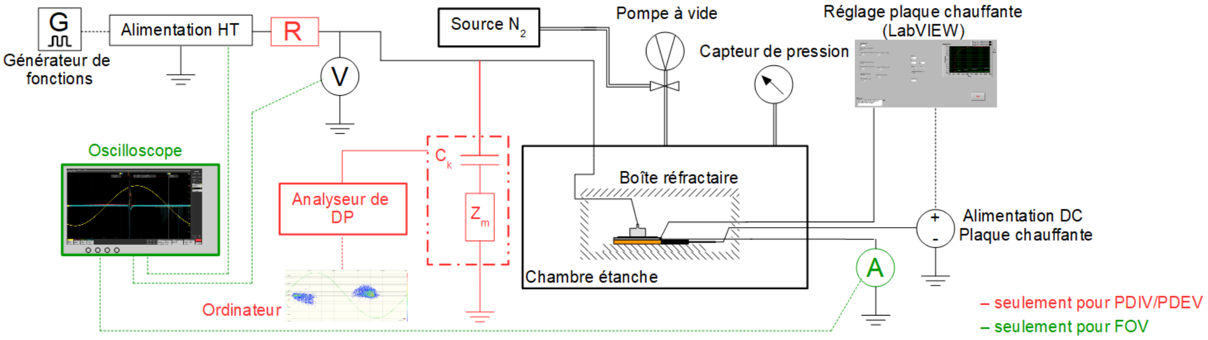

Figure 3. Schéma du dispositif expérimental pour la détermination de la PDIV/PDEV et de la FOV.

L’électrode de tungstène a été connectée à une alimentation haute tension, contrôlée par un générateur de fonctions (50 Hz AC), et placée en série avec une résistance de protection (10 MΩ) (seulement pour les mesures de PDIV/PDEV). La PDIV ainsi que la PDEV ont été déterminées conformément à la norme IEC 60270 en utilisant un analyseur de décharges partielles commercial (OMICRON MPD 600) connecté en parallèle à l’assemblage du point triple via un condensateur de couplage de 250 pF, tandis que pour les mesures de la FOV, seule une sonde de courant (CT-2) connectée à un oscilloscope a été utilisée. La tension appliquée a été mesurée en utilisant une sonde de tension (Tektronix P6015A), connectée à l’oscilloscope.

Toutes les expériences ont été effectuées dans la chambre étanche permettant d’ajuster la pression d’azote, gaz choisi pour éviter des effets indésirables liés à l’oxydation des électrodes dans la boîte réfractaire, en préservant des propriétés électriques proches de celles de l’air. Une pompe à vide ainsi qu’une alimentation en azote ont été connectées à la chambre étanche et la pression a été mesurée par un capteur de pression (Pfeiffer PCR 280).

Une surveillance précise de la température et un réglage adapté de la plaque chauffante étaient primordiaux pour cette étude. Des mesures de la température au point triple et dans le gaz proche de ce dernier n'ont montré qu'une légère différence de la température entre ces deux points. Par conséquent, la densité du gaz au point triple, l'endroit où l'on s'attend à un déclenchement des décharges, et de sa proximité peut être considérée comme similaire.

En considérant que la géométrie du point triple restait inchangée tandis que la pression et la température étaient variables et que le paramètre de distance n'avait pas de sens pour cette géométrie (contrairement à une situation de distance inter-électrodes bien définie et donc représentable par une courbe de Paschen), il a été convenu de présenter les résultats seulement en fonction de la pression / densité du gaz.

Chaque expérience a été réalisée en partant de la température la plus basse (température ambiante) à la température la plus élevée (400 °C) et, pour chaque température, de la pression la plus élevée (pression atmosphérique) à la pression la plus basse (50 mbar).

Afin d'assurer des mesures uniformes, une procédure standardisée pour la détection de la PDIV/PDEV ainsi que de la FOV a été utilisée. Pour la détermination de la PDIV, une tension d'environ 100 V au-dessous de la PDIV attendue était d'abord appliquée, puis augmentée par paliers de 10 V d'une durée de 10 s. Si une décharge (seuil de détection : 3 pC) était détectée, la tension était maintenue durant 30 s et si plus de 30 décharges étaient détectées sur cet intervalle de temps, la valeur de PDIV (valeur crête) était retenue. Sinon, la tension était de nouveau augmentée par paliers de 10 V. Pour obtenir la valeur de la PDEV, la tension appliquée était, en partant de la PDIV, diminuée par paliers de 10 V sans contrainte de durée pour chaque palier et la valeur était retenue si aucune décharge n'était détectée pendant 30 s.

Une procédure similaire a été appliquée pour la détermination de la FOV : une tension de 1 kV au-dessous de la FOV attendue était d'abord appliquée, puis augmentée toutes les 10 s par paliers de 100 V jusqu'à ce que le claquage fût atteint.

En complément aux mesures décrites, d'autres mesures ont été réalisées sur le même disque d'alumine et dans la même gamme de températures : des mesures de permittivité relative pour différentes fréquences comprises entre 20 Hz et 1 kHz, en mesurant la capacité du disque d'alumine par un LCR-Meter (Wayne Kerr LCR Meter 4300), ainsi que de résistivité volumique, en mesurant le courant par un pico-ampèremètre (Keithley Model 6485 Picoammeter).

Dans un premier temps, l'influence de différentes propriétés géométriques et diélectriques des isolants solides sur la PDIV à température ambiante et à différentes pressions dans une gamme entre la pression atmosphérique et 50 mbar a été analysée.

Les résultats principaux ont montré que plus l'isolant solide est épais, plus la PDIV est élevée, du fait de la diminution de la capacité qui mène à un champ électrique plus faible dans le gaz. Inversement, plus la permittivité relative est augmentée, plus la PDIV est faible, à cause d'un champ électrique renforcé dans le gaz, rendant le déclenchement des DP plus facile.

En outre, la présence d'une couche métallisée (épaisseur de 100 nm) sur la surface de l'isolant solide en contact avec le potentiel de haute tension mène à une augmentation significative de la PDIV. Ceci est dû à une géométrie changée à la lisière de la couche métallique qui, en comparaison avec la géométrie constituée par l'électrode cylindrique posée à même la surface de l'alumine, rend le déclenchement des décharges, à défaut d'un intervalle gazeux suffisamment grand pour le développement d'une avalanche électronique, plus difficile.

Ensuite, l'influence des conditions variées de température et de pression sur la PDIV et la PDEV a été analysée. La Figure 4 montre, à titre d'exemple, les résultats de mesure de PDIV pour différentes températures en fonction de la densité du gaz pour une plaque d'alumine d'une pureté de 99,7 %. Pour faciliter la lecture, tous les points appartenant aux mêmes températures sont reliés par une ligne de tendance (polynôme du second degré). Chaque point de mesure a été calculé à partir de la valeur moyenne de 15 mesures (cinq répétitions pour chaque pression et trois répétitions de chaque température). Les barres d'erreur sont calculées pour un écart type de 1σ et pour la densité du gaz, l'incertitude de mesure de la jauge de pression selon le fabricant, dépendant de la gamme de pression, a été considérée.

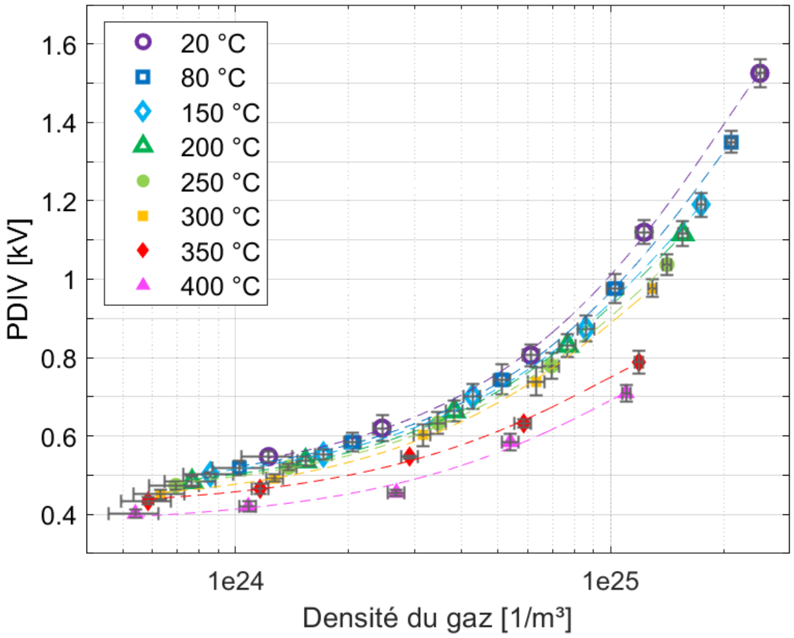

Figure 4. PDIV en fonction de la densité du gaz pour différentes températures ; plaque d'alumine (99,7 %) ; azote.

Les résultats sur la Figure 4 montrent, conformément à ce qui était attendu, que la PDIV augmente pour toutes les températures avec la pression. En outre, les résultats montrent qu'une augmentation de la température mène à une diminution de la PDIV, ce qui est conforme à la théorie. Par exemple, la différence de PDIV entre 20 °C et 400 °C à pression atmosphérique s'élève à 820 V. Néanmoins, en supposant que la densité du gaz dans le gaz proche du point triple soit similaire avec celle au point triple, on devrait s'attendre à ce que toutes les lignes de tendance se rejoignent lorsqu'elles sont, comme ici, tracées en fonction de la densité du gaz. Toutefois, en augmentant la température jusqu'à 400 °C, chaque série de PDIV se trouve légèrement au-dessous de la précédente tandis qu'un écart plus important entre 300 °C et 350 °C peut être observé. Par conséquent, à une pression donnée, la diminution de la densité du gaz due à l'augmentation de la température n'explique plus à elle seule la diminution de la PDIV.

Pour pouvoir expliquer ce phénomène, il faut considérer l'influence de la température sur les propriétés diélectriques de la plaque d'alumine. C'est pourquoi des mesures diélectriques ont été effectuées, notamment de la résistivité volumique et de la permittivité relative en fonction de la température (voir Figure 5 et Figure 6).

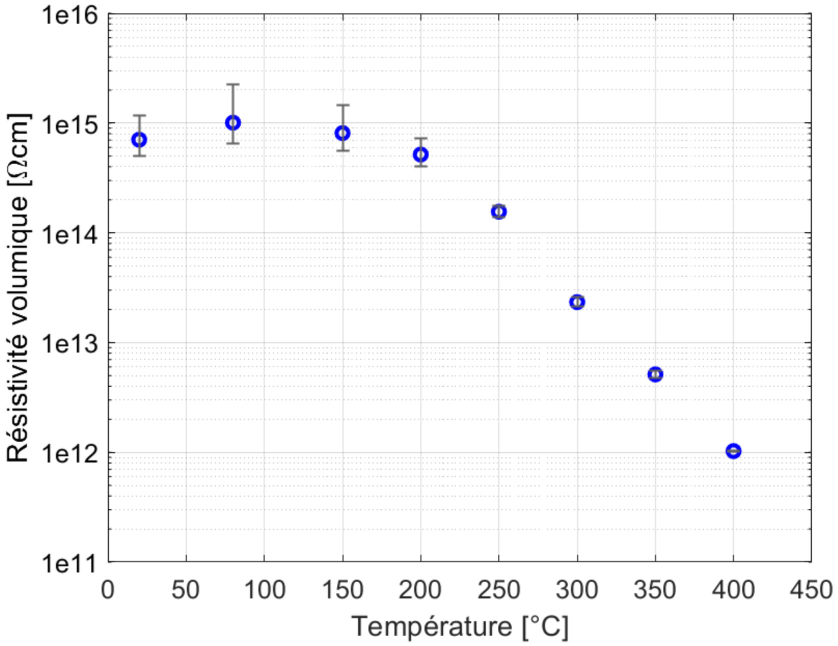

Figure 5. Résistivité volumique en fonction de la température ; plaque d'alumine (99,7 %).

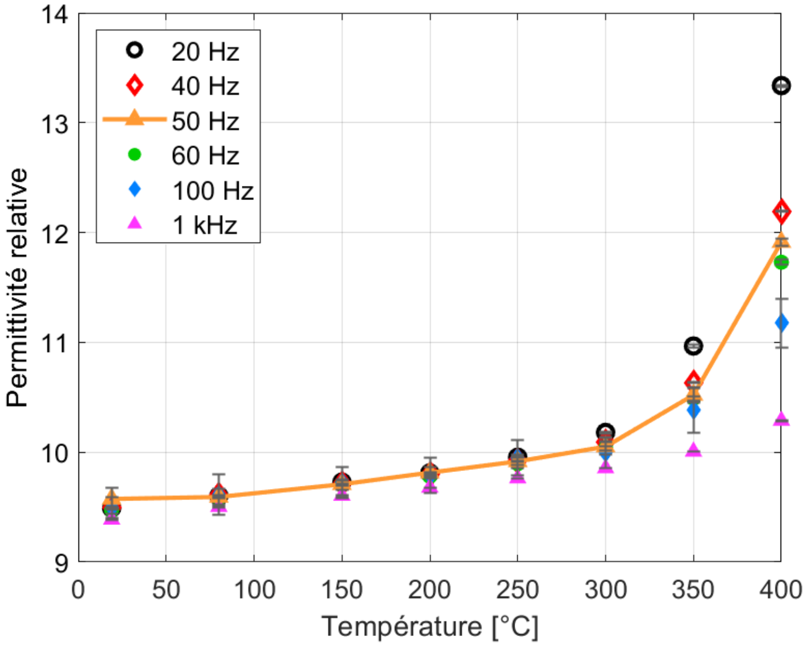

Figure 6. Permittivité relative en fonction de la température pour différentes fréquences ; plaque d'alumine (99,7 %). Le trait plein souligne le cas de 50 Hz.

La Figure 5 montre que la résistivité volumique diminue avec la température, ce qui mène à une plus grande activité de DP, de sorte que la probabilité de détecter des DP est, en considérant la procédure définie pour la détermination de la PDIV, augmentée. Ceci résulte en une diminution de la PDIV. La diminution de la résistivité volumique avec la température peut également expliquer l'augmentation de la permittivité relative (voir Figure 6) puisque le déplacement des porteurs de charge est facilité. Cette augmentation avec la température mène à un renforcement du champ électrique dans le gaz proche du point triple. Par conséquent, la PDIV diminue, surtout à cause de l'augmentation de la permittivité relative, davantage avec la température que ce qui était attendu du seul fait de la diminution de la densité du gaz.

Après ces expériences, l'influence des conditions variées de température et de pression sur la FOV a été déterminée. La Figure 7 montre les résultats pour différentes températures en fonction de la densité du gaz. Chaque point de mesure représente la valeur moyenne de dix mesures (cinq répétitions pour chaque pression et deux répétitions pour chaque température).

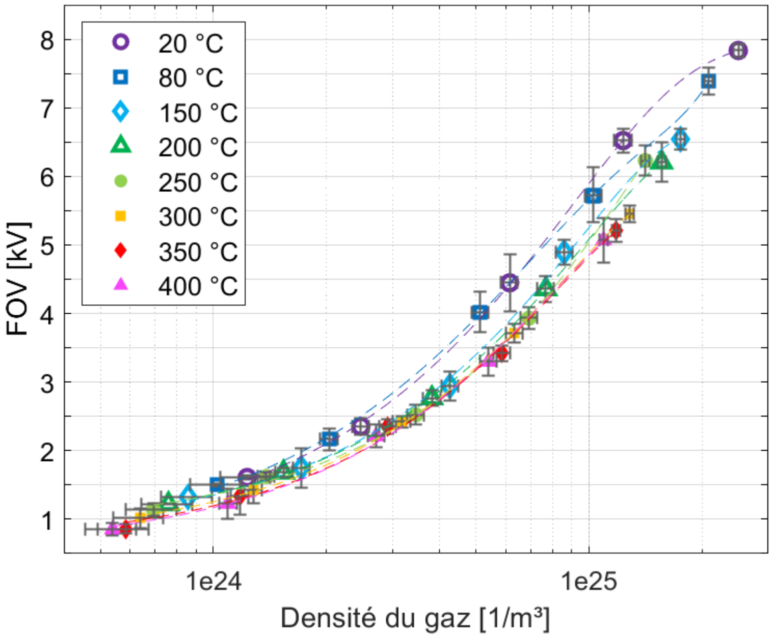

Figure 7. FOV en fonction de la densité du gaz pour différentes températures ; plaque d'alumine (99,7 %) ; azote.

Contrairement aux résultats présentés pour la PDIV en fonction de la densité du gaz (voir Figure 4), les courbes pour la FOV ont tendance à se rejoindre pour les températures élevées (> 150 °C). Ceci laisse donc supposer que la FOV n'est pas influencée par l'augmentation de la permittivité relative de l'alumine.

Une interprétation possible de cette différence s'appuie sur la polarisation non instantanée de l'alumine. En effet, une décharge de type streamer, ayant à pression atmosphérique une vitesse de propagation de 10^5 m/s, se déplace très rapidement sur la surface de l'isolant. Si on considère une distance de 1,1 cm entre l'électrode alimentée et la contre-électrode, le claquage a lieu en 10^{-7} s, ce qui correspond à une fréquence de 10 MHz. Or, comme le montre la Figure 6, l'augmentation de la permittivité relative de l'alumine est, indépendamment de la température, aux fréquences élevées très faible. Par conséquent, il est possible de formuler l'hypothèse qu'il n'y a aucune influence importante de la permittivité relative pour la fréquence considérée et qu'elle n'intervient donc pas dans la décharge menant au claquage.

Zusammenfassung auf Deutsch

In zahlreichen industriellen Anwendungen bildet das Vorhandensein einer Kontaktstelle zwischen einer Feststoffisolierung, einem elektrischen Leiter und dem umgebenden Gas einen Tripelpunkt, siehe Abbildung 1.

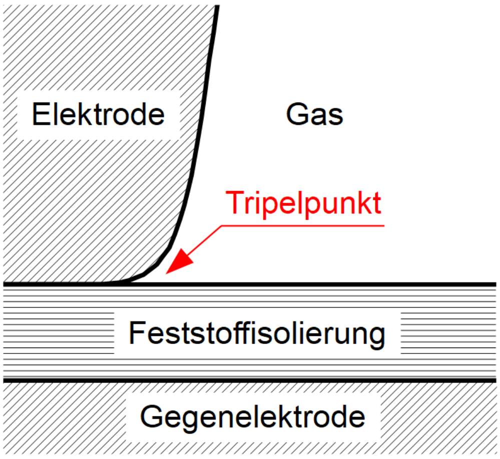

Abbildung 1. Schema einer Tripelpunktverbindung.

Obwohl auf die Geometrie der Tripelpunktverbindung geachtet wird, um das lokale elektrische Feld zu kontrollieren, ist letzteres wegen der Elektrodenkrümmung und des Unterschiedes in der relativen Permittivität zwischen der Feststoffisolierung und dem Gas erhöht. Dies begünstigt die Entstehung von Entladungsphänomenen wie Teilentladungen (TE) oder, bei höheren Spannungen, Oberflächenentladungen (Streamer). Die TE sind imstande, zu einer progressiven Verschlechterung der Isolierung beizutragen und letztendlich zum Versagen der Isolierung (Durchschlag, Überschlag) zu führen.

Tripelpunkte sind häufig in industriellen Anwendungen zu finden, in denen Feststoffisolierungen genutzt werden, um Hochspannungsleiter von anderen Systemkomponenten oder dem Erdpotential zu isolieren. Unter Umständen können diese extremen Umweltbedingungen (Temperatur, Druck) ausgesetzt sein, zum Beispiel im Luftfahrt- (Drücke bis zu 100 mbar) oder im Nuklearsektor (Temperaturen bis zu 650 °C).

Ziel dieser Studie ist es, zu einem besseren Verständnis der am Tripelpunkt unter verschiedenen Temperatur- und Druckbedingungen auftretenden Entladungsphänomene zu kommen. Dafür wurden Messungen der TE-Ein- (*Partial Discharge Inception Voltage*, PDIV) und der TE-Aussetzspannung (*Partial Discharge Extinction Voltage*, PDEV) sowie der Überschlagspannung (*Flashover Voltage*, FOV) durchgeführt. Dabei bestand der Versuchsaufbau aus einer Aluminiumoxidscheibe (Al_2O_3) zwischen einer geerdeten Edelstahlscheibe und einer mit Hochspannung (50 Hz AC) versorgten zylindrischen Wolframelektrode unter Gasdruckbedingungen (N_2) zwischen 50 mbar und Atmosphärendruck und Temperaturbedingungen zwischen Umgebungstemperatur und 400 °C.

Grundsätzlich können Gasentladungen unter der Bedingung entstehen, dass Anfangselektronen (hervorgerufen durch kosmische Strahlung, natürliche Radioaktivität, usw.) durch ein externes elektrisches Feld beschleunigt werden. Falls die Elektronen entlang ihrer mittleren freien Weglänge genügend Energie aufnehmen und ionisierend mit den Gasatomen/ Gasmolekülen kollidieren, kann sich eine Elektronenlawine ausbilden. Die Entladung wird selbsterhaltend, wenn die Anfangselektronen durch einen Sekundäremissionsmechanismus erneuert werden.

Der Einfluss der Temperatur auf die Entladungsentstehung kann unter Zuhilfenahme der allgemeinen Gasgleichung (1), der Gleichung für die mittlere freie Weglänge (2) und des elektrischen Feldes (3), welches in diesem Fall als homogen angenommen wird, beschrieben werden:

$$N = \frac{p}{k_B \cdot T} \quad (1) \qquad \lambda = \frac{1}{\sigma \cdot N} \quad (2) \qquad E = \frac{W_i}{e \cdot \lambda} \propto \frac{V}{d} \quad (3)$$

wobei N die Gasdichte, p der Druck, k_B die Boltzmann-Konstante, T die Temperatur, λ die mittlere freie Weglänge, σ der Wirkungsquerschnitt, E das elektrische Feld, W_i die Gasionisationsenergie, e die Elementarladung, V die Spannung und d der Elektrodenabstand ist.

Die Gleichungen zeigen, dass eine Temperaturerhöhung eine Verringerung der Gasdichte zur Folge hat, was wiederum zu einer Zunahme der mittleren freien Weglänge führt. Für eine gegebene Gasionisationsenergie nimmt demzufolge das elektrische Feld und damit die notwendige Spannung, um eine Entladung hervorzurufen, ab.

Um die Tripelpunktverbindung unter hohen Temperaturen und verschiedenen Gasdrücken/ Gasdichten untersuchen zu können, wurde eine für diese Studie entworfene und in Abbildung *2* dargestellte Versuchsanordnung in einer Vakuumkammer platziert.

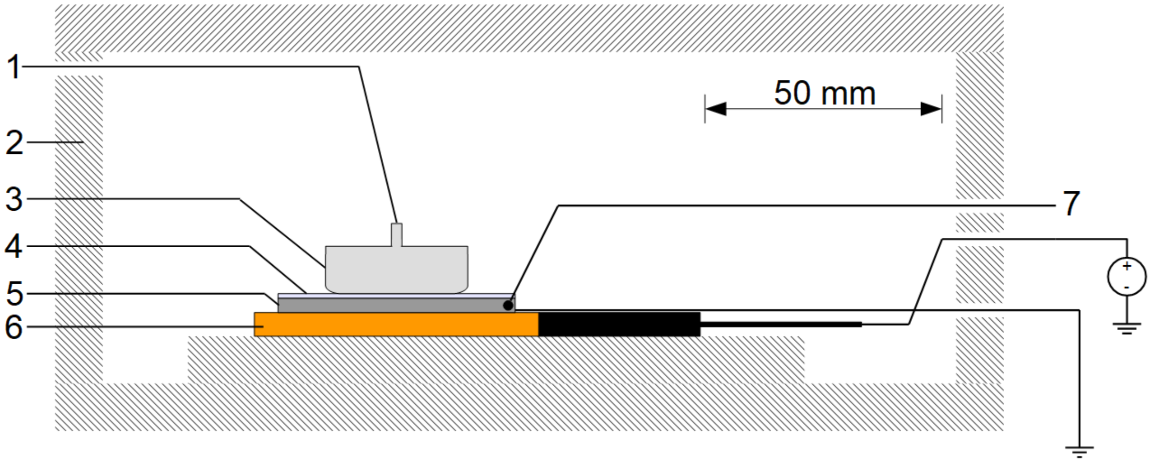

1 – Hochspannungsanschluss, 2 – Hitzebeständige Box, 3 – Elektrode (Wolfram),
4 – Feststoffisolierung, 5 – Gegenelektrode (Edelstahl), 6 – Heizplatte, 7 – Thermoelement

Abbildung 2. Schema der Tripelpunktanordnung inklusive der Heizplatte im Inneren der hitzebeständigen Box.

Die Tripelpunktanordnung besteht aus einer zylindrischen Wolframelektrode (Durchmesser von 30 mm) mit Rogowski-Profil (3), die mit Hochspannung (50 Hz AC) versorgt wird (1), einer Aluminiumoxidscheibe (Al_2O_3, Reinheit von 99,7 %, Durchmesser von 50 mm und Dicke von 1 mm) (4) als Feststoffisolierung und einer Edelstahlscheibe (Durchmesser von 50 mm) (5), die an das Erdpotential angeschlossen ist. Dieser Aufbau befindet sich auf einer keramischen Heizplatte (Siliziumnitrid) (6), welche separat durch eine Gleichspannungsquelle (0-64 V, 0-6 A) versorgt und bis zu einer Temperatur von 400 °C (gemessen in der Nähe des Tripelpunktes) betrieben wurde. Die Temperatur der Edelstahlscheibe wurde mithilfe eines Thermoelements (Typ K) (7) gemessen und diente als Eingangssignal für die Temperaturregelung der Heizplatte, welche mit LabVIEW unter Verwendung eines PI-Regler umgesetzt wurde. Die Tripelpunktanordnung wurde in einer hitzebeständigen Box (2) platziert, die aus einem porösen Aluminiumoxid mit geringer Wärmeleitfähigkeit bestand, um die Temperatur um den Tripelpunkt herum zu homogenisieren und die Vakuumkammer aus PMMA (Polymethylmethacrylat) zu schützen, in welcher sich die hitzebeständige Box befand.

Abbildung 3 zeigt schematisch den Versuchsaufbau einschließlich der hitzebeständigen Box mit der Tripelpunktanordnung.

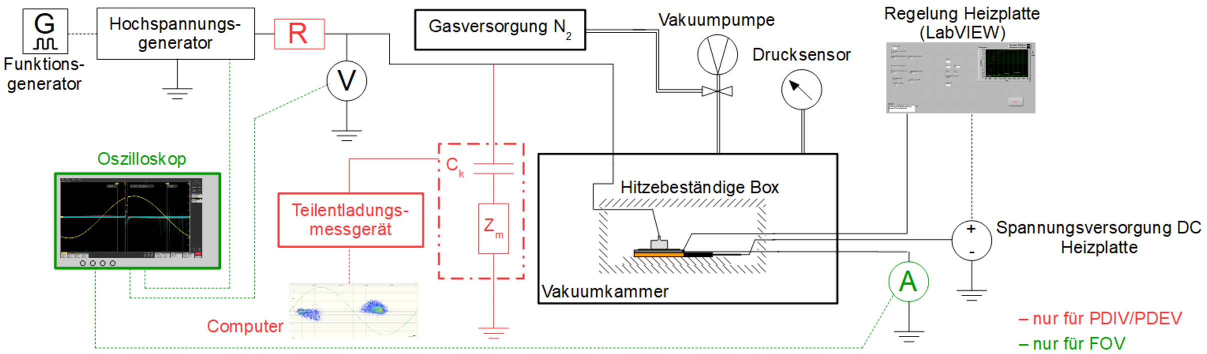

Abbildung 3. Schema des Versuchsaufbaus zur Bestimmung der PDIV/PDEV und der FOV.

Die Wolframelektrode wurde an eine Hochspannungsquelle angeschlossen, die mittels eines Funktionsgenerators (50 Hz AC) gesteuert und mit einem Schutzwiderstand (10 MΩ) in Reihe geschaltet wurde (nur für die PDIV/PDEV-Messungen). Die PDIV sowie die PDEV wurden gemäß der Norm IEC 60270 unter Nutzung eines handelsüblichen Teilentladungsmessgerätes (OMICRON MPD 600) bestimmt, welches über einen 250 pF-Koppelkondensator parallel zur Tripelpunktanordnung geschaltet war, während für die FOV-Messungen nur eine an ein Oszilloskop angeschlossene Strommesssonde (CT-2) verwendet wurde. Die angelegte Spannung wurde mittels einer am Oszilloskop angeschlossenen Spannungssonde (Tektronix P6015A) gemessen.

Alle Experimente wurden innerhalb einer Vakuumkammer durchgeführt, welche eine genaue Einstellung des Stickstoffdrucks ermöglichte. Dieses Gas wurde gewählt, um unerwünschte Effekte durch die Oxidation der Elektroden in der hitzebeständigen Box zu vermeiden und um gleichzeitig die elektrischen Eigenschaften zu wahren, die denen von Luft nahekommen. Eine Vakuumpumpe sowie eine Stickstoffversorgung wurden an die Vakuumkammer angeschlossen und der Druck innerhalb dieser wurde mittels eines Drucksensors (Pfeiffer PCR 280) gemessen.

Eine genaue Überwachung sowie eine geeignete Regelung der Heizplatte waren für diese Studie unerlässlich. Temperaturmessungen am Tripelpunkt und im Gas in der Nähe von diesem ergaben lediglich einen geringen Temperaturunterschied zwischen diesen beiden Punkten. Somit konnte die Gasdichte am Tripelpunkt, an welchem die Entladungsentstehung zu erwarten ist, und in seiner nahen Umgebung als ähnlich angesehen werden.

Unter Berücksichtigung, dass die Geometrie des Tripelpunktes unverändert blieb, während Druck und Temperatur variabel waren, sowie dass der Parameter des Elektrodenabstandes für diese Geometrie bedeutungslos war (im Gegensatz zu einer Situation mit klar definiertem Elektrodenabstand, die folglich anhand einer Paschenkurve veranschaulicht werden kann), wurde festgelegt, die Ergebnisse lediglich in Abhängigkeit des Drucks/der Gasdichte darzustellen.

Jedes Experiment wurde von der niedrigsten Temperatur (Umgebungstemperatur) hin zur höchsten (400 °C) und für jede Temperatur vom höchsten Druck (Atmosphärendruck) hin zum niedrigsten (50 mbar) durchgeführt.

Um einheitliche Messungen zu gewährleisten, wurde ein standardisiertes Verfahren zur Bestimmung der PDIV/PDEV sowie der FOV genutzt. Für die Bestimmung der PDIV wurde zunächst eine Spannung von etwa 100 V unterhalb der erwarteten PDIV angelegt und anschließend in 10 V-Schritten mit einer Dauer von 10 s erhöht. Falls eine Entladung (Detektionsschwelle: 3 pC) registriert wurde, wurde die Spannung für 30 s beibehalten und sobald in diesem Zeitintervall mehr als 30 Entladungen registriert wurden, wurde die Spannung (Scheitelwert) als PDIV festgehalten. Anderenfalls wurde die Spannung erneut um 10 V erhöht. Für die Ermittlung der PDEV wurde, ausgehend von der PDIV, die angelegte Spannung in 10 V-Schritten ohne zeitliche Beschränkung verringert und der PDEV-Wert dann festgehalten, wenn innerhalb von 30 s keine Entladungen mehr registriert wurden.

Ein ähnliches Verfahren wurde zur Bestimmung der FOV angewandt: Zunächst wurde eine Spannung von etwa 1 kV unterhalb der erwarteten FOV angelegt und diese dann solange alle 10 s in 100 V-Schritten erhöht, bis der Überschlag auftrat.

Zusätzlich zu den beschriebenen Messungen, wurden für dieselbe Aluminiumoxidscheibe und im selben Temperaturbereich noch andere Messungen durchgeführt: Messungen der relativen Permittivität für verschiedene Frequenzen zwischen 20 Hz und 1 kHz durch Ermittlung der Kapazität der Aluminiumoxidscheibe mittels eines LCR-Meters (Wayne Kerr LCR Meter 4300) sowie des spezifischen Volumenwiderstandes durch Messung des Stromes mittels eines Piko-Amperemeters (Keithley Model 6485 Picoammeter).

Zunächst wurde zunächst der Einfluss verschiedener geometrischer und dielektrischer Eigenschaften der Feststoffisolierung auf die PDIV bei Umgebungstemperatur und verschiedenen Drücken im Bereich zwischen Atmosphärendruck und 50 mbar untersucht.

Es kann festgehalten werden, dass die PDIV mit der Dicke der Feststoffisolierung zunimmt, da die dadurch kleinere Kapazität zu einem schwächeren elektrischen Feld im Gas führt. Die PDIV nimmt hingegen mit Zunahme der der relativen Permittivität ab, da dies zu einer

Verstärkung des elektrischen Feldes im Gas führt, welche das Auslösen von Entladungen erleichtert.

Ferner führt eine metallische Schicht (Dicke von 100 nm) auf der Oberfläche der Feststoffisolierung in Kontakt mit dem Hochspannungspotential zu einer signifikativen Erhöhung der PDIV. Dies ist durch eine geänderte Geometrie am Rand der metallischen Schicht bedingt, da hier das Auslösen von Entladungen mangels eines ausreichend großen Gasintervalls für die Entwicklung von Elektronenlawinen erschwert ist – im Gegensatz zu der sich ergebenden Geometrie der auf die bloße Oberfläche der Aluminiumoxidscheibe gestellten zylindrischen Elektrode, welche ein genügend großes Gasintervall bietet.

Als nächstes wurde der Einfluss verschiedener Temperatur- und Druckbedingungen auf die PDIV und die PDEV analysiert. Abbildung 4 zeigt als Beispiel die Messergebnisse für die PDIV für verschiedene Temperaturen in Abhängigkeit der Gasdichte für eine Aluminiumoxidplatte einer Reinheit von 99,7 %. Um das Ablesen zu erleichtern, wurden alle Punkte, die zur selben Temperatur gehören, mit einer Trendlinie (Polynom zweiten Grades) verbunden. Jeder Messpunkt entspricht dem Mittelwert von 15 Messungen (fünf Wiederholungen jedes Druckpunktes und drei Wiederholungen jeder Temperatur). Die Fehlerbalken wurden für eine 1σ-Standardabweichung berechnet und für die Gasdichte wurde die vom Druckbereich abhängige Messunsicherheit des Drucksensors gemäß den Herstellerangaben berücksichtigt.

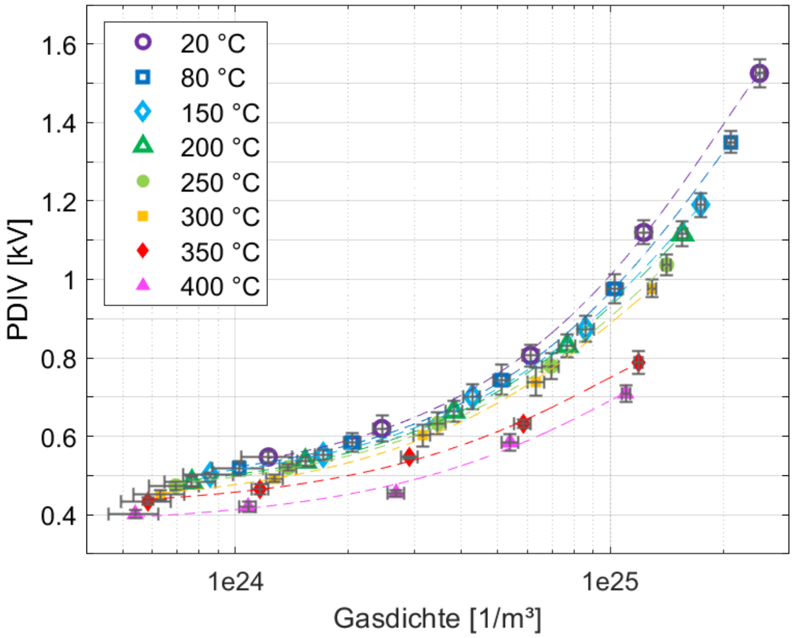

Abbildung 4. PDIV in Abhängigkeit der Gasdichte für verschiedene Temperaturen; Stickstoff; Aluminiumoxidscheibe (99,7 %).

Die Ergebnisse in Abbildung 4 zeigen, dass die PDIV erwartungsgemäß für alle Temperaturen mit dem Druck zunimmt. Ferner zeigen die Ergebnisse, dass eine Erhöhung der Temperatur zu einer Verringerung der PDIV führt, was konform mit der Theorie ist. Die Differenz der PDIV zwischen 20 °C und 400 °C bei Atmosphärendruck beläuft sich beispielsweise auf 820 V.

Nichtsdestotrotz sollte unter der Annahme, dass die Gasdichte in der Nähe des Tripelpunktes ähnlich ist, erwartet werden, dass alle Trendlinien zusammenlaufen, wenn sie, wie hier, in Abhängigkeit der Gasdichte dargestellt werden. Bei einer Erhöhung der Temperatur auf 400 °C liegt jedoch jede PDIV-Reihe leicht unterhalb der vorherigen. Zudem ist ein größerer Unterschied zwischen 300 °C und 350 °C erkennbar. Somit erklärt die bei einem gegebenen Druck die Abnahme der Gasdichte mit der Temperatur nicht mehr allein die Verringerung der PDIV.

Um dieses Phänomen erklären zu können, muss der Einfluss der Temperatur auf die dielektrischen Eigenschaften der Aluminiumoxidscheibe berücksichtigt werden. Deshalb wurden dielektrische Messungen, vor allem des spezifischen Volumenwiderstandes und der relativen Permittivität, in Abhängigkeit der Temperatur durchgeführt, siehe Abbildung 5 und Abbildung 6.

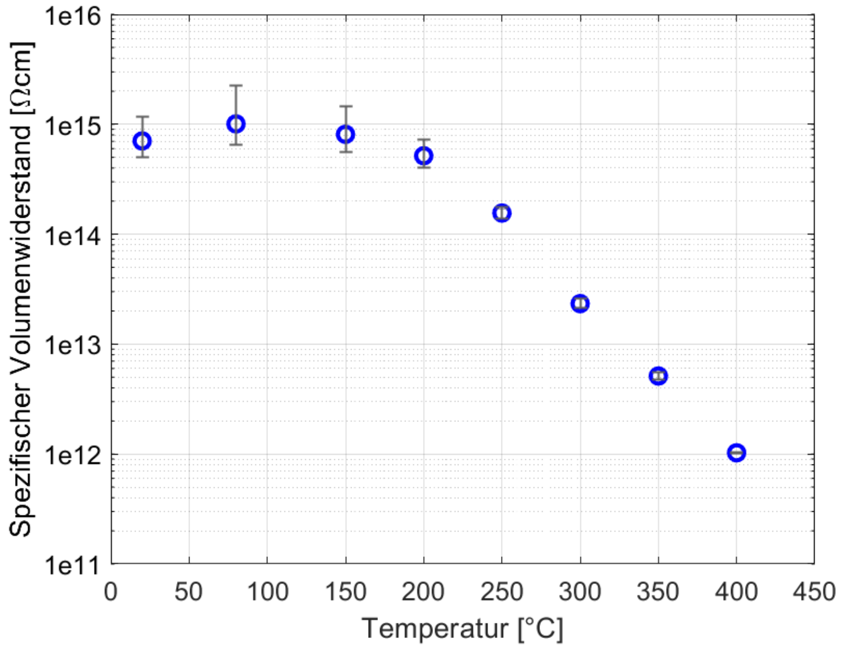

Abbildung 5. Spezifischer Volumenwiderstand der Aluminiumoxidscheibe (99,7 %) für verschiedene Temperaturen.

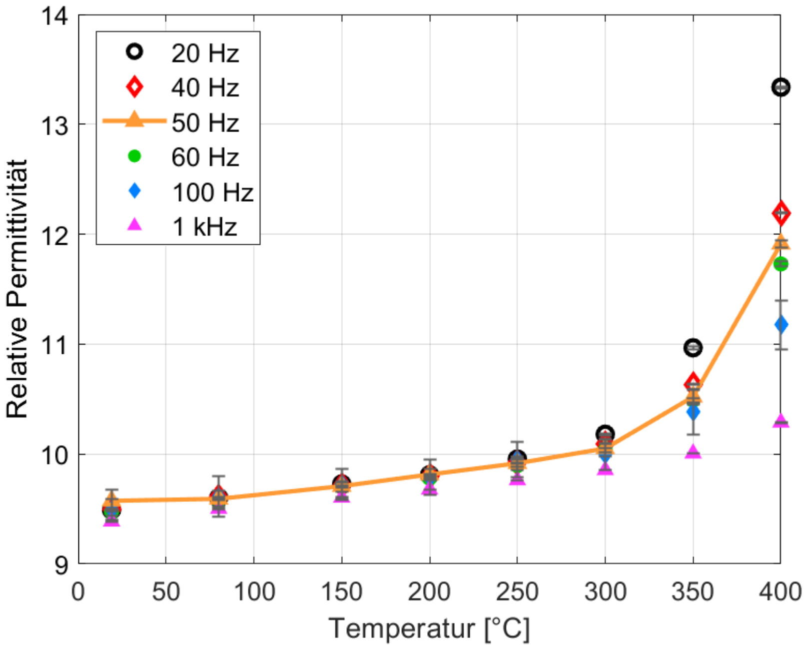

Abbildung 6. Relative Permittivität der Aluminiumoxidscheibe (99,7 %) für verschiedene Temperaturen und Frequenzen. Die Messung bei einer Frequenz von 50 Hz ist durch eine durchgezogene Linie hervorgehoben.

Abbildung 5 zeigt, dass der spezifische Volumenwiderstand mit der Temperatur abnimmt, was zu einer höheren TE-Aktivität führt. Damit steigt, unter Berücksichtigung des standardisierten Verfahrens zur Bestimmung der PDIV, die Wahrscheinlichkeit, TEs zu detektieren. Dies resultiert in einer Verringerung der PDIV. Die Abnahme des spezifischen Volumenwiderstandes kann auch die Zunahme der relativen Permittivität erklären, siehe Abbildung 6, da die Ladungsträgerbewegung erleichtert wird. Diese Erhöhung mit der Temperatur führt zu einer Verstärkung des elektrischen Feldes im Gas in der Nähe des Tripelpunktes. Folglich nimmt die PDIV, vor allem aufgrund der Zunahme der relativen Permittivität, mit der Temperatur stärker ab, als allein durch die Verringerung der Gasdichte zu erwarten gewesen wäre.

Nach diesen Experimenten wurde der Einfluss verschiedener Temperatur- und Druckbedingungen auf die FOV untersucht. Abbildung 7 zeigt die Ergebnisse für verschiedene Temperaturen in Abhängigkeit der Gasdichte. Jeder Messpunkt entspricht dem Mittelwert von zehn Messungen (fünf Wiederholungen jedes Druckpunktes und zwei Wiederholungen jeder Temperatur).

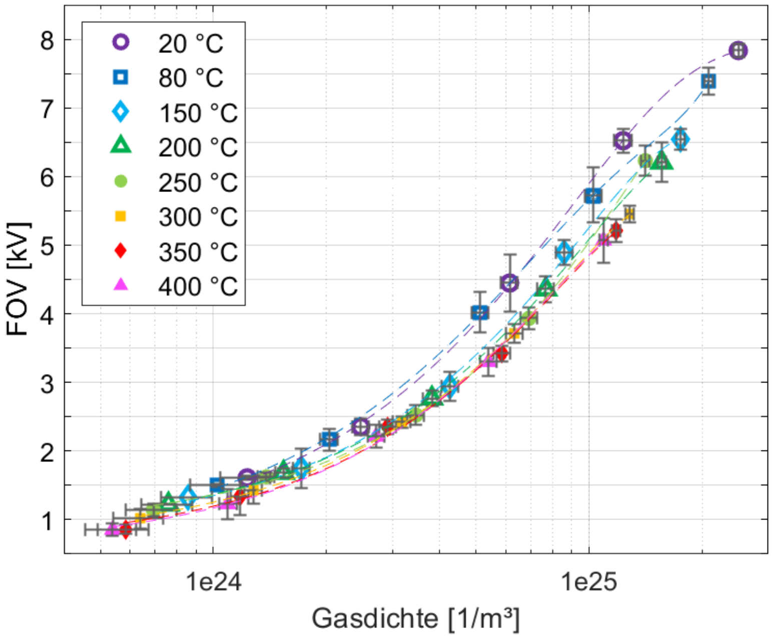

Abbildung 7. FOV in Abhängigkeit der Gasdichte für verschiedene Temperaturen; Stickstoff; Aluminiumoxidscheibe (99,7 %).

Im Gegensatz zu den für die PDIV in Abhängigkeit der Gasdichte präsentierten Ergebnissen (siehe Abbildung 4) tendieren die Kurven für die FOV dazu, sich für erhöhte Temperaturen (> 150 °C) zu vereinen. Dies lässt daher vermuten, dass die FOV nicht durch die Zunahme der relativen Permittivität beeinflusst wird.

Eine mögliche Interpretation dieses Unterschiedes stützt sich auf die nicht unmittelbare Polarisation des Aluminiumoxides. Eine Streamerentladung, welche bei Atmosphärendruck eine Ausbreitungsgeschwindigkeit von 10^5 m/s hat, bewegt sich sehr schnell auf der Oberfläche der Isolierung. Wenn ein Abstand zwischen der mit der Spannung versorgten und der geerdeten Elektrode von 1,1 cm angenommen wird, erfolgt der Überschlag innerhalb von 10^{-7} s, was einer Frequenz von 10 MHz entspricht. Wie Abbildung 6 zeigt, nimmt die relative Permittivität von Aluminiumoxid für hohe Frequenzen und unabhängig von der Temperatur nur wenig zu. Daher kann angenommen werden, dass es keinen bedeutenden Einfluss der relativen Permittivität für die betrachtete Frequenz gibt und diese demzufolge nicht die zum Überschlag führende Entladung beeinflusst.